



AFRL-AFOSR-VA-TR-2016-0254

Energy Flow in Dense Off-Equilibrium Plasma

Seth Putterman
UNIVERSITY OF CALIFORNIA LOS ANGELES
11000 KINROSS AVE STE 102
LOS ANGELES, CA 90095-0001

07/15/2016
Final Report

DISTRIBUTION A: Distribution approved for public release.

Air Force Research Laboratory
AF Office Of Scientific Research (AFOSR)/RTB1

Arlington, Virginia 22203
Air Force Materiel Command

DISTRIBUTION A: Distribution approved for public release.

REPORT DOCUMENTATION PAGE

Fonn Approved
OMB No. 071J4.0188

The public reporting burden for this collection of information is estimated to average 1 hour per response, including the time for reviewing instructions, searching existing data sources, gathering and maintaining the data needed, and completing and reviewing the collection of information. Send comments regarding this burden estimate or any other aspect of this collection of information, including suggestions for reducing the burden, to the Department of Defense, Executive Service Directorate (0704-0188). Respondents should be aware that notwithstanding any other provision of law, no person shall be subject to a penalty for failing to comply with a collection of information if it does not display a currently valid OMB control number.

PLEASE DO NOT RETURN YOUR FORM TO THE ABOVE ORGANIZATION.

1. REPORT DATE (DD-MM-YYYY) 12-07-2016			12. REPORT TYPE Final		3. DATES COVERED (From - To) April 1, 2012 - Jun 30, 2016	
4. TITLE AND SUBTITLE Energy Flow in Dense Off-Equilibrium Plasma					5a. CONTRACT NUMBER	
					5b. GRANT NUMBER FA9550-12-1-0062	
					5c. PROGRAM ELEMENT NUMBER	
6. AUTHOR(S) Seth Putterman Alex Battler John Koulakis Seth Pree Alexandra Latshaw					5d. PROJECT NUMBER	
					5a. TASK NUMBER	
					5i. WORK UNIT NUMBER	
7. PERFORMING ORGANIZATION NAME(S) AND ADDRESS(ES) UCLA					8. PERFORMING ORGANIZATION REPORT NUMBER	
9. SPONSORING/MONITORING AGENCY NAME(S) AND ADDRESS(ES) Air Force Office of Scientific Research 875 North Randolph Street Suite 325, Room 3112 Arlington VA, 22203					10. SPONSOR/MONITOR'S ACRONYM(S) AFOSR	
					11. SPONSOR/MONITOR'S REPORT NUMBER(S)	
12. DISTRIBUTION/AVAILABILITY STATEMENT DISTRIBUTION A: Distribution approved for public release.						
13. SUPPLEMENTARY NOTES						
14. ABSTRACT We created warm, dense plasmas with sonoluminescence, laser breakdown, and sparks - very different systems that all produce plasmas with a similar thermodynamic state. Probing sonoluminescence with visible-wavelength lasers yielded measurements of ionization potential lowering and collision times in dense plasmas, allowing us to distinguish between competing dense-plasma models. Hydrodynamic analysis of shockwaves generated by sparks yielded similar measurements in a different, more accessible system. Ultra-fast observations of laser breakdown have revealed a new phase of off-equilibrium plasma that has a tensile strength similar to a liquid, and reduced ion-electron collision cross-sections. By working at micron length scales, and nanosecond time scales, we are able to use table-top experiments to elucidate the properties of these exotic plasmas.						
15. SUBJECT TERMS dense plasma, sparks, laser breakdown, sonoluminescence, ionization potential lowering, shockwaves						
16. SECURITY CLASSIFICATION OF:			17. LIMITATION OF ABSTRACT	18. NUMBER OF PAGES	19a. NAME OF RESPONSIBLE PERSON Seth Putterman	
a. REPORT U	b. ABSTRACT U	c. THIS PAGE U			19b. TELEPHONE NUMBER (Include area code) 310-825-2269	

DISTRIBUTION A: Distribution approved for public release.

Standard Form 298 (Rev. 8198)
Prescribed by ANSI Std. Z39.18
Adobe Professional 7.0

Energy Flow in Dense Off-Equilibrium Plasma

Final Report

FA9550-12-1-0062

Submitted by Seth Putterman, July 2016

Jason Marshall PM – AFOSR

Part 1: Energy Balance in Sonoluminescing Dense Plasma

Part 2: Tensile Strength in Off-Equilibrium, Dense Plasma

*Part 3: Broadband, High-Power Light Switch Enabled by
Ionization Lowering in Spark Discharges*

Part 4: Publications

Part 5: Slides from Previous Reports

Part 1: Energy Balance in Sonoluminescing Dense Plasma

Sonoluminescence occurs from rapid implosion of gas bubbles caused to pulsate by an externally imposed sound wave. Adiabatic compression, and in some cases shock waves, heat the gas during the collapse phase. At maximum compression, energy density transforms gas into cold ($\sim\text{eV}$), dense ($>10^{21}\text{ cm}^{-3}$) plasma. Light emission occurs due to thermal bremsstrahlung. This research is driven by the fact that Sonoluminescence provides a laboratory for the study of dense plasmas, formed in a process that concentrates energy density by 12 orders of magnitude. We study this system through i) Mie scattering [Figure 1] which measures the radius of the bubble, ii) spectral analysis of the emitted light which gives the temperature, and iii) light scattering which is sensitive to the plasma density. The clock-like nature of Sonoluminescence facilitates data acquisition. In a 40kHz sound field there are 40,000 flashes of light per second due to an implosion rate of 40kHz. Figure 2 shows the radius versus time for a xenon bubble in 85% sulfuric acid, as determined by Mie scattering. In this case the acoustic frequency is 28.5kHz. A photograph of the setup is shown in Figure 3 along with a finite time exposure of the light emission blue [which occurs at the minimum radius and the response to a single pulse of Mie scattering [red] at the maximum radius.

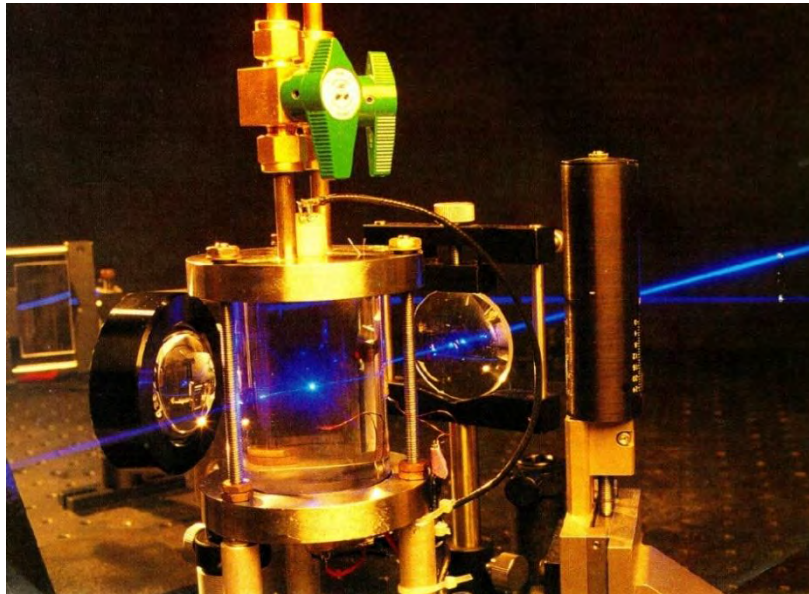


Figure 1: S. Putterman, Scientific American 272 (2) 46-51, 1995

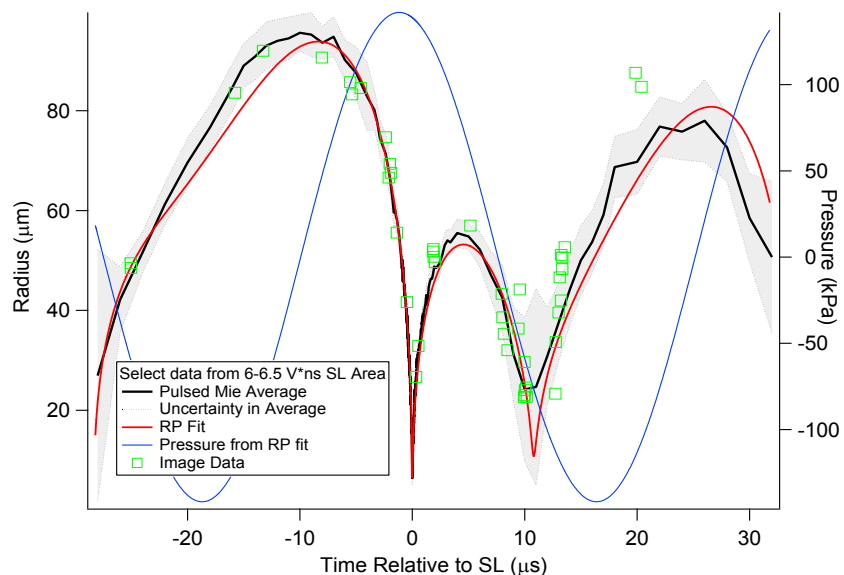


Figure 2: B. Kappus et al. Phys. Rev. Lett. 2013.

The radius vs time curve at the moment of bubble collapse is shown in Figure 4, along with the energy/atom available for ionization, calculated from the bubble dynamics. The energetics analysis reveals that there is only 2.1 eV/atom available for ionization at the time of the minimum bubble radius. The ionization energy of an isolated xenon atom is 12 eV.

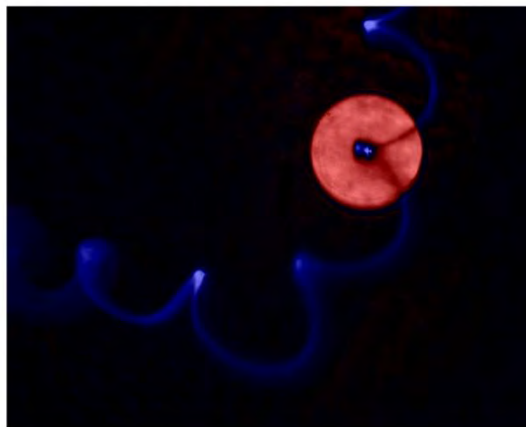
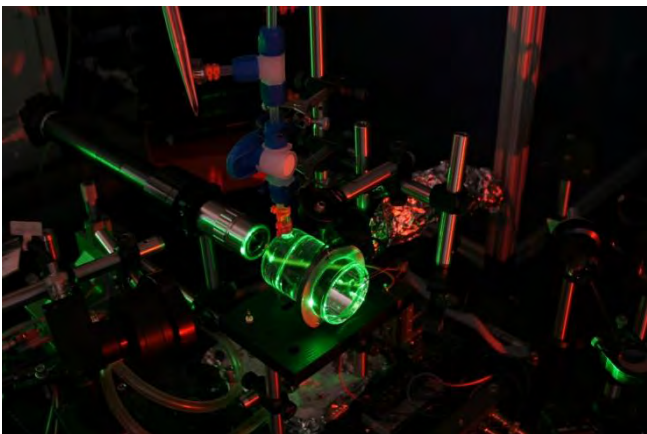


Figure 3: Sonoluminescing Xenon bubble in sulfuric acid, driven at 28.5 kHz. Mie scattering (right) provides complete characterization of the hydrodynamics.

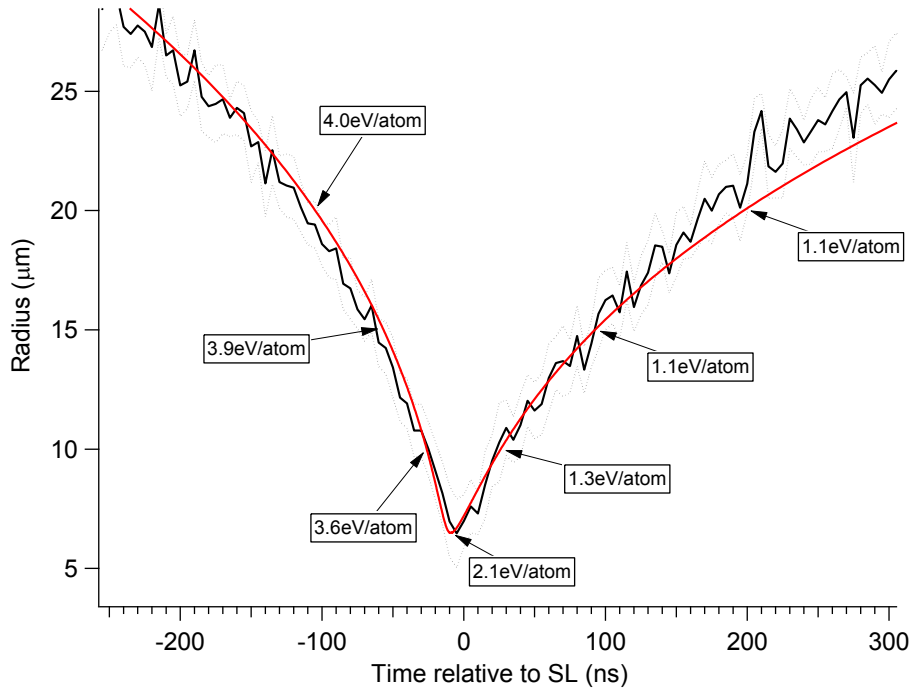


Figure 4: Radius vs Time of a sonoluminescing Xenon bubble at the time of collapse. Energy analysis shows that there is only 2.1 eV/atom available for ionization.

On the other hand, spectral measurements of the 13 ns flash reveal that the emission is a blackbody spectrum [see Figure 5], and the blackbody size matches the radius obtained from Mie scattering (6.5 micron). This means that the emissivity of the sonoluminescence plasma is close to 1 and implies that it is opaque to light. We directly observed the opacity to visible light by shooting the sonoluminescing bubble with a laser. Eight frames of the interaction of the laser pulse with the dense plasma was captured with a nanosecond framing camera, shown in Figure 6 (frame to frame time is 10 ns). The laser comes in from the right and hits the bubble creating a hot, brighter region that propagates across the bubble over ~ 80 ns. A very high charge density is required for these phenomena to occur. We therefore conclude that the ionization potential is dramatically lowered inside the sonoluminescing plasma.

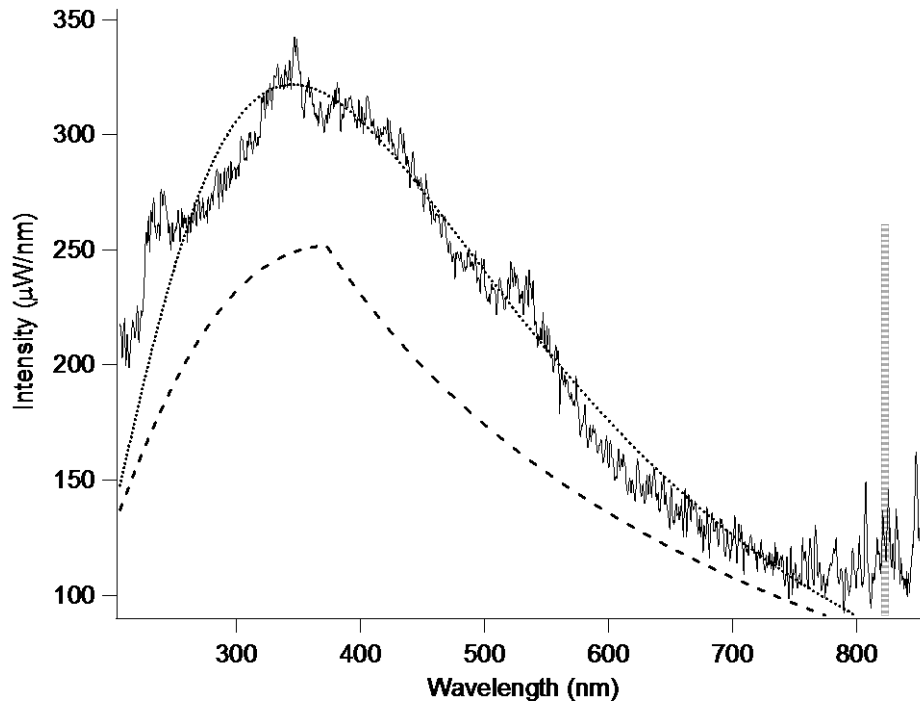


Figure 5: Spectroscopy of 13 ns sonoluminescence flash matches ideal Planck blackbody. Kappus et al, Phys Rev Let 2013.

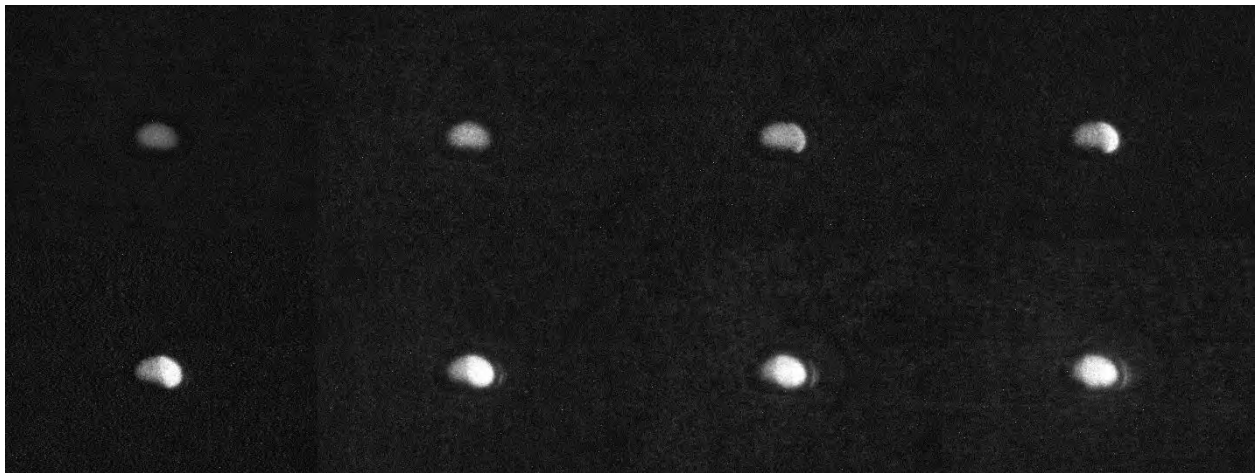


Figure 6: Frames from a movie of the propagation of an energy pulse across a dense plasma. Time between frames is 10 ns. Prof K. Weninger and Dr. B. Kappus.

We probed the dense plasma inside a sonoluminescing bubble at two wavelength, 532 nm, and 1064 nm, with the experimental setup shown in Figure 7. Here, the laser pulse is scanned in time to interact with the bubble at different times relative to the emission of sonoluminescence. Figure 8 shows the results. The red points represent the Mie scattering (proportional to bubble size) and the black points represent the light emission from the bubble. The scatter is due to random misalignments of the laser and bubble, however the maximum of the scattered points can be interpreted as a direct hit. As the bubble approaches its minimum

size (Mie scattering goes down) the plasma becomes dense, and begins to interact with visible light. If the plasma absorbs the laser pulse, the light emission will increase, otherwise it will stay the same. Before the bubble becomes small, there is only emission from the usual sonoluminescence (band at 1 on the PMT intensity), because the plasma does not interact with the laser. When the bubble is small and the plasma is dense, we see that the 532 nm is always absorbed to varying degrees, and the emission increases. However, the 1064 is less readily absorbed, as is visible by the 'gap' between 2 and 10 on the PMT intensity. In other words, our measurements find that 532 nm always interacts with the plasma, whereas for 1064, there is a threshold for interaction.

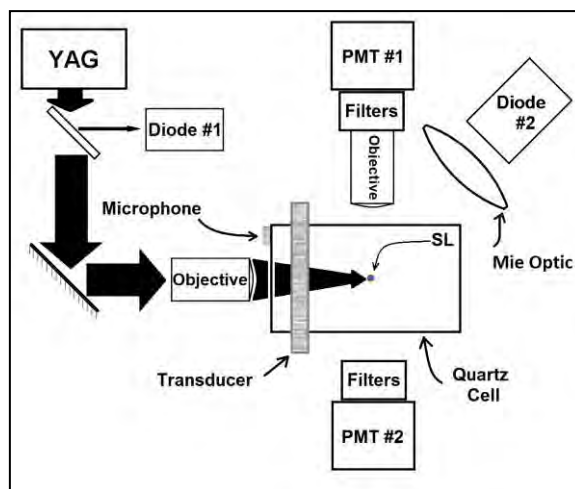


Figure 7: Simultaneous Mie scattering and light emission measurements from sonoluminescence interacting with a laser pulse at 1064 or 532 nm.

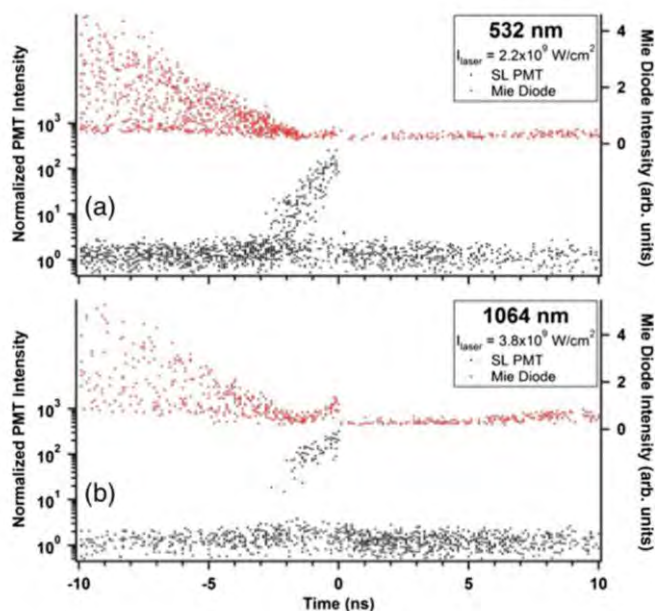
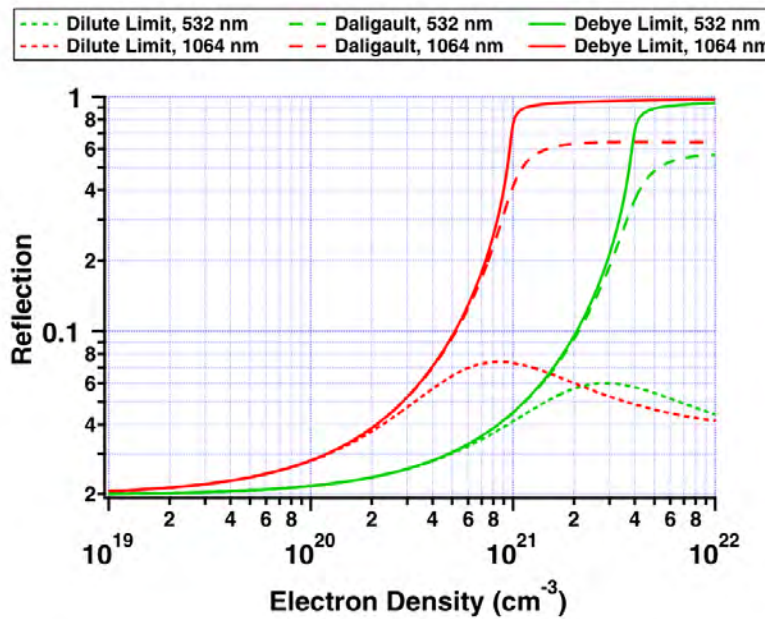


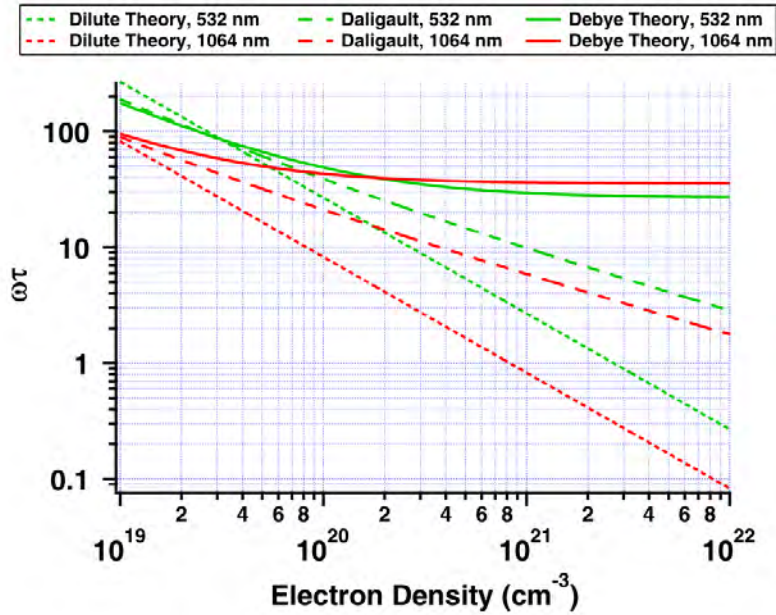
Figure 8: Scatter plots showing the Mie scatter intensity (red dots) and the SL intensity (black dots) for (a) 532 and (b) 1064 nm. The SL intensity is normalized by the intensity distribution of SL flashes

without an incident laser pulse and can be seen as a band of points centered on unity. For each SL intensity point, there is a corresponding Mie scatter point which is a measure of the bubbles' radius and confirms successful spatial synchronization. SL-laser interactions only occur when the laser and SL flash overlap in time. The spread in Mie scatter points is due to the drift in bubble location relative to the laser focus during the laser's repetition rate (10 Hz). As SL-laser interactions grow stronger, the accompanying Mie scatter signal increases due to an enlarged plasma radius.

This can be ascribed to a large degree of reflection by 1064nm and a large absorption rate for 532, a behavior that occurs for plasmas with low collisionality compared to the interacting light's wavelength. We can use these observations to choose between dispersion relationships given by different dense plasma models. See (Battaler 2014) for details, but in short, the reflection and absorption expected based on various theories is calculated (Figure 9), and compared with experiment to choose the best model. The proposed theories of dense plasmas give very different predictions. Our data selects in favor of the screening theory of Baalrud and Daligault.



a)



b)

Figure 9: a) Plasma reflection of 532 and 1064 nm light as a function of electron density for various collision theories. The Debye theory (solid curves) represents a highly screened plasma, where $\omega\tau \gg 1$ and high levels of reflection are observed for $\omega < \omega_p$. The dilute theory (dotted curves) diverges from the high reflectivity behavior due to strong damping ($\omega\tau \lesssim 1$) in the high density regime. The Daligault theory (dashed curves) experiences an intermediate level of reflection in the dense regime and is capable of describing both reflection at 1064 nm and spectral opacity at 532 nm. b) Collision time of 532 and 1064 nm light as a function of electron density for various collision theories. The collision time for the Debye theory (solid curves) is large for all electron densities and becomes density-independent for large plasma parameters. The dilute theory (dotted curves) represents the shortest collision time. The intermediate theory of Daligault (dashed curves) lies between these limiting theories and scales with ωp for large densities.

Part 2: Tensile Strength in Off-Equilibrium, Dense Plasma

In this section we describe evidence for strong pressure reduction in plasmas formed in the laser-breakdown of dense gases. Collective processes lower the effective ionization threshold, and lead to a tensile strength in off-equilibrium plasmas.

1. EXPERIMENTAL DESCRIPTION OF LASER-BREAKDOWN SYSTEM

Before showing that a plasma formed in a dense gas can have a tensile strength, we describe the experimental setup of the laser breakdowns system. A femto-second laser pulse is focused into the center of a high-pressure (up to 75 atm) gas chamber through windows in the chamber wall (chamber shown in Figure 10a). The small size and fast dynamics of the system require specialized diagnostic equipment. Magnifying optics project an image of the breakdown onto the entrance slit of a spectrometer which can be set in two modes: 1) when the grating is set to image the zeroth order diffraction, it acts as a simple mirror, relaying the image to the spectrometer output, and 2) when the grating is set to image the first order diffraction, it separates the light by wavelength acting as a spectrometer. The output of the spectrometer is imaged by a streak camera, which resolves sub-nanosecond dynamics. Both modes of the spectrometer are useful and important. In zeroth order, the streak image gives time-resolved information about the size of the plasma, while in first order the streak image gives time-resolved information about the plasma emission spectrum. The spectrometer and streak camera can be seen in Figure 10b, and Figure 11 shows a block diagram of the imaging optics.

An example of a streak image acquired in the spatial information mode (zeroth order) is shown in Figure 12a, which displays the width of the cigar-shaped laser breakdown in time, with the false-coloring indicating its brightness. In this case, the gas is 5 atm of Xe. Super-Gaussian fits at every time point of the streak image give the plasma width over time, displayed in Figure 12b. Data acquired in spectrum mode (first order) is shown in Figure 13. At low pressures, we see that the spectrum is line dominated (Figure 13a) – indicative of a transparent gas. In contrast, at high pressures (Figure 13b) the spectrum becomes broad, and fits well to a Plank (blackbody) spectrum (Figure 14). We extract the temperature of the plasma from the best-fit Plank curve.

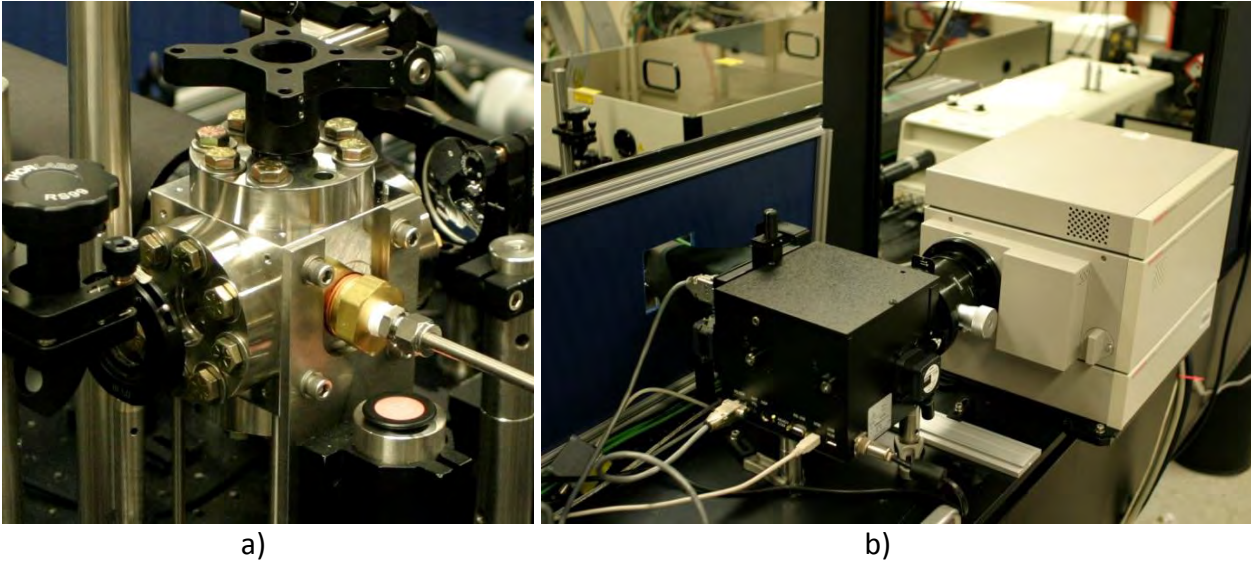


Figure 10: a) Photo of the high-pressure chamber. The chamber has 5x quartz windows for optical diagnostics and laser focusing. The focusing lens is located directly above the chamber and is aligned using a rail system. b) Optical diagnostics for the laser breakdown micro-plasma. An imaging triplet lens (not in photo due to scale) produces a magnified image onto the entrance slit of the Acton spectrometer (black instrument). The Hamamatsu streak camera (white instrument) spreads the micro-plasma light emission in time. In the background are the lasers that produce the ultra-short pulses needed for micro-plasma generation.

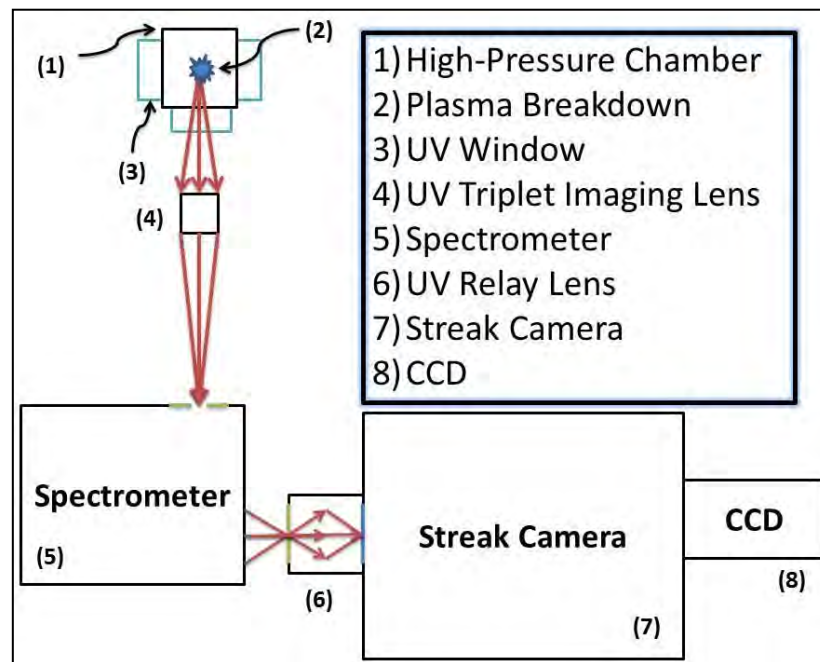


Figure 11: Block Diagram of apparatus used to image dwell time of dense microplasma, and to collect spectra. Band pass filters can be inserted into the path of the light and the spectrometer can be operate in reflection mode.

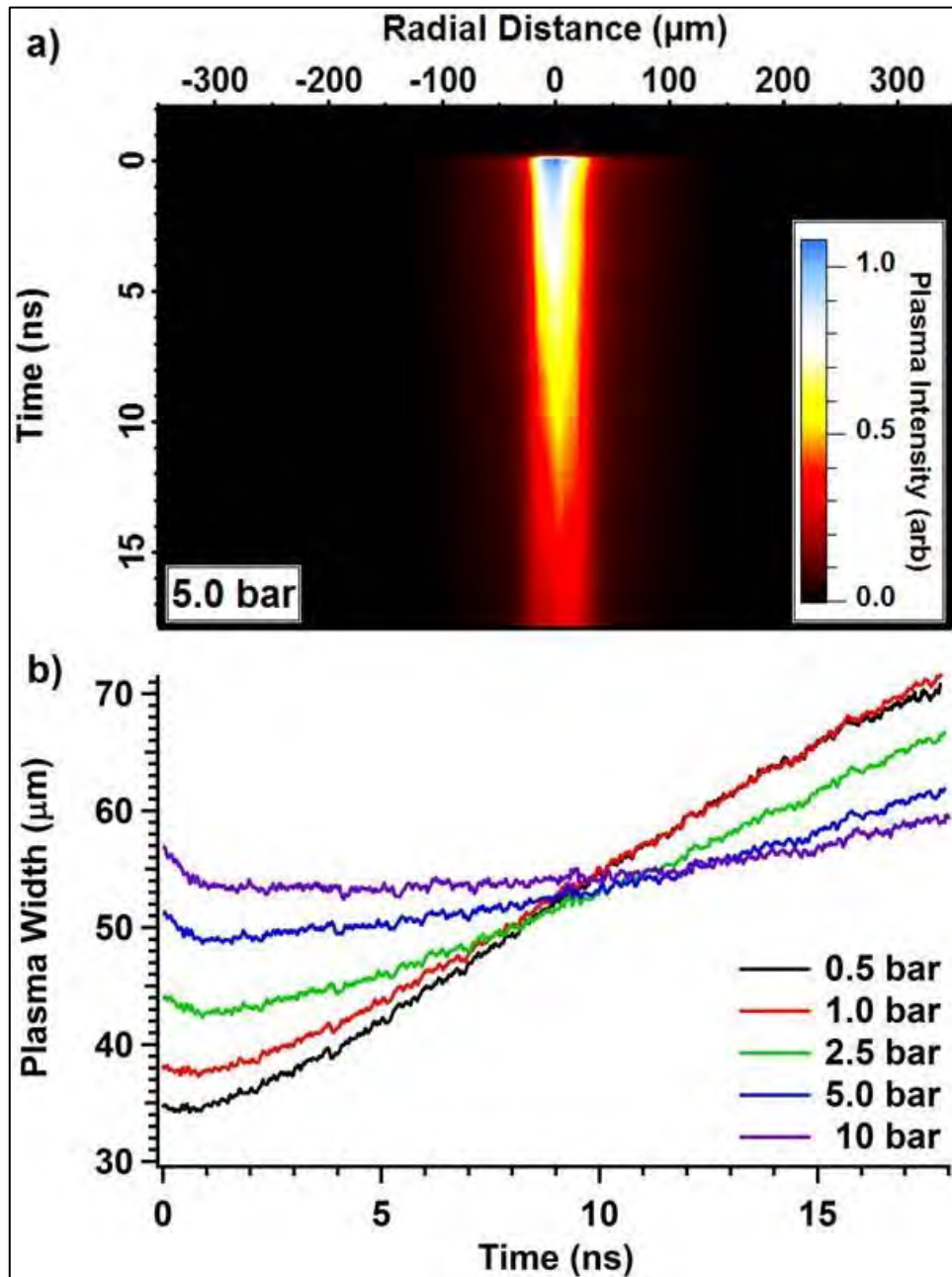


Figure 12: Spectrally integrated plasma emission (>495 nm) vs. radius and time. The streaked image a) was acquired for 5 bar xenon breakdown using a laser energy of 235 ± 4 $\mu\text{J}/\text{pulse}$, where $t=0$ indicates the moment of laser breakdown. The plasma's waist (FWHM) is plotted vs. time b) for various pressures. Plasma expansion becomes hindered with increasing pressure until ~ 5 bar is reached, at which point the plasma waist dwells before expanding.

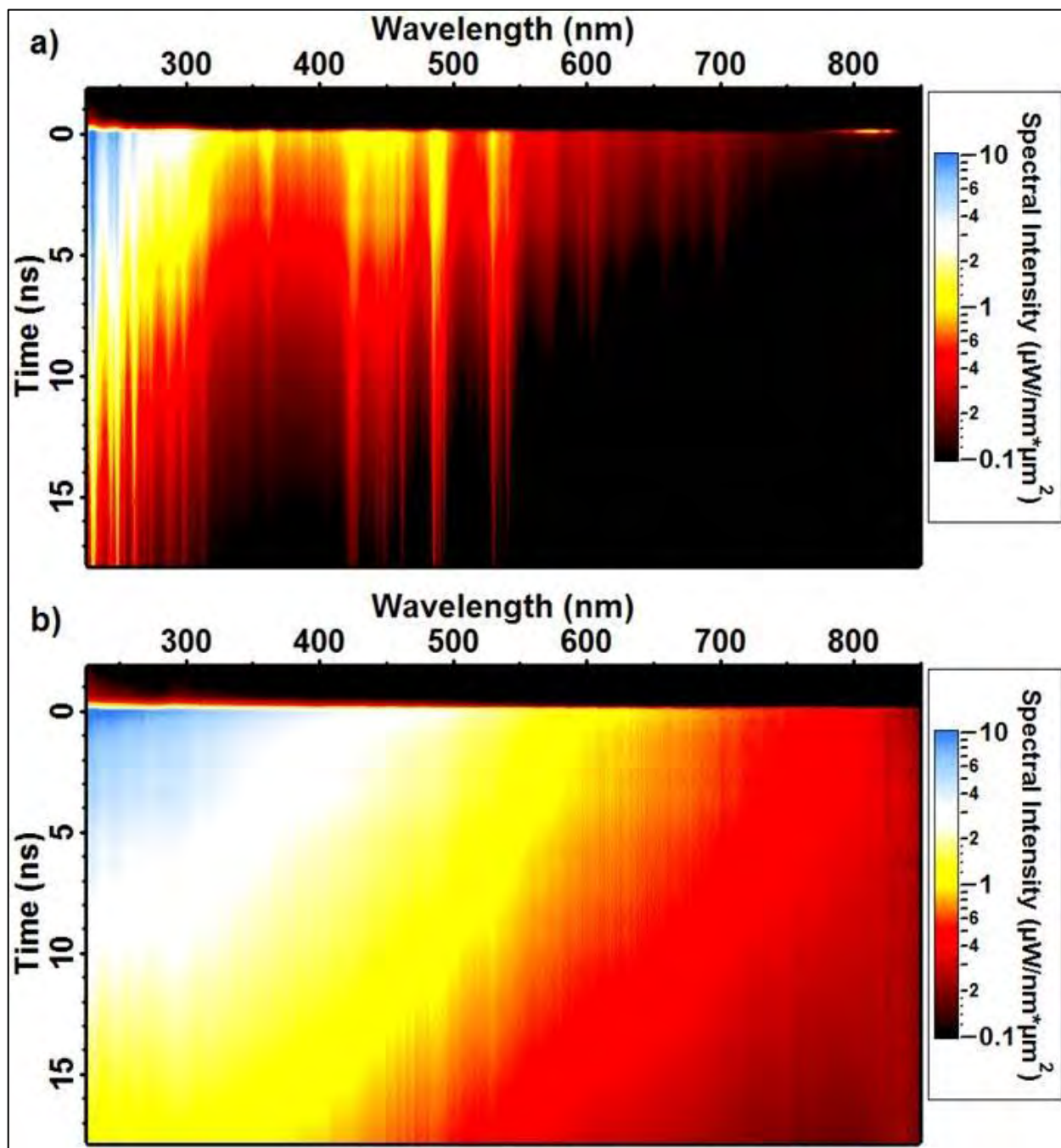


Figure 13: Calibrated spectrum vs. time for Xenon breakdown at a) 0.5 and b) 5 bar using a laser energy of $235 \pm 4 \mu\text{J}/\text{pulse}$. At lower pressures, the plasma spectrum is dominated by atomic line emission. With increasing pressure, the spectrum is broadened until it becomes completely continuous (~ 5 bar).

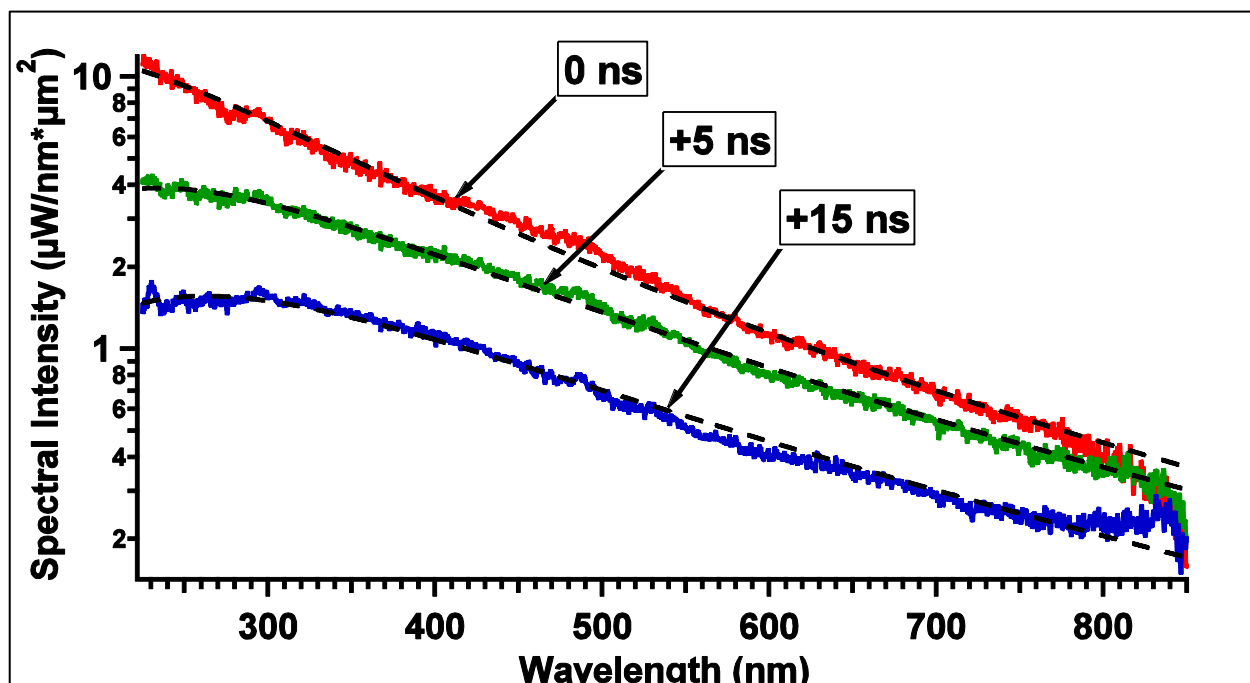
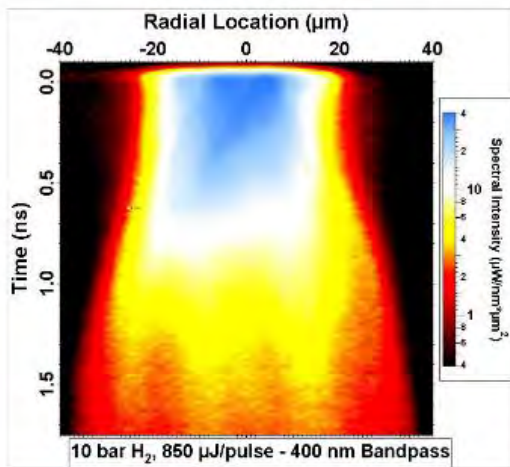


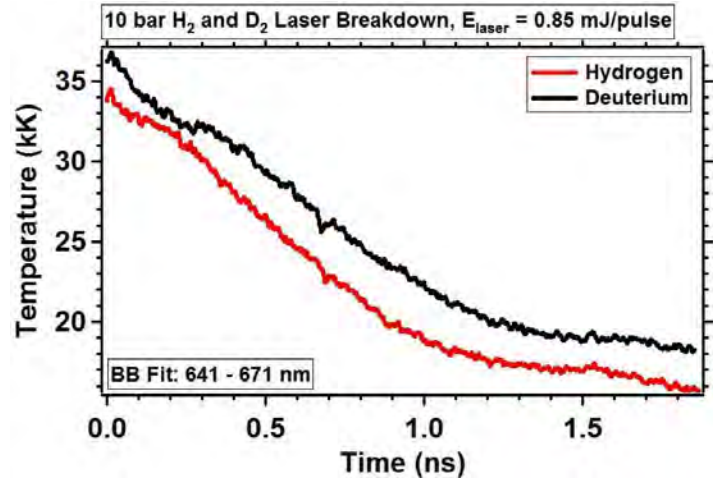
Figure 14: Spectral intensity for 5 bar xenon breakdown at different times relative to the plasma formation. Blackbody fits (dashed curves) are plotted for each spectrum with values of $T=16350$, 12350 , and 11050 K for $t=0$, $+5$, and $+15$ ns, respectively.

2. EVIDENCE FOR TENSILE STRENGTH IN LASER-BREAKDOWN PLASMA

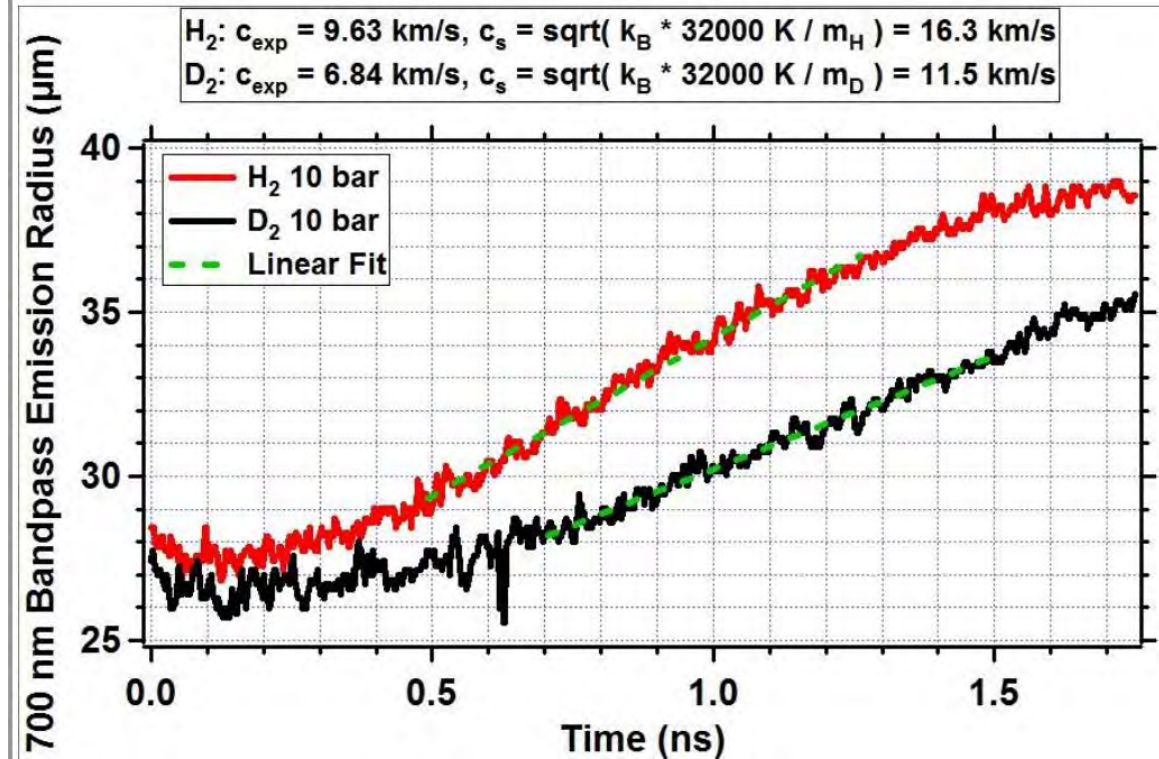
We now describe the experiments which lead us to claim that a dense plasma can have a tensile strength. We make the argument for Hydrogen gas, because it is the cleanest, best-understood system. Similar behavior is observed in other gases, but over different timescales. In femto-second laser breakdown in hydrogen gas (Figure 15), we create a plasma that emits as a 34,000 K blackbody (Figure 15b). The pressure of an ideal gas at that temperature would be thousands of atmospheres, which is much larger than the 10 atmospheres of neutral gas in the chamber surrounding it. Fluid mechanics would predict that in such a configuration, the hot fluid would start expanding immediately, at the speed of sound of the hot gas. We do not see this. In startling contrast, the Hydrogen plasma stays the same size – and possibly contracts somewhat – for 200 picoseconds (Figure 15c). We refer to this stand-still time as the “dwell time”. This phenomenon is also observed more dramatically in Helium, Argon, and Xenon, where the dwell can be 10ns or greater Figure 16.



a) Streak Image of Plasma Width



b) Temperature over Time



c) Radius Over Time

Figure 15: Femto-second laser breakdown of dense hydrogen gas displays interesting features. a) A streak image of the plasma width shows that the plasma does not begin expanding immediately, but dwells, and possibly slightly contracts, at early times. b) The initial temperature is 35,000K and decays to half the value over 1 nanosecond, before the cooling rate dramatically slows. c) The plasma radius over time shows the dwell time is 200 picoseconds.

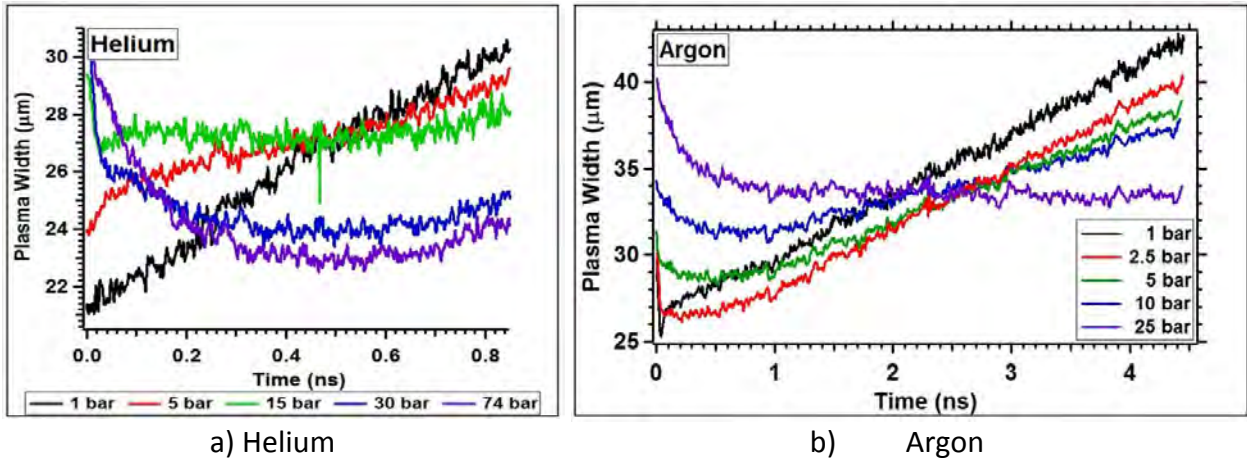


Figure 16: The dwell of the plasma radius is more pronounced in heavier gases, as seen above in a) Helium, and b) Argon. Xenon data was shown in Figure 12b.

We consider the dwell time – and possible contraction – to be a stunning result. Its deviation from fluid theory is so spectacular that we suspected that there was something wrong in our measurements – such as an artifact of the optical system. To rule out this possibility we measured the size of the plasma using transmission. The plasma was created with a pump laser pulse, and shot with a second probing pulse that was scanned over the plasma width. The fraction of the probing pulse transmitted is shown in Figure 17 at various times after breakdown. Incredibly, the plasma width dwells in the transmission measurements as well, a compelling confirmation of the phenomenon. The transmission measurements have been made in Hydrogen so far. We would like to make them in the heavier gases to search for confirmation of the contraction/dwell effect, which was more pronounced in the heavier gases. We also propose to carry out these measurements at higher pressures such as 40 atm of hydrogen and deuterium.

The lack of expansion of the hot plasma must be due to its pressure being lower. In fact, it must be of the same order as the ambient gas, 10 atm, which implies a pressure reduction of $\sim 100\times$. This pressure reduction is indicative of collective attractive stress which is similar to a tensile strength, such as is exhibited by a solid.

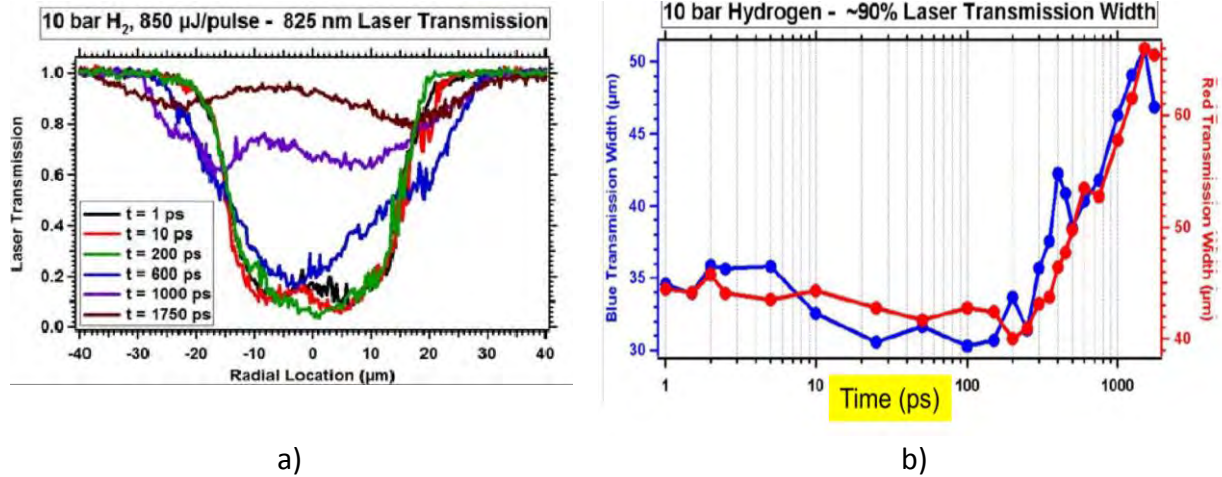


Figure 17: The width of a femto-second breakdown plasma measured in transmission. This measurement verified that the dwell-time seen in emission was real and not an artifact.

3. ELECTRON SCREENING

We have two hypothetical explanations for the reduction of the pressure. The first theory is that electron screening is large. For our relatively cool plasmas, and extreme electron densities of order $5 \times 10^{20}/\text{cm}^3$, the Debye screening length, $\delta_D = \sqrt{kT/8\pi n_e e^2}$, is sub-nanometer, and about the same size as the inter-particle spacing! We are clearly beyond the high-temperature, weak-coupling limit of Debye theory, but let us use the small perturbation limit to predict the effects we might expect. For weak coupling, Debye screening reduces the effective ionization potential; if the positive nucleus is partially screened, it is easier to remove a bound electron. The effective potential is $\chi \approx \chi_0 - \frac{e^2}{\delta_D}$, where χ_0 is the unmodified ionization potential. Inserting this term into the free energy modifies it as,

$$F = F_0 - N_0 \frac{2e^2}{3\delta_D},$$

Where F_0 is the unmodified, ideal gas free energy. The pressure is then calculated as,

$$P = -\partial F/\partial V = P_0 - n_0 \frac{e^2}{3\delta_D}.$$

We see that the screening term lowers the pressure, and further, the pressure lowering term is on the order of 1000 atm.

Additional evidence of strong electron screening is given by careful analysis of the spark breakdown in Xenon gas. In short, the emission spectrum, and opacity of the spark can only be explained by the presence of about 3 levels of ionization. Further, energy density measurements give the energy per ion as being less than what is needed to achieve that level of ionization if the reduction of the ionization potential is not included. The details of this argument are given below, as they would be a considerable digression at this point; for now let us return to possible explanations of the dwell time.

4. ION CORRELATIONS

The second hypothesis of the dwell time is related to correlations (liquefaction) between the ions. In a classic paper by Edward Teller (Monte Carlo Study of a One-Component Plasma 1966), the behavior of a one-component plasma is described. Teller's model is that ions are immersed in a neutralizing background and are confined to stay within a fixed-volume box. This model is applicable in the limit that the electrons are very hot and approximate a uniform background. Physically, "hot enough" means that kT is large in comparison to the difference in attraction between the nearest and next-nearest ions; i.e., the electron motion is not perturbed by its nearest ion. This is exactly the situation we have in femto-second laser breakdown, because the incoming laser pulse couples only to electrons. The pulse length is much shorter than the time required for electrons to thermalize with ions, therefore the ions remain at ambient temperature for a short while.

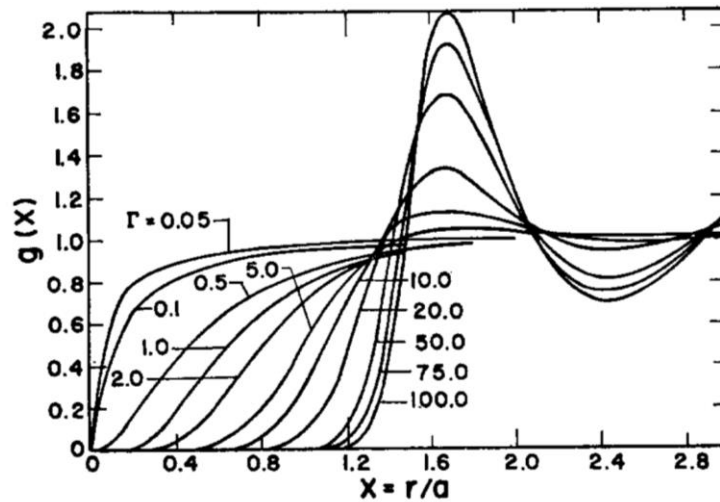


Figure 18: Fig 5 of Teller 1966. Radial distribution functions $g(x)$ for $0.05 < \Gamma < 100$.

The behavior of the ions in such a "one-component" plasma is determined by the plasma parameter of the ions, $\Gamma_{ions} = \left[\frac{(Ze)^2}{kT} \right] (4\pi n/3)^{1/3}$. Figure 18 plots the ion-ion spatial correlation function $g(x)$ for various values of Γ_{ions} . For $\Gamma_{ions} < 1$, the ions behave as an ideal gas and are not correlated. For $\Gamma_{ions} > 1$, their motion becomes correlated, and as Γ_{ions} approaches 50 their correlation looks quantitatively like redistribution functions for ordinary fluids. The key point is that for our experiments such as shown in Figure 15, the ions are initially at ambient temperature, so $T_{ions} = 300$ K, and Γ_{ions} comes out to be around 70 for 10 atm of Hydrogen gas. For 10 atm of triply-ionized Xenon, Γ_{ions} is closer to 500!

Importantly, Teller also calculated the pressure required to keep the volume of the one-component plasma fixed. At low Γ_{ions} , this is the same as the ideal gas pressure. As Γ_{ions} increases, the pressure drops, and in-fact, becomes negative at $\Gamma_{ions} = 16$. The implication is that the plasma wants to contract, and it requires an outward pressure to keep its size fixed. If

allowed to contract, it would do so until a separate phenomenon provides a counter-force to balance it out.

We propose a phenomenological adjustment to the free energy of the form,

$$F = F_0 - N_0 B k T_i \Gamma_i \tanh \Gamma_i,$$

where B is an adjustable coupling constant. The pressure is modified as,

$$P = -\partial F / \partial V = P_0 - n_0 B k T_i \Gamma_i \tanh \Gamma_i.$$

In this model, transport of heat to ions is determined by electron-phonon interactions and not binary electron-ion collisions. Therefore equilibration is slow and the dwell time is prolonged, beyond what it would be for transport that is dominated by binary collisions in a charged gas.

Part 3: Broadband, High-Power Light Switch Enabled by Ionization Lowering in Spark Discharges

In this section we argue that collective processes lower the effective ionization threshold based on the high-ionization deduced by the observed opacity and energy density measurements in the spark system. We have data pointing to the fact that the energy-per-ion in our dense plasmas cannot account for the high level of ionization without a reduction of the ionization potential. Key to this conclusion is a measurement of the internal energy density of the plasma, which is based on a technique we developed that allows us to probe the internals of a blackbody without looking inside directly. Our measurement of the internal energy density of these dense plasmas represents a key advance towards understanding their equation of state. We first describe our experimental apparatus, then explain how we use energetics to peer inside a blackbody, and finally give our argument for the reduced ionization potential. The spark system we study here is also at the core of the rapid optical switch we present subsequently.

1. Experimental Description of Spark-Breakdown System (Electrical Trigger)

Figure 19b is a block diagram of the system. A high-pressure gas chamber (photograph in Figure 19a) with tungsten needle electrodes and high-voltage feedthrough is at the core of the experiment. A high-voltage (5kV) circuit (Figure 19c) with a fast-rise-time (10ns) switch sends a high-voltage pulse to the electrodes in the chamber. Gas breakdown occurs when the field between electrodes exceeds the breakdown threshold, creating a dense plasma. To measure the opacity of the plasma, a 2ns laser pulse of 532 nm light probes the plasma, and the amount of light transmitted is measured on a CCD. A fiber-coupled spectrometer records the spark emission spectrum in 10 ns gated exposures.

Figure 20a,b display the transmission and emission of a spark in 2 and 10 atmosphere respectively of Xenon gas. At 2 atmosphere, the plasma is still partially transparent. At 10 atmosphere the transmission is smaller than the noise of the system. Figure 20c,d are framing camera images of the laser pulse hitting the spark column at 2 and 10 atmosphere respectively. The laser pulse is impinging on the spark from the left. At 2 atmosphere, the laser is seen to punch through the plasma, creating an extra volume of plasma on the right. At 10 atmosphere, the laser is completely stopped on the left side of the spark, and a heat wave is seen to propagate down the spark channel.

The emission spectrum of the spark discharge in 2 and 10 atmosphere respectively is displayed in Figure 21. In parallel to laser-breakdown, line emission is visible at low pressure, which transitions to a broad, blackbody spectrum at high pressure, an indirect indication of the system opacity.

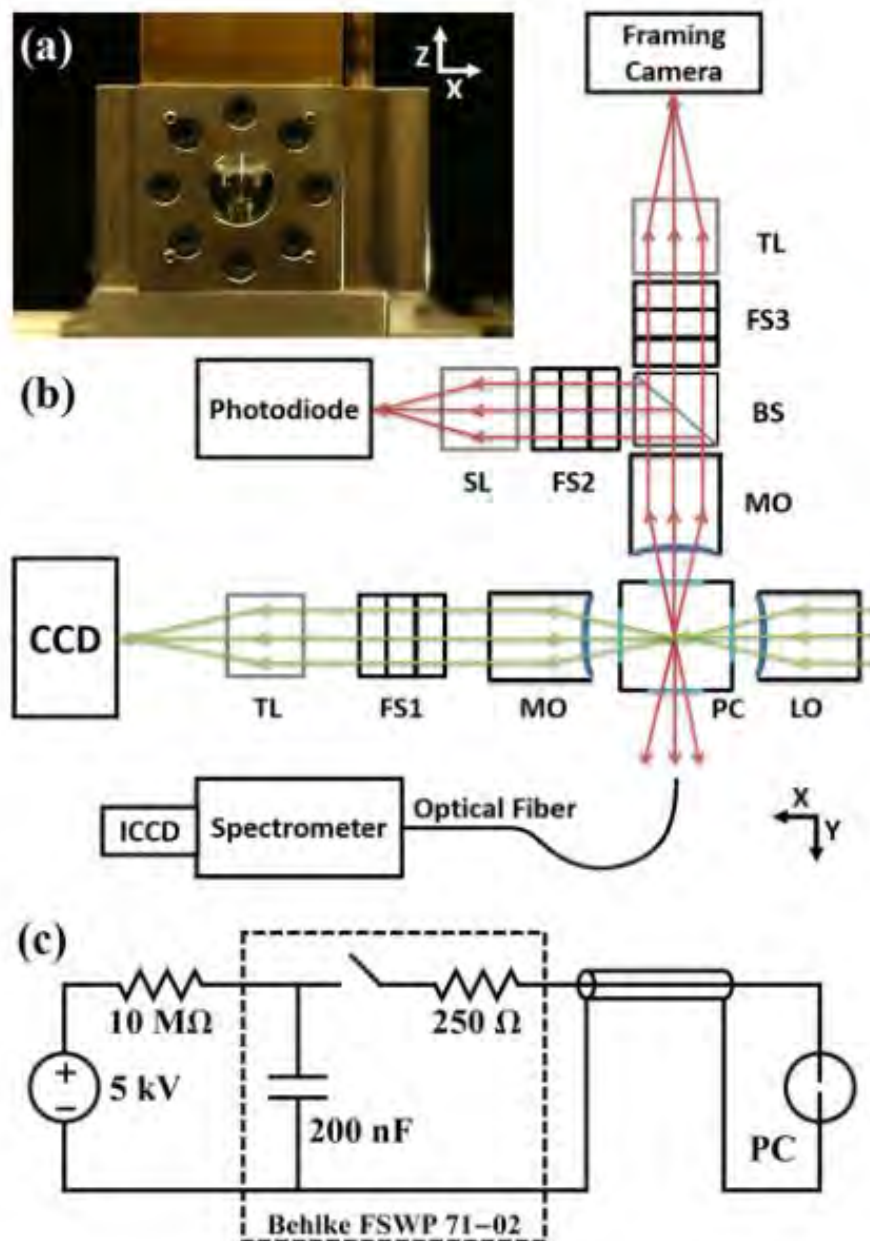


Figure 19: Spark system experimental setup: (a) Photograph of pressure chamber with tungsten needle electrodes. (b) Optical block diagram for measuring laser transmission and plasma emission, and for fast spark imaging (framing). Included are laser (green arrows) and plasma emission (red arrows) ray traces. A portion of the plasma emission is collected by an optical fiber and directed to a gated spectrometer. The x, y, and z axes are defined by the arrows in a) and b), the origin of which is taken to be the plasma center. (c) High-voltage circuit diagram.

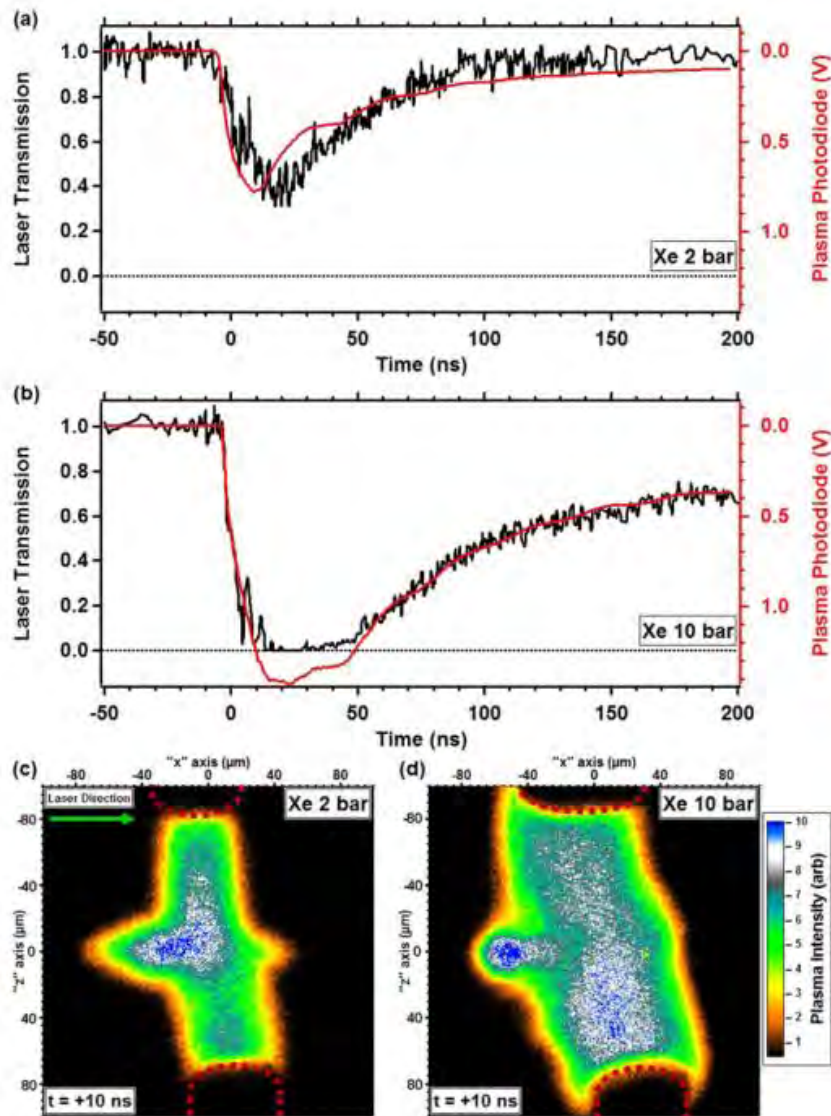


Figure 20: Laser transmission and plasma emission of spark discharges formed in (a) 2 and (b) 10bar Xenon gas as a function of time. Laser transmission (black curve) was recorded for 532nm laser pulses focused through the center of the spark plasma. Plasma emission (red curve) was recorded with a fast photodiode. False color images representing plasma light emission were taken with a framing camera during the moment of laser-plasma interaction for (c) 2 and (d) 10bar discharges. Red dashed curves indicate the location of the HV electrodes. Laser pulses propagating from the left are absorbed by the spark volume and surface for 2 and 10bar discharges, respectively. These transmission curves and images were obtained using laser intensities below the breakdown threshold.

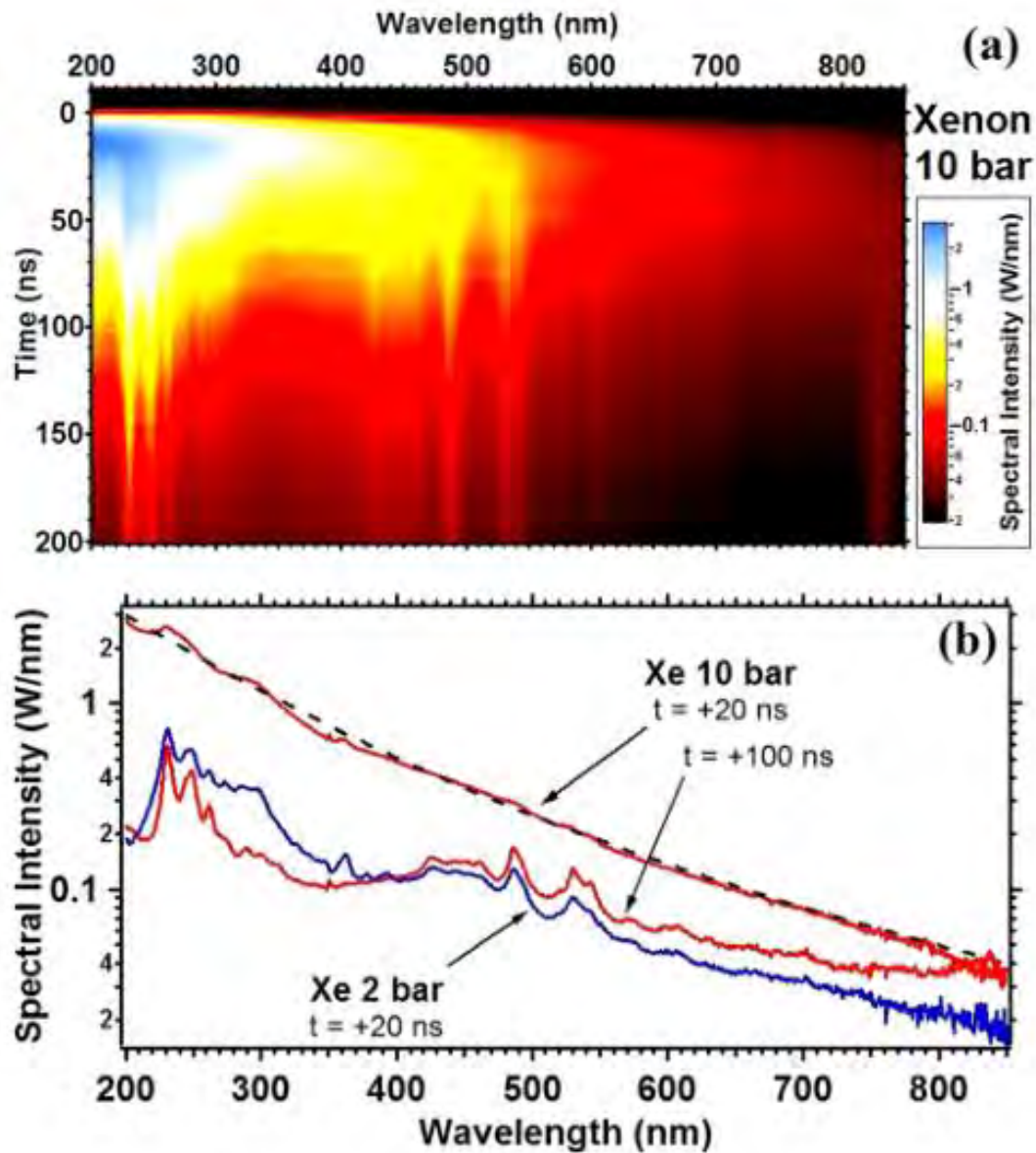


Figure 21: Calibrated spectrum for 10bar xenon discharges. (a) Temporally resolved spectral image shows continuous broadband emission for early times. As the plasma expands, xenon line emission emerges from the continuum for later times. (b) Spectral line-outs reveal opaque behavior during the early moments of discharge and is well fit to blackbody emission (black dashed curve, $T=24000\text{K}$ and $4.9 \times 10^4 \mu\text{m}^2$ blackbody emission area). Blackbody spectrum is observed concurrently with complete absorption from Figure 20(b).

While the broad spectrum itself indicates the system is opaque, we measured the transmission directly over 6 orders of magnitude in laser intensity (Figure 22). There is a qualitative change in the behavior of the spark system depending on whether the laser intensity is above or below the laser breakdown threshold. For intensities below the laser-breakdown threshold, the transmission over time was about the same: the spark was opaque for about 20

nanoseconds. For laser intensities above the laser-breakdown threshold, the opacity time increased with laser intensity. The laser was creating more plasma, which helped absorb more laser! This highlights an important point: since plasmas are already the ‘broken’ state of matter, they cannot break further. The spark is indestructible; it can handle as much power as can be sent to it. We also emphasize that the spark remains opaque, at the other extreme, at very *low* laser intensities. We verified the opacity remains at laser intensities down to 2500x less than the laser breakdown threshold. That the spark itself is opaque, even when the incoming laser does not create more plasma, in contrast to the conclusions drawn by others [Levko and Raja; Physics of Plasmas 22, 123518 (2016)] based on simulations at 10x lower ambient pressure.

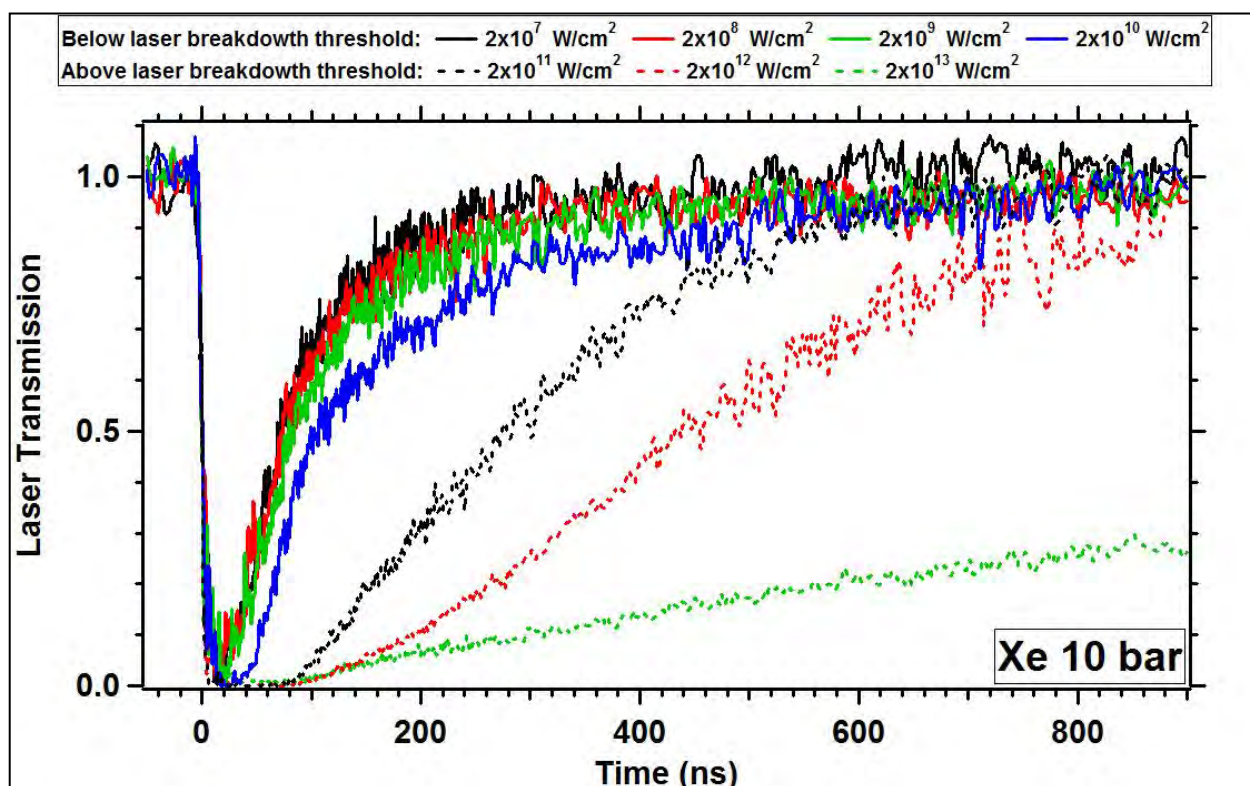


Figure 22: Normalized laser transmission of spark discharges formed in 10 bar xenon gas as a function of time and spanning 6 orders of magnitude in laser intensity. Laser transmission was recorded for 532 nm laser pulses focused through the center of the spark plasma. Intensities below the laser breakdown threshold (solid curves) produced nearly identical transmission curves indicating a linear laser-plasma response. Intensities above the laser breakdown threshold (dashed curves) deviated from the former curves with an increasingly nonlinear laser-plasma response, resulting in greater opacity for a longer period of time. Importantly, even low-intensity pulses (tested to 2500x less than the breakdown threshold) are blocked, indicating that the spark itself is opaque to visible light. At intensities near and above the breakdown threshold, the laser creates additional plasma that further increases its opacity, and extends the opacity time.

The spark laser-absorption process is displayed in Figure 23 at different times relative to the discharge time. Row a) is to be used as a reference, there is no spark – only the laser breakdown itself is visible (the laser intensity is above the laser-breakdown threshold). In row

b), a spark is formed and the laser pulse hits it at +25 ns. The laser energy is absorbed by the plasma, and a heat wave is seen to propagate through the spark channel. No energy is transmitted. In row c), a spark is formed and a laser pulse hits it at +90 ns. Sufficient time has passed since spark inception, that it is now becoming transparent. The extra plasma produced on the far side of the plasma indicates that the laser has punched through the spark channel.

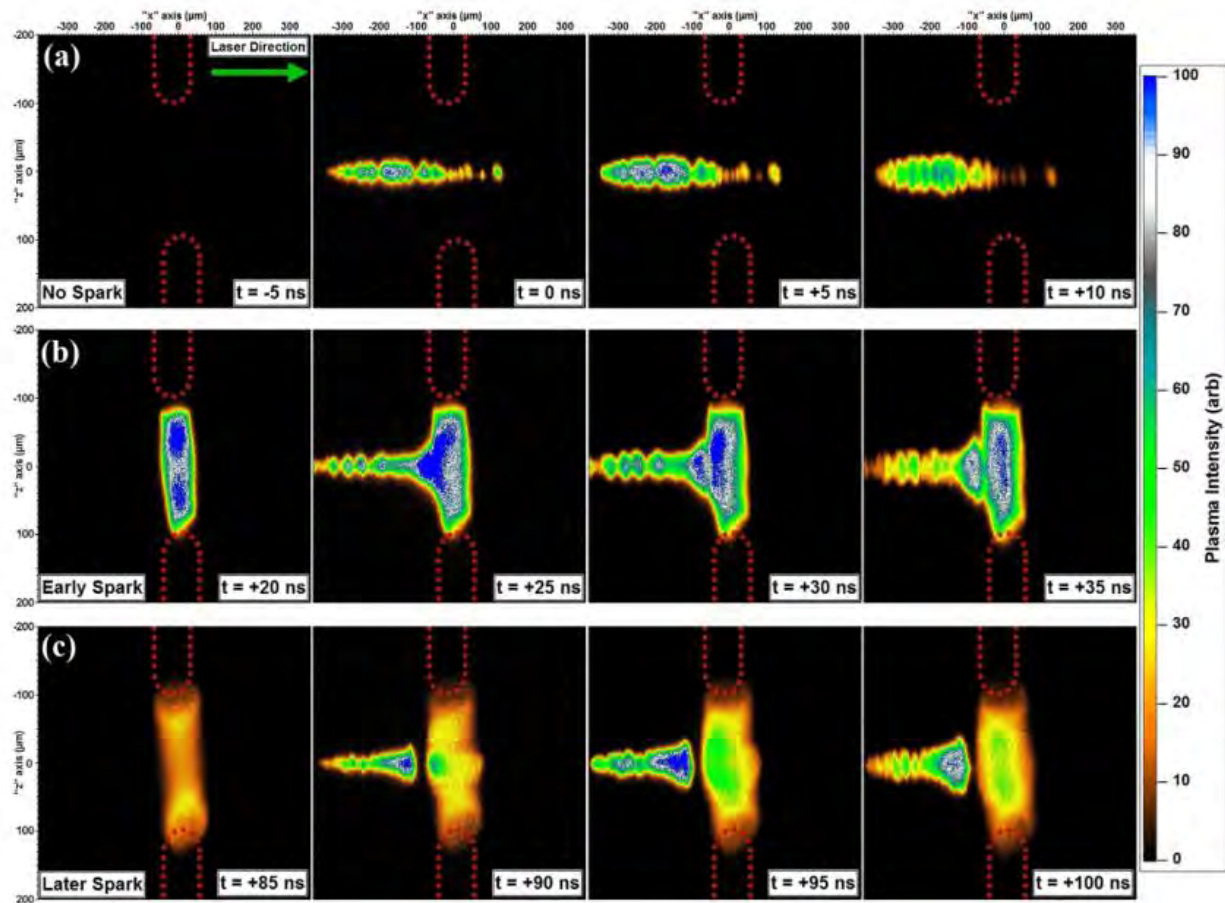


Figure 23: 5 ns framing images (false color) of three individual events: (a) Laser breakdown without a spark and (b) laser absorption at +25ns and (c) +90ns after spark discharge initiation in 10bar xenon gas. The timestamps given in (b) and (c) indicate the moment the image was taken relative to the spark discharge. For the case of (a) no spark, the image was taken relative to the arrival of the laser pulse. In all cases, the laser intensity (1.9×10^{12} W/cm²) was set above the breakdown threshold and centered between the electrode gap. Laser arrival occurred during the second frame of each row and resulted in a laser-plasma interaction. Red dashed curves indicate the location of the HV electrodes. A dark region exists between the laser breakdown and spark plasma for $t > 50$ ns and grows larger with later laser pulses. Shadowgraph measurements have shown this effect is due to laser breakdown induced by a shock front generated by the spark discharge.

2. *Experimental Description of Spark-Breakdown System (Optical Trigger)*

One difficulty with working with an electronic switch to trigger the spark breakdown is the relatively large jitter associated with the time between closing the switch, and the time breakdown occurs. When the switch is closed, the high voltage cable going to the electrodes begins to charge. When it charges to the breakdown threshold, the spark is triggered. We believe that the shot to shot jitter is as result of fluctuations in the breakdown threshold.

The breakdown threshold may change for at least two reasons. First, we know that the electrodes burn off at a rate of about 2 micrometer per 2000 shots. This mean that the electrode surface is constantly changing, and further, the closest point between electrodes – which determine the breakdown threshold – changes through melting, evaporation, and re-solidifying. Second, the repetition rate of the sparks is observed to effect the temporal, and spatial jitter of the breakdown, with high repetition rates corresponding with larger jitter of both types. Remnants of the previous breakdown can affect the next breakdown threshold through variations in the gas temperature, or possibly even low levels of residual ionization. We have reduced the repetition rate to $\sim 1\text{Hz}$ to minimize these effects.

To take advantage of high speed diagnostic equipment available in our lab, especially our streak camera, we decided to trigger the spark discharge with a femtosecond laser pulse, which lowered the jitter by over an order of magnitude. A block diagram of the setup is shown in Figure 24 below. The electrodes are connected to the high voltage supply and a parallel capacitor. We set the high voltage to a level that does not trigger breakdown on its own. A femtosecond laser pulse (not shown) is focused in between the electrodes and creates a small breakdown, which triggers the spark. In this manner we can observe the sub-nanosecond dynamis of the spark with the streak camera.

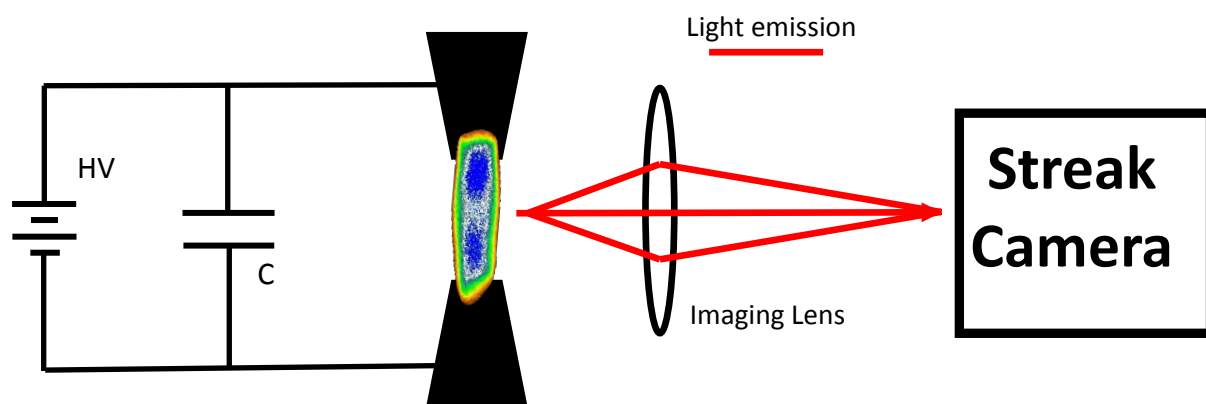


Figure 24: Block diagram of experimental setup of a streak camera imaging a nanosecond spark.

We measured the speed of the spark formation, including the opacity risetime, by taking a streak image in a vertical plane between the electrodes (Figure 25). The light emission 10%-90% rise time is measured to be 650ps, for 5kV across a 170 μ m gap. The discharge reaches full opacity in \sim 0.1% the speed of light!

Now we look at the plasma in a horizontal plane. A streak image is shown in Figure 26b, followed by lineouts in time and in space. Once again, we see that the plasma turns on in \sim 0.5 ns (Figure 27a), and has a very sharp boundary in space (Figure 27b). The transition from neutral gas to dense plasma occurs over 4 micron. Note that the plasma surface temperature, 24,000K, is uniform in both time and space during the first 20 ns (Figure 26b). The plasma column expands at 2 km/s.

Streak Camera
Slit Aperture

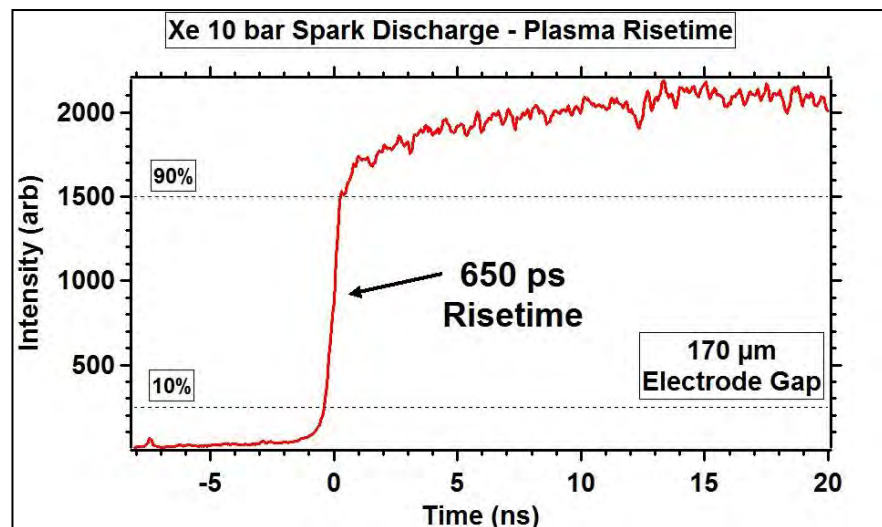
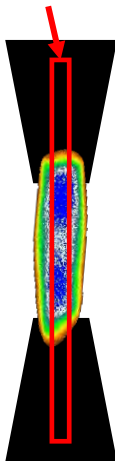


Figure 25: Rise-time of spark along its length.

Streak Camera
Slit Aperture

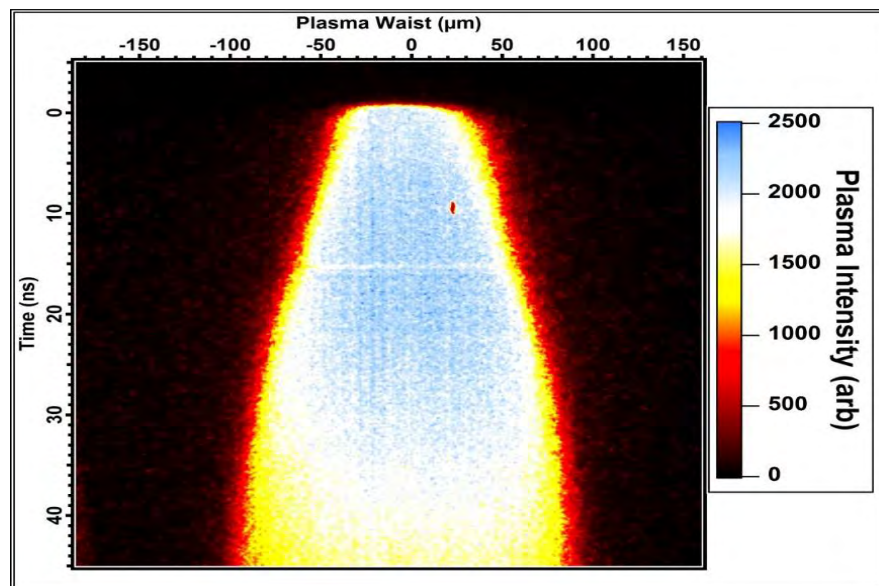
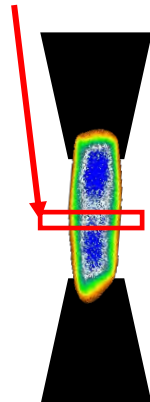


Figure 26: Rise-time of spark width.

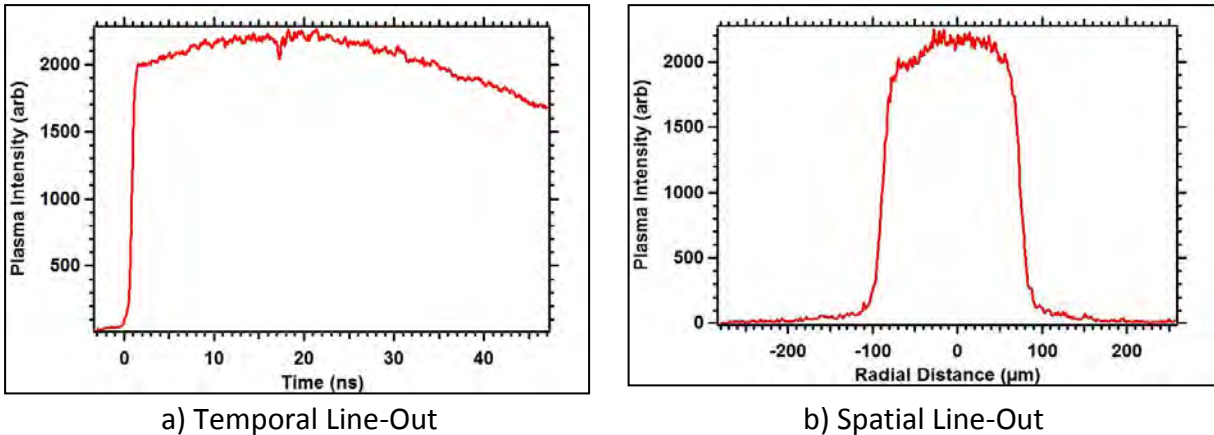


Figure 27: a) Temporal line-out: The intensity is a flattop in time, indicating a uniform temperature and a blackbody which blocks incident light for over 20 ns. b) Spatial line-out: Again the intensity flattop in space indicates a blackbody. Furthermore, the plasma has a uniform temperature across the plasma surface. This feature is robust and not fully understood

3. Energetics Inside a Blackbody

In our work with a spark discharges, we have observed the generation of an outgoing shockwave (Figure 28). We have realized that understanding the evolution of the shockwave is key to determining the energy inside the spark column at its inception. Information about the obscured interior of a blackbody can be inferred from the dynamics of the shock wave coming off of it.

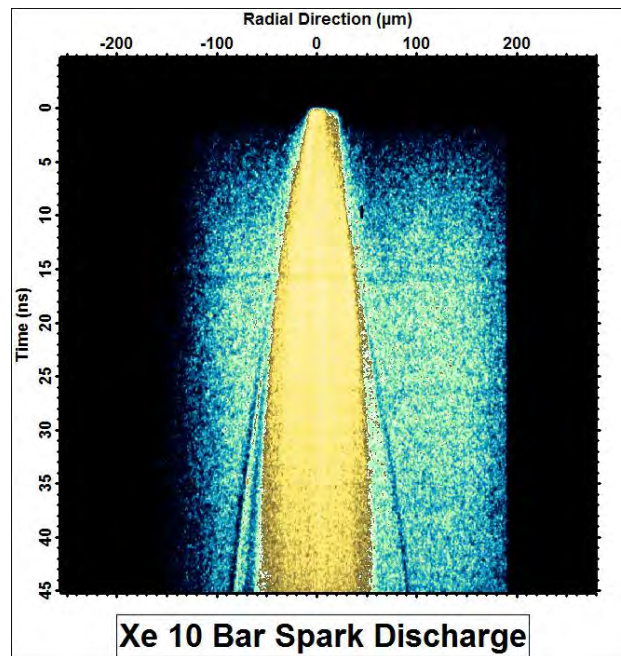


Figure 28: Streak image of a spark discharge. The spark is backlit with an out-of-focus reflection of its own light. A shockwave is seen to separate from the hot, central column at about 20ns.

From scaling theory, one can derive the Sedov-Taylor solution for the expansion of a shockwave triggered by a delta-function energy input in the limit that the radius is much larger than the initial radius. The radius of a cylindrical shock is given by,

$$R(t) = \sqrt{Bt}, \quad \text{where } B = 2 \sqrt{\frac{(\gamma-1)(\gamma+1)^2}{\pi(3\gamma-1)} \frac{E_0}{\rho_0 L}},$$

where E_0/L is the energy per length, ρ_0 is the ambient density, and γ is the adiabatic index, assumed constant, of the gas surrounding the shock. We see that the radius grows with $t^{1/2}$, with coefficient that is proportional to $(E_0/\rho_0 L)^{1/4}$. In other words, we can extract the amount of energy internal to the plasma by following the shock position in time. Combined with a photograph of the initial spark size, we have measured the energy per particle. An example of this type of analysis is shown in Figure 29. At early times, the radius is not large compared with its initial size, so the Sedov-Taylor solution does not apply. From about 10-30 ns, the radius does follow the Sedov-Taylor solution, and fits to that part of the curve give the internal energy per length of the spark. At about 30 ns, the shock separates from the shock channel (as seen in Figure 28), a phenomenon called “Breakaway”. The shock continues expanding at $t^{1/2}$ (not shown in Figure 29), but the luminous channel expansion slows down. In our preliminary work, we followed the luminous channel diameter, and fit the $t^{1/2}$ expansion between roughly 10-30ns. In future work we plan on following the shock further in time to obtain more reliable measurements of the internal energy.

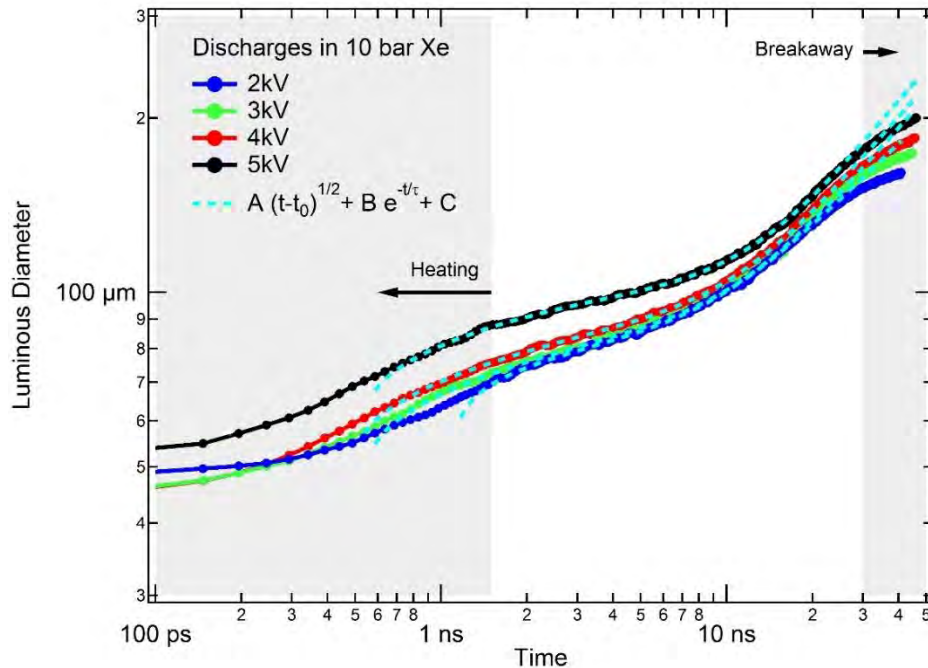


Figure 29: Plot of the spark radius as a function of time. Between about 10-30 ns, the expansion is proportional to $t^{1/2}$, as predicted by the Sedov-Taylor scaling theory. Fits to this part of the curve allow extraction of the energy/length internal to the spark.

It is important to point out that the energy input to our spark breakdown is approximated by a delta function in time, as assumed by the Sedov-Taylor solution. During the formation of the spark channel, its resistance starts out large (equal to neutral gas) and drops to 10s of milliohm over a nanosecond. The final resistance is estimated based on the high electron density and the electron-ion collision time. Once the channel resistance drops, the coupling of energy to the spark is dramatically reduced. Consequently, the energy absorbed after the first nanosecond is substantially reduced, and the energy input can be approximated as a delta-function when looking at dynamics after 10ns.

From the energy/length extracted from the shockwave fits, we estimate that the energy per ion (including electrons liberated from that ion) is about 35 eV. This value remains constant as we change the ambient gas pressure (density) and the drive voltage, and the size of the channel changes to accommodate. For simplicity, let us assume that all atoms are triply ionized as required for the opacity of the system at a temperature of 29,000K determined by spectral measurements, and calculate the energy per ion required by both the non-screened and screened theory. If screening is not important, then the energy per ion is,

$$\epsilon_0 = \frac{3}{2}(3 + 1)kT + \sum_{m=1}^3 \chi_m = 80 \text{ eV}$$

where the χ_m are the unscreened ionization potentials of Xenon ($\chi_1=12.1$ eV, $\chi_2=21.2$ eV, and $\chi_3=32.1$ eV). The first term represents the kinetic energy contributions from the electrons and ions. With screening, the energy per particle is modified as,

$$\epsilon_0 = \frac{3}{2}(3 + 1)kT + \sum_{m=1}^3 (\chi_m - \frac{m e^2}{\delta_D}) = 15 \text{ eV} + (5.4 \text{ eV} + 7.6 \text{ eV} + 10.9 \text{ eV}) = 38.9 \text{ eV}.$$

The screened model comes within uncertainties of experiment, while the unscreened is a factor of 2 off. Electron screening reduces the energy per particle by 40 eV - a factor of 2!

Part 4:

Publications

- a) ***Energy Balance for a Sonoluminescence Bubble Yields a Measure of Ionization Potential Lowering*** - B. Kappus, A. Bataller, and S. J. Putterman. *Physical Review Letters* (2013).
- b) ***Collision Time Measurements in a Sonoluminescing Microplasma with a Large Plasma Parameter*** – A. Bataller, B. Kappus, C. Camara, and S. Putterman. *Physical Review Letters* (2014).
- c) ***Blackbody Emission from Laser Breakdown in High-Pressure Gases*** – A. Bataller, G. R. Plateau, B. Kappus, and S. Putterman. *Physical Review Letters* (2014).
- d) ***Nanosecond high-power dense microplasma switch for visible light*** – A. Bataller, J. Koulakis, S. Pree, and S. Putterman. *Applied Physics Letters* (2014).
- e) ***Observation of Shell Structure, Electronic Screening, and Energetic Limiting in Sparks*** – A. Bataller, S. Putterman, S. Pree and J. Koulakis. *Submitted to Physical Review Letters* (2015).

Energy Balance for a Sonoluminescence Bubble Yields a Measure of Ionization Potential Lowering

B. Kappus,¹ A. Bataller,¹ and S. J. Putterman^{1,2}

¹*Department of Physics and Astronomy, University of California, Los Angeles, California 90095, USA*

²*California Nano-Systems Institute, University of California, Los Angeles, California 90095, USA*

(Received 9 December 2011; revised manuscript received 27 August 2013; published 6 December 2013)

Application of energy conservation between input sound and the microplasma which forms at the moment of sonoluminescence places bounds on the process, whereby the gas is ionized. Detailed pulsed Mie scattering measurements of the radius versus time for a xenon bubble in sulfuric acid provide a complete characterization of the hydrodynamics and minimum radius. For a range of emission intensities, the blackbody spectrum emitted during collapse matches the minimum bubble radius, implying opaque conditions are attained. This requires a degree of ionization $>36\%$. Analysis reveals only 2.1 ± 0.6 eV/atom of energy available during light emission. In order to unbind enough charge, collective processes must therefore reduce the ionization potential by at least 75%. We interpret this as evidence that a phase transition to a highly ionized plasma is occurring during sonoluminescence.

DOI: 10.1103/PhysRevLett.111.234301

PACS numbers: 78.60.Mq, 43.25.+y

Sonoluminescence (SL) is the emission of light from a bubble whose pulsations are so strong that the energy density of a surrounding sound field is concentrated by many orders of magnitude. This can be achieved in cavitation clouds [1–3] or in a single driven cavity [3–11]. Figure 1 shows how a single spherical bubble of xenon in sulfuric acid expands to a maximum radius R_m during the rarefaction part of a 28.5 kHz standing wave and then rapidly collapses to a minimum radius R_c during the ensuing compression. For this example of sonoluminescence the flash of light emitted at R_c has a 13 nanosecond duration and its spectroscopy (Fig. 2) reveals an accurate match to an ideal Planck blackbody [12]. A blackbody must be opaque and so the mean free path ℓ of light inside the light-emitting region must be smaller than its size, or to the accuracy of our measurements, $\ell < R_c$. As SL originates in a plasma, the charge density required for opacity for this $6.5 \pm 0.9 \mu\text{m}$ radius bubble is $n_e > 4.0 \times 10^{20}/\text{cm}^3$ fundamental unbound charges/cc, or $N_e > 4\pi R_c^3 n_e / 3$ unbound charges in the blackbody [13,14]. In order to independently produce N_e free ions, the plasma requires an energy $N_e \chi_0$ where χ_0 (~ 12.1 eV) is the ionization potential of a single xenon atom. Via a detailed analysis of measurements of bubble radius “ R ” as a function of time “ t ”, we will show that the total acoustic potential energy available to the bubble on each cycle is *much less* than $N_e \chi_0$. There are three possible conclusions: (i) opacity is due to a mechanism other than the scattering of light by free charges, (ii) SL originates in a strongly interacting Coulomb plasma which lowers the ionization potential to such an extent that the microplasma becomes opaque, and (iii) SL has its origins in a higher temperature emitter which is a transparent blackbody imposter. The discovery [15] that spectral line shifts imply free charge densities $\sim 10^{21}/\text{cc}$, the analysis of spectral intensity [16],

the observation that sonoluminescence can be a bubble filling blackbody [17–19], and the use of laser pulses to measure the opacity of a sonoluminescing bubble [20], select in favor of (ii); however, an evaluation of case (iii) is included in our discussion.

In order to quantify the energy contained in the dynamically evolving bubble, we acquired extremely detailed measurements of the radius as a function of time with pulsed Mie scattering. Experiments presented here are carried out in an aqueous solution that is 85% sulfuric acid (SA) by weight with 50 torr of xenon mixed in before pressurizing with 1 atm of xenon. SL in SA is characterized by extremely bright flashes of light [21] but also by extreme jitter in space (~ 2 mm) and time ($1 \mu\text{s}$). This is accompanied by SL intensity jitter due to the variety of collapse conditions brought upon by the chaotic bubble motion and resulting range of driving amplitudes [22]. A histogram of measured SL integrated intensities is shown in Fig. 3. To overcome these difficulties, we used a 100 fs, 1 mJ pulsed Ti:Sa laser at 830 nm to illuminate the bubble and collect the scattered light in a Mie scattering arrangement with a large area (1 cm^2) photodiode. This allowed us to simultaneously take a “snapshot” of the bubble radius while saving details of the light emission (Hamamatsu PMT) with every pulse of the laser. By recording every event independently, we could discriminate based on SL integrated intensity after the fact to build a set of radius versus time curves for selected SL conditions. Further details can be found in the Supplemental Material [23].

To calibrate the Mie scattering signal, the laser could be steered into a backlighting configuration and collected with a microscope ($5\times$ Mitutoyo Plan Apo Long WD Objective). At 16 different phases of the acoustic cycle, images of the bubble were taken to obtain an independent determination of the bubble radius throughout its motion.

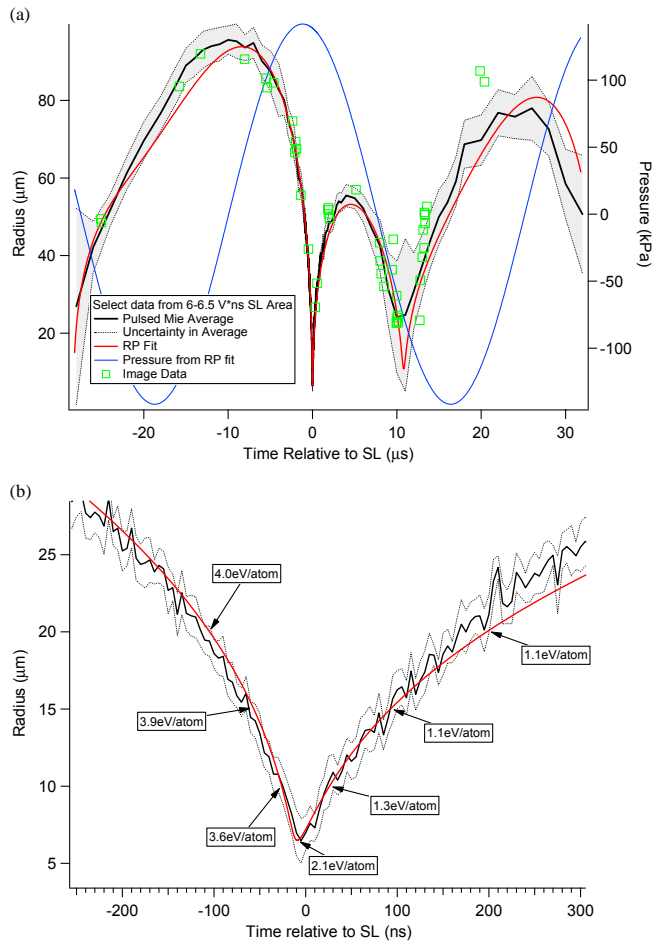


FIG. 1 (color online). Radius versus time from Mie scattering data, backlighting image data, and RP simulation fit in sulfuric acid from flashes between 6 and 6.5 V ns integrated intensity. (a) illustrates bubble motion for just over one cycle of the sound field. (b) shows the same data scaled to reveal details of near the minimum radius and includes points of reference to delineate energy availability at various points on the curve. Uncertainty is calculated as the standard deviation of the Mie scattering points from a given time-grouping added in quadrature with the predicted velocity multiplied by the width of the grouping.

In a similar manner to the Mie scattering data, SL integrated intensity and timing information was captured with each backlit image and this could be used to select appropriate images for each Mie scattering set. In addition, the ambient radius of the bubble (R_0) could also be measured in this configuration by briefly interrupting the drive. For purposes of illustration, what follows is the analysis of a selection with SL integrated intensities ranging from 6 to 6.5 V ns. The postprocessed radius versus time curve resulting from this discrimination is shown in Fig. 1.

This Mie scattering data is fit to a solution of the Rayleigh-Plesset (RP) equation and includes thermal transport between the ideal gas in the bubble and the surrounding fluid [24–26]. The maximum Mach number M of the bubble wall relative to the speed of sound in the gas is

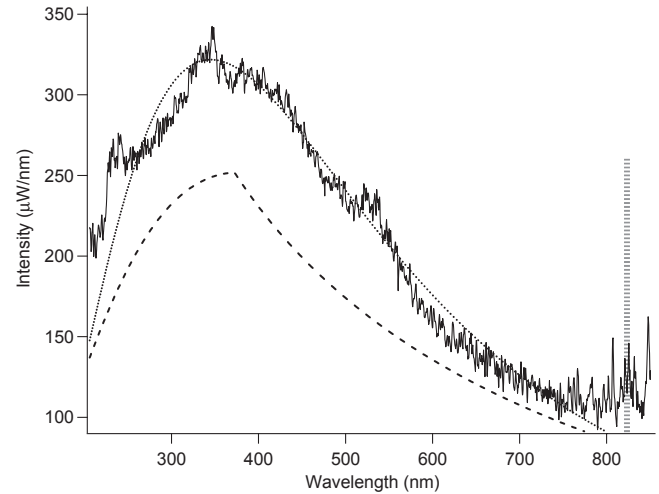


FIG. 2. Integrated spectrum from sonoluminescence in sulfuric acid from flashes between -6 and -6.5 V ns integrated intensity. The dotted line is a fit (from 250 to 800 nm) to a Planck black body which gives $T = 8400$ K and $R_e = 6.9$ μm . The dashed line is a theoretical transparent spectrum following Hammer *et al.* [32]. This model uses a fixed size of 6.5 μm radius, a temperature of 15900 K, and 5.4% ionization (The upper limit of our uncertainty in both temperature and density of the SL plasma). The associated 823 nm line emission for this hot, dilute model is represented by the dashed gray bar.

~ 0.2 , so it is expected that the RP equation describes $R(t)$ to a good approximation. For the purpose of theoretical analysis, this is an important advantage over other single bubbles in water which exhibit greater stability but which implode with $M > 1$ [27,28]. For the vast majority of the cycle, the xenon in sulfuric acid bubble behaves as an ideal

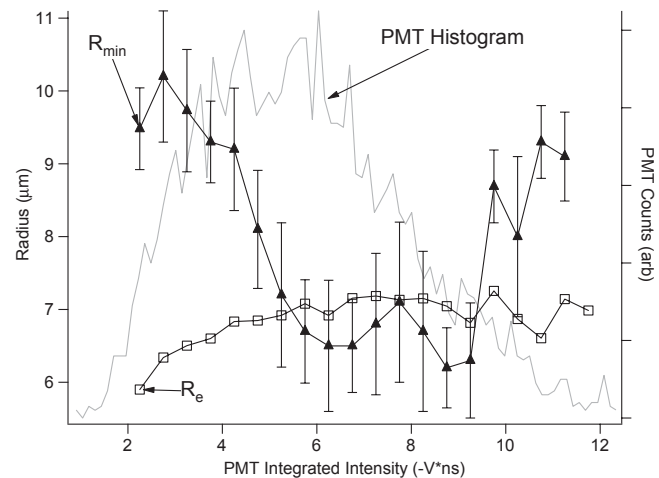


FIG. 3. PMT histogram shows the relative frequency of integrated PMT intensities during one data acquisition. R_e is the radius of emission from black body fits of calibrated spectrum data. R_{\min} is the minimum radius measured from Mie scattering data like that of Figure 1. Both R_e and R_{\min} data are discriminated by 0.5 V ns ranges of PMT integrated intensity.

gas and the simulation contains all necessary terms to accurately describe its motion. We find that the applied acoustic pressure is 1.4 ± 0.05 atm with its phase shown in Fig. 1. Near the minimum, the necessary equations to describe its equation of state, while simultaneously satisfying all past experimental observations, do not exist. The fit we present near the minimum should be viewed in this context then as merely an accurate parametrization of the data and not a description of the internal state of the compressed matter. Nonetheless, an accurate description of the maximum collapse speed and its resulting acoustic radiation can be obtained using our methods.

During a given cycle of sound, the maximum potential energy available to heat and ionize the contents of a bubble is $E_p = 4\pi(R_m^3 - R_c^3)p_0/3$, where p_0 is the ambient pressure which for Fig. 1 is 1 atm [29]. The number of atoms in the steady state bubble is $N_0 = 4\pi R_0^3 p_0 / 3kT_0$, where R_0 is the ambient radius which occurs when the total pressure acting on the bubble equals p_0 , and kT_0 is the product of Boltzmann's constant with the ambient temperature. We measured the R_0 via backlighting with sound off to be 22 ± 2 μm which equates to $N_0 = 1.1 \pm 0.3 \times 10^{12}$ atoms and a collapse density of $n_c = 1.1 \pm 0.5 \times 10^{21}/\text{cm}^3$ using $R_c = 6.5$ μm . The energy available to ionize atoms when the minimum radius is reached is equal to the potential energy plus the work done by the acoustic field, minus the energy lost to acoustic radiation, viscosity, and heating the gas, or:

$$E_c = E_p + \Delta W_a - \Delta E_{\text{rad}} - \Delta E_\eta - \Delta U_T, \quad (1)$$

where ΔE_{rad} and ΔE_η are the energy lost to acoustic radiation and viscosity, respectively, and ΔU_T is the energy required to heat the bubble to temperature T so that:

$$\Delta W_a = - \int p_a dV; \quad (2)$$

$$\Delta E_{\text{rad}} = \frac{4\pi}{c} \int R^3 \dot{R} \frac{d(p_g - p)a}{dt} dt,$$

$$\Delta E_\eta = 16\pi \int R \dot{R}^2 dt; \quad (3)$$

$$\Delta U_T = \frac{3}{2} N_0 (1 + x) k (T_c - T_0),$$

where “ x ” is the degree of ionization and p_a is the applied acoustic pressure. For the Xe bubble in sulfuric acid pulsating as in Fig. 1, $E_p/N_0 = 2.8$ eV/atom, $\Delta W_a/N_0 = 1.7$ eV/atom, $\Delta E_{\text{rad}}/N_0 = 1.8$ eV/atom, and $\Delta E_\eta/N_0 = 0.7$ eV/atom. This leaves 2.1 ± 0.6 eV/atom at R_c . This energy must provide for heating of electrons and ions, as well as for ionization.

We characterized the thermodynamic state of the plasma by measuring the emitted spectrum with a fiber-coupled Acton spectrometer attached to a Princeton Instruments ICCD. Individual spectrums were captured by the gated

ICCD and averaged using PMT data. The spectrum associated with the dynamics of Fig. 1 is shown in Fig. 2. The calibrated spectrum when fit to a Planck blackbody yields a definite emitting radius. In this case, the size of the emitting region is 6.4 μm at 8400 K. This agrees with the measurement of the bubble radius on collapse [Fig. 1(b)]. Given the low Mach-number motion of the bubble wall, this allows us to infer that the system is opaque across the visible spectrum and nearly homogenous in both temperature and density.

Heating to 8400 K requires 1.1 eV/free particle. At an example wavelength of 400 nm, an ionization of more than 36% of the atoms, or $N_e > 4 \times 10^{11}$, is required for opacity. With these additional electrons, the minimum energy needed for heating is $\Delta U_T/N_0 = 1.5$ eV. The remaining energy [$\sim N_0(0.6$ eV)] is used to form the free electrons. Per electron-ion pair, this gives 1.7 ± 1.7 eV/particle to form the free charges. Even at the limits of our uncertainty, the available energy by this reckoning is a factor of 3 lower than the ionization potential.

According to statistical mechanics, the degree of ionization for a dilute gas follows from Saha's equation:

$$\frac{x^2}{1-x} = \frac{2g_1}{n_0\lambda^3} \exp\{-\chi/kT\}, \quad (4)$$

where g_1 is the effective degeneracy of the electronic states of the ion, at 8400 K g_1 is 2.7, $\lambda = h/\sqrt{2\pi m_e kT}$ is the electron thermal de Broglie wavelength (8.1 \AA at 8400 K), and $n_0 = N_0/V_c \sim 1.1 \pm 0.5 \times 10^{21}/\text{cm}^3$ is the atomic density when the radius of the bubble has reached R_c . Using the value of the ionization potential for an isolated atom $\chi_0 = 12.1$ eV yields $x = 7 \times 10^{-4}$ which is orders of magnitude below the level required for opacity. In order to reach 36% ionization, this system would require the presence of a collective process that reduces χ from 12.1 to 2.7 eV. In the event of such a process, the energy available inside of the collapsed bubble would be sufficient to produce the number of ions needed for opacity.

While the interpretation of the spectrum infers opacity and the required high level of ionization, the bubble dynamics and resulting available energy makes no such assumption. For the purposes of discussion, we can distribute the available energy to the plasma formed inside the bubble in the ideal limit where Saha's equation is applied using the bare ionization potential $\chi = \chi_0 = 12.1$ eV. The available energy of 2.1 ± 0.5 eV/atom at a density of $1.1 \pm 0.5 \times 10^{21}/\text{cm}^3$ distributes itself according to ideal statistical mechanics to a temperature of 13400 ± 2500 K and a degree of ionization of $3\% \pm 2.4\%$. As has been emphasized [30], the spectrum of light emission at this temperature and degree of ionization should include bound-free transitions in addition to free-neutral and free-free Bremsstrahlung processes. In this manner, the best-fit transparent spectrum is calculated within the bounds of uncertainty and leads to the dashed plot in Fig. 2. In this

case, both maximum temperature (15 900 K) and atomic density ($1.6 \times 10^{21}/\text{cm}^3$) were needed to best match the intensity of the data. As mentioned [31,32], the peak in the transparent 15 900 K spectrum is close to the peak in the 8400 K blackbody. Given the various uncertainties and the fact that the measured spectrum is an average over the entire implosion event, these spectra are in reasonable qualitative agreement.

Various theoretical and experimental insights can be used to distinguish between the opaque and transparent “blackbody-imposter” solutions for the light emitting state. First, consider the strong spectral line at 823 nm from a transition that has the metastable Xe^* as its ground state. This is an opaque line and its peak will lie on a blackbody curve with the plasma’s temperature [13] (p. 247). The predicted line intensity is shown in Fig. 2, supposing this was a transparent system at 15 900 K. Yasui [33] has presented a detailed analysis of quenching of molecular lines in sonoluminescence from single bubbles in water and has argued that they are quenched by collisions. What makes SL from sulfuric acid so interesting is that the gas density at the moment of collapse is so low—being an order of magnitude less than SL in water. This system is therefore more amenable to modeling and it will be interesting to see if theory exhibits quenching of the atomic lines by collisions. Time resolved spectra of a single xenon bubble in phosphoric acid [19] were acquired at collapse gas densities and temperatures comparable to this Letter. These data show that the opaque atomic line does not disappear until it is swallowed by the broadband blackbody spectrum. For these reasons, we propose that the absence of the Xe^* 823 nm line in Fig. 2 supports our assertion that the light emitting region is not transparent. Finally, there is an argument based upon well-known, first order corrections to Saha’s equation [13,34]. At 15 900 K with $n_0 = 1.6 \times 10^{21}/\text{cm}^3$, Eq. (4) yields a degree of ionization of $x = 5.4\%$ which we now argue is unstable at the first order of perturbation. Following Landau and Zeldovich [13,34], the ionization potential is corrected at first order to

$$\chi \approx \chi_0(1 - 2\gamma a_B n_0^{1/3}) - Ae^2/\delta_D, \quad (5)$$

where $A = 1$ is the coefficient of the Debye screening term which reduces the distance an electron must move from an atom to be liberated to $\delta_D = \sqrt{kT/8\pi n_e e^2}$, a_B is the Bohr radius, and $\gamma = 1.78$ is a coefficient determined by photon induced conductivity in cold xenon at high pressure [35]. The first term reduces the ionization potential via the hybridization of nearest neighbor xenon atoms. This term has been applied to SL previously by Yasui [36]. For 15 900 K and $n_0 = 1.6 \times 10^{21}$, Eq. (2) yields a reduction in ionization potential of 4.8 eV. Plugging this back into Eq. (1) dramatically increases the degree of ionization and the transparent fit in Fig. 2 is no longer valid. We have proposed that for such large T and atomic density, the effects of screening cannot be treated as a simple perturbation.

Instead one must seek a self-consistent solution to Eqs. (4) and (5) subject to the available total energy (this possibility was realized in [37]). For the parameter space discussed in this Letter and with $A = 1$, no self-consistent solution exists indicating a degree of ionization approaching $x = 1$.

The high degree of ionization inside of an SL plasma is due to the fact that SL occurs at a relatively high atomic density. Ebeling *et al.* has calculated $x(n_0)$ for given temperatures for xenon and found that at densities above $\sim 10^{22}/\text{cm}^3$ there is a rapid increase in “ x ” which looks like a first order phase transition [38]. For the 28 kHz xenon bubble in sulfuric acid discussed above and for the 40 Hz xenon bubble in phosphoric acid [19], blackbody behavior and therefore, a large value of “ x ” is found at $n_0 \sim 1.1 \times 10^{21}/\text{cc}$. In these cases, the phase transition to opacity occurs at an unexpectedly low value of the density. A simple picture of how this can happen is provided by Eq. (5). If A is chosen to be a weakly varying function of the thermodynamic parameters then a reduction of the ionization potential to 2.7 eV as required for opacity can be achieved. At 8400 K and $n_0 = 1.1 \times 10^{21}/\text{cc}$, the electrostatic potential at the Debye radius is $e^2/\delta_D = 10.7\sqrt{x}$ eV, so that lowering of χ due to hybridization of 2.4 eV when added to a lowering of 7.0 eV due to electrostatic screening provides the requisite ionization potential. This occurs with $A \geq 1.1$ and a self-consistent solution to Eq. (5), for the best fit parameters used in this analysis.

The above analysis was carried out for data where the PMT integrated intensity was 6–6.5 V ns. A summary of the spectrum blackbody radius fits (R_e) and Mie scattering collapse radius (R_c) for other selections can be found in Fig. 3. For a range of PMT areas, R_c and R_e agree and it is clear that blackbody behavior is attained. The analysis of potential lowering for all values is in the Supplemental Material [24]. In all of these cases, the ionization potential needs significant reduction to attain the required ionization.

Sonoluminescence in a weakly collapsing bubble is well described by hydrodynamics. We have detailed a new technique whereby input sound and bubble dynamics can be measured with sufficient accuracy so that via application of energy conservation, one can elucidate thermodynamic properties of the plasma which form inside the bubble at the moment of light emission. In the case of a bubble in sulfuric acid driven at 28 kHz, we can apply energy conservation and find only 2.1 ± 0.6 eV/atom available to the interior gas for ionization and light emission. A transparent theory for this dense plasma can be discounted as it is unstable to well-known first order perturbation theory and fails to describe line intensity. Likewise, sufficient ionization for opacity cannot be achieved with this amount of energy using the Saha model of a dilute gas. As a result, we argue that the ionization potential must be lowered dramatically by screening and hybridization. How this theory is put on a first principles

statistical mechanics basis along the lines of Teller *et al.* [39] remains to be seen.

We gratefully acknowledge support from the Air Force Office of Scientific Research. We thank Brian Naranjo, Keith Weninger, and Carlos Camara for valuable discussions.

-
- [1] H. Frenzel and H. Schultes, *Z. Phys. Chem., Abt. B* **27**, 421 (1934).
 - [2] T. J. Matula, R. A. Roy, P. D. Mourad, W. B. McNamara III, and K. S. Suslick, *Phys. Rev. Lett.* **75**, 2602 (1995).
 - [3] H. X. Xu and K. S. Suslick, *Phys. Rev. Lett.* **104**, 244301 (2010).
 - [4] P. R. Temple, master's thesis, University of Vermont, 1970.
 - [5] H. Xu, N. G. Glumac, and K. S. Suslick, *Angew. Chem., Int. Ed.* **49**, 1079 (2010).
 - [6] B. P. Barber and S. J. Putterman, *Nature (London)* **352**, 318 (1991).
 - [7] C.-K. Su, C. Camara, B. Kappus, and S. J. Putterman, *Phys. Fluids* **15**, 1457 (2003).
 - [8] C. Camara, S. Putterman, and E. Kirilov, *Phys. Rev. Lett.* **92**, 124301 (2004).
 - [9] D. F. Gaitan, Ph.D. thesis in physics, University of Mississippi, 1990.
 - [10] Q. D. Chen and L. Wang, *Phys. Lett. A* **339**, 110 (2005).
 - [11] K. S. Suslick and D. J. Flannigan, *Annu. Rev. Phys. Chem.* **59**, 659 (2008).
 - [12] S. D. Hopkins, S. J. Putterman, B. A. Kappus, K. S. Suslick, and C. G. Camara, *Phys. Rev. Lett.* **95**, 254301 (2005).
 - [13] Y. B. Zel'dovich and Y. P. Raëizer, *Physics of Shock Waves and High-Temperature Hydrodynamic Phenomena* (Dover Publications, Mineola, 2002).
 - [14] H. R. Griem, *Principles of Plasma Spectroscopy*, Cambridge Monographs on Plasma Physics Vol. 2 (Cambridge University Press, Cambridge, U.K., 1997).
 - [15] D. J. Flannigan and K. S. Suslick, *Nat. Phys.* **6**, 598 (2010).
 - [16] L. Yuan and H. Ping, *Mod. Phys. Lett. B* **19**, 1711 (2005).
 - [17] G. Vazquez, C. Camara, S. J. Putterman, and K. Weninger, *Phys. Rev. Lett.* **88**, 197402 (2002).
 - [18] G. Vazquez, C. Camara, S. Putterman, and K. Weninger, *Opt. Lett.* **26**, 575 (2001).
 - [19] B. Kappus, S. Khalid, A. Chakravarty, and S. Putterman, *Phys. Rev. Lett.* **106**, 234302 (2011).
 - [20] S. Khalid, B. Kappus, K. Weninger, and S. Putterman, *Phys. Rev. Lett.* **108**, 104302 (2012).
 - [21] D. J. Flannigan and K. S. Suslick, *Nature (London)* **434**, 52 (2005).
 - [22] R. Urteaga and F. J. Bonetto, *Phys. Rev. Lett.* **100**, 074302, 074302 (2008).
 - [23] See Supplemental Material at <http://link.aps.org/supplemental/10.1103/PhysRevLett.111.234301> for further descriptions of experimental technique and supplemental data.
 - [24] A. Prosperetti, *J. Fluid Mech.* **222**, 587 (1991).
 - [25] B. Kappus, S. Khalid, and S. Putterman, *Phys. Rev. E* **83**, 056304 (2011).
 - [26] A. Prosperetti and Y. Hao, *Phil. Trans. R. Soc. A* **357**, 203 (1999).
 - [27] C. C. Wu and P. H. Roberts, *Proc. R. Soc. A* **445**, 323 (1994).
 - [28] W. C. Moss, D. B. Clarke, J. W. White, and D. A. Young, *Phys. Fluids* **6**, 2979 (1994).
 - [29] R. Lofstedt, B. P. Barber, and S. J. Putterman, *Phys. Fluids A* **5**, 2911 (1993).
 - [30] S. Hilgenfeldt, S. Grossmann, and D. Lohse, *Nature (London)* **398**, 402 (1999).
 - [31] S. Hilgenfeldt, S. Grossmann, and D. Lohse, *Phys. Fluids* **11**, 1318 (1999).
 - [32] D. Hammer and L. Frommhold, *J. Mod. Opt.* **48**, 239 (2001).
 - [33] K. Yasui, *Phys. Rev. Lett.* **83**, 4297 (1999).
 - [34] L. D. Landau, E. M. Lifshietis, and L. P. Pitaevski, *Statistical Physics, Course of Theoretical Physics* (Butterworth-Heinemann, Oxford, 1980), 3rd ed., Vols. 5 and 9.
 - [35] K. A. Goettel, J. H. Eggert, I. F. Silvera, and W. C. Moss, *Phys. Rev. Lett.* **62**, 665 (1989).
 - [36] K. Yasui, T. Tuziuti, J. Lee, T. Kozuka, A. Towata, and Y. Iida, *J. Chem. Phys.* **128**, 184705 (2008).
 - [37] M. Gitterman and V. Steinberg, *Phys. Rev. Lett.* **35**, 1588 (1975).
 - [38] W. Ebeling, A. Förster, W. Richert, and H. Hess, *Physica (Amsterdam)* **150A**, 159 (1988).
 - [39] S. G. Brush, H. L. Sahlin, and E. Teller, *J. Chem. Phys.* **45**, 2102 (1966).



Collision Time Measurements in a Sonoluminescing Microplasma with a Large Plasma Parameter

A. Bataller,* B. Kappus, C. Camara, and S. Putterman

¹*Department of Physics and Astronomy, University of California, Los Angeles, Los Angeles, California 90095, USA*

(Received 29 March 2014; published 7 July 2014)

The plasma which forms inside of a micron-sized sonoluminescing bubble in water for under a nanosecond has been probed with 3 ns long laser pulses. A comparison of the response to 532 and 1064 nm light indicates that the plasma number density is about $2 \times 10^{21} \text{ cm}^{-3}$ and that transport properties are dominated by strong screening and correlation effects. The spherical shape, well-defined atomic density, and blackbody temperature make the sonoluminescing plasma a test bed for theories of strongly coupled plasmas. The plasma in this experiment distinguishes between competing theories of strong, intermediate, and weak effective screening.

DOI: 10.1103/PhysRevLett.113.024301

PACS numbers: 43.35.Hl, 52.27.Gr, 52.38.-r, 78.60.Mq

The passage of a planar sound wave through a fluid leads to pulsations of a trapped bubble that are so large that the energy density of sound is concentrated by 12 orders of magnitude to generate flashes of ultraviolet light that can be as short as 35 ps [1–3]. The mechanism of energy concentration and the state of the bubble contents at the moment of light emission constitute the study of sonoluminescence (SL). During the rarefaction part of the sound field, the radius R of the bubble expands to a maximum value, where the internal pressure of the gas it contains is low compared to the ambient value of 1 atm. In a 30 kHz sound field, the subsequent implosion is supersonic as it passes through the ambient radius R_0 on the way to a collapse radius R_c [4]. The ideal gas law gives an ambient density of $n_0 = 2.4 \times 10^{19} \text{ cm}^{-3}$ and for xenon gas $R_0/a \sim 7.6$, where a is the radius of the bubble when the gas is compressed all the way to its van der Waals hard core. Light scattering measurements indicate that for a trapped single bubble in a 30 kHz sound field, $R_c \sim a$, so that the atomic density in the collapsed xenon bubble is $n_c \sim 10^{22} \text{ cm}^{-3}$ [5].

At the moment of maximum compression, $R \sim R_c \sim 1/2 \mu\text{m}$, a flash of light is emitted. Its spectral density closely matches an ideal Planck blackbody [6–9]. As a blackbody is opaque, the free charge density must be very high. According to the simplest formulas for opacity, where it is due to scattering of light by free charges [10], a photon mean free path of $1/2 \mu\text{m}$ at 532 nm and the measured temperature of 9250 K requires a charge density $n_e > 10^{21} \text{ cm}^{-3}$. Analysis of line spectra in other sonoluminescing systems has been interpreted in terms of similar charge densities and temperatures [11–13].

The repetitive attainment of such dense plasmas in spherical geometries with a controlled atomic density at temperatures $T \sim 1 \text{ eV}$ enables the use of SL for studying transport properties of dense plasmas. For this case, the plasma coupling parameter is $2.9 < \Gamma < 6.3$, where

$$\Gamma = \frac{e^2}{kT} \left(\frac{4\pi n_e}{3} \right)^{1/3}. \quad (1)$$

In this Letter we explore this new direction in SL research by comparing the response of the SL plasma to input laser light at two different wavelengths, 1064 and 532 nm. This test is motivated by the fact that the free charge densities are so high that the corresponding plasma frequency $\omega_p = \sqrt{4\pi n_e e^2 / m}$ (where m is the electron mass) is comparable to the angular frequency ω of the light in the laser pulses, which can be used to probe the SL microplasma. According to whether $\omega > \omega_p$ or $\omega < \omega_p$, the incident light is transmitted or reflected by an ideal plasma. We note that $n_e \sim 10^{21} \text{ cm}^{-3}$ corresponds to a plasma wavelength $\lambda_p \sim 1000 \text{ nm}$, which lies between the 1064 and 532 nm probe pulses. The goal of studying the interaction of a laser with SL was first introduced by Diebold [14] with the purpose of generating high plasma temperatures. A recent experiment by Khalid *et al.* [15] demonstrated successful SL-laser coupling and provided further evidence that SL arises from a highly ionized plasma [13,16]. Our experiment entails both spatial and temporal challenges. The laser must hit the bubble at a properly synchronized moment during the acoustic cycle.

Figure 1 shows the main experimental observation that (a) a weak pulse of 532 nm light can interact with the SL plasma and lead to an increase in light emission, whereas (b) the 1064 nm light interacts with the SL plasma only above an intensity threshold. The upper data set on each panel shows the Mie scattering signal from the bubble, which is a measure of its radius. The lower curve shows the intensity of SL during that same acoustic cycle as recorded by a photomultiplier tube (PMT). The diagonal data set in the middle shows the increase in light output of the bubble when the laser hits the bubble during the lifetime of the SL microplasma. Theoretical analysis of this data permits one

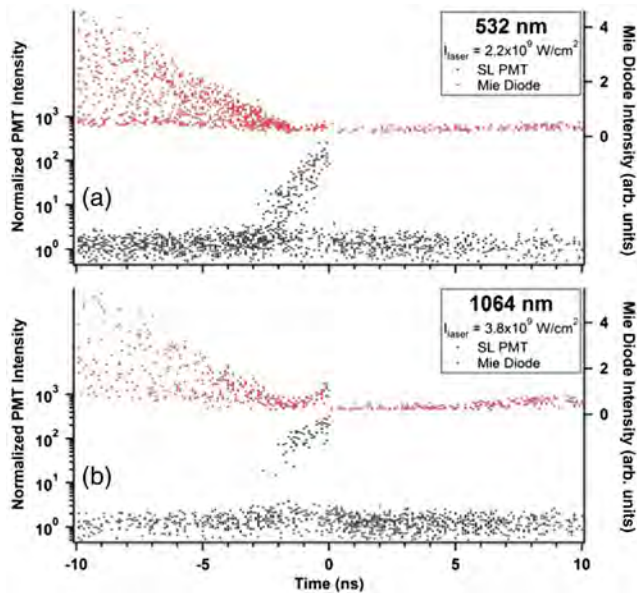


FIG. 1 (color online). Scatter plots showing the Mie scatter intensity (red dots) and the SL intensity (black dots) for (a) 532 nm and (b) 1064 nm. The SL intensity is normalized by the intensity distribution of SL flashes without an incident laser pulse and can be seen as a band of points centered on unity. For each SL intensity point, there is a corresponding Mie scatter point which is a measure of the bubbles' radius and confirms successful spatial synchronization. SL-laser interactions only occur when the laser and SL flash overlap in time. The spread in Mie scatter points is due to the drift in bubble location relative to the laser focus during the laser's repetition rate (10 Hz). As SL-laser interactions grow stronger, the accompanying Mie scatter signal increases due to an enlarged plasma radius.

to select between the transport theory of dilute plasmas and various density modifications put forward by different authors [17–19].

Into degassed water we dissolve 150 torr of a gas mixture that is 99% nitrogen and 1% xenon. The water is in a 30 kHz quartz resonator driven by piezoelectric transducers. A bubble is seeded into the resonator near the velocity node of the standing wave resonance and is driven to large pulsations and sonoluminescence. A seeded YAG (TEM00) laser is synchronized with the bubble by timing from the previous SL emissions, as the flashes have a subnanosecond clocklike repetition [20]. Three light detectors are used: a photodiode which records the scattered laser light, a photodiode that measures the intensity and timing of the laser pulse, and a PMT with a laser-blocking filter (Notch) that records the broadband SL as well as the additional broadband emission which results from a laser pulse that is successfully synchronized with a SL flash. The acquisition of many scattering events and many flashes of SL is displayed in Fig. 1. The intensities of each event are plotted as a function of the time elapsed between the leading edge (10% peak intensity) of the laser pulse and the SL flash (which occurs at $t = 0$). For instance, the SL

events plotted at -4 ns (on the lowest trace) correspond to acoustic cycles where the leading edge of the laser hit the bubble 4 ns before the SL flash. Such an early hit corresponds to a bubble with a radius larger than R_c , and so the laser light scattered from the bubble as shown on the upper trace is much larger than occurs at the minimum radius, which happens at $t = 0$. If the bubble is not at its minimum radius, i.e., if it is not in the process of emitting SL, then the PMT records the intensity of the SL flash for that cycle and it is plotted below the time of the laser hit. This is shown by the PMT events close to the abscissa. As the laser pulse is ~ 3 ns in duration, a laser-plasma interaction can occur even when the leading edge of the laser reaches a bubble 3 ns before SL. These laser on plasma events can be weak (532 nm) or zero (1064 nm) because the laser is turning off as the SL is turning on. A laser hit can also result in a weak interaction if the bubble is not centered on the laser's focus, which results in a spread in Mie intensities for a given time. Because of the maximum available pulse energy, the largest events are seen when the laser arrives at the bubble as SL is turning on. In this case, we find broadband emission with an energy that can be much higher than a typical flash of SL.

The SL-laser interaction gap (see Fig. 1) for 532 vs 1064 nm is apparent in the histogram of events shown in Fig. 2. Figure 2 displays the frequency of events during the SL-laser temporal overlap as a function of the intensity of total light emission from the bubble. This includes the usual SL plus the energy grabbed from the laser by the SL plasma. The peak at unity is the strength of a typical free running flash of SL and the gap from 4–20 reflects the difference in interaction of the 532 vs 1064 nm laser wavelengths with the SL plasma. What we measure is clearly below the breakdown threshold which occurs at an intensity 50 000 times that of SL and 200 times larger than the minimum observable laser bubble interaction. This

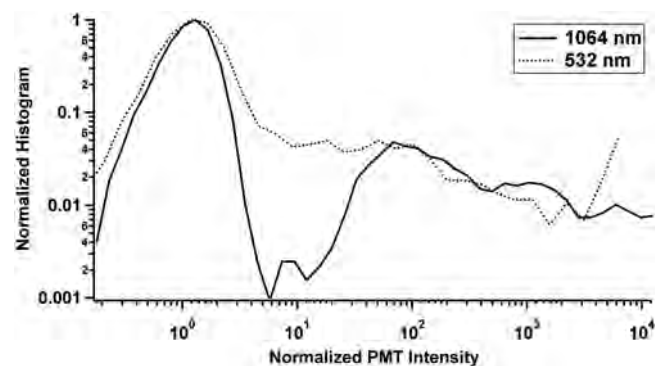


FIG. 2. Normalized histogram of the SL intensity for a range of laser intensities ($0.5\text{--}25 \times 10^9$ W/cm²) at 1064 (solid curve) and 532 nm (dotted curve). Only points within the interaction region of -4 to $+1$ ns (532 nm) and -8 to $+1$ ns (1064 nm) were used for the histogram. Although concurrent to the SL, a large number of laser shots did not result in an interaction due to the lack of spatial overlap caused by the bubbles' drift in location.

confirms that we are seeing an interaction between the laser and the SL plasma.

The interaction of a laser pulse with a plasma is affected by the plasma frequency and the collisionality (or absorptivity) of the plasma. The reflection of light by a sufficiently dense plasma when $\omega < \omega_p$, assumes an ideal plasma with $\omega\tau \gg 1$, where τ is the collision time. In this limit the motion is reversible and no energy is absorbed by the plasma. A theory which explains the conversion of incoming light into plasma energy must include a finite τ .

Reflectivity in the limit $\tau \rightarrow \infty$ is graphed in Fig. 3. The solid curves give the plasma reflectance as a function of the free charge density for 532 and 1064 nm. On Fig. 3 this is labeled as the Debye theory of transport. The transition to complete reflectance at high charge density is the well-known plasma frequency effect which motivated this experiment. When interactions are included according to the transport theory of a dilute plasma (see below), one obtains the dotted line in Fig. 3. Application of the theory of dilute plasmas to high charge densities leads to short collision time, $\omega\tau < 1$. In this limit absorption shorts out plasma reflection. An explanation of the SL-laser interaction requires a theory of the collision time for dense plasmas which follows.

Electrons of mass m and velocity \vec{v} are accelerated by an electric field \vec{E} according to the Drude model,

$$m \frac{d\vec{v}}{dt} + \frac{m}{\tau} \vec{v} = -e\vec{E}. \quad (2)$$

When coupled to Maxwell's equations in the presence of a disturbance driven at frequency ω , one obtains the dispersion law for the plasma wave number k_p given by [21]

$$k_p^2 = \frac{\omega_p^2}{c^2} \frac{i\omega\tau}{1 - i\omega\tau} + \frac{\omega^2}{c^2}. \quad (3)$$

For the frequency dependent collision time in the gaseous plasma, we take

$$\tau = \frac{3\hbar\omega}{4\pi n_e e^4 [1 - e^{-\beta\hbar\omega}]} \sqrt{\frac{3mkT}{2\pi}} \frac{1}{\ln \Lambda}. \quad (4)$$

This term includes the limit of $\hbar\omega \rightarrow 0$, where τ is determined by small energy collisions in a Coulomb plasma, as well as free-free scattering in which an electron absorbs a photon of frequency ω . In the limit where $\omega > \omega_p$, $\omega\tau \gg 1$, and $\ln \Lambda = 1$, Eqs. (3) and (4) yield a $2\text{Im}(k_p)$ consistent with inverse bremsstrahlung attenuation of light (Eq. 5.21 of [10] corrected for induced emission).

For a strongly coupled plasma (SCP) where $\Gamma > 1$, screening and correlations must be included to determine the effective collision frequency. Particle interactions are well described in the framework of binary collisions, even in the dense plasma limit [22]. In this spirit, we present a simplified theory where the effects of SCPs are included in our choice of the collision time. For this analysis, we consider three models that assign a formulation for the Coulomb logarithm in Eq. (4). The first is an extreme screening model that utilizes the logarithmic formulation presented by Valuev [17] and sets the Debye length as the maximum impact parameter [Eq. 5(a)]. The second model proposed by Daligault [18] represents an intermediate scaling of the impact parameter [Eq. 5(b)] and includes correlation effects. The dilute theory is also considered for comparison [Eq. 5(c)], where screening is weak and held constant. These models are given by

$$\text{Debye: } \ln \Lambda = \frac{\sqrt{3}}{\pi} \ln \sqrt{\frac{1}{6} \Gamma_\omega^{-3} + 1}, \quad (5a)$$

$$\text{Daligault: } \ln \Lambda = \frac{\sqrt{3}}{\pi} \ln \left(\frac{0.7}{\sqrt{6}} \Gamma_\omega^{-3/2} + 1 \right), \quad (5b)$$

$$\text{Dilute: } \ln \Lambda = \frac{\sqrt{3}}{\pi}, \quad (5c)$$

where

$$\Gamma_\omega = \Gamma \left(\frac{kT}{\hbar\omega} (1 - e^{-\beta\hbar\omega}) \right). \quad (6)$$

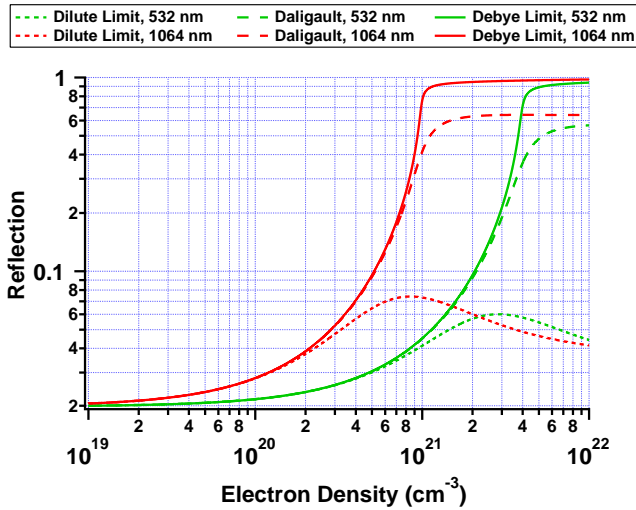


FIG. 3 (color online). Plasma reflection of 532 and 1064 nm light as a function of electron density for various collision theories. The Debye theory (solid curves) represents a highly screened plasma, where $\omega\tau \gg 1$ and high levels of reflection are observed for $\omega < \omega_p$. The dilute theory (dotted curves) diverges from the high reflectivity behavior due to strong damping ($\omega\tau \lesssim 1$) in the high density regime. The Daligault theory (dashed curves) experiences an intermediate level of reflection in the dense regime and is capable of describing both reflection at 1064 nm and spectral opacity at 532 nm.

As we apply transport theory over a range of frequencies we include the possibility of the plasma coupling parameter becoming a function of frequency [Eq. (6)] as has been included by Dawson [23]. Furthermore, we have also included an overall factor of ~ 2 in Eq. (4) that distinguishes Dawson and Daligault from Zel'dovich.

Strong effective screening [Eqs. 5(a) and 5(b)] lengthens the collision time for $\Gamma > 1$, and, according to Eq. (6), this effect varies with wavelength. Figure 4 shows the distance light travels before decaying to $1/e$ as a function of electron density for the Daligault theory [Eq. 5(b)]. The region labeled τ dominated occurs when the laser frequency is greater than the plasma frequency. For the Daligault theory at a charge density of $\sim 2 \times 10^{21} \text{ cm}^{-3}$, the 532 nm light is τ dominated while the 1064 nm light is ω_p dominated and is strongly reflected. In this range of charge density, the 532 nm penetrates most of the bubble while the 1064 nm penetrates just a fraction of the bubble radius.

We appeal to the Daligault theory and the region of parameter space with a charge density of $\sim 2 \times 10^{21} \text{ cm}^{-3}$ to explain the interaction of a laser with the microplasma in a sonoluminescing bubble. First, at this density the decay length of 532 nm light is approximately equal to the bubble radius which is consistent with the observed Planckian spectrum. Next, the 532 nm light penetrates the bubble whereas the 1064 nm light is restricted to a depth less than 20% of the bubble radius. Furthermore, the intensity of light at 1064 nm to penetrate into the surface region is down by a factor of 2.5 from the 532 nm light. It is important to note that for all of the theories discussed, densities lower

than 10^{21} cm^{-3} would result in weak laser-plasma coupling due to the long decay length (Fig. 4).

A full explanation of the absorption gap shown in Figs. 1 and 2 still requires some nonlinear threshold phenomenon that allows for weak interactions at 532 nm but precludes the absorption of weak laser light at 1064 nm. This phenomenon goes beyond processes that we have included in the theory of τ (Fig. 5). To this end we note that the average laser intensity at 1064 nm is $3.8 \times 10^9 \text{ W/cm}^2$, which corresponds to an electric field $E \sim 10^6 \text{ V/cm}$. From Fig. 5 the collision time is about 5 fs so that between collisions, an electron with thermal velocity $\sim 7 \times 10^7 \text{ cm/s}$ moves about 3.5 nm. The change in electron velocity during a period of light is about 10^6 cm/s . The number of velocity increments of this size required to double the energy is 50, if the collisions were all additive. Because of the randomness of collisions and due to $\omega\tau \sim 4$, the total number of collisions required to double the energy is $50 \times 50 \times 4 \times 4 = 40000$. During this time the electron walks a distance $\sim 1 \mu\text{m}$. This distance is much greater than the electric fields' penetration depth, which we interpret as implying that at 1064 nm, externally driven diffusion precludes finite energy transfer. At 532 nm the response is τ dominated and the field penetrates most of the bubble and finite transfer is possible. The time required for the energy of an electron to double in the externally applied field is about 0.5 ns. Possible threshold phenomena include breakdown at the water interface and higher levels of ionization.

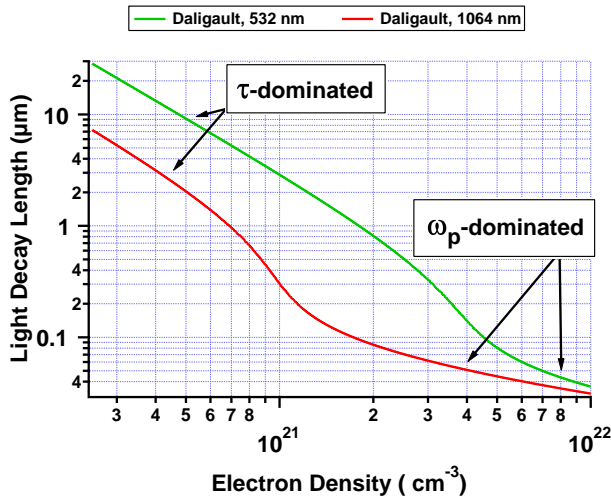


FIG. 4 (color online). Decay length of light in a dense plasma for 532 and 1064 nm using the collision theory of Daligault. Two absorption regimes are present for the electron density under consideration and are separated at the critical density ($\omega_p = \omega$). Based on the suggested electron density of $\sim 2 \times 10^{21} \text{ cm}^{-3}$ for the SL measured in this experiment, the absorption is τ dominated for 532 nm and ω_p dominated for 1064 nm.

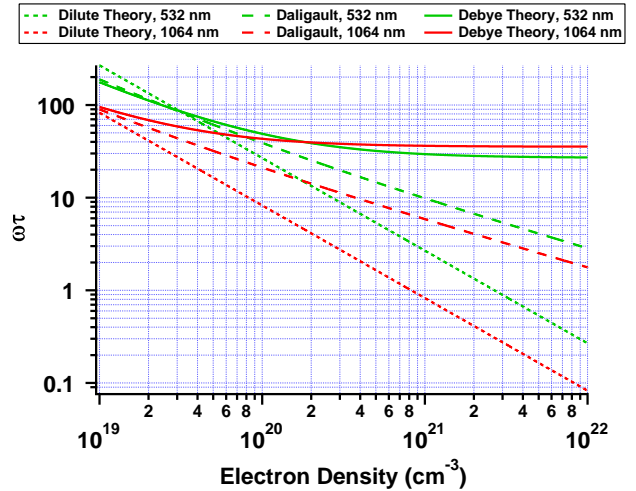


FIG. 5 (color online). Collision time of 532 and 1064 nm light as a function of electron density for various collision theories. The collision time for the Debye theory (solid curves) is large for all electron densities and becomes density-independent for large plasma parameters. The dilute theory (dotted curves) represents the shortest collision time. The intermediate theory of Daligault (dashed curves) lies between these limiting theories and scales with ω_p for large densities.

The plasma which forms in a collapsing noble gas bubble reaches a density with a plasma coupling parameter in excess of unity. The bubble has a well-defined number of atoms, a blackbody temperature, and is spherical in shape. It therefore becomes a test bed for the study of transport phenomena in dense plasmas. We have probed the sonoluminescing micro-plasma by targeting it with synchronized laser pulses at 532 and 1064 nm. Light emissions from the resulting interactions enable one to decide between various transport theories of dense plasmas and to determine that the plasma density is about $2\text{--}3 \times 10^{21} \text{ cm}^{-3}$. This technique has provided an electron density measurement for single-bubble SL in water, which has remained elusive for almost 25 years after its discovery. The measured plasma density of $\sim 3 \times 10^{21} \text{ cm}^{-3}$ corresponds to a Fermi temperature of 8700 K, which is slightly less than the spectral temperature. The possibility remains that some regions of the SL parameter space can exhibit Fermi degeneracy as well as dense plasma kinetics [24,25].

We gratefully acknowledge support from DARPA MTO for research on microplasmas and AFOSR for research on transport in dense plasmas. We thank Guillaume Plateau and Keith Weninger for valuable discussions.

*bataller@physics.ucla.edu

- [1] R. Hiller, S. J. Putterman, and B. P. Barber, *Phys. Rev. Lett.* **69**, 1182 (1992).
- [2] B. Gompf, R. Günther, G. Nick, R. Pecha, and W. Eisenmenger, *Phys. Rev. Lett.* **79**, 1405 (1997).
- [3] R. Hiller, S. J. Putterman, and K. R. Weninger, *Phys. Rev. Lett.* **80**, 1090 (1998).
- [4] K. R. Weninger, B. P. Barber, and S. J. Putterman, *Phys. Rev. Lett.* **78**, 1799 (1997).
- [5] B. P. Barber, R. A. Hiller, R. Löfstedt, S. J. Putterman, and K. R. Weninger, *Phys. Rep.* **281**, 65 (1997).
- [6] G. Vazquez, C. Camara, S. Putterman, and K. Weninger, *Opt. Lett.* **26**, 575 (2001).
- [7] C. Camara, S. Putterman, and E. Kirilov, *Phys. Rev. Lett.* **92**, 124301 (2004).
- [8] D. J. Flannigan and K. S. Suslick, *Nature (London)* **434**, 52 (2005).
- [9] S. Hopkins, S. Putterman, B. Kappus, K. Suslick, and C. Camara, *Phys. Rev. Lett.* **95**, 254301 (2005).
- [10] Ya. B. Zel'dovich and Yu. P. Raizer, *Physics of Shock Waves and High-Temperature Hydrodynamic Phenomena* (Dover, New York, 1966).
- [11] K. S. Suslick and D. J. Flannigan, *Annu. Rev. Phys. Chem.* **59**, 659 (2008).
- [12] D. J. Flannigan and K. S. Suslick, *Nat. Phys.* **6**, 598 (2010).
- [13] B. Kappus, S. Khalid, A. Chakravarty, and S. Putterman, *Phys. Rev. Lett.* **106**, 234302 (2011).
- [14] G. Cao, S. Danworaphong, and G. J. Diebold, *Eur. Phys. J. Spec. Top.* **153**, 215 (2008).
- [15] S. Khalid, B. Kappus, K. Weninger, and S. Putterman, *Phys. Rev. Lett.* **108**, 104302 (2012).
- [16] B. Kappus, A. Bataller, and S. Putterman, *Phys. Rev. Lett.* **111**, 234301 (2013).
- [17] Y. K. Kurilenkov and A. A. Valuev, *Contrib. Plasma Phys.* **24**, 161 (1984).
- [18] G. Dimonte and J. Daligault, *Phys. Rev. Lett.* **101**, 135001 (2008).
- [19] S. A. Khrapak, *Phys. Plasmas* **20**, 054501 (2013).
- [20] B. P. Barber and S. J. Putterman, *Nature (London)* **352**, 318 (1991).
- [21] S. Eliezer, *Plasma Phys. Controlled Fusion* **45**, 181 (2003).
- [22] S. D. Baalrud and J. Daligault, *Phys. Rev. Lett.* **110**, 235001 (2013).
- [23] T. W. Johnston and J. M. Dawson, *Phys. Fluids* **16**, 722 (1973).
- [24] S. Ichimaru, *Rev. Mod. Phys.* **54**, 1017 (1982).
- [25] S. Ichimaru, *Statistical Plasma Physics, Volume I: Basic Principles*, Frontiers in Physics Series (Westview, New York, 2008).

Blackbody Emission from Laser Breakdown in High-Pressure Gases

A. Bataller,^{*} G.R. Plateau, B. Kappus, and S. Putterman

Department of Physics and Astronomy, University of California, Los Angeles, Los Angeles, California 90095, USA

(Received 14 April 2014; published 15 August 2014)

Laser induced breakdown of pressurized gases is used to generate plasmas under conditions where the atomic density and temperature are similar to those found in sonoluminescing bubbles. Calibrated streak spectroscopy reveals that a blackbody persists well after the exciting femtosecond laser pulse has turned off. Deviation from Saha's equation of state and an accompanying large reduction in ionization potential are observed at unexpectedly low atomic densities—in parallel with sonoluminescence. In laser breakdown, energy input proceeds via excitation of electrons whereas in sonoluminescence it is initiated via the atoms. The similar responses indicate that these systems are revealing the thermodynamics and transport of a strongly coupled plasma.

DOI: 10.1103/PhysRevLett.113.075001

PACS numbers: 52.50.Jm, 52.20.-j, 52.27.Gr, 78.60.Mq

The passage of a sound wave through a fluid can lead to pulsations of a gas bubble that are so strong that a dense plasma forms at its minimum radius. The degree of ionization $n_e \sim 10^{21} \text{ cm}^{-3}$ is much larger than follows from Saha's equation at the measured temperature $T \sim 10\,000 \text{ K}$. Experiments on sonoluminescence (SL) have been interpreted in terms of screening and correlations which modify the equation of state at atomic densities that are over an order of magnitude lower than expected from theories of strongly coupled plasma (SCP) [1–8]. The SL microplasma is created via direct heating of the atoms. Mechanical energy from the sound field sets up an implosion that compresses and heats the atoms to the point where they ionize. The liberated electrons are brought up to the ion or atom temperature via collisions. The emitted thermal spectrum is mainly due to collisions of hot electrons with ions. In low frequency ($\sim 40 \text{ Hz}$) experiments the flash width is hundreds of nanoseconds and the electron temperature is in local thermodynamic equilibrium (LTE) with the ions and light. If the unexpected high ionization and resulting opacity of a sonoluminescing bubble is due to fundamental changes in the equation of state of SCPs, then these effects should be independent of the path by which the temperature and density are reached. To test whether the SL microplasma is a manifestation of a new thermodynamic state, we have generated similar plasmas using laser breakdown in high-pressure gases with atomic densities between 10^{19} – 10^{21} cm^{-3} , which reaches the density of SL in acids [2,5,6,9]. In this case, the path for energy flow is the reverse of SL as femtosecond laser pulses instantly ionize and energize the electrons while the ions remain cold. We report observation of an opaque plasma that persists well after the laser has turned off, and for times much longer than the recombination time scale. The plasma properties are consistent with the equations of state of the SL microplasmas and temporal evolution of the blackbody temperature provides insights into transport in SCPs.

The focusing of high-intensity laser pulses into gaseous media begins with a rapid ionization and heating of electrons. This is followed by a plasma expansion into the surrounding gas, whose luminous front vs time is shown in Fig. 1. The microplasma in Fig. 1 was generated using a 120 fs Ti:sapphire laser (Spectra-Physics) operating at 1 kHz with an adjustable energy of 0–1 mJ/pulse. The laser was focused with a 6 cm lens into the center of a pressure chamber. Optical access through the chamber was provided by fused silica viewports (Rayotek). The plasma's

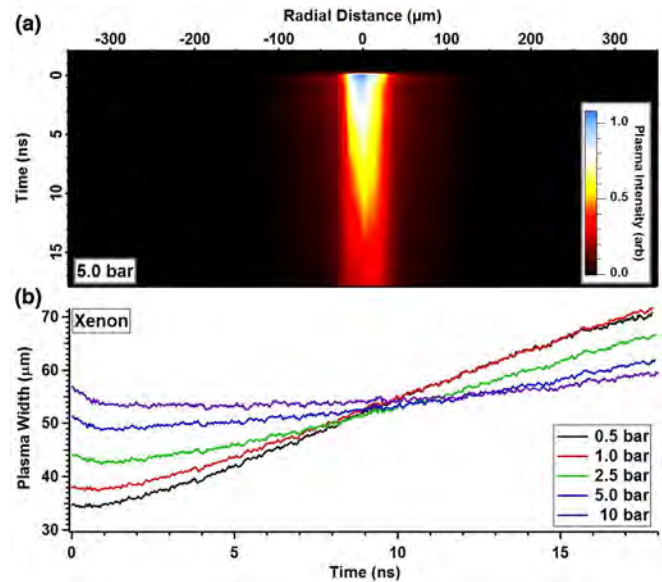


FIG. 1 (color online). Spectrally integrated plasma emission ($> 495 \text{ nm}$) vs radius and time. The streaked image (a) was acquired for 5 bar xenon breakdown using a laser energy of $235 \pm 4 \mu\text{J/pulse}$, where $t = 0$ indicates the moment of laser breakdown. The plasma's waist (FWHM) is plotted vs time (b) for various pressures. Plasma expansion becomes hindered with increasing pressure until $\sim 5 \text{ bar}$ is reached, at which point the plasma waist dwells before expanding.

light emission was collected and imaged by a 90 mm UV-to-near-infrared triplet lens (Edmund Optics). The plasma image was magnified by 5.34 and imaged onto the entrance slits of a 150 mm Czerny-Turner spectrometer (Princeton Instruments). The spectrally resolved plasma image was temporally resolved by aligning the spectrometer's output onto the entrance slits of a streak camera (Hamamatsu). The streak image in Fig. 1(a) is produced by keeping the spectrometer's entrance slits fully open (3 mm) and moving the grating to 0th order. Similarly, the spectral images in Fig. 2 were acquired by closing down the spectrometer's entrance slits (30 μm) and moving the grating to 1st order. The total amount of incident light entering the system in either mode is defined by the overlapping slit areas. The plasma image could be moved relative to the imaging system allowing spectral analysis at any plasma location. The spectral measurements presented in this Letter contain light from a plasma area of 32 μm^2 and was located at the center of the plasma column.

Because of the limited amount of light entering the imaging system, each spectral image (Fig. 2) consisted of an average of 6×10^5 breakdown events. However, shot-to-shot plasma intensity fluctuated by only $\sim 10\%$ and optical triggering resulted in a minimal temporal jitter of 20 ps. Both streak and spectral images show the plasma emission as a function of time, where $t_0 = 0$ ns marks the moment of laser breakdown. Indeed, laser-plasma scattering can enter the imaging system at the moment of breakdown and provide both a breakdown time stamp and a measurement for the system's temporal resolution. An example of this is present in Fig. 2(a) for t_0 and at the laser wavelength of 825 nm.

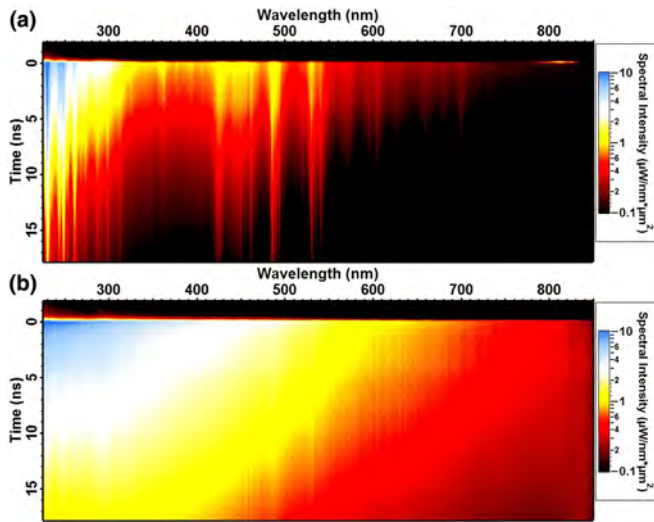


FIG. 2 (color online). Calibrated spectrum vs time for xenon breakdown at (a) 0.5 and (b) 5 bar using a laser energy of $235 \pm 4 \mu\text{J}/\text{pulse}$. At lower pressures, the plasma spectrum is dominated by atomic line emission. With increasing pressure, the spectrum is broadened until it becomes completely continuous (~ 5 bar).

A plasma's absolute spectral intensity provides important information regarding its opacity and mechanism of light emission. For this purpose, the imaging system was calibrated against known sources (deuterium and quartz tungsten halogen lamps) and corrected for solid angle. A temporal correction (< 30 ps) was made to account for chromatic dispersion within the imaging optics. Finally, an intensity correction was applied due to chromatic aberration and tested against the known sources.

Spectral images were measured as a function of static pressure p_0 for xenon, argon, and helium while maintaining a fixed laser power. For low p_0 [Fig. 2(a)], the plasma spectrum is dominated by atomic lines for all times recorded. As p_0 is increased, the continuum radiation rises while the atomic lines become heavily broadened. This trend continues until a critical pressure p_c is reached, where the spectrum becomes completely continuous for early times [Fig. 2(b)], which has been observed in a similar system [10]. The gas-dependent value of p_c is ~ 5 , 20, and 60 bar for xenon, argon, and helium, respectively. The continuous nature at p_c is visualized in Fig. 3, where individual spectra are extracted from Fig. 2(b) and plotted vs wavelength. For $p_0 = p_c$, continuous emission persists for a characteristic time scale t_{line} . This time scale is also gas dependent and is approximately 5, 1.5, and 0.15 ns for xenon, argon, and helium, respectively. For $t > t_{\text{line}}$, line emission emerges from the continuum and grows in strength relative to the continuum. This effect is observed in Fig. 3 for the Xe I transition line at 823 nm.

In the field of SL and SCP, testing spectra for opacity has proven to be a powerful technique for uncovering plasma properties [2,5–7,11–13]. The spectral intensity radiated by an ideal blackbody at temperature T is

$$I_\lambda = \frac{2\pi hc^2}{\lambda^5 (\exp\{\frac{hc}{\lambda k_B T}\} - 1)}. \quad (1)$$

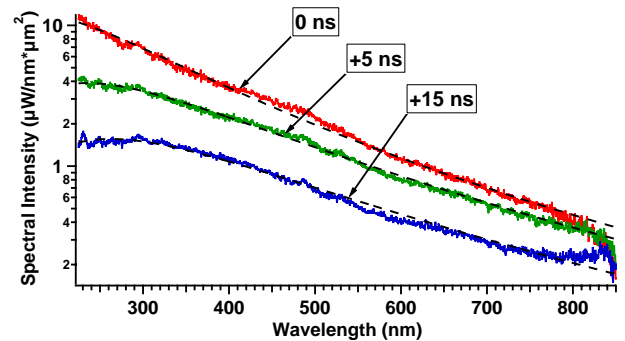


FIG. 3 (color online). Spectral intensity for 5 bar xenon breakdown at different times relative to the plasma formation. Blackbody fits (dashed curves) are plotted for each spectrum with values of $T = 16\,350$, $12\,350$, and $11\,050$ K for $t = 0$, $+5$, and $+15$ ns, respectively.

Deviation from blackbody behavior is quantified by multiplying I_λ by an effective emissivity ϵ , where $\epsilon = 1$ represents an ideal blackbody. Blackbody curves are presented in Fig. 3 and are well fit to the spectra. Fits were performed using a standard iterative method that minimizes the value of χ^2 . T and ϵ from the blackbody fits are plotted vs time in Fig. 4(a). High opacity is observed as $\epsilon > 0.8$ for $t < 14$ ns and approaches $\epsilon \approx 1$ at $t \approx 5$ ns. Consistent with the definition of a blackbody as the ideal radiator at a given temperature, the emissivity in Fig. 4(a)

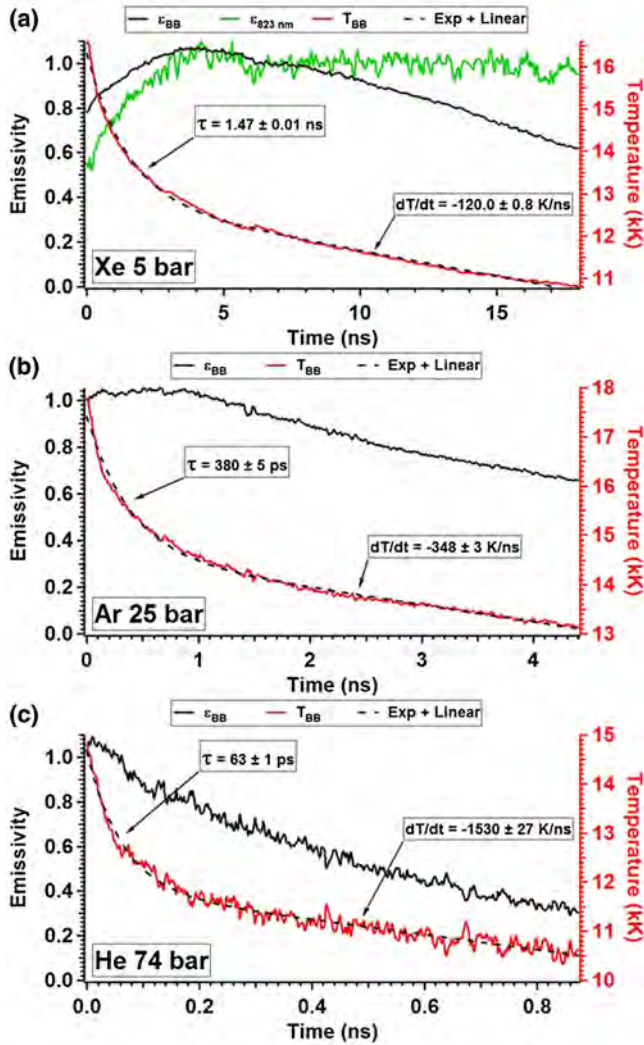


FIG. 4 (color online). Blackbody temperature (red curve) and effective emissivity (black curve) as a function of time for (a) 5 bar xenon, (b) 25 bar argon, and (c) 74 bar helium. Laser energies of 235 ± 4 , 325 ± 3 , and 570 ± 6 $\mu\text{J}/\text{pulse}$ were used for xenon, argon, and helium, respectively. For all gases, the temperature initially decays exponentially and is followed by a long linear decay. A fit to an exponential plus linear function is plotted (dashed curve) for each gas with characteristic time scales indicated. For xenon, the emissivity for the opaque Xe I transition is plotted (green curve) using the spectral intensity at 823 nm and the blackbody temperature.

never grows above unity (within experimental error $\sim 15\%$) even though the plasma temperature is decreasing exponentially. Further blackbody behavior is observed by measuring the emissivity value of the opaque 823 nm Xe I transition line ϵ_{823} . Using the blackbody temperature, the intensity at 823 nm, and Eq. (1), ϵ_{823} is plotted vs time in Fig. 4(a). For $t > t_{\text{line}}$, the plasma becomes increasingly transparent as indicated by the reduced emissivity and increased atomic line contribution to the spectrum. However, the emissivity for the strong 823 nm line remains opaque ($\epsilon_{823} \approx 1$) for $t > t_{\text{line}}$. Like ϵ , ϵ_{823} is never greater than unity, which has been observed in other blackbody plasmas [2]. High opacity is also observed for 25 bar argon and 74 bar helium in Figs. 4(b) and 4(c), respectively. With the exception of 5 bar xenon, ϵ begins near unity and drops after a time corresponding to the end of the exponential temperature decay. Possible reasons for the initial growth in ϵ for xenon breakdown are an increasing electron density after breakdown (as observed in [10]) and a plasma temperature gradient producing a near-blackbody spectrum.

When the observed opacity is interpreted in terms of transport theory in SCPs, an estimate of the charge density can be obtained. A key condition for opacity is that the photon mean free path is smaller than the radiating body, written as $\kappa R > 1$, where R is the plasma thickness and κ is the absorption coefficient of light. For dense plasma, the dominant form of absorption is the process of free-free inverse bremsstrahlung where an electron absorbs light during a “collision” with an ion [14]. The collisionality in SCP is greatly affected by collective screening effects. In the presence of an oscillating electromagnetic field of frequency ω , the collisionality is characterized by the unitless parameter $\omega\tau_\omega$, where τ_ω is the collision time of an electron with an ion. For an SCP in the multi-ionization regime [7]

$$\omega\tau_\omega = \left[\frac{2}{\sqrt{6\pi}} \gamma^{1/2} \Gamma^{1/2} \Gamma_\omega \ln \left(\frac{0.7}{\sqrt{3}} \Gamma_\omega^{-3/2} + 1 \right) \right]^{-1}, \quad (2)$$

where γ is a unitless parameter representing the plasma frequency, Γ is the plasma coupling parameter, and Γ_ω is the plasma coupling parameter in the presence of an electromagnetic field. These quantities are given by

$$\gamma = \left(\frac{\omega_p}{\omega} \right)^2 = \frac{4\pi n_0 \bar{Z} e^2}{m_e \omega^2}, \quad \Gamma = \left(\frac{\bar{Z} e^2}{k_B T} \right) \left(\frac{4\pi n_0}{3} \right)^{1/3},$$

$$\Gamma_\omega = \Gamma \left[\frac{k_B T}{\hbar \omega} \left(1 - \exp \left(-\frac{\hbar \omega}{k_B T} \right) \right) \right],$$

where $\bar{Z} = n_e/n_0$ is the effective ionization level, $n_0(n_e)$ is the nuclei(electron) density, and m_e is the electron mass. For $\bar{Z} < 1$, $\Gamma = (e^2/k_B T)(4\pi \bar{Z} n_0/3)^{1/3}$. The Coulomb logarithm in Eq. (2) represents screening effects and was

found using a molecular dynamics simulation [15] and later supported in a laser-SL coupling experiment [7]. In the plasma regime where $\gamma \ll 1 \ll \omega\tau_\omega$, the absorption coefficient reduces to $\kappa = (\omega/c)(\gamma/\omega\tau_\omega)$. For 5 bar xenon breakdown at $t = 5$ ns, $T = 12350$ K, $n_0 = 1.25 \times 10^{20} \text{ cm}^{-3}$, $R = 50 \text{ }\mu\text{m}$ [Fig. 1(b)], and selecting a spectral region relatively void of strong line emission (400 nm), an electron density of $n_e > 4.0 \times 10^{20} \text{ cm}^{-3}$ is needed to satisfy the observed opacity ($\kappa R \approx \pi$). This electron density requires over 3 levels of ionization and results in an SCP with $\Gamma > 3.5$. The initial attainment of such high levels of ionization is well known [16,17]. We find that this level persists for an extended time and is a property of the equation of state of SCP.

The temporal evolution of the opaque spectrum yields the temperature as a function of time when $\epsilon \approx 1$ (Fig. 4). This behavior can be connected to the transport in SCP, in particular, the electron-ion collision time

$$\tau_{e-i} = \lim_{\hbar\omega \rightarrow 0} \tau_\omega = \left[\frac{2}{\sqrt{6\pi}} \omega_p \Gamma^{3/2} \ln \left(\frac{0.7}{\sqrt{3}} \Gamma^{-3/2} + 1 \right) \right]^{-1}. \quad (3)$$

This is the time scale for electron-ion energy transfer and follows from Eq. (2) in the limit of no electric field. We argue that τ_{e-i} accounts for the initial exponential drop in temperature soon after the laser-gas interaction. The intense laser pulse forms a plasma in the pressurized gas via the process of multiphoton ionization [18]. Recombination rapidly brings the electron density and light emission into LTE at the measured spectral temperature while leaving the ions cold. Because of their large mass, the ions take a longer time to heat up via collisions with the energetic electrons in a time scale $\tau_{th} \approx (M/m_e)\tau_{e-i}$, where M is the ion mass [14]. As the ions heat up, the electron temperature drops exponentially (Fig. 4). Opacity as deduced from the blackbody spectrum only yields a lower bound on the plasma density. However, this bound becomes the actual electron density for plasmas transitioning from opaque to transparent spectrum. This is the point at which ϵ first drops below 1. This also corresponds to the end of the exponential temperature decay at $t \approx 5/1/0.1$ ns for 5/25/74 bar Xe/Ar/He breakdown [Figs. 4(a), 4(b), 4(c)]. Using $T = 12350/14550/12550$ K, $R = 50/37/25 \text{ }\mu\text{m}$, $n_e = 4.0/6.3/7.0 \times 10^{20} \text{ cm}^{-3}$ (required for opacity at 400 nm), and Eq. (3) the calculated thermalization time is 1170/305/28 ps. For the range of Γ given above, Eq. (3) can be approximated as $\omega_p \tau_{e-i} \approx 5.37$ matching [15]. Therefore, the theory of τ_{th} in this regime is approximately temperature-independent and can be reasonably approximated using plasma values at the end of the exponential decay. This allows us to extrapolate the exponential behavior to the initial temperature decay and obtain the best fit values of 1470/380/63 ps. Comparison of all gases results in a τ_{th} that is roughly linear to the ion

mass. Normalizing to argon, the ratio of atomic masses is 3.3:1:0.10 (Xe:Ar:He). Similarly, the ratio of the measured decay time divided by τ_{e-i} is 3.3:1:0.13, which is consistent with the screened theory of collisions in SCP as applied via Eq. (3) [15]. Had we used the collision time appropriate to dilute plasma theory we would have found $\tau_{th} = 160/71/5.2$ ps.

Although rapid ionization from high-intensity laser pulses has been achieved in a variety of systems [10,19–21], we further observe that high ionization is maintained for a surprisingly long period of time. Is the persistent electron density due to local electronic thermodynamic equilibrium or far off-equilibrium behavior due to a long recombination time? In other words, is the plasma in ionization equilibrium at each time step in Fig. 4? To address this question, we consider the three-body recombination time scale τ_{rec} from plasma theory (photorecombination plays a minor role [14]) which occurs from the capture of an electron by an ion in the presence of an additional electron, given by

$$\tau_{rec} = (\bar{v}_e \pi^2 r_0^5 \bar{Z}^4 n_0^2)^{-1}, \quad (4)$$

where $\bar{v}_e = \sqrt{8k_B T/m_e \pi}$ is the mean thermal electron speed and $r_0 = 2e^2/3k_B T$ is the impact parameter for recombination in a Coulomb collision. Equation (4) and the plasma properties for xenon at $t = 5$ ns results in an impossibly fast recombination time of 0.15 fs. This is a result of dilute plasma theory applied to the dense plasma which we study. In formulating Eq. (4), screening processes are not accounted for and will result in an overestimation of the probability of finding a second electron in the vicinity of the electron-ion collision. To this end, we account for screening by replacing r_0 with the screened impact parameter ρ given by $\sigma = \pi \rho^2 = (\bar{Z} n_0 \bar{v}_e \tau_{e-i})^{-1}$. The result of this substitution is that every electron-ion collision can result in a recapturing of the electron, and, therefore, $\tau_{rec} \approx \tau_{e-i}$. This time scale is still much faster than any experimental time scale and is necessarily smaller than τ_{th} . We conclude the ionization is in a state of LTE with the electron temperature and light emission.

Ionization for an electron plasma in LTE is governed by Saha's equation given as

$$\frac{x_{m+1} x_e}{x_m} = \frac{2}{n_0} \frac{u_{m+1}}{u_m} \left(\frac{m_e k_B T}{2\pi \hbar^2} \right)^{3/2} \exp \left(-\frac{\chi_m}{k_B T} \right), \quad (5)$$

where $x_m(x_e)$, u_m , and χ_m is the ion(electron) concentration, electronic partition function, and ionization potential for the m th ion, respectively [14,22]. Although the electrons and ions are at different temperatures for $t < \tau_{th}$, Eq. (5) still applies by using the electron temperature [23]. For 5 bar xenon at $t \approx 5$ ns, the charge density is $> 4 \times 10^{20} \text{ cm}^{-3}$ while the temperature is only ~ 12000 K. According to Saha's equation, the degree of ionization

for the first ionization level ($m = 0$ and $\chi_1 = 12.1$ eV) should be less than 3%. Yet the opacity suggested by our data requires over 3 levels of ionization. Therefore, the collective processes at work in SCP must reduce the overall ionization potential by an amount comparable to χ_3 . In particular, the lowering of χ_m through Debye screening results in a change of the average ionization potential by [14,22]

$$\bar{\Delta}\chi = 2(\bar{Z} + 1)e^3 \sqrt{\frac{\pi\bar{Z}(\bar{Z} + 1)n_0}{k_B T}}. \quad (6)$$

Using the measured plasma properties of xenon breakdown ($\bar{Z} = 3.2$), the ionization potential is dramatically reduced by $\bar{\Delta}\chi = 32$ eV. This value of potential reduction, albeit remarkably high, is consistent with the observed level of ionization as it lies between $\chi_3 = 31.1$ and $\chi_4 = 41.0$ eV.

Application of calibrated streaked spectroscopy to femtosecond laser breakdown in high-pressure gases reveals both transport and thermodynamic properties of strongly coupled plasmas. We observe micron-scale blackbody spectra that persist long after the exciting laser has been turned off. Spectral analysis indicates the presence of a plasma with a higher ionization when compared to Saha's equation. We conclude a strongly coupled LTE plasma is formed in an unexpected region of parameter space (defined by atomic density and temperature). The time scale for thermal relaxation depends strongly on density effects and its measurement discriminates between various theories, selecting in favor of [15]. Future work will study the dwell time and expansion of the strongly coupled plasma. These systems may possibly reach regions of parameter space occupied by matter obeying quantum statistics. The discovery of an opaque microplasma as a thermodynamic state suggests electric discharges in pressurized gases as a new route toward optical switches.

We gratefully acknowledge support from DARPA MTO for research on microplasmas. We thank Brian Naranjo, Keith Weninger, Carlos Camara, Gary Williams, and John Koulakis for valuable discussions.

*bataller@physics.ucla.edu

- [1] K. S. Suslick and D. J. Flannigan, *Annu. Rev. Phys. Chem.* **59**, 659 (2008).
- [2] B. Kappus, S. Khalid, A. Chakravarty, and S. Putterman, *Phys. Rev. Lett.* **106**, 234302 (2011).
- [3] B. Kappus, S. Khalid, and S. Putterman, *Phys. Rev. E* **83**, 056304 (2011).
- [4] K. S. Suslick, N. C. Eddingsaas, D. J. Flannigan, S. D. Hopkins, and H. Xu, *Ultrason. Sonochem.* **18**, 842 (2011).
- [5] S. Khalid, B. Kappus, K. Weninger, and S. Putterman, *Phys. Rev. Lett.* **108**, 104302 (2012).
- [6] B. Kappus, A. Bataller, and S. J. Putterman, *Phys. Rev. Lett.* **111**, 234301 (2013).
- [7] A. Bataller, B. Kappus, C. Camara, and S. Putterman, *Phys. Rev. Lett.* **113**, 024301 (2014).
- [8] D. J. Flannigan and K. S. Suslick, *Nat. Phys.* **6**, 598 (2010).
- [9] S. Hopkins, S. Putterman, B. Kappus, K. Suslick, and C. Camara, *Phys. Rev. Lett.* **95**, 254301 (2005).
- [10] S. V. Garnov, V. V. Bukin, A. A. Malyutin, V. V. Strelkov, P. R. Bolton, H. Daido, and S. V. Bulanov, *AIP Conf. Proc.* **1153**, 37 (2009).
- [11] O. Baghdassarian, B. Tabbert, and G. A. Williams, *Phys. Rev. E* **75**, 066305 (2007).
- [12] M. Skowronek, J. Rous, A. Goldstein, and F. Cabannes, *Phys. Fluids* **13**, 378 (1970).
- [13] Y. Vitel and M. Skowronek, *J. Phys. B* **20**, 6477 (1987).
- [14] Y. P. Zel'dovich and Ya. B. Raizer, *Physics of Shock Waves and High-Temperature Hydrodynamic Phenomena* (Dover, New York, 1966), ISBN 0-486-42002-7.
- [15] G. Dimonte and J. Daligault, *Phys. Rev. Lett.* **101**, 135001 (2008).
- [16] W. M. Wood, C. W. Siders, and M. C. Downer, *Phys. Rev. Lett.* **67**, 3523 (1991).
- [17] B. M. Penetrante, J. N. Bardsley, W. M. Wood, C. W. Siders, and M. C. Downer, *J. Opt. Soc. Am. B* **9**, 2032 (1992).
- [18] J. Noack and A. Vogel, *IEEE J. Quantum Electron.* **35**, 1156 (1999).
- [19] N. Bloembergen, *IEEE J. Quantum Electron.* **10**, 375 (1974).
- [20] T. Ditmire, J. W. G. Tisch, E. Springate, M. B. Mason, N. Hay, R. A. Smith, J. Marangos, and M. H. R. Hutchinson, *Nature (London)* **386**, 54 (1997).
- [21] F. Quéré, S. Guizard, and P. Martin, *Europhys. Lett.* **56**, 138 (2001).
- [22] H. R. Griem, *Phys. Rev.* **128**, 997 (1962).
- [23] X. Chen and P. Han, *J. Phys. D* **32**, 1711 (1999).

Nanosecond high-power dense microplasma switch for visible light

A. Bataller,^{a)} J. Koulakis, S. Pree, and S. Putterman

Department of Physics and Astronomy, University of California Los Angeles, Los Angeles, California 90095, USA

(Received 28 July 2014; accepted 16 November 2014; published online 1 December 2014)

Spark discharges in high-pressure gas are known to emit a broadband spectrum during the first 10 s of nanoseconds. We present calibrated spectra of high-pressure discharges in xenon and show that the resulting plasma is optically thick. Laser transmission data show that such a body is opaque to visible light, as expected from Kirchoff's law of thermal radiation. Nanosecond framing images of the spark absorbing high-power laser light are presented. The sparks are ideal candidates for nanosecond, high-power laser switches. © 2014 AIP Publishing LLC.

[<http://dx.doi.org/10.1063/1.4902914>]

A Planck blackbody spectrum is emitted from a cavitating gas bubble as its implosion reaches a minimum radius. Blackbody radiation from cavitation can be observed in a wide-ranging parameter space that includes temperatures as low as ~ 1 eV and atomic densities as low as $\sim 10^{21} \text{ cm}^{-3}$.^{1–5} These parameters can also be achieved in a spark discharge in a high-pressure gas. Furthermore, sparks have an advantage over sonoluminescence in that sparks can be triggered on demand. As blackbodies are opaque, experiments on sonoluminescence suggest using sparks in high-pressure gases as an active optical limiter for high-power visible light. Our goal of achieving blackbody behavior in non-cavitating systems is supported by the observed blackbody response in laser breakdown of high-pressure gases.⁶ The opacity of high-pressure sparks at early times has been inferred from their broadband emission.⁷ Here, we demonstrate a calibrated Planck spectrum and measure transmission under the above conditions. The experimental conditions employed in this letter lead to a nanosecond microplasma switch that is capable of high-power handling. A potential application that utilizes this opaque switching behavior is the protection of sensitive imaging devices from high-power lasers.

The application of high-voltage (HV) between two gas-separated electrodes can generate plasma through dielectric breakdown. This rapid breakdown is known as spark discharge. Sparks can be developed in nanosecond timescales and heated to thousands of degrees through time-varying resistive heating.⁸ At these temperatures, gases become ionized and radiate light. This rapid increase of light emission is shown in Figs. 1(a) and 1(b) for sparks generated in high-pressure xenon gas. At high values of light emission, the plasma becomes more absorptive of the incoming light as plotted in Figs. 1(a) and 1(b). Figs. 1(c) and 1(d) show false color images (5 ns gate) of spark plasmas absorbing light from a 532 nm pulsed laser. For a system with temperature T , emission and absorption of light are related by Kirchoff's law

$$\frac{J_\nu}{A_\nu} = S_\nu = \frac{2\pi h \nu^3}{c^2} \frac{1}{e^{h\nu/kT} - 1}, \quad (1)$$

^{a)}Electronic address: bataller@physics.ucla.edu

where J_ν is the amount of radiation emitted per unit time per unit surface area, A_ν is the absorptivity, and S_ν is the radiant energy flux of a blackbody at frequency ν . This law states that the ratio of a body's emission to its absorption is equal to blackbody emission, which only depends on T and ν . The attainment of the blackbody limit ($A_\nu = 1$) is suggested by Fig. 1 not only because transmission drops to zero but also because the transmission remains zero while the light emission continues to increase. A similar response has also been observed for laser breakdown studies in atmospheric pressure gases.⁹ In general, plasma emission becomes more intense with increasing density. This trend is observed in Fig. 1 for 2 and 10 bar discharges. Similarly, the amount of transmitted laser energy decreases with increasing pressure. Eventually, a critical pressure is reached where the plasma becomes opaque⁷ and laser transmission falls to zero. For pressures ≥ 10 bar, laser pulses are completely blocked and absorption occurs only on the plasma's surface (Fig. 1(d)). From Eq. (1), the condition for opacity is given by $A_\nu = 1$ and therefore $J_\nu = S_\nu$. This states that an opaque body must emit blackbody radiation for a given frequency. The transmission curve for 10 bar discharges in Fig. 1(b) indicates complete absorption at 532 nm and must therefore radiate as a blackbody at 532 nm. To confirm this requirement, calibrated spectrum was measured as a function of time as shown in Fig. 2. For early moments, the discharge radiates a continuous broadband spectrum followed later in time by xenon line emission. Temporal line-outs from the spectral images are shown in Fig. 2(b). Indeed, this spectrum is well fit to blackbody emission (S_ν) during the same moments as complete laser absorption (Fig. 1(b)).

Spark discharges were generated using two tungsten needles (40 μm tip radius) centered in a stainless-steel pressure chamber (PC), as shown in Fig. 3(a). Optical access was granted with four UV fused-silica windows mounted on the PC. The distance between the electrode tips was 165 μm and adjusted using a custom high-pressure actuator. HV pulses were generated by an external circuit shown in Fig. 3(c). A variable-length fast pulser (Behlke FSWP71-02, 10 ns rise time) was charged with a +5 kV power supply through a 10 M Ω resistor. Upon triggering, +5 kV pulses were sent through a 1.36 m RG58C/U cable ending with a SHV

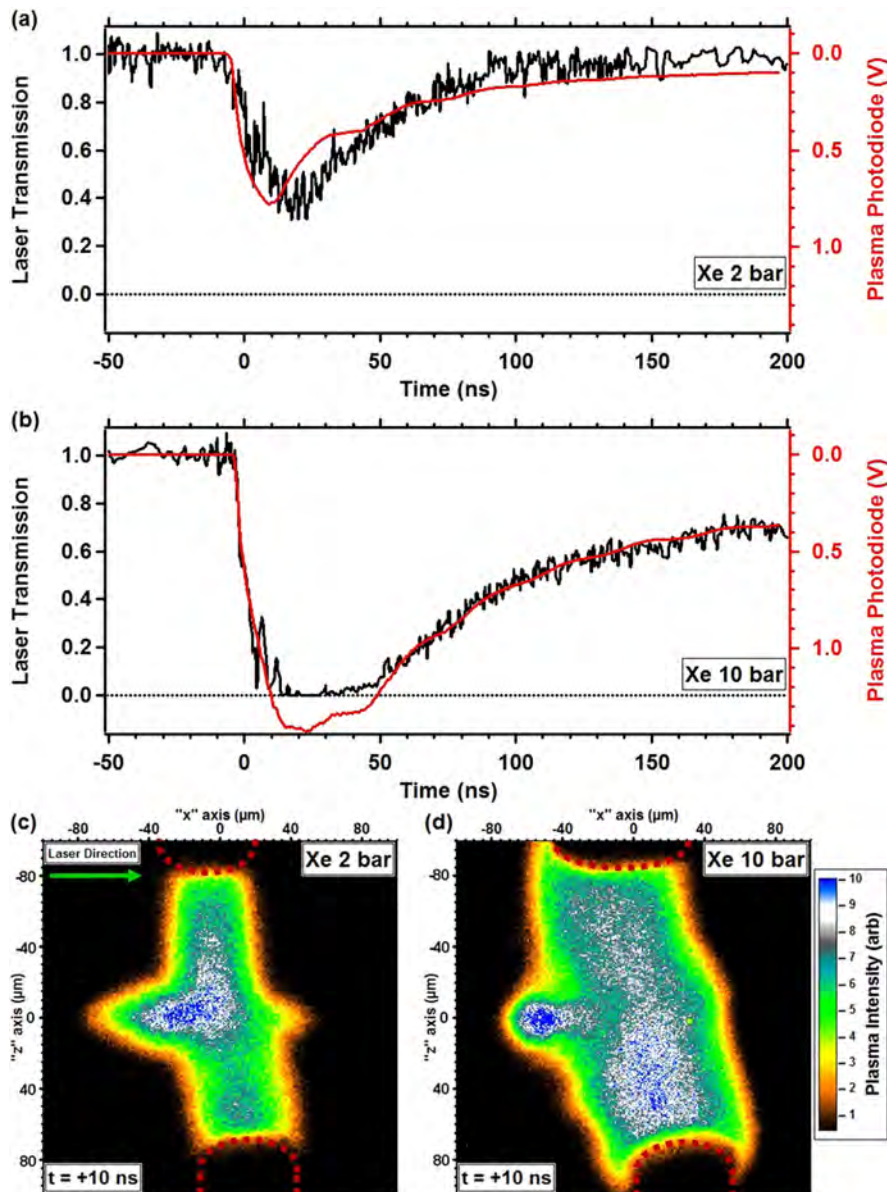


FIG. 1. Laser transmission and plasma emission of spark discharges formed in (a) 2 and (b) 10 bar xenon gas as a function of time. Laser transmission (black curve) was recorded for 532 nm laser pulses focused through the center of the spark plasma. Plasma emission (red curve) was recorded with a fast photodiode. False color images representing plasma light emission were taken with a framing camera during the moment of laser-plasma interaction for (c) 2 and (d) 10 bar discharges. Red dashed curves indicate the location of the HV electrodes. Laser pulses propagating from the left are absorbed by the spark volume and surface for 2 and 10 bar discharges, respectively. These transmission curves and images were obtained using laser intensities below the breakdown threshold.

connection. The HV electrode was connected to the external circuit through a SHV feed-through and the ground electrode was connected to the chamber body. The spark is achieved when the stray capacitance of the cable and electrodes charges to the breakdown threshold, as described in Ref. 10. Although pulse lengths were set to 1 μ s for the discharges presented in this letter, the plasma is opaque for only the first ~ 50 ns. This timescale is set by a combination of circuit properties and the expansion of the heated gas.^{11–13} Sparking was conducted at a rate of 5 Hz or slower to minimize any lingering effects of the previous shot. Due to the voltage being near the breakdown threshold, 10 bar discharges jittered in time by 100s of nanoseconds relative to the input trigger. To improve the temporal jitter, seed electrons were created through the photoelectric effect by projecting a UV light source (deuterium lamp) onto the electrodes.¹⁴

The plasma images in Fig. 1 were acquired using a framing camera (Specialised-Imaging, Custom SIMD-052) capable of capturing four 3 ns images in a 12 ns interval. Following Fig. 3(b), plasma emission was collected by a

Mitutoyo infinity-corrected microscope objective (MO) and imaged onto the framing camera with a tube lens (TL). The imaging system has a $10\times$ magnification and a $2.0\ \mu$ m spatial resolution. A filter stack (FS) was placed between the objective and tube lens. In FS3 were neutral density filters and a 532 nm notch filter (Stopline 532/1064 nm dual-notch) to protect the framing camera from incidental laser scattering and pass broadband plasma emission.

Laser transmission curves from Fig. 1 were measured by focusing laser pulses through the spark discharge. TEM00 pulses from a seeded YAG (Coherent Infinity) were focused into the PC (green arrows in Fig. 3(b)) with a 40 mm focal length objective (LO). The measured flashwidth, energy, beam waist, and peak focal intensity was 2.2 ± 0.15 ns, $8.0 \pm 0.9\ \mu$ J/pulse, $9.5 \pm 1.0\ \mu$ m, and $1.9 \pm 0.4 \times 10^{10}$ W/cm², respectively. After passing through the spark discharge at minimum focus, the laser is collected, filtered, and imaged onto a triggerable CCD camera (Mightex CCE-B013-U). In FS1 were neutral density filters and a 532 nm line filter to protect the camera from strong laser intensities and block

DISTRIBUTION A: Distribution approved for public release.

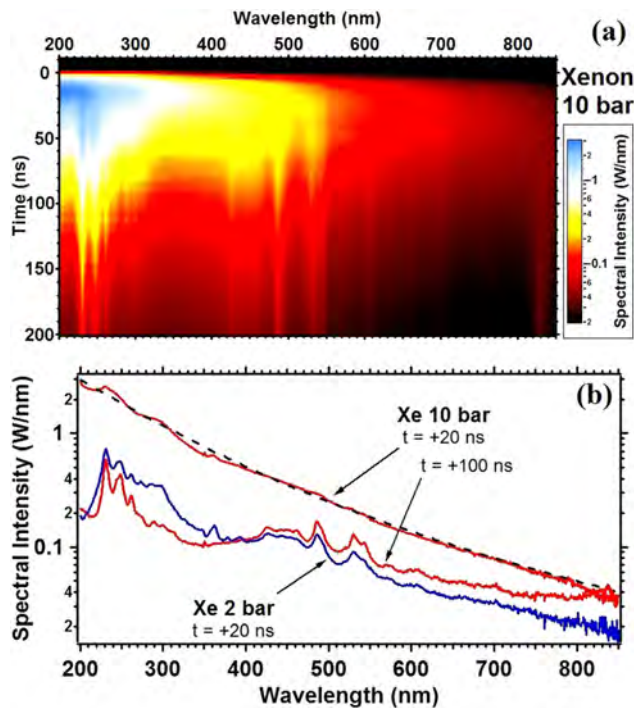


FIG. 2. Calibrated spectrum for 10 bar xenon discharges. (a) Temporally resolved spectral image shows continuous broadband emission for early times. As the plasma expands, xenon line emission emerges from the continuum for later times. (b) Spectral line-outs reveal opaque behavior during the early moments of discharge and is well fit to blackbody emission (black dashed curve, $T = 24000$ K and $4.9 \times 10^4 \mu\text{m}^2$ blackbody emission area). Blackbody spectrum is observed concurrently with complete absorption from Fig. 1(b).

broadband plasma emission. Transmission is normalized using the integrated laser intensity on the CCD for pulses arriving before the spark discharge.

Due to the spark's temporal jitter, a signal representing plasma emission ("Plasma Photodiode" in Fig. 1) was needed to sort the CCD and framing camera images as a function of time. As shown in Fig. 3(b), a 50:50 broadband beamsplitter sends a portion of the plasma emission to a fast photodiode (1 ns rise time). The broadband light sent to the photodiode was filtered by FS2 (532 nm notch) and demagnified $0.6\times$ by a 25 mm focal length singlet lens (SL). Timing signals from the plasma photodiode and cameras were recorded on an oscilloscope for every laser pulse. A timestamp was assigned for each event based on the time difference between the plasma photodiode and the camera signals. Timing to each instrument was controlled through a delay generator (SRS DG645).

Temporally resolved spectrum was acquired using a calibrated fiber-coupled spectrometer (Acton SpectraPro 300i) and gated to 10 ns exposures with an ICCD (Princeton Instruments PI-MAX). Once more, a timestamp from the plasma photodiode is recorded for every discharge. In this way, spectra are sorted in time and averaged (2 ns time-bins) to make the spectral image in Fig. 2(a). Because the spectrum is calibrated in intensity, the fit in Fig. 2(b) provides both a blackbody temperature (24 000 K) and area of emission ($4.9 \times 10^4 \mu\text{m}^2$), with a fitting error of $\sim 20\%$. This is in rough agreement with the plasma's luminous area ($2\pi R h = 2\pi \times 40 \mu\text{m} \times 165 \mu\text{m} = 4.1 \times 10^4 \mu\text{m}^2$) taken from

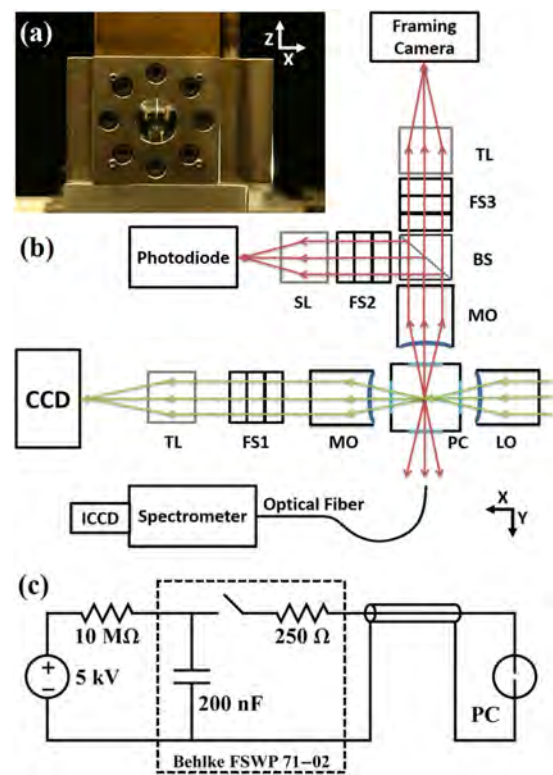


FIG. 3. Experimental setup: (a) Photograph of pressure chamber with tungsten needle electrodes. (b) Optical block diagram for measuring laser transmission and plasma emission, and for fast spark imaging (framing). Included are laser (green arrows) and plasma emission (red arrows) ray traces. A portion of the plasma emission is collected by an optical fiber and directed to a gated spectrometer. The x, y, and z axes are defined by the arrows in (a) and (b), the origin of which is taken to be the plasma center. (c) High-voltage circuit diagram.

the framing camera images. For times ≥ 50 ns, xenon lines emerge from the continuum and increase in strength. The appearance of these lines indicates a transparent plasma and is consistent with the absorption measurement in Fig. 1(b). This increase in line emission is due primarily to the plasma's hydrodynamic expansion into the surrounding gas, resulting in a lowered atomic density. For comparison, spectrum at 2 bar xenon discharge is provided in Fig. 2(b) and shows reasonable agreement.

Normalized transmission curves were constructed for peak laser intensities spanning 6 orders of magnitude (1.9×10^7 – 10^{13} W/cm², Ref. 15). These curves were independent of laser intensity until the laser breakdown threshold was reached, indicating that the loss of laser light is due to linear absorption by the spark plasma. The laser breakdown threshold was measured at $7.7 \pm 1.5 \times 10^{11}$ W/cm² and $1.9 \pm 0.4 \times 10^{11}$ W/cm² for 2 and 10 bar, respectively (consistent with Ref. 16). Beyond the laser breakdown threshold, the transmission curves deviated toward lower transmission due to energy loss from laser breakdown.¹⁷ This trend suggests that there is no limit to the plasma's power handling capability and can be utilized at very high laser intensities. To demonstrate this capability, Fig. 4 shows framing images of 10 bar spark-laser interactions for a laser intensity ten times larger than laser breakdown (1.9×10^{12} W/cm²). Each image was exposed for 5 ns with 0 ns interframe time. In Fig. 4(a),

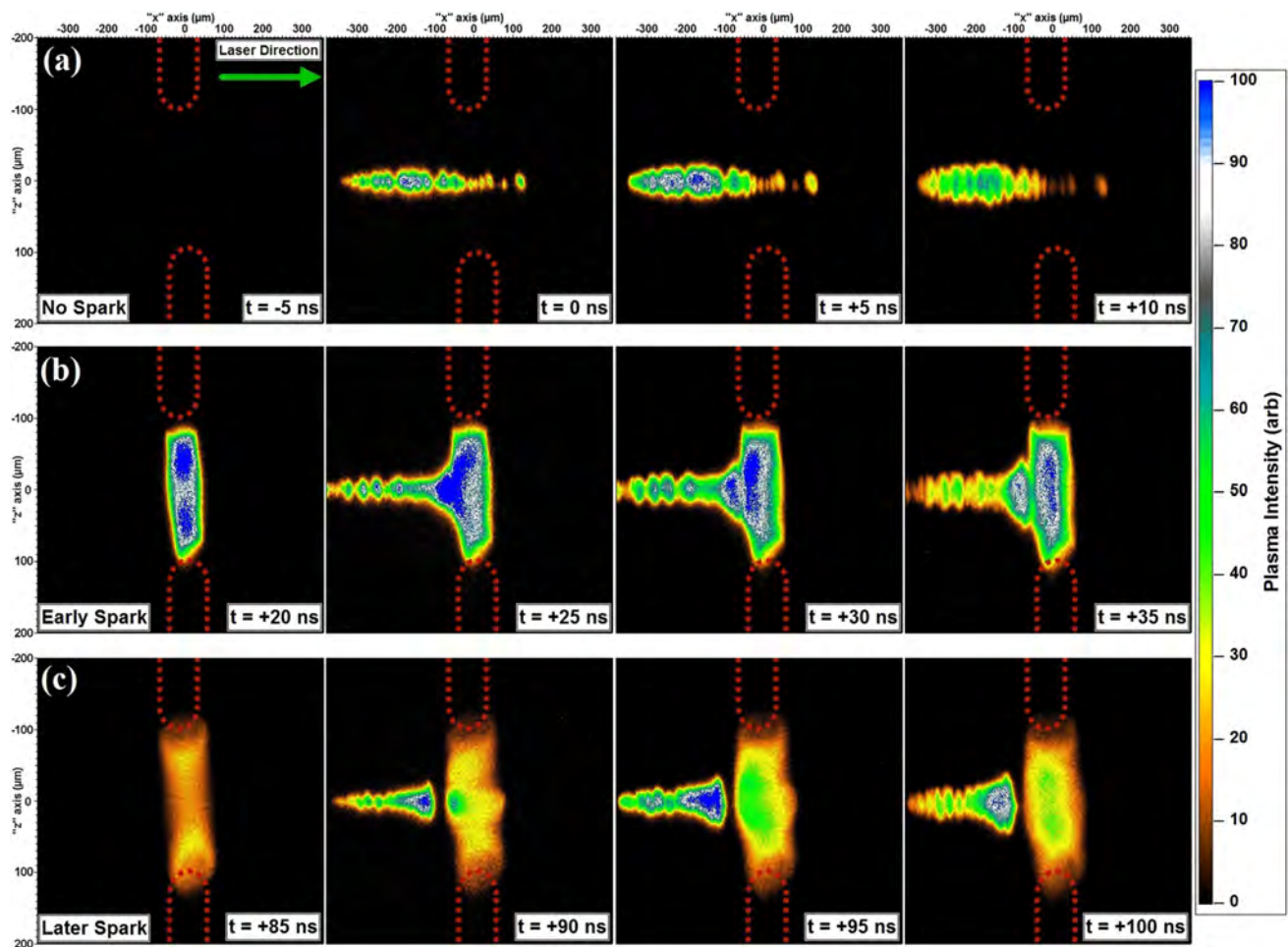


FIG. 4. 5 ns framing images (false color) of three individual events: (a) Laser breakdown without a spark and (b) laser absorption at +25 ns and (c) +90 ns after spark discharge initiation in 10 bar xenon gas. The timestamps given in (b) and (c) indicate the moment the image was taken relative to the spark discharge. For the case of (a) no spark, the image was taken relative to the arrival of the laser pulse. In all cases, the laser intensity ($1.9 \times 10^{12} \text{ W/cm}^2$) was set above the breakdown threshold and centered between the electrode gap. Laser arrival occurred during the second frame of each row and resulted in a laser-plasma interaction. Red dashed curves indicate the location of the HV electrodes. A dark region exists between the laser breakdown and spark plasma for $t \geq 50 \text{ ns}$ and grows larger with later laser pulses. Shadowgraph measurements have shown this effect is due to laser breakdown induced by a shock front generated by the spark discharge. (Multimedia view) [URL: <http://dx.doi.org/10.1063/1.4902914.1>][URL: <http://dx.doi.org/10.1063/1.4902914.2>][URL: <http://dx.doi.org/10.1063/1.4902914.3>]

the incident laser pulse (from left to right) is focused between the tungsten electrodes with the spark switched off (no HV). In this configuration, laser breakdown is formed both before and after the electrodes, and $\sim 25\%$ of the laser energy is transmitted to the CCD camera. With the spark activated, the laser pulse is focused onto the plasma column and is completely absorbed (Fig. 4(b)). Once more, no laser energy passes through to the CCD camera for early times (~ 0 – 50 ns after spark initiation). Laser energy is absorbed only on the surface of the spark plasma, which further indicates an opaque body. The laser energy deposited to the spark plasma is so large that a luminous wave propagates within the plasma (from left to right in Fig. 4(b)). Conversely, laser energy is deposited to the plasma volume at later times as shown in Fig. 4(c). Here too a luminous wave propagates within the plasma (from middle to top/bottom in Fig. 4(c)). This observation is consistent with both the measured spectrum and absorptivity, as a volume emitter is also a volume absorber.

The nanosecond optical switch device presented in this letter was motivated by the observation of a dense plasma

inside a sonoluminescing bubble. The dense microplasma exists at an unexpectedly low temperature and has its origin in collective processes in a strongly coupled plasma.⁶ We have generated an opaque plasma using spark discharges in high-pressure xenon. As an active optical limiter, this plasma has seemingly limitless power handling, as laser energy is converted into higher temperature and more plasma. In other words, the switch reported in this letter cannot be damaged because it is already broken. This optical switch can now be optimized in parameter space for faster discharge speeds, lower energy consumption, and longer periods of opacity. In addition to device applications, the system discussed in this letter could lead to new probes of strongly coupled plasmas. By varying the density and other parameters typically inaccessible to sonoluminescence, new equations of state can be discovered for this exotic state of matter.

We gratefully acknowledge support from the Air Force Office of Scientific Research and DARPA MTO for

DISTRIBUTION A: Distribution approved for public release.

research on micro-plasmas. We thank Adam Collins, Brian Kappus, Brian Naranjo, and Guillaume Plateau for valuable discussions.

¹D. J. Flannigan and K. S. Suslick, *Nat. Phys.* **6**, 598 (2010).

²B. Kappus, S. Khalid, A. Chakravarty, and S. Putterman, *Phys. Rev. Lett.* **106**, 234302 (2011).

³S. Khalid, B. Kappus, K. Weninger, and S. Putterman, *Phys. Rev. Lett.* **108**, 104302 (2012).

⁴B. Kappus, A. Bataller, and S. Putterman, *Phys. Rev. Lett.* **111**, 234301 (2013).

⁵A. Bataller, B. Kappus, C. Camara, and S. Putterman, *Phys. Rev. Lett.* **113**, 024301 (2014).

⁶A. Bataller, G. R. Plateau, B. Kappus, and S. Putterman, *Phys. Rev. Lett.* **113**, 075001 (2014).

⁷L. Michel and H. Fischer, *Appl. Opt.* **11**, 899 (1972).

⁸H. Fischer, *J. Opt. Soc. Am.* **51**, 543 (1961).

⁹V. Hohreiter, J. Carranza, and D. Hahn, *Spectrochim. Acta B* **59**, 327 (2004).

¹⁰T. Iwata, T. Tanaka, T. Komatsu, and T. Araki, *Rev. Sci. Instrum.* **71**, 4045 (2000).

¹¹H. Fischer, *J. Opt. Soc. Am.* **47**, 981 (1957).

¹²H. Fischer and C. C. Gallagher, *Appl. Opt.* **4**, 1151 (1965).

¹³J. B. Higham and J. M. Meek, *Proc. Phys. Soc., Sect. B* **63**, 649 (1950).

¹⁴T. Komatsu, T. Iwata, and T. Araki, *Rev. Sci. Instrum.* **71**, 1621 (2000).

¹⁵See supplementary material at <http://dx.doi.org/10.1063/1.4902914> for all 10 bar Xe transmission curves.

¹⁶D. I. Rosen and G. Weyl, *J. Phys. D: Appl. Phys.* **20**, 1264 (1987).

¹⁷C. V. Bindhu, S. S. Harilal, M. S. Tillack, F. Najmabadi, and A. C. Gaeris, *J. Appl. Phys.* **94**, 7402 (2003).

Observation of Shell Structure, Electronic Screening, and Energetic Limiting in Sparks

A. Bataller,¹ S. Putterman,¹ S. Pree,¹ and J. Koulakis¹

¹*Department of Physics and Astronomy, University of California,
Los Angeles, Los Angeles, California 90095, USA**

We study the formation of micron-sized spark discharges in high-pressure xenon on the nanosecond timescale. The spark's energy per length is measured through the expansion dynamics of the generated shockwave, and is observed to scale linearly with the spark radius. At the same time, the surface temperature of the spark channel remains constant. Together, these observations allow us to conclude that the spark channel, which is $15 - 40 \mu\text{m}$ in overall radius, is actually an energetically hollow shell about $10 \mu\text{m}$ thick. Further, the energy per nucleus in the shell is about 15 eV , independent of size and density. To reconcile these findings with the opacity to visible light, we appeal to collective screening processes that dramatically lower the effective ionization potential, allowing a much higher electron density than is expected. Thus nanosecond measurements of sparks provide access to the thermodynamics and kinetics of strongly correlated plasmas.

PACS numbers:

Examples of systems that become dense plasmas when driven off-equilibrium are high-voltage electrical breakdown (spark discharges [1]), ultra-fast laser breakdown [2], adiabatic heating of gases in shock fronts [3, 4], and bubble implosions (sonoluminescence [5]). As these systems are driven harder, their brightness is observed to saturate. This luminosity saturation, first recognized by Glaser [6, 7], exists over a wide range of parameter space. Although this phenomenon has been known for over 60 years, its explanation is still in contention [8, 9]. Attempts to find the thermodynamic and kinetic origins of this effect are shrouded by the simultaneous onset of opacity at unexpectedly low temperatures and energy inputs. We use the acoustic and hydrodynamic response of the dense plasma expansion to peek inside of dense xenon sparks which are formed in a nanosecond - fast compared to hydrodynamic timescales. We find that the spark current flows in a shell structure where the energy per atom is a constant, independent of both the absorbed energy (or spark diameter) and the initial density. Furthermore, the surface temperature remains constant for 25 ns , a period much longer than the energy input time. Opacity is established in under 1 ns , and this property of the plasma is due to processes that strongly reduce the ionization potential. Dense plasmas in the parameter space described here are useful as ultra-violet sources, rapid optical switches with broadband functionality extending to the ultra-violet, and precision discharge machining tools.

Luminosity saturates at a brightness corresponding to blackbody emission at a gas-dependent temperature T_{sat} . The saturation occurs in both time and space as shown by the streak image in Fig. 1(a). The image was taken along a radial cross-section (streak slit indicated in Fig. 2(a)) for a spark discharge in 42 bar xenon. In Fig. 1(c), a temporal lineout centered on the spark channel shows that the gas breakdown process forms in $< 1 \text{ ns}$ with a rapidly rising intensity indicated at $t = 0 \text{ ns}$. The luminosity saturates at $5 \pm 0.5 \mu\text{W}/\text{nm} \mu\text{m}^2$ within the first nanosecond and continues for $20 - 25 \text{ ns}$. During this time, the luminous profile (Fig. 1(d)) is well fit to a flattop function (super-Gaussian), indicating saturation in space as well.

Hydrodynamic analysis of Fig. 1 is the basis for insights regarding the interior of the blackbody emitter. This image was taken with a Hamamatsu streak camera aligned to a $10\times$ long-range Mitutoyo microscope objective as shown in Fig. 2(b). A 550 nm bandpass filter (10 nm bandwidth) was placed between the objective and streak camera, whose spectral intensity was cross-calibrated with the fiber spectrometer system (Fig. 2(b)). Details of the pressure chamber and electrical circuit used to generate the discharges can be found elsewhere [10]. Briefly, spark discharges were generated in a stainless-steel pressure chamber between $80 \mu\text{m}$ diameter tungsten needles that were dulled through a series of spark discharges. A 50Ω coaxial cable attached to the electrodes through a feedthrough in the chamber walls was charged to 5 kV through a 250Ω isolation resistor. In contrast to [10] where a fast-rise-time switch was used to charge the cable to a voltage surpassing the breakdown threshold, here the gap length is increased so that the potential stays below threshold. The breakdown is then initiated with a weak ($< \mu\text{J}$) femtosecond laser pulse focused between the electrodes. This represents a significant advancement in spark triggering that lowers timing jitter by over an order of magnitude and makes possible ultra-fast measurements on the micron scale.

Importantly, the luminosity-saturated sparks we present are in a different regime than those considered by others [6, 7], and particularly Yusupaliev, whose brightness-saturation theory [11] assumes that power continues to drive the system well after the hydrodynamic shockwave has been formed. In contrast, we consider sparks whose energy source

*Electronic address: awbatall@ncsu.edu

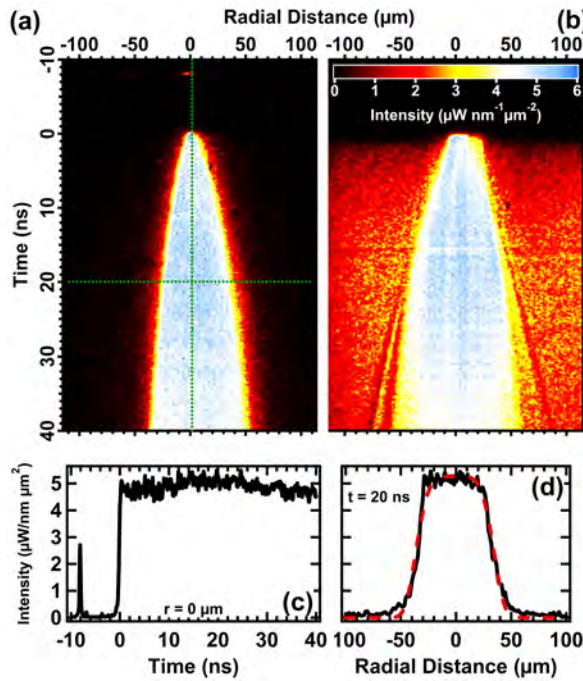


Figure 1: Time-resolved radial cross-section of a spark discharge in 42 bar (a) and 10 bar (b) Xe. In (b), a backlight renders the emitted shockwave visible. Temporal (c) and radial (d) line-outs, whose position is indicated by the green dotted lines in (a), reveal brightness saturation occurring both in time and space. A weak femtosecond laser pulse initiates the discharge, indicated by emission at -10 ns in (a) and (c). Red-dashed curve in (d) is the best-fit super-Gaussian.

has been exhausted before hydrodynamic expansion even begins, and therefore the atomic density remains equal to the ambient. We achieved this regime by relying purely on the capacitive energy stored within our drive cable and the parasitics of the chamber, which discharge quickly. There remains an opportunity for a luminosity-saturation theory on such rapid timescales.

A key feature of the luminosity saturation regime is the blackbody nature of the plasma emission. The flattop radial profile observed in Fig. 1(d) is suggestive of this, as a blackbody is a Lambertian radiator. To confirm the presence of blackbody radiation and the gas-dependent T_{sat} , calibrated, time-resolved spectra were obtained for xenon spark discharges. Indeed, Fig. 3 shows spectrum taken at 3 ns matching a 29 000 K blackbody, in agreement with previous studies of xenon discharges [12, 13]. Along with increasing power input, T_{sat} can also be reached by increasing gas pressure as long as the power input is above a minimum value [14]. Fig. 3 demonstrates this trend as the spectral intensity reaches its limiting value between 10 and 20 bar. Spectrum was acquired with a fiber-coupled ICCD spectrometer (Princeton Instruments), where individual spark emission spectra were recorded in 1 ns exposures, averaged, and reconstructed as a function of discharge time. The spectra were then divided by their averaged plasma dimensions from corresponding streak images and electrode separation. The spectrometer system was calibrated to an uncertainty of 10% using deuterium and tungsten sources, limiting the blackbody fitting parameters to only temperature and allowing quantitative radiative analysis.

Fitting radial lineouts to a super-Gaussian function $I(x) = I_0 \exp(-2|(\frac{x-x_0}{\sigma})^n|)$ at each time point (red-dashed curve in Fig. 1(d)) provides the spark channel radius (half-width-at-half-max) over time (Fig. 4). The spark expansion dynamics can be categorized into four temporal phases referenced to the onset of light emission:

1. **Leader Phase ($t < 0$ ns)** - This is the earliest phase of the discharge where seed ions created from the weak femtosecond laser pulse (Figs. 1(a)&(c)) migrate and collide with the cathode. Secondary emission initiates a cascade, a plasma leader races across the electrode gap, and a luminous spark channel becomes visible [15].
2. **Ionization Wave Phase ($0 < t < 3$ ns)** - Once the spark leader has bridged the electrodes, the channel diameter grows rapidly as circuit energy pours into heating and creating a larger plasma. This phase is likely an ionization wave front, considering the fast expansion speed (>5 km/s) and the absence of a radiated shock front subsequent to its rapid deceleration around 3 ns. During this phase, the plasma reaches T_{sat} .

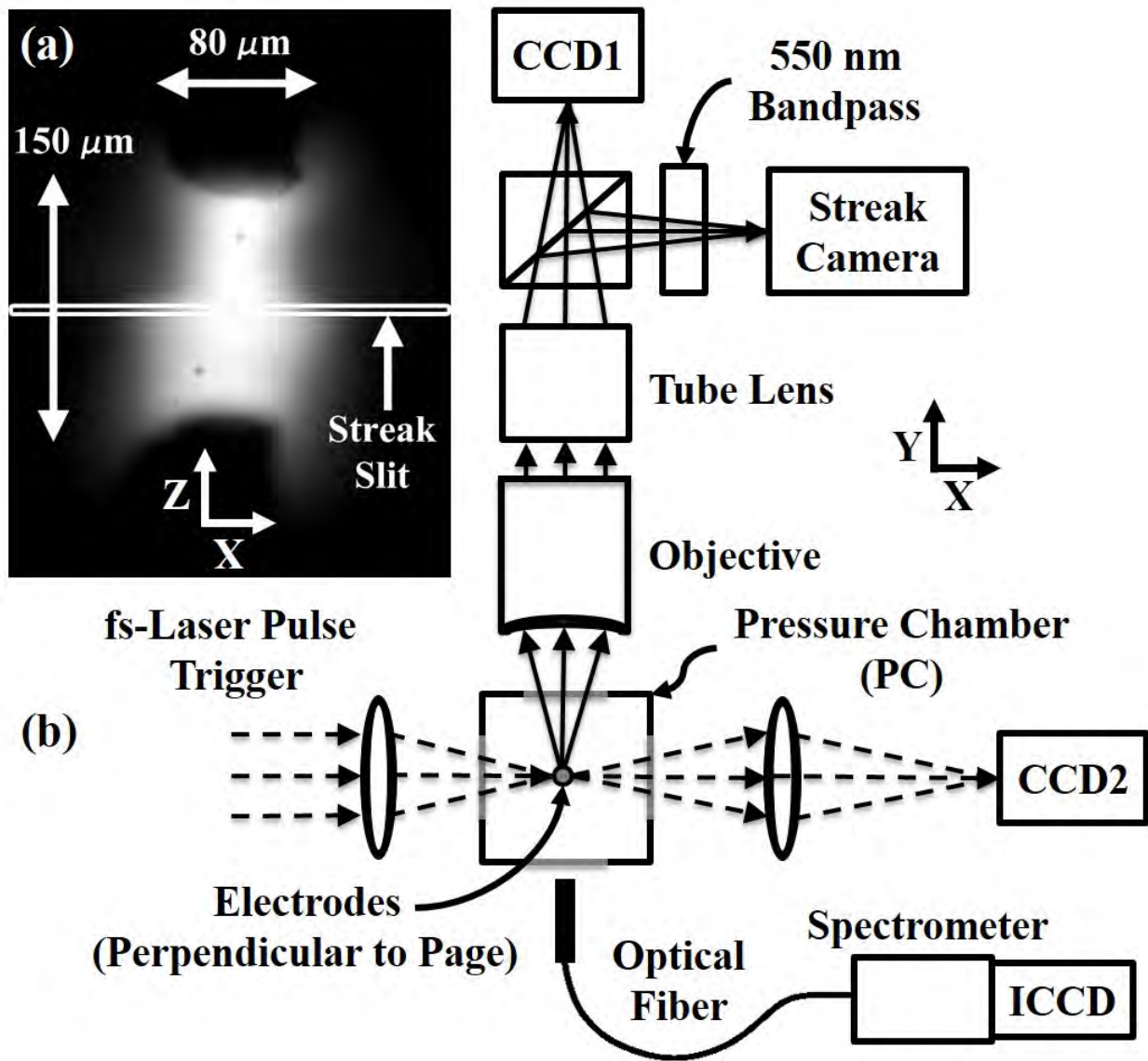


Figure 2: Block diagram (b) of the system used to study spark discharges in 10-42 bar Xe. (a) is a time-integrated photograph of a single spark event in 20 bar Xe as captured by CCD1. The pressure chamber contains two $80\ \mu\text{m}$ diameter tungsten needles (perpendicular to the plane of the block diagram and seen as silhouettes in (a)), held $170\ \mu\text{m}$ apart, that are charged to 5 kV with the circuit shown in (c). CCD1 and CCD2 are used for alignment and diagnostics. Sub-nanosecond dynamics are resolved by the streak camera (Fig.1), which images a narrow band across the spark width, indicated as “Streak Slit” in (a).

3. **Hydrodynamic Phase ($3 < t < 25\ \text{ns}$)** - Additional heating is limited by the small stray circuit capacitance and the sharply-dropping plasma resistance. Once power input has ended, the channel undergoes a hydrodynamic expansion near the speed of sound of a 29 000 K xenon plasma. This phase ends when the plasma size is so large that the initial energy input can no longer sustain the expansion, ending with a radiated shock wave (Fig. 1(b)).
4. **Cooling Phase ($t > 25\ \text{ns}$)** - Lasting 100s of nanoseconds, this phase represents the spark’s death as the plasma cools off from T_{sat} to room temperature. During this phase, the plasma becomes dilute and optically thin.

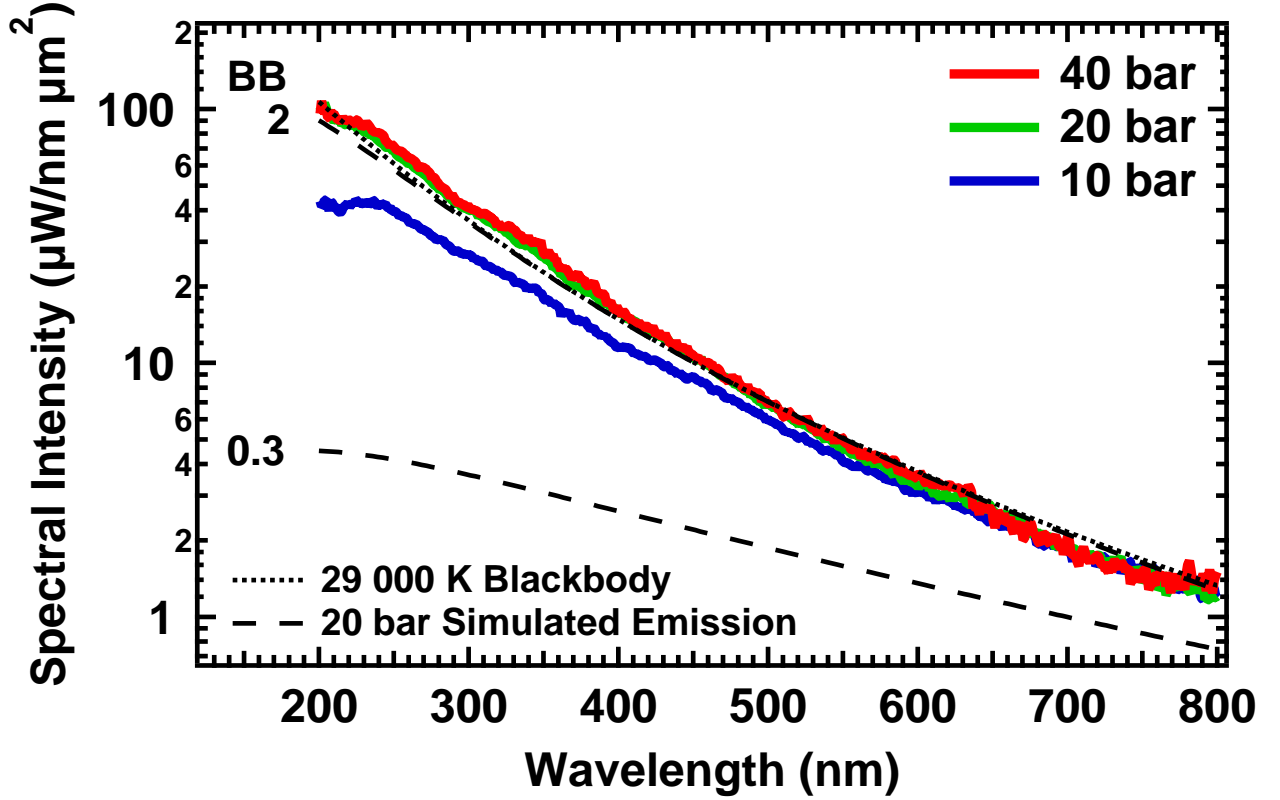


Figure 3: Absolute spectral intensity of Xe discharges at 3 ns for various static pressures. Spectral saturation throughout the measured spectrum occurs for pressures >10 bar and are well-fit to a 29 000 K blackbody spectrum (dotted). Simulated spectra (dashed) at 20 bar were calculated for various levels of ionization ($Z = 0.3$ and 2) using Eq. 7 at $T_{sat} = 29\,000$ K and $l = 40\,\mu\text{m}$.

We find the dynamics of the spark channel radius between 3 – 25 ns (Fig. 4) are well-described by the function,

$$R(t) = A \exp\left(-\frac{t}{\tau}\right) + \sqrt{Bt}. \quad (1)$$

The second term captures the asymptotic behavior of a cylindrical shock as expected from the Sedov-Taylor self-similar solution, which assumes the initial energy input is a delta-function in time and the shock radius is much larger than the initial radius. Because the channel resistance drops rapidly, the vast majority of the energy deposition occurs in the first nanosecond. The initially rapid expansion of the channel diameter slows dramatically when the power input becomes negligible, as seen between 2 – 4 ns in the velocity curves of Fig. 4. Further expansion is driven by hydrodynamics rather than ionization, and the velocity flattens out at around the speed of sound. Additional evidence that further energy input is negligible is provided by the observation that changing the charging cable length does not affect the channel dynamics. We empirically insert the exponential term to account for the shock acceleration, and fit the radius-time curves during the hydrodynamic phase (3 – 25 ns) to Eq. 1 to extract the best-fit parameters A , τ , and B . We have also observed the shock post-separation with the use of a backlight (Fig 1(b)), and find that it continues to follow the \sqrt{t} expansion until the radius becomes comparable to the electrode distance, after which the shock becomes spherical.

Unit analysis and self-similar theory gives the coefficient B as being proportional to the half power of the energy per length E/L , over the mass density $\rho = n_0 M_{Xe}$, with the proportionality constant being a function of the adiabatic

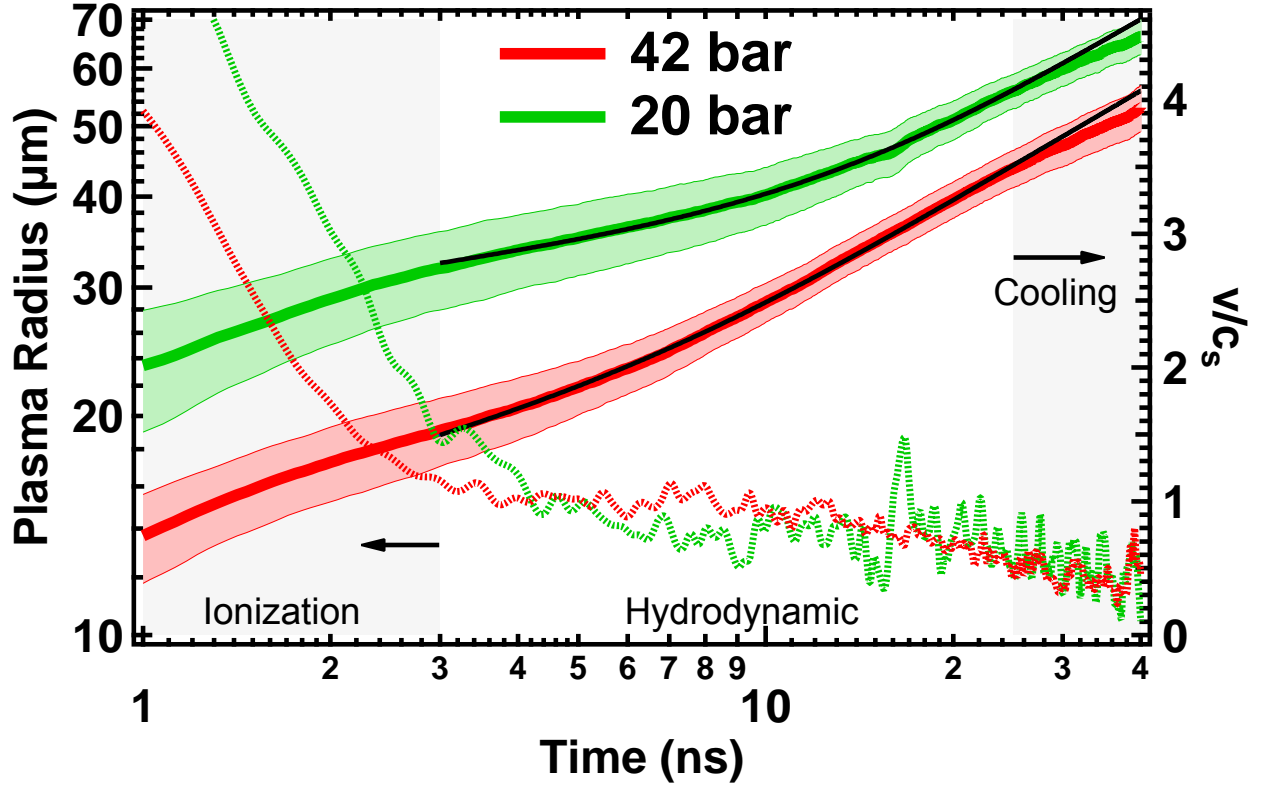


Figure 4: Plasma radius (solid) and velocity (dotted) as a function of time for 20 and 42 bar discharges. Discharge sizes varied from shot-to-shot within the range indicated by the shaded regions bounding the radius curves. The radial expansion is fit (black) to Eq. 1 between 3–25 ns. A shockwave is released from the plasma surface between 20–25 ns as indicated in the shaded region. The plasma velocity is shown normalized to the isothermal speed of sound of a 29 000 K gas ($c_s = \sqrt{kT_{sat}/M_{Xe}} = 1.36 \mu\text{m/ns}$).

index γ [16, 17],

$$B^2 = \left[\frac{4(\gamma-1)(\gamma+1)^2}{\pi(3\gamma-1)} \right] \frac{E}{L\rho} = f(\gamma) \frac{\pi R_0^2 \bar{\epsilon}}{M_{Xe}}, \quad (2)$$

$$\text{where } \bar{\epsilon} = \frac{2}{R_0^2} \int_0^{R_0} \epsilon(r) r dr, \quad (3)$$

is the spatial average of the energy per nucleus $\epsilon(r)$, over the initial radius R_0 , n_0 is the initial atomic density, and M_{Xe} is the atomic mass of xenon. R_0 is the radius of the spark channel after the majority of the energy has been deposited, i.e. after the ionization wave phase, but before the hydrodynamic expansion begins. This occurs at $t = 4$ (3) ns for 20 (42) bar, as that is when the velocity of the early, rapid expansion has dropped to approximately the speed of sound [30], and flattens off (Fig. 4). We use the shockwave asymptotic dynamics to back-out the energy absorbed by the spark, and then assign that energy to the number of particles in the initial channel volume. At 3 ns, the channel density is assumed uniform and equal to the ambient density, as sound in a 29 000 K ideal gas of particle mass M_{Xe} travels a distance small compared to the channel radius during that time.

Variations in R_0 occur naturally from shot-to-shot. Fig. 5(a) is a scatter plot of $B^2 M_{Xe} \propto E/Ln_0$ vs. R_0 for individual sparks in 20 and 42 bar xenon, all at 5 kV and 170 μm electrode distance. From this plot, we find that,

$$\frac{E}{Ln_0} \propto B^2 M_{Xe} = K(R_0 - R_{min}), \quad (4)$$

with $K = 870(830) \pm 25(30) \text{ eV } \mu\text{m}$ and $R_{min} = 10(9) \pm 1(1) \mu\text{m}$ for 20 (42) bar. Remarkably, $B^2 M_{Xe}$ is linear in R_0 and density-independent within experimental error. The spark brightness vs. initial radius shown in Fig. 5(b) emphasizes that the surface temperature, and by extension the energy/nucleus at the surface, is independent of the spark size in the brightness saturation regime.

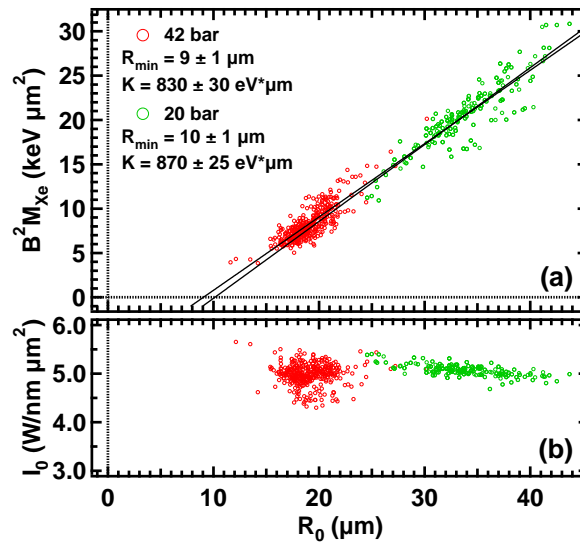


Figure 5: Scatter plots of (a) $B^2 M_{Xe}$ and (b) the brightness of the spark channel vs. the initial plasma radius for individual discharges at 20 and 40 bar. $B^2 M_{Xe}$ is proportional to $(R_0 - R_{min})$ and is pressure independent, while the surface brightness is independent of both spark size and pressure.

These results considerably restrict models of the internal structure of the spark channel at the end of the ionization wave phase (~ 3 ns), after the energy has been deposited, but before hydrodynamic expansion has begun. The simplest consistent model is a shell structure with an energetically hollow core, and constant energy per nucleus ϵ_0 within a shell of thickness Δ , i.e.,

$$\epsilon(r) = \begin{cases} \epsilon_0 & R_0 - \Delta < r < R_0 \\ 0 & \text{otherwise} \end{cases}, \quad (5)$$

$$\text{and } \bar{\epsilon} = \frac{2\Delta\epsilon_0}{R_0^2} (R_0 - \frac{\Delta}{2}). \quad (6)$$

Comparing Eqs. 2&4 with Eq. 6 yields the shell thickness $\Delta = 2R_{min}$ and energy per nucleus $\epsilon_0 = K/4\pi f(\gamma)R_{min}$, which is independent of R_0 as required for consistency with Fig. 5(a). Such a structure might arise when a moderately-conducting spark leader bridges the electrode gap, followed by a rush of current that is confined within an electrical skin depth. Heating within the skin-depth increases the conductivity of the shell relative to the rest of the channel, so that the shell draws the majority of the current density. At later times, this shell can spread inwards due to thermal conduction and radiation transport. Although γ is not strictly a fixed quantity, it is typically treated as a constant value of ~ 1.2 (consistent with 2 levels of ionization) for spark discharges and dense plasmas [1, 16, 18–20]. With this value of γ , the linear fit coefficients yield $\epsilon_0 = 14.4$ (15.3) ± 1.3 (1.2) eV/nucleus for 20 (42) bar discharges.

To better understand these observations, it is necessary to consider the state of matter associated with the initial spark plasma. In this dense regime, screening effects and interparticle forces are dominant and can lead to unexpectedly high levels of ionization [1, 2, 9, 18, 21]. To determine whether this plasma is strongly ionized, the electron density can be estimated using the requirements for opacity [1, 2, 22, 23]. The absolute spectral intensity I_λ at wavelength λ can be calculated using [24],

$$I_\lambda = I_p (1 - \mathbb{R}) \frac{1 - \exp(-\kappa_\lambda l)}{1 - \mathbb{R} \exp(-\kappa_\lambda l)}, \quad (7)$$

where I_p is the Planck spectrum at T_{sat} , \mathbb{R} is the plasma reflectivity, $l = 4\Delta$ is the plasma thickness, and $\kappa_\lambda(T_{sat}, n_0, Z)$ is the absorption coefficient, where Z is the ionization level. Using the plasma conditions for 20 bar at 3 ns ($T_{sat} = 29000$ K and $l = 40$ μm) and the free-free bremsstrahlung formula for κ_λ [22] with dense screening corrections [25], 2 levels of ionization is required to match the observed spectrum (Fig. 3). In contrast, the ionization calculated using Saha's equation in the dilute limit gives $Z = 0.3$ and cannot reproduce the plasma opacity. The high level of ionization potential reduction required is estimated by comparing the energy to ionize and heat these free electrons with $\epsilon_0 = 15$ eV/nucleus. Using $Z = 2$, the thermal energy is $\frac{3}{2}(Z+1)kT_{sat} = 11$ eV/nucleus. The vacuum ionization

energy is $\sum_{i=1}^Z \chi_i = 33$ eV, giving a total of 44 eV/nucleus. Therefore, a dramatic reduction in the ionization potential must occur. Although formulated in a perturbative limit, the Debye screening formula suggests significant ionization potential lowering given by $\chi_D = -3e^2/\delta_D$, where $\delta_D = \sqrt{kT/24\pi e^2 n_0}$ is the Debye length and all atoms are assumed doubly-ionized [16]. For the parameters given above, $\Delta\chi = -20$ eV/nucleus, leaving a significantly lowered total energy of 22 eV/nucleus.

Our measurement of ionization potential lowering makes this system a platform for studying the equations of state and transport properties of strongly correlated plasmas. The plasma studied in this Letter is a robust state of matter, as the saturation temperature and opacity is maintained long after the input energy has ceased. Further study of dense plasmas on rapid timescales will lead to discoveries of exotic phases of gaseous coulombic systems that parallel unusual phases seen in liquid electrolytes [26] as a result of strong screening [27]. Due to its opacity, the screened plasma phase generated by spark discharges will make an excellent sub-nanosecond means of switching off ultra-violet probes, so as to make improved measurements for the state of trapped ion Q-bits [28, 29]. Other unexpected properties and applications of condensed plasmas remain to be discovered.

Acknowledgments

We gratefully acknowledge support from the Air Force Office of Scientific Research and the DARPA MTO for research on microplasmas.

-
- [1] M. Skowronek, *Physics of Fluids* **13**, 378 (1970), ISSN 00319171.
 - [2] A. Bataller, G. R. Plateau, B. Kappus, and S. Putterman, *Physical Review Letters* **113**, 075001 (2014), ISSN 0031-9007, URL <http://link.aps.org/doi/10.1103/PhysRevLett.113.075001>.
 - [3] I. Model, *Soviet Physics JETP* **5** (1957).
 - [4] M. Liverts and N. Apazidis, *Physical Review Letters* **116**, 014501 (2016), ISSN 0031-9007, URL <http://link.aps.org/doi/10.1103/PhysRevLett.116.014501>.
 - [5] G. Vazquez, C. Camara, S. Putterman, and K. Weninger, *Optics Letters* **26**, 575 (2001), ISSN 01469592, 0009057.
 - [6] G. Glaser, *Optik* **7**, 33 (1950).
 - [7] G. Glaser, *Zeitschrift für Naturforschung A* **6**, 706 (1951).
 - [8] M. P. Vanyukov and A. A. Mak, *Physics-Uspekhi* **1**, 137 (1958).
 - [9] U. Yusupaliev, *Bulletin of the Lebedev Physics Institute* **34**, 264 (2007), ISSN 1068-3356.
 - [10] A. Bataller, J. Koulakis, S. Pree, and S. Putterman, *Applied Physics Letters* **105**, 223501 (2014), ISSN 0003-6951, URL <http://scitation.aip.org/content/aip/journal/apl/105/22/10.1063/1.4902914>.
 - [11] U. Yusupaliev, *Bulletin of the Lebedev Physics Institute* **36**, 44 (2009).
 - [12] F. Frungel, *Optik* **3**, 128 (1948).
 - [13] M. P. Vanyukov and A. A. Mak, *Doklady Akad. Nauk S.S.S.R.* **Vol: 123** (1958).
 - [14] H. Fischer and L. Michel, *Applied Optics* **6**, 935 (1967), ISSN 0003-6935.
 - [15] E. M. Bazelyan and Y. P. Raizer, *Spark Discharge*, Raizer (Taylor & Francis, 1977), ISBN 0-8493-2868-3.
 - [16] Y. P. Zel'dovich, Ya. B., Raizer, *Physics of Shock Waves and High-temperature Hydrodynamic Phenomena* (Dover Publications, 1966), ISBN 0-486-42002-7.
 - [17] L. I. Sedov, M. Friedman, M. Holt, and J. D. Cole, *Journal of Applied Mechanics* **28**, 159 (1961), ISSN 00218936.
 - [18] E. a. Martin, *Journal of Applied Physics* **31**, 255 (1960), ISSN 00218979, URL <http://scitation.aip.org/content/aip/journal/jap/31/2/10.1063/1.1735555>.
 - [19] R. Drake, *High-Energy-Density Physics: Fundamentals, Inertial Fusion, and Experimental Astrophysics* (2006), ISBN 9783540293149.
 - [20] U. Yusupaliev, *Bulletin of the Lebedev Physics Institute* **37**, 71 (2010), ISSN 1068-3356.
 - [21] Z. Wen-Juan and A. Yu, *Chinese Physics B* **24**, 47802 (2015), URL <http://stacks.iop.org/1674-1056/24/i=4/a=047802>.
 - [22] A. Bataller, B. Kappus, C. Camara, and S. Putterman, *Physical Review Letters* **113**, 024301 (2014), ISSN 0031-9007, URL <http://link.aps.org/doi/10.1103/PhysRevLett.113.024301>.
 - [23] B. Kappus, A. Bataller, and S. Putterman, *Physical Review Letters* **111**, 234301 (2013), ISSN 0031-9007.
 - [24] G. Bekefi and S. C. Brown, *American Journal of Physics* **29**, 404 (1961), ISSN 00029505.
 - [25] G. Dimonte and J. Daligault, *Physical review letters* **101**, 135001 (2008), ISSN 0031-9007.
 - [26] J. Jacob, M. A. Anisimov, A. Kumar, V. A. Agayan, and J. V. Sengers, *International Journal of Thermophysics* **21** (2000).
 - [27] V. A. Kozlov, S. V. Sokolova, and N. A. Trufanov, *Soviet Physics JETP* **71** (1990).
 - [28] A. H. Myerson, D. J. Szwerc, S. C. Webster, D. T. C. Allcock, M. J. Curtis, G. Imreh, J. A. Sherman, D. N. Stacey, A. M. Steane, and D. M. Lucas, *Physical Review Letters* **100** (2008), ISSN 00319007, 0802.1684.
 - [29] J. Mizrahi, B. Neyenhuis, K. G. Johnson, W. C. Campbell, C. Senko, D. Hayes, and C. Monroe, *Applied Physics B* **114**, 45 (2014), ISSN 0946-2171, 1432-0649.

- [30] Considering that the speed of sound is much less than the ionization wave velocity, picking R_0 at a late time results in a small error compared to picking R_0 at too early in time. Therefore we prefer to err on the late side.

Part 5:

Slides from Previous Reports

a) 2013 Report

b) 2014 Report

c) 2015 Report

Plasma and Electroenergetics Annual Portfolio

Energy Flow in Dense Off-Equilibrium Plasmas



Submitted by Seth Putterman

December 19, 2014

UCLA

Equation of State and Transport Properties in a Dense Plasma

- We have demonstrated 3 different desktop labs for dense plasma science
- Kinetic theory of a dense plasma is easier than you think
- Ionization potential is dramatically lowered in a dense plasma
- Subnanosecond establishment of opacity in a dense plasma
- Transition to opacity occurs on micron length scale → **subns switch to block high power pulses!**
- Idea for a paradigm shifting 4th lab of warm dense plasma

Dense Plasma Lab "SL"

Concentrating a sound wave energy density by 12 orders: UCLA in a sperical geometry

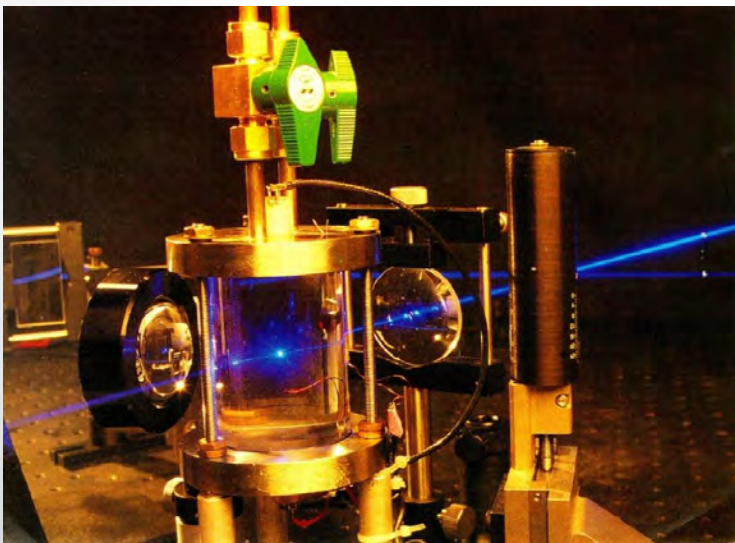
Background---

Sonoluminescence occurs from rapid collapse of oscillating gas bubble driven by an acoustic field.

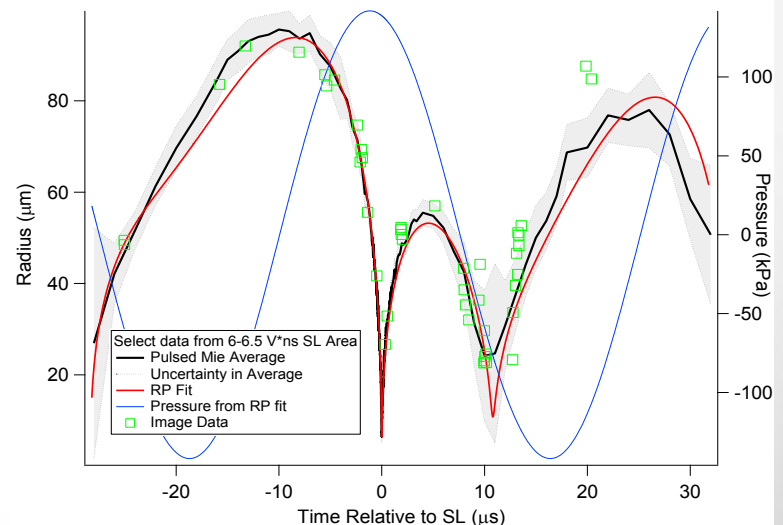
Adiabatic/shock--compression heats the gas during the collapse phase.

At maximum compression, energy density transforms gas into cold (\sim eV) dense ($>10^{21}$ cm $^{-3}$) plasma.

Light emission occurs due to thermal bremsstrahlung.

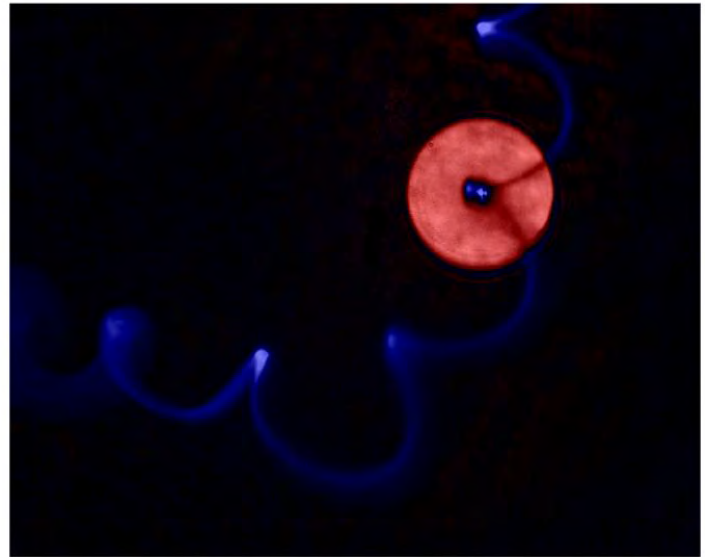
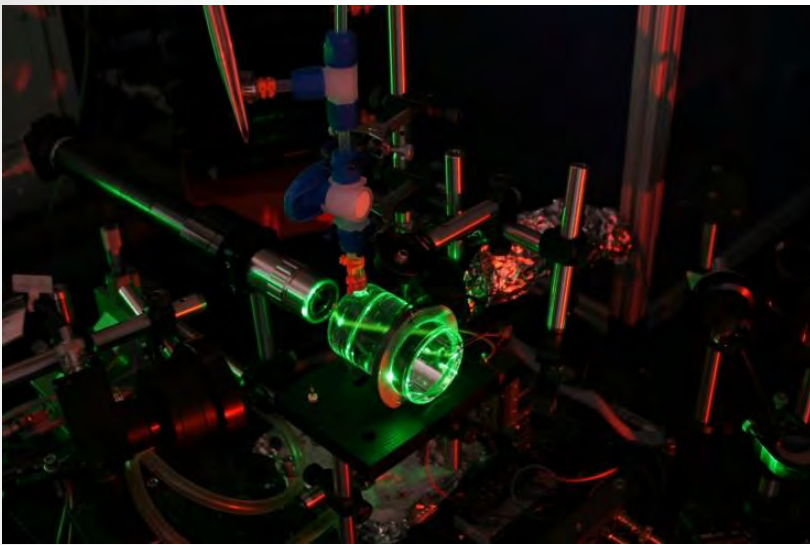


S. Putterman, Scientific American 272 (2) 46-51, 1995



B. Kappus et al., Phys. Rev. Lett., Accepted Nov. 6th 2013

Xenon Bubble in Sulfuric Acid Obeys Low UCLA Mach Number Hydrodynamics



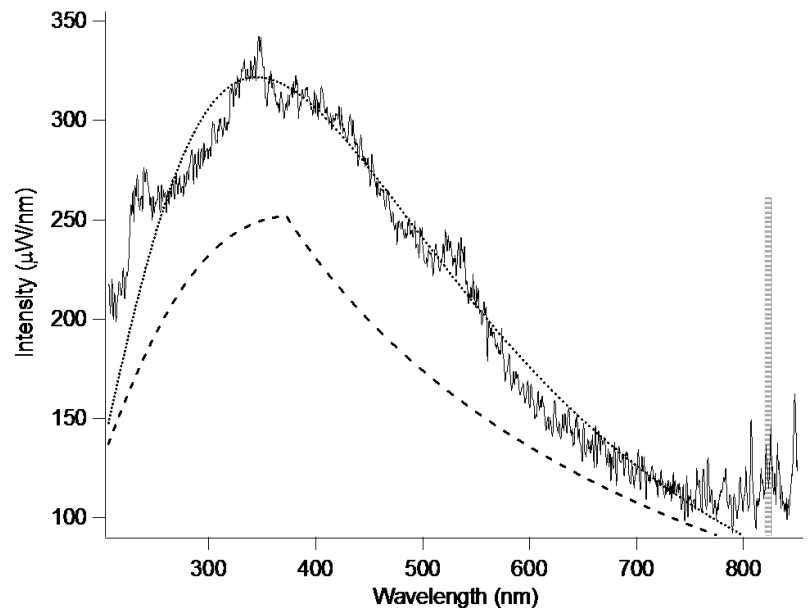
Xenon bubble in 85% sulfuric acid (low vapor pressure) was driven at 28.5 kHz.

Detailed Mie scattering provide complete characterization of hydrodynamics.

Blackbody spectrum emitted matches min UCLA radius, implying opacity is attained

Spectroscopy of 13 ns flash match ideal Planck blackbody (Mie radius matches blackbody emission radius)

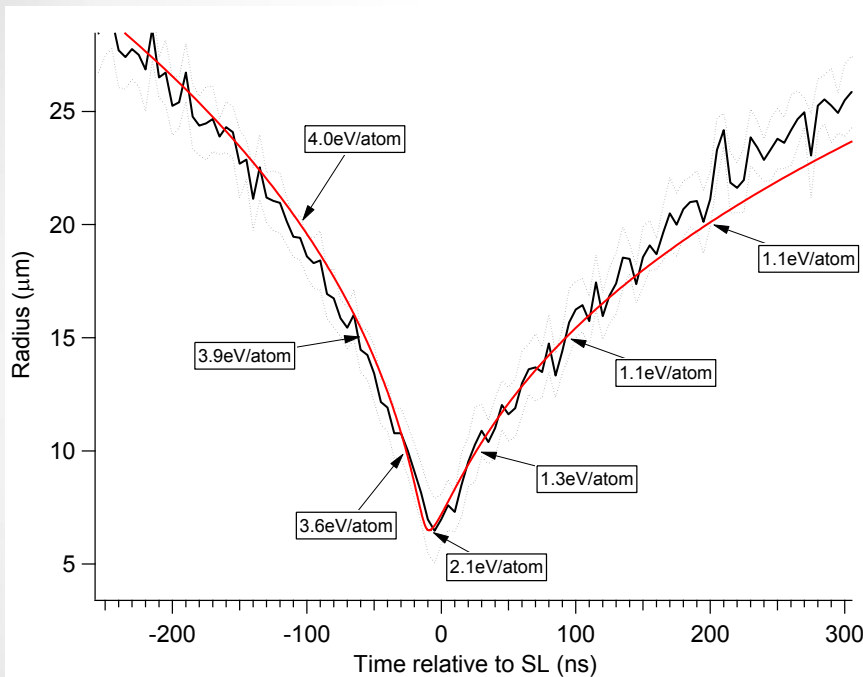
$\Rightarrow n_e > 4 \times 10^{20} \text{ cm}^{-3}$
required to satisfy opacity
($R_c = 6.5 \pm .9 \mu\text{m}$)



B. Kappus et al., Phys. Rev. Lett.,

Energy Balance Reveals That Ionization Potential is Lowered by > 80% in a Sonoluminescing Dense Plasma

UCLA



Analysis shows only 2.1 ± 0.6 eV/atom available at light emission: too low to explain >36% degree of ionization!

Collective processes reduce ionization potential by at least 80% (12.1 eV to 2.5 eV): highly-ionized plasma occurs during SL.

$$\frac{x^2}{1-x} = \frac{2g_1}{n_a \lambda^3} e^{-\chi_{\text{eff}}/kT}$$

$$\chi_{\text{eff}} = \chi_0 \left(1 - 2\gamma a_B n_a^{1/3} \right) - e^2 / 4\pi\epsilon_0 \delta_d$$

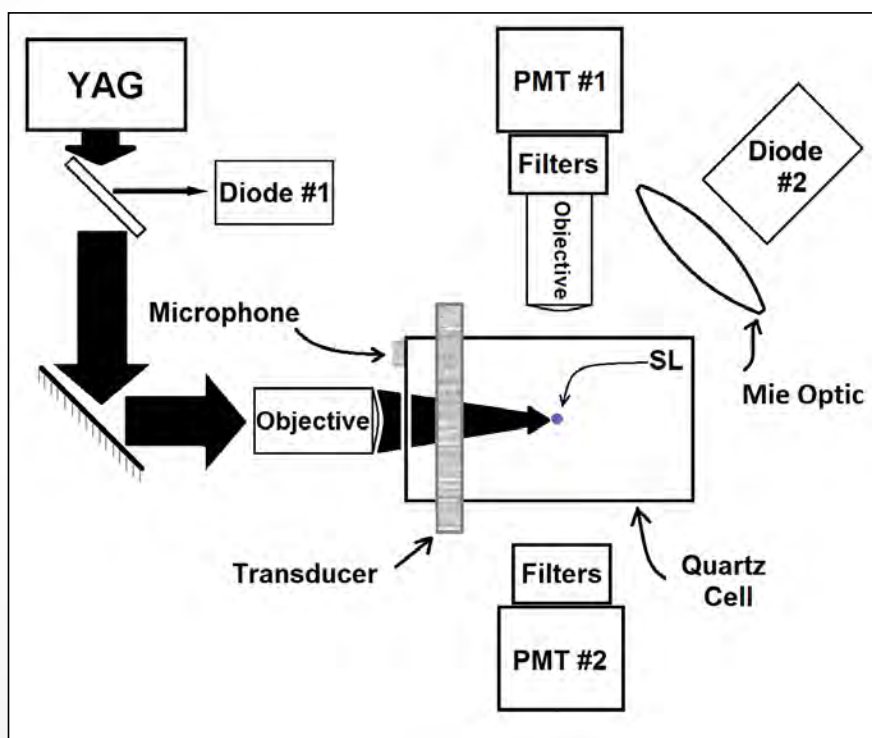
Model for Ionization potential lowering in a cold dense plasma

A complete equation of state also requires the pressure - - - - ->

Laser Probe of the Dense Plasma Inside a Sonoluminescing Bubble– 532nm and 1064nm

UCLA

The goal is to determine the collision time/kinetics of a dense plasma.

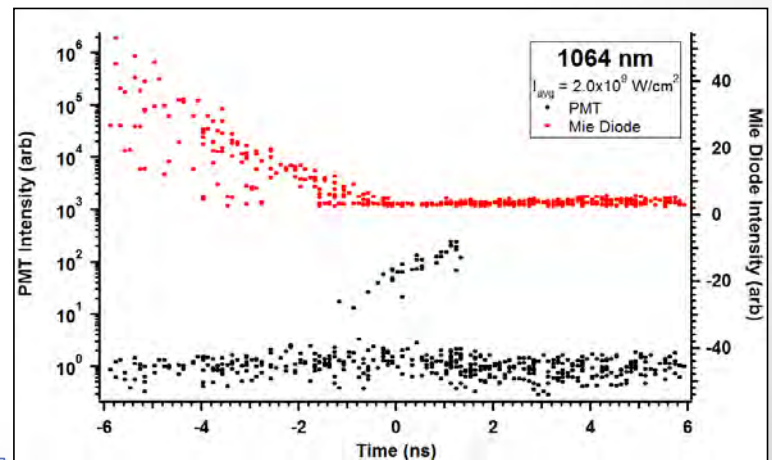
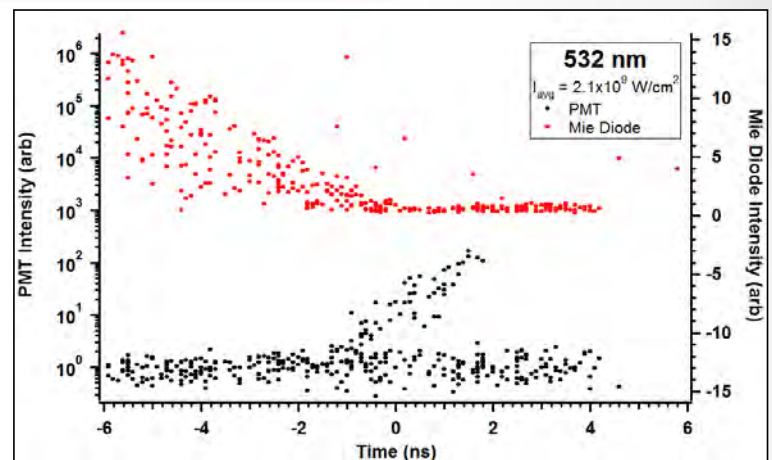


Interaction “gap” vs. wavelength

Measurement of both Mie scattering [red] and light emission [black] from a xenon gas bubble that implodes to about a one micron diameter where it forms a dense plasma, which corresponds to $t = 0$ in the bottom axis.

Our measurements find that 532nm always interacts with the plasma whereas for 1064nm there is a threshold for interaction.

This interaction “gap” can be ascribed to a large degree of reflection by 1064nm and a large absorption rate by 532 nm. This behavior occurs for plasma with low collisionality compared to the interacting light’s wavelength.



Bataller - Kappus

Collision Time in a Dense Microplasma

UCLA Strong Screening

$$\ln \Lambda = 2\sqrt{3} \ln \left(\sqrt{\frac{1}{6} \Gamma_{\omega}^{-3} + 1} \right)$$

Daligault-Weak Screening

$$\ln \Lambda = 2\sqrt{3} \ln \left(\frac{0.7}{\sqrt{6}} \Gamma_{\omega}^{-3/2} + 1 \right),$$

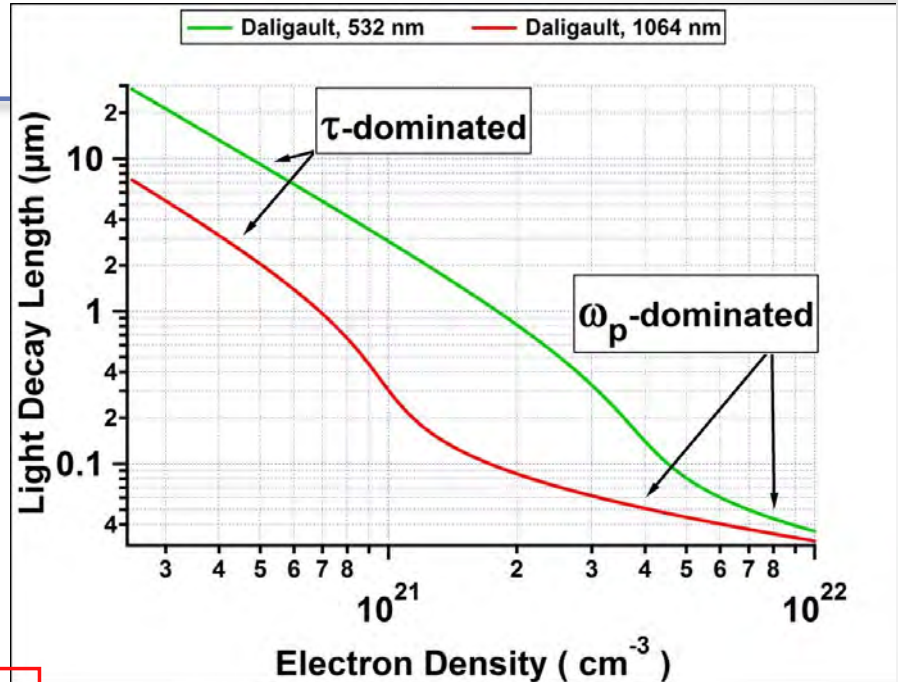
Dilute Plasma Theory

$$\ln \Lambda = 2\sqrt{3},$$

$$\tau = \frac{16\pi^2 \epsilon_0^2 \hbar \omega}{n_e e^4 [1 - e^{-\beta \hbar \omega}]} \frac{3}{2} \sqrt{\frac{3mkT}{2\pi}} \frac{1}{\ln \Lambda}$$

$$\Gamma_{\omega} = \frac{e^2}{\epsilon_0} \left(\frac{1 - e^{-\beta \hbar \omega}}{\hbar \omega} \right) \left(\frac{n_e}{3(4\pi)^2} \right)^{1/3}$$

Theory of dilute plasma is way off when applied to dense microplasmas



Plasma Coupling Parameter is $\Gamma \sim 5$

$$\frac{k^2 c^2}{\omega^2} = (1 - \gamma \beta) + \left(\gamma \frac{\beta}{\omega \tau} \right) i$$

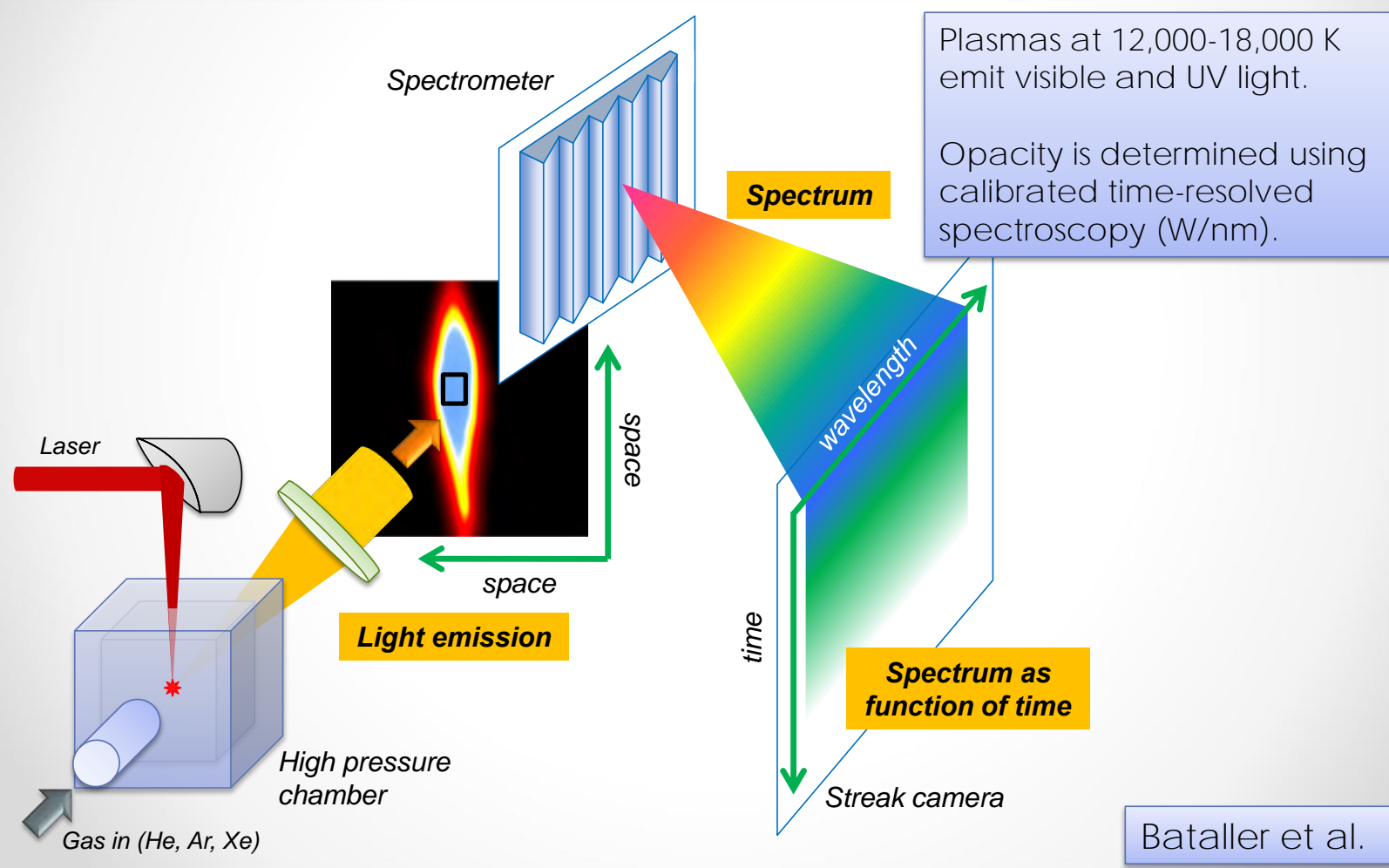
$$\gamma = \frac{\omega_p^2}{\omega^2} \text{ and } \beta = \frac{\omega^2 \tau^2}{1 + \omega^2 \tau^2}$$

Closed form Dense Plasma Dispersion Law

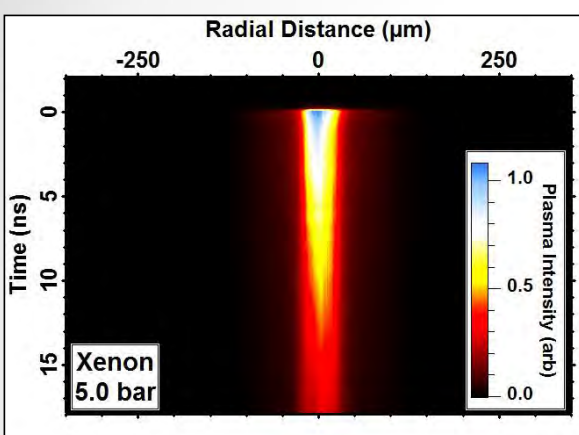
Dense Plasma Lab via Laser Breakdown Achieved Via Use of High Pressure Gases that Match Atomic Density in SL Bubble

UCLA

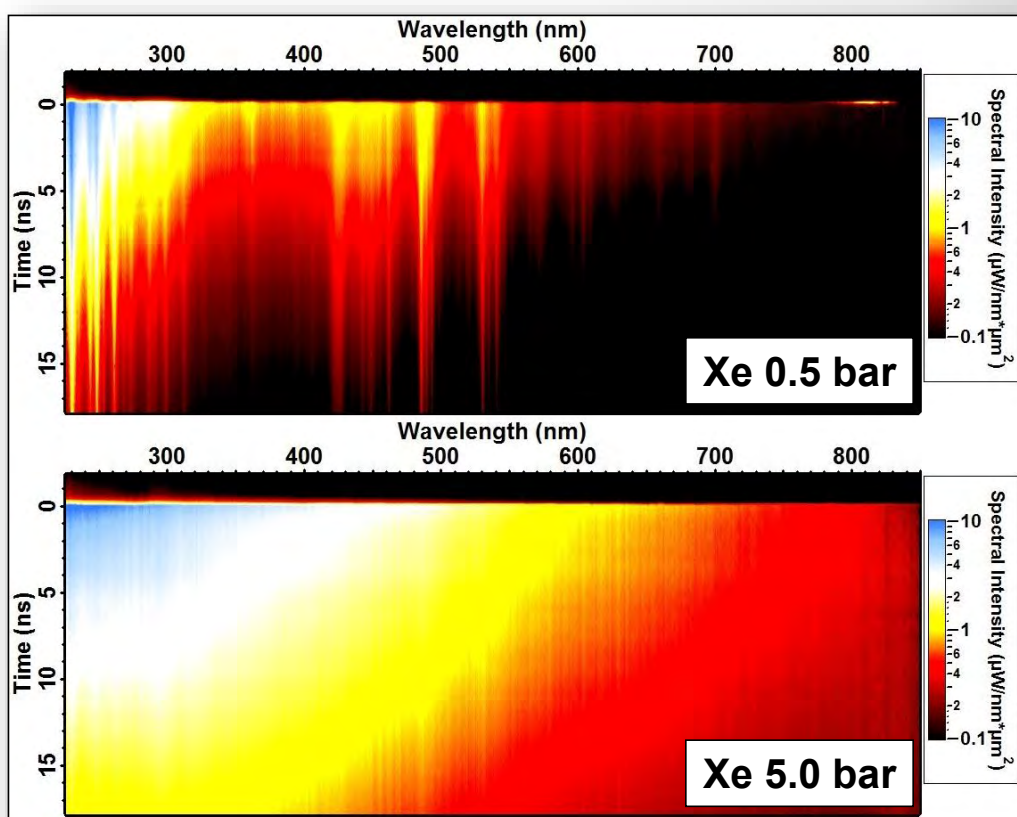
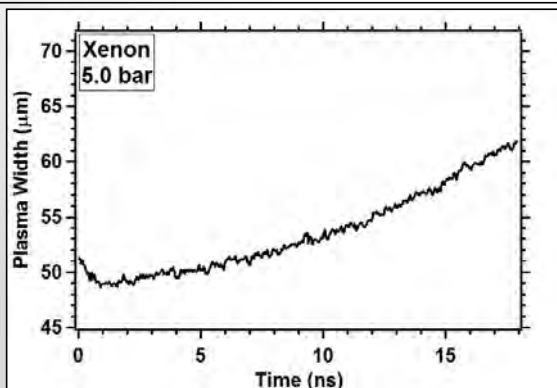
Bubble



UCLA Sonoluminescence blackbodies reproduced in Ar, Xe, and He !



Radial slice of breakdown as a function of time

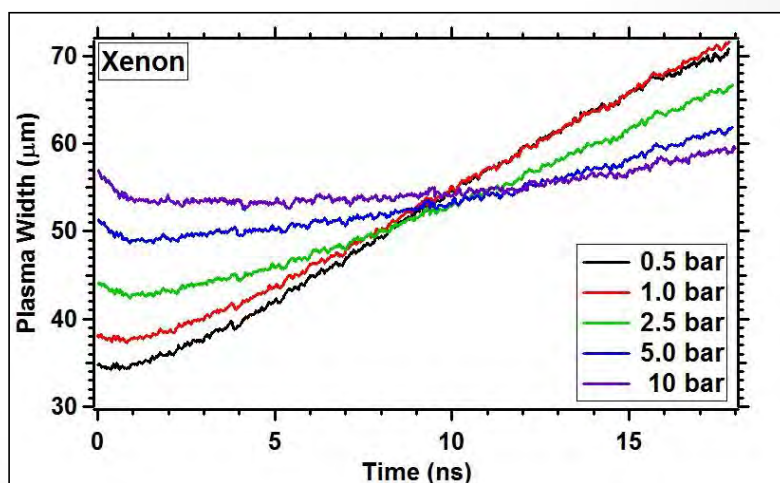
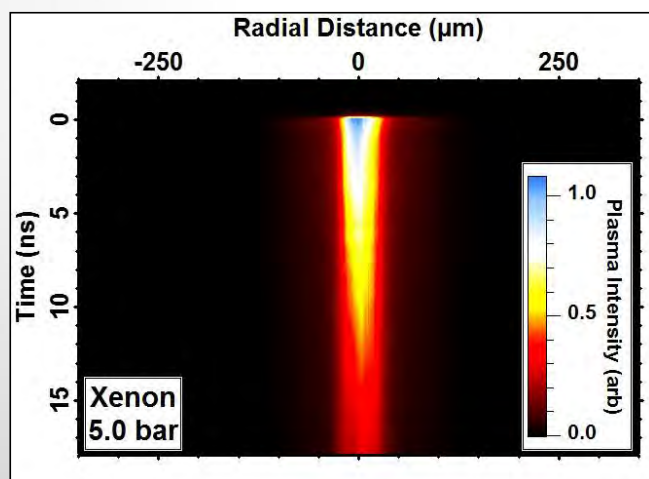
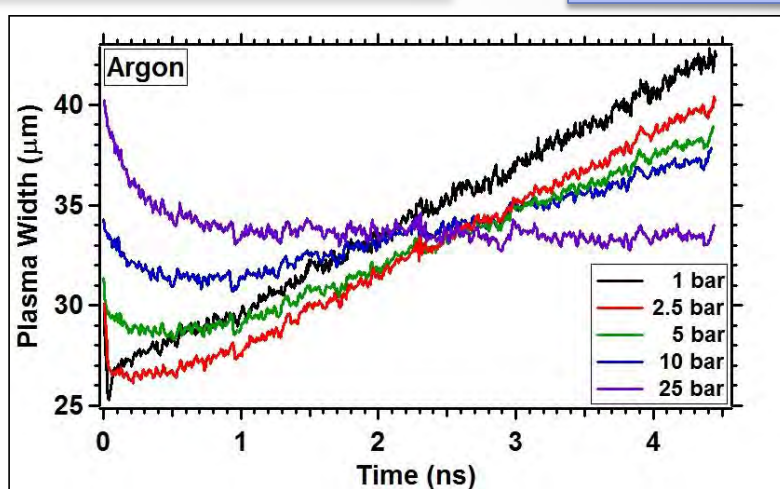
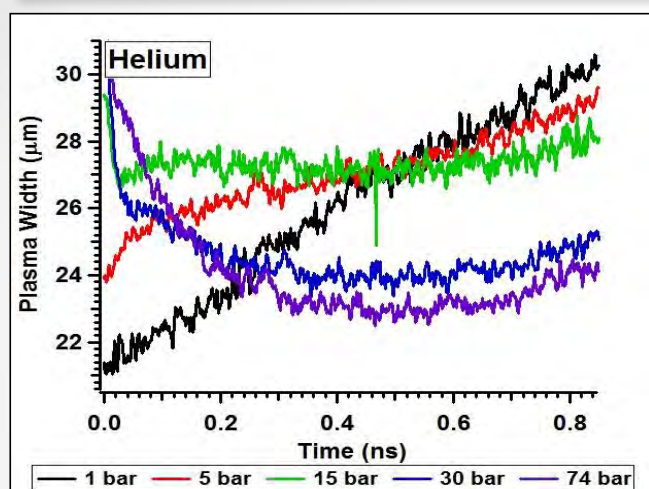


Spectrum transitions to blackbody emission at elevated pressures

Does Plasma Contraction at Short Times Imply that a Cold Dense Plasma acts like it has a Tensile Strength

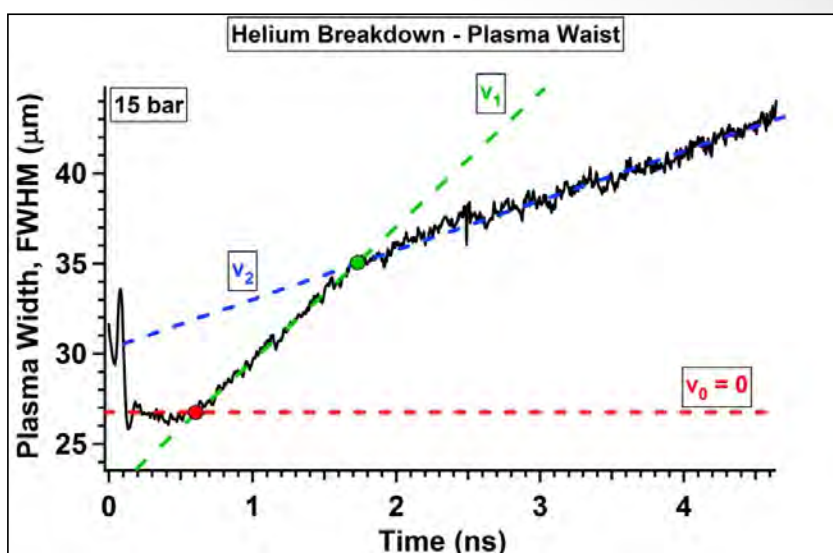
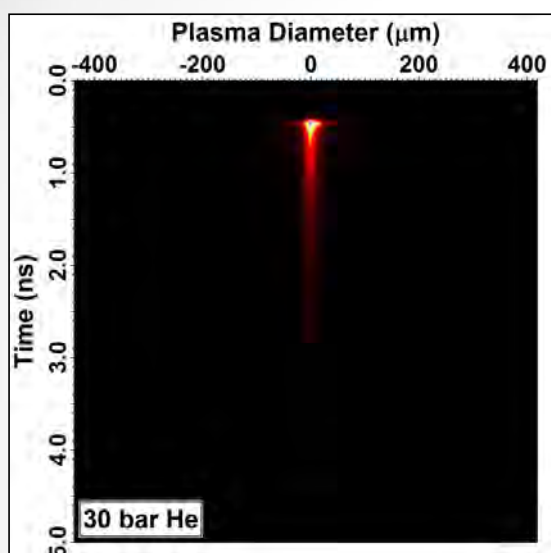
UCLA

Bataller et al.



Comparison of Plasma Sound Velocity to Plasma Expansion Velocity

UCLA



Helium			Linear Fit	Linear Fit
Pressure (bar)	t_{flat} (ns)	t_2 (ns)	v_1 (km/s)	v_2 (km/s)
1	< 0.05	~1.75	12.78 ± 0.07	3.07 ± 0.02
5	0.095	~1.75	7.58 ± 0.06	3.45 ± 0.05
15	0.85	~1.75	7.39 ± 0.06	2.57 ± 0.02
30	0.85	~1.75	5.75 ± 0.05	2.14 ± 0.02
40	0.85	~1.75	6.76 ± 0.05	2.19 ± 0.02

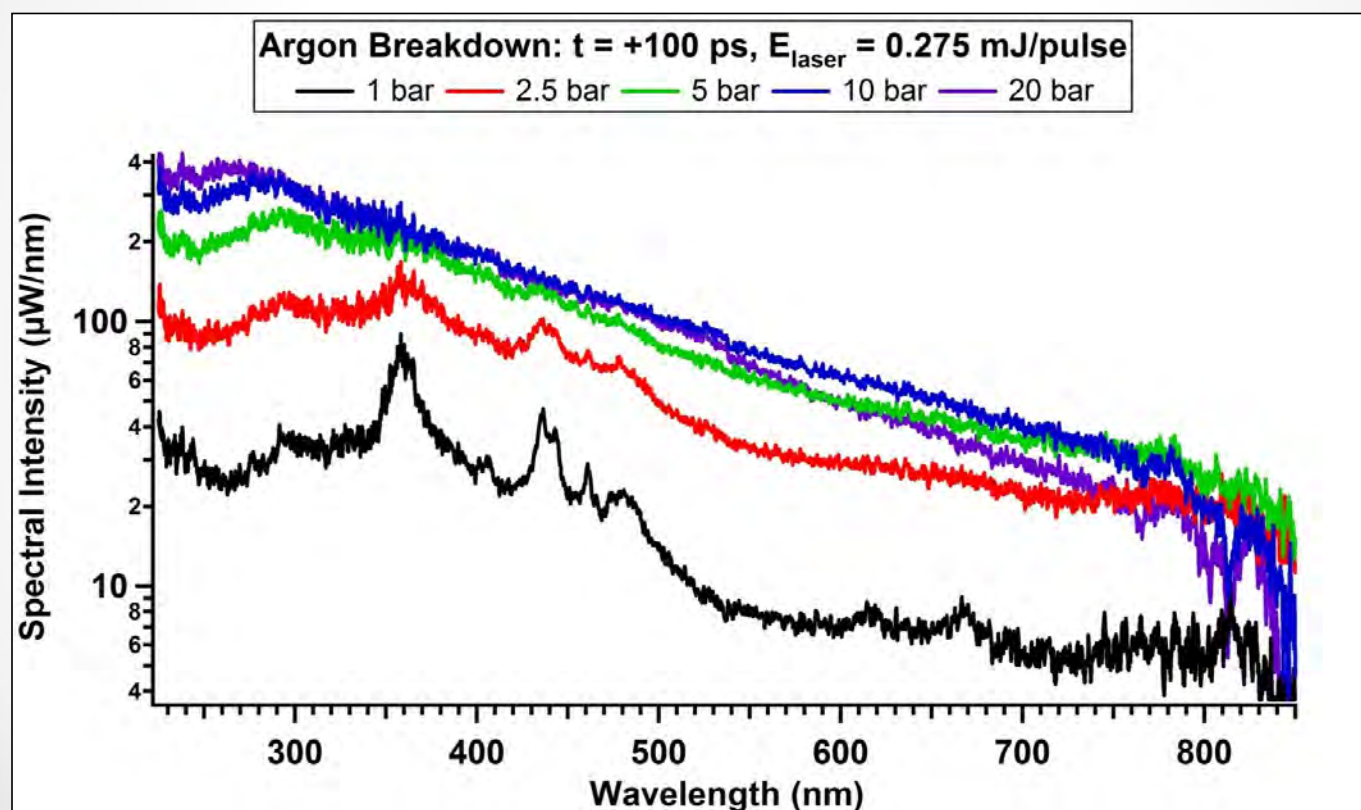
$$c_s = \sqrt{\frac{ZkT_e + 3kT_i}{m_i}}$$

For helium at $T = 11,000$ K, $Z = 1$, and $T_i \ll T_e$,

$$c_s = 4,780 \text{ m/s}$$

Dense Plasma Formation Under Pressure

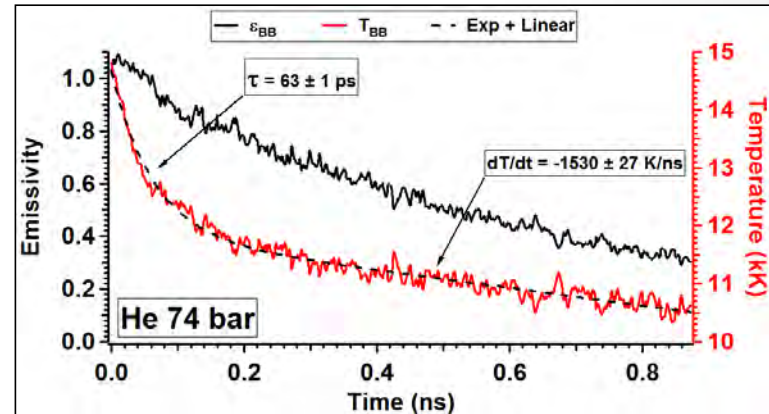
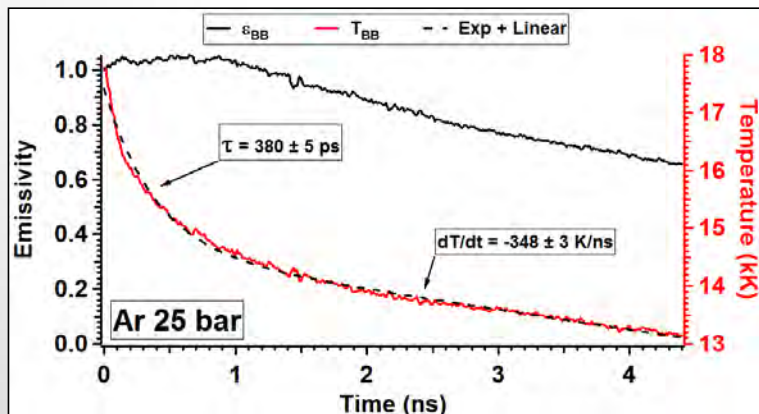
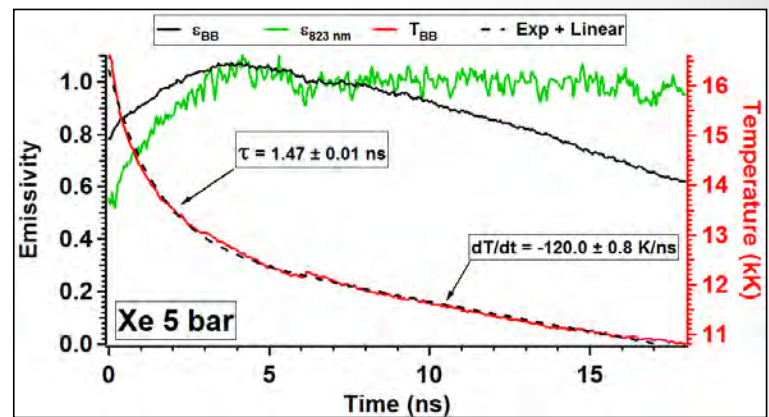
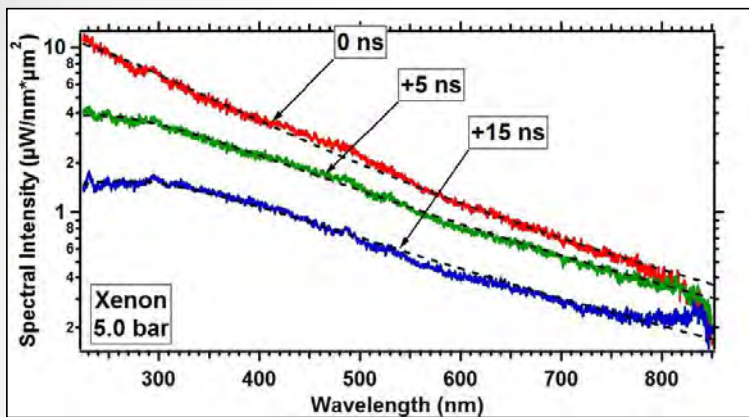
UCLA



Plasma Temperature Evolution

UCLA

12,000 – 18,000K
Blackbody fits



Ionization Required for Opacity

Opacity at 400 nm

- For measurements made, opacity condition governed by R_{BB}/ℓ_ν
- Bremsstrahlung is the dominant source of broadband emission/absorption in high density plasma.
- ℓ_ν is modified by high density effects (G. Dimonte and J. Daligault, Phys. Rev. Lett. **101**, 135001 (2008)).

	Helium	Argon	Xenon
t (ns)	+0.1	+1	+5
R (μm)	26	34	50
T (K)	12,550	14,550	12,350
n _a (cm ⁻³)	1.85x10 ²¹	6.3x10 ²⁰	1.25x10 ²⁰
Z	>0.38	>1.0	>3.2
n _e (cm ⁻³)	>7.0x10²⁰	>6.3x10²⁰	>4.0x10²⁰
Γ	>1.9	>1.6	>3.6

Thermalization Timescale Measured

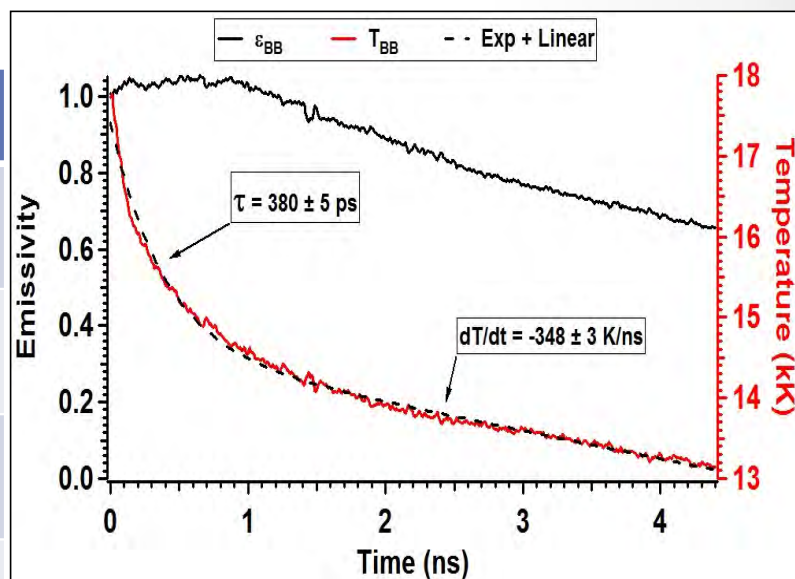
UCLA

- Thermalization time measured

$$\tau_{th} \approx \frac{M}{m} \tau_{e-i}$$
- τ_{e-i} is calculated using temperature and ionization with dense plasma theory (G. Dimonte and J. Daligault, Phys. Rev. Lett. **101**, 135001 (2008) *screened collisions*)

SELF-CONSISTENT VALIDATION OF TRANSPORT THEORY AND PROVIDES COLLISION TIME MEASUREMENT FOR A STRONGLY COUPLED PLASMA

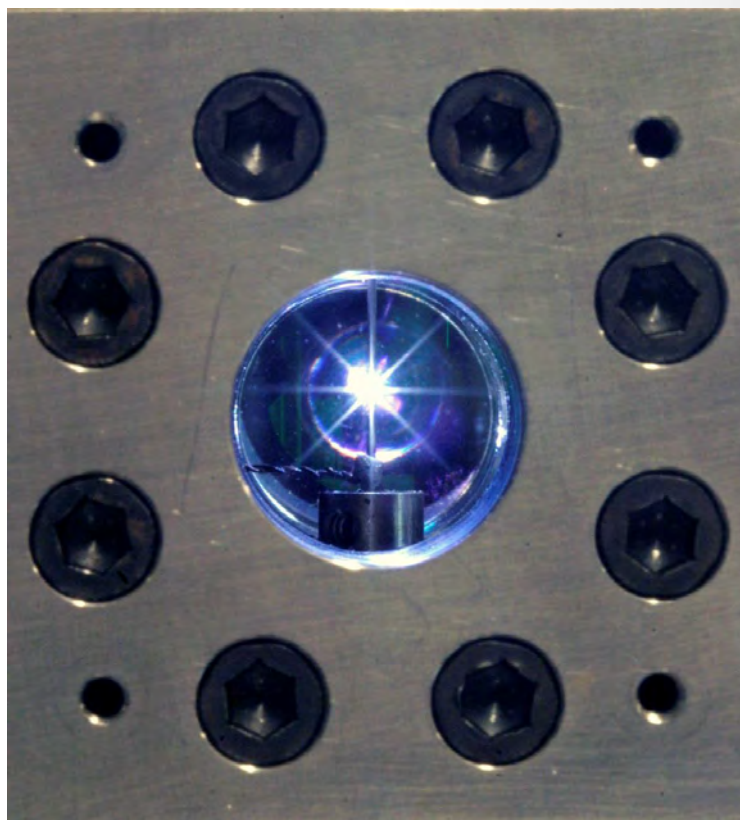
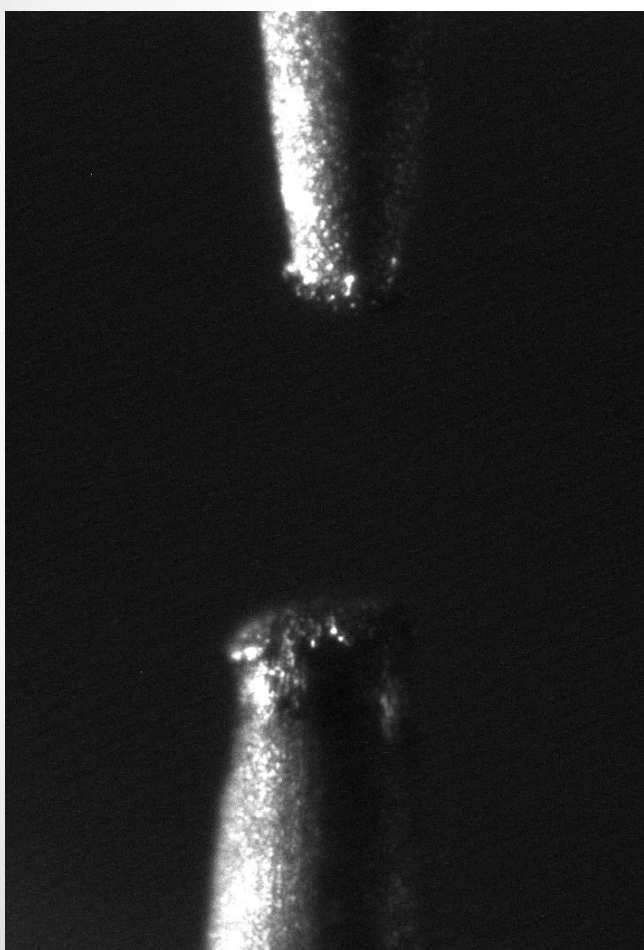
	Helium	Argon	Xenon
τ_{th} (meas.)	63 ps	380 ps	1.47 ns
τ_{th} (calc.)	37 ps	305 ps	1.17 ns
Mass Ratio	0.10	1.0	3.3
$\frac{\tau_{th}}{\tau_{e-i}}$	0.13	1.0	3.3



Ar 25 bar

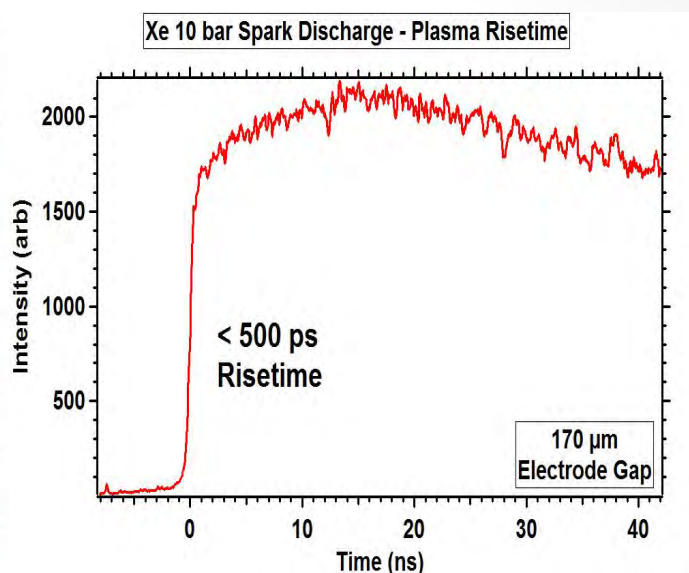
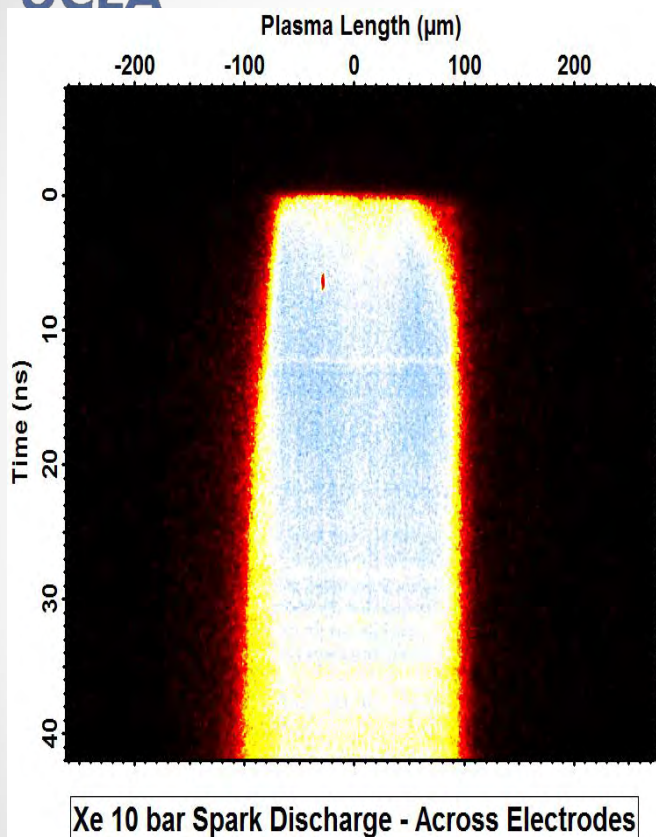
UCLA

Spark Discharges in a Dense Gas are also a – [New Ancient] Platform for Dense Plasmas



Sub-ns Homogeneous Arc Discharge Formation

UCLA

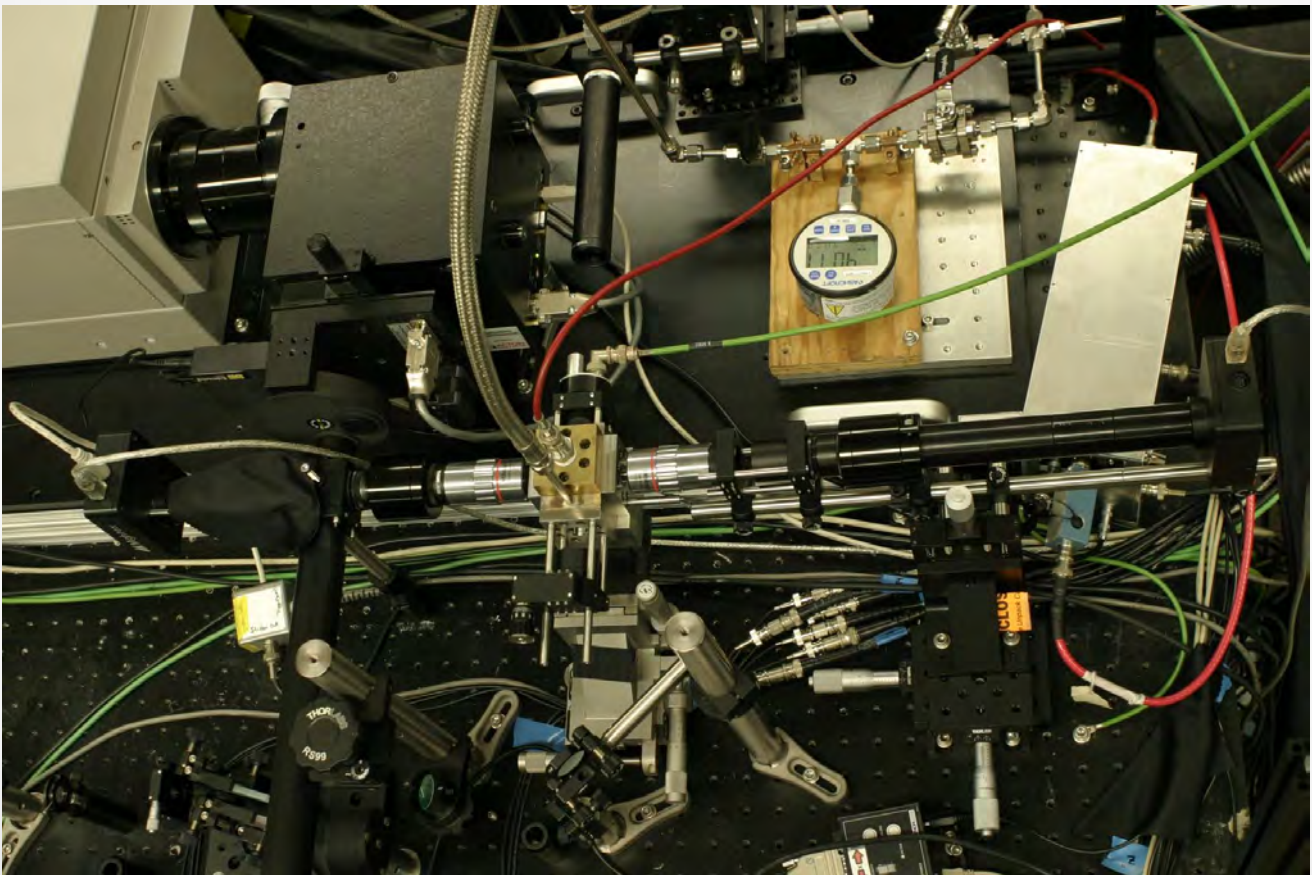


Ongoing measurements indicate that this is a very fast process as all measurements so far are instrument limited

Flat-top in intensity indicates that blackbody formation is 'immediate'

UCLA

Going Forward: Transport Measurements of Dense Spark Plasmas Using Fast Diagnostics



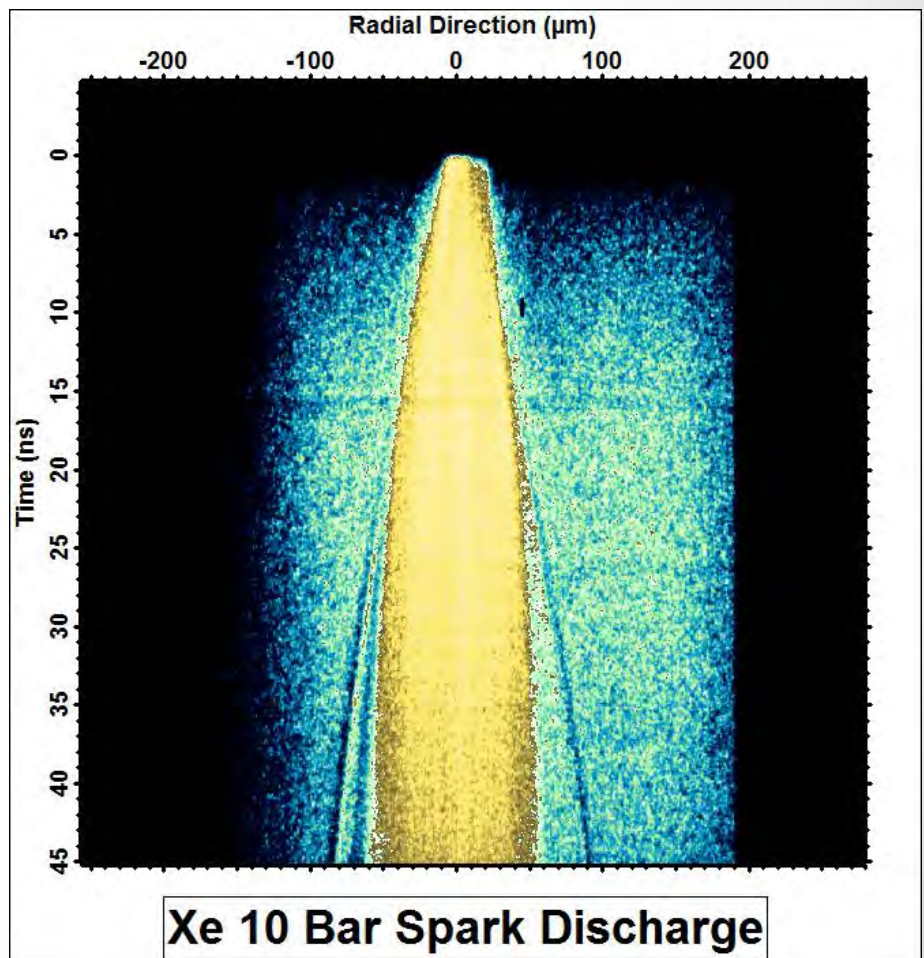
Battaller – Koulakis - Pree

Speed of Sound Measurements and Equation of State

UCLA

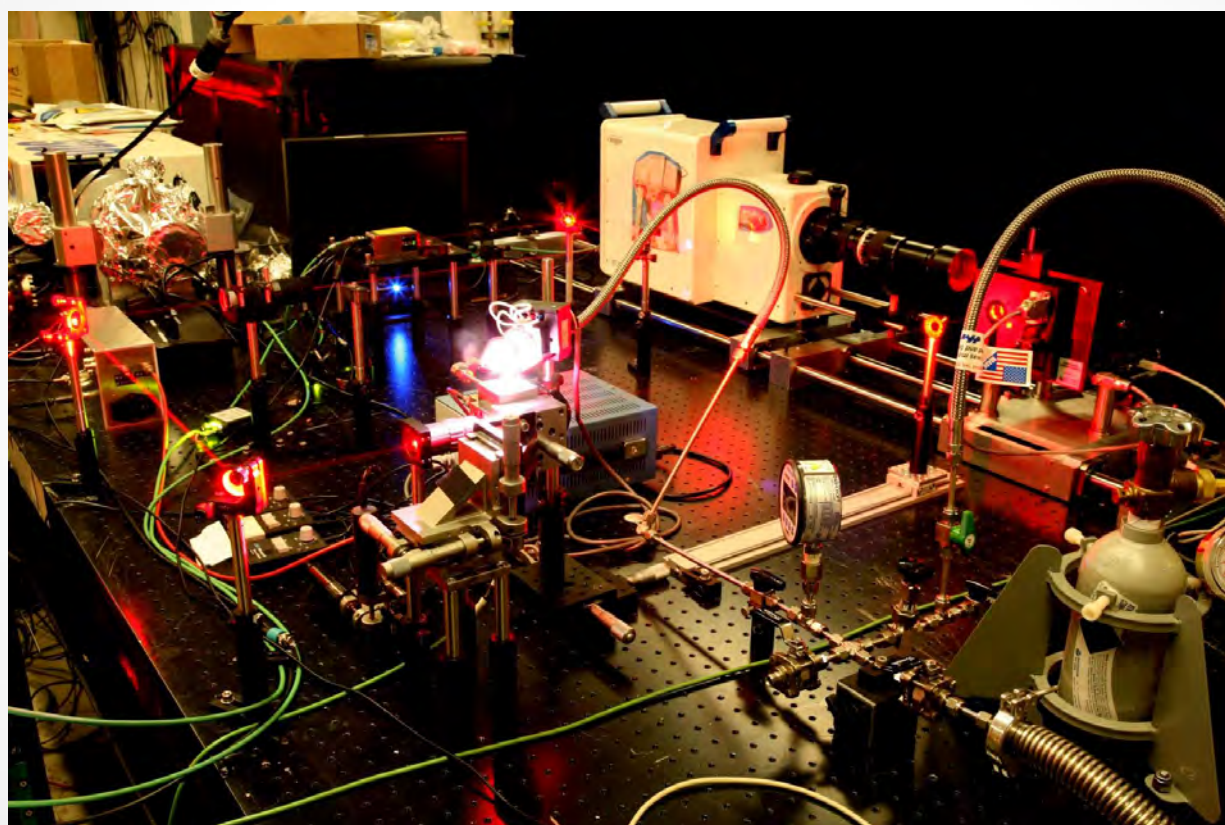
- Time-resolved shadowgraph of spark discharges test blast wave theory for dense plasmas.
- Femtosecond laser-plasma interactions can act as an acoustic probe –
“Spark Seismology”=missing part of dense plasma eq state

Battaller – Koulakis - Pree



UCLA

Nanosecond UV Framing Camera for Diagnosing Transport in Dense Plasmas



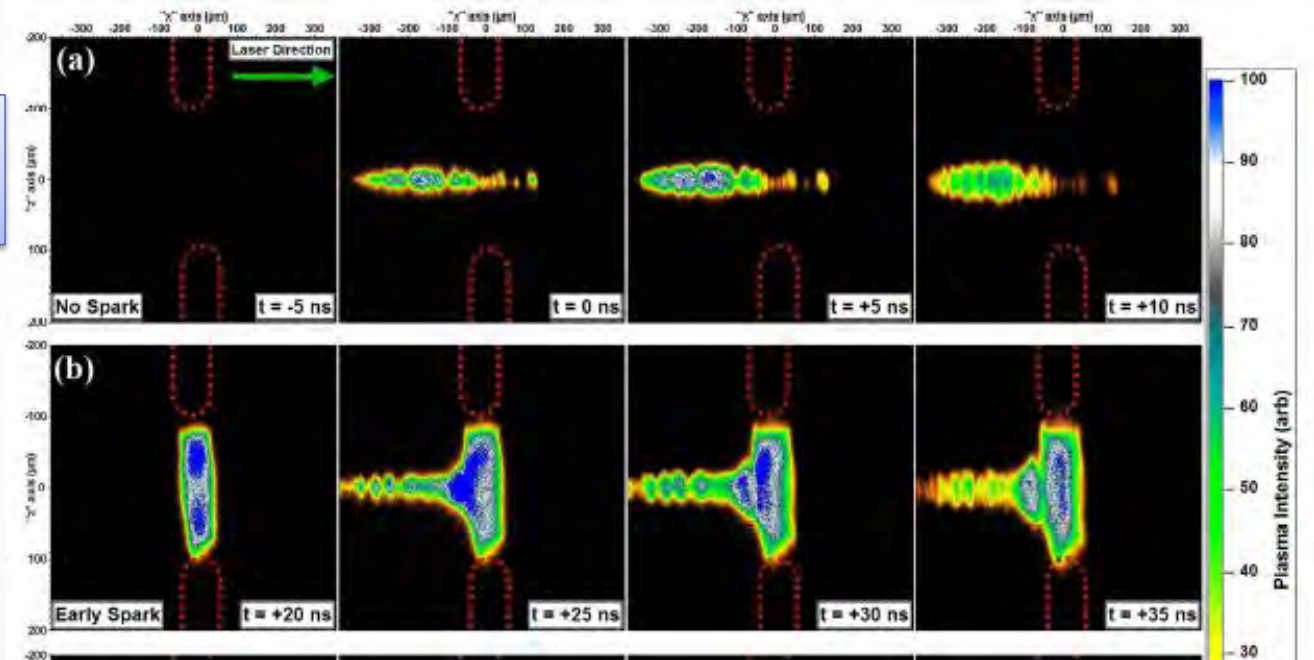
Bataller – Koulakis - Pree

Not Just a Pretty Plasma: Deterrence of High-Intensity Laser Pulses

UCLA

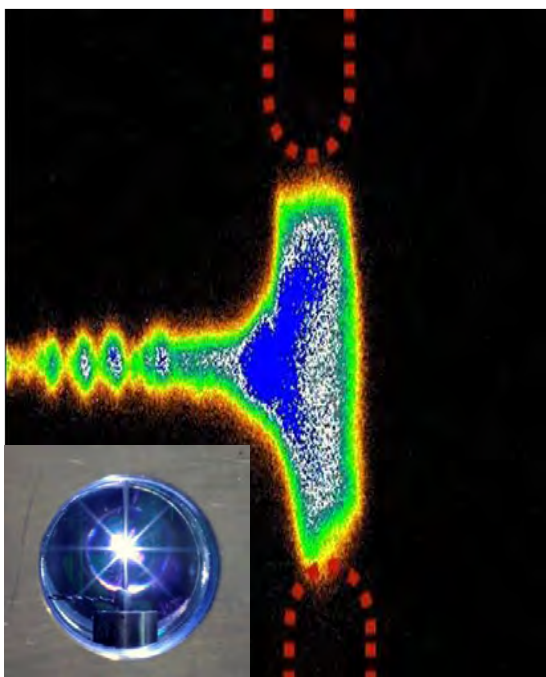
Practically limitless power handling capability. The switch cannot be broken as it is already the broken state of matter!

No spark protection



Spark activated

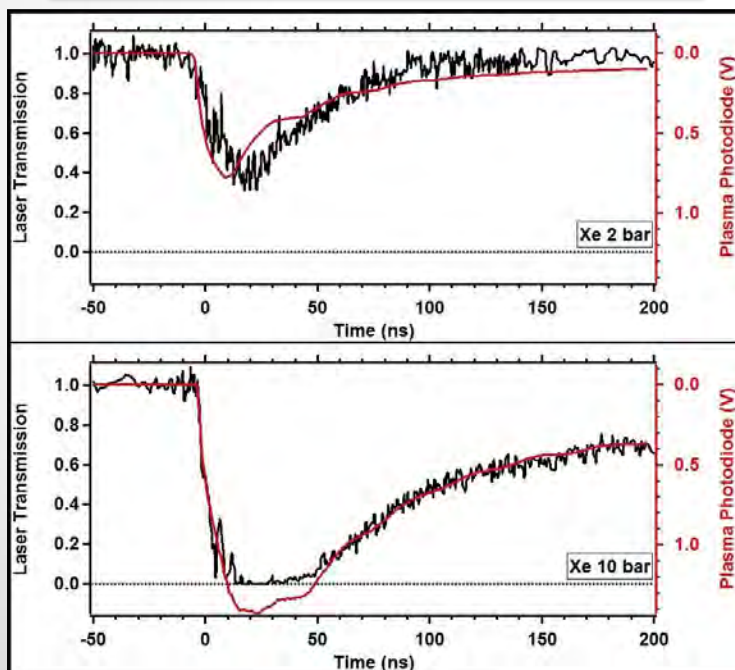
A. Bataller, J. Koulakis, S. Pree, S. Putterman, *Appl. Phys. Lett.* **105**, 223501 (2014)



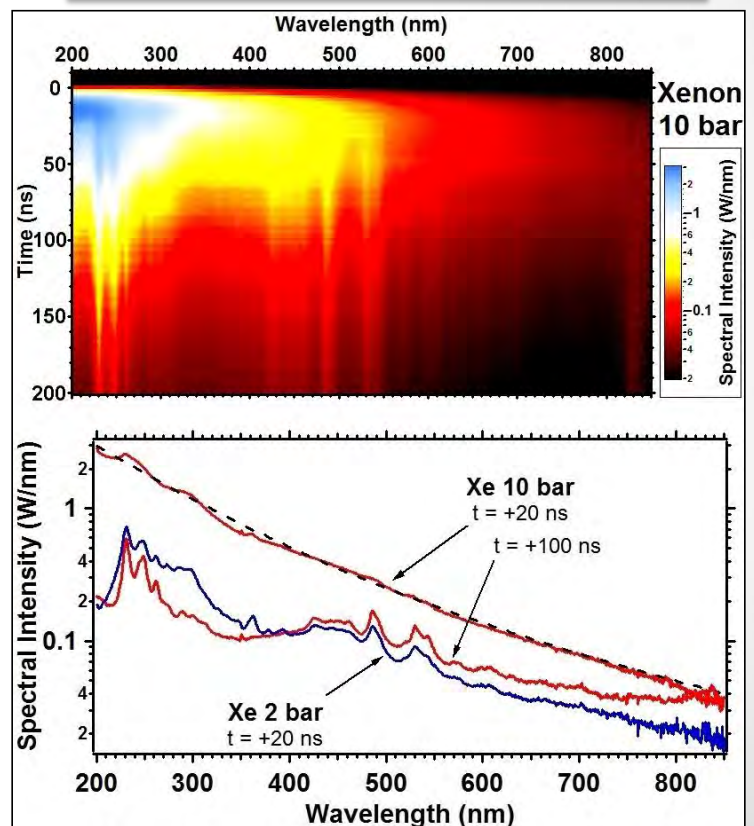
UCLA

Spark Opacity Determined Through BOTH Spectral Emission and Absorption

Laser Transmission



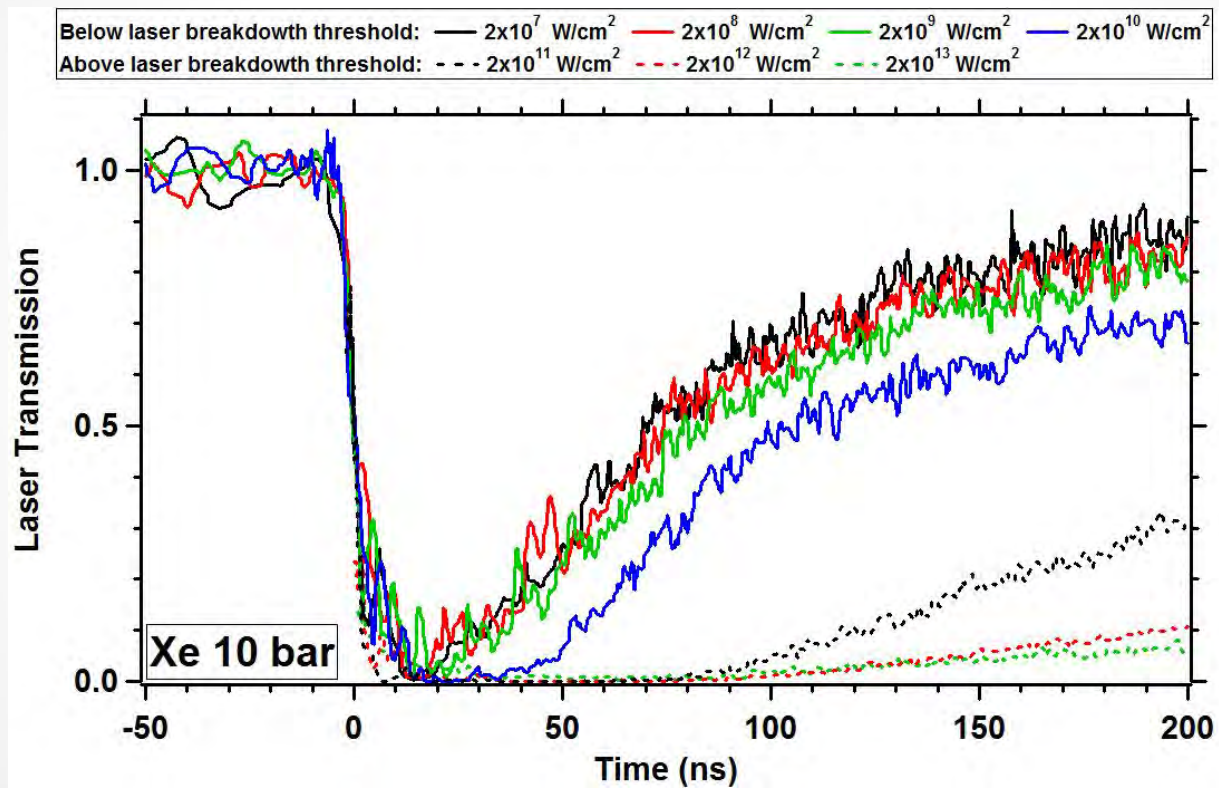
Blackbody Emission



A. Bataller, J. Koulakis, S. Pree, S. Putterman, *Appl. Phys. Lett.* **105**, 223501 (2014)

Sparking blocking laser over 6 orders of magnitude range

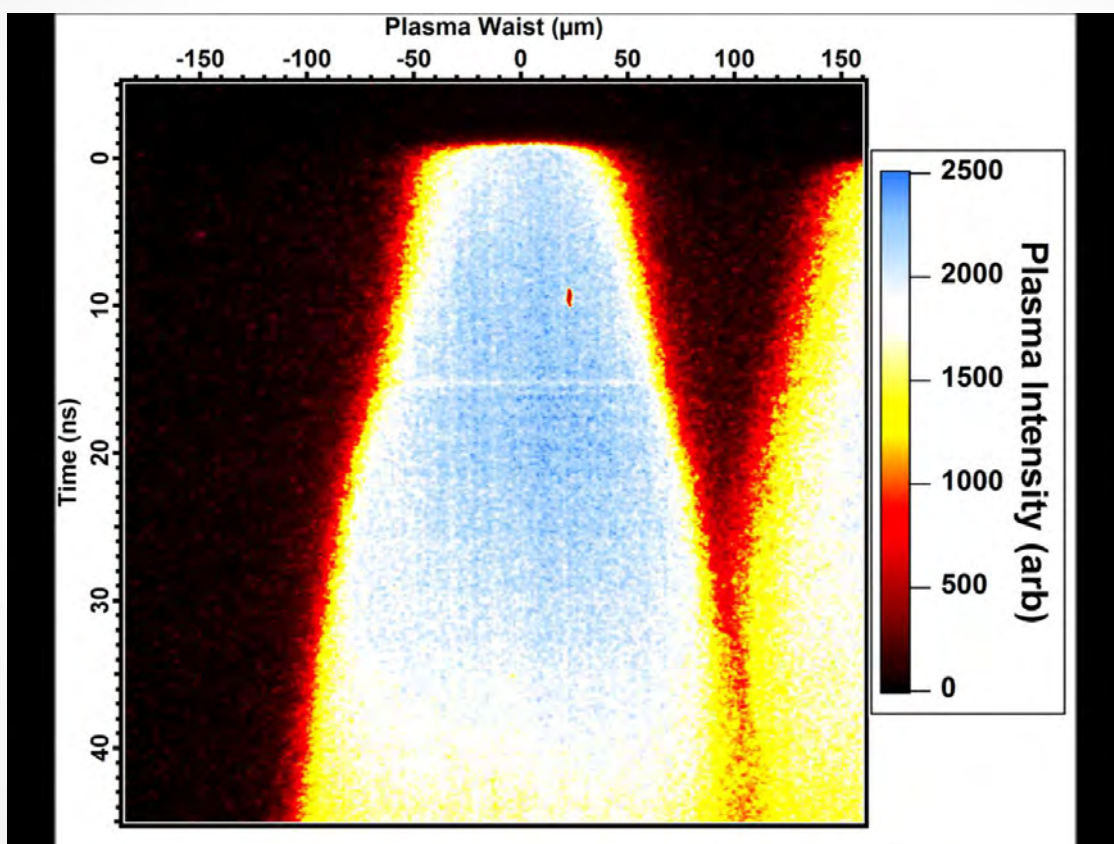
UCLA



With subns rise and micron edge

Demonstration of Spark Discharge Blocking Visible Light

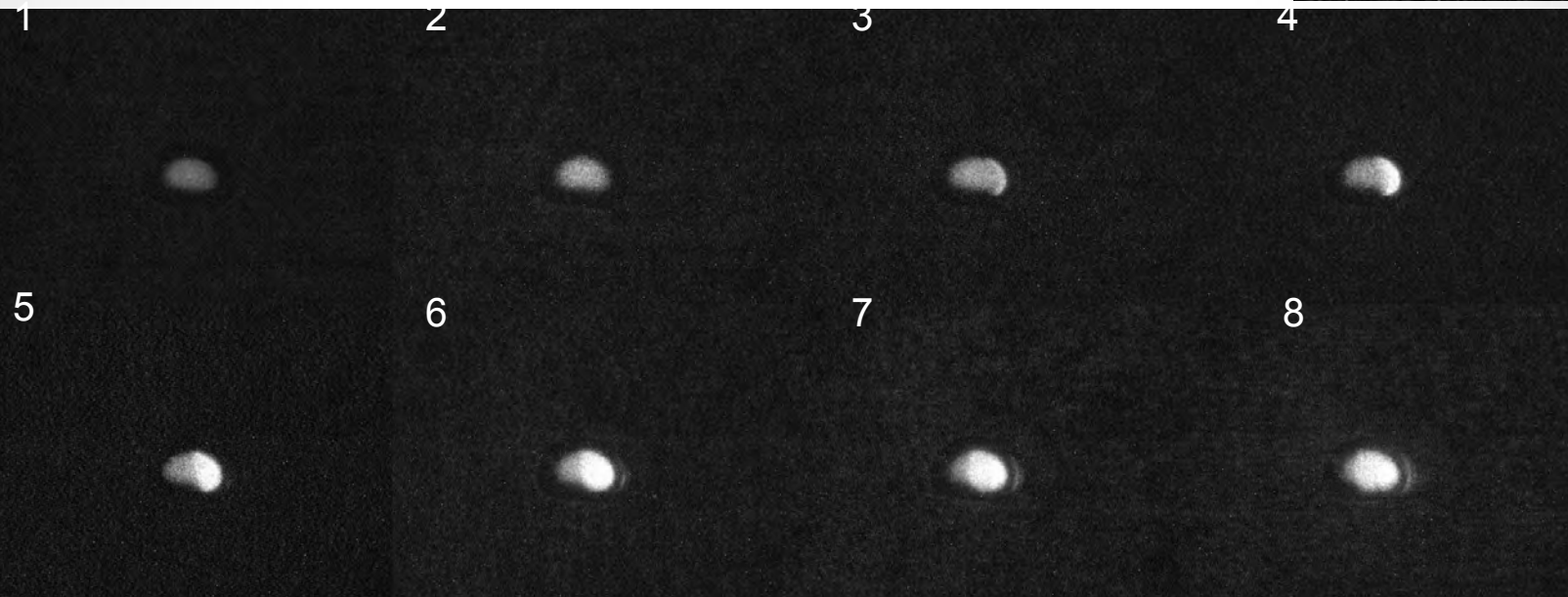
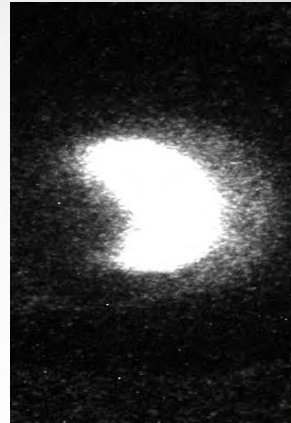
UCLA



Nanosecond Movies of Transport in a Dense Plasma

UCLA

Nanosecond framing camera reveals heat transport for a strong laser-Sonoluminescence interaction.



Frames from a movie of the propagation of an energy pulse across a dense plasma.
Free charge density = $10^{21}/\text{cc}$; diameter = $100.\mu\text{m}$; time between frames = 10ns.

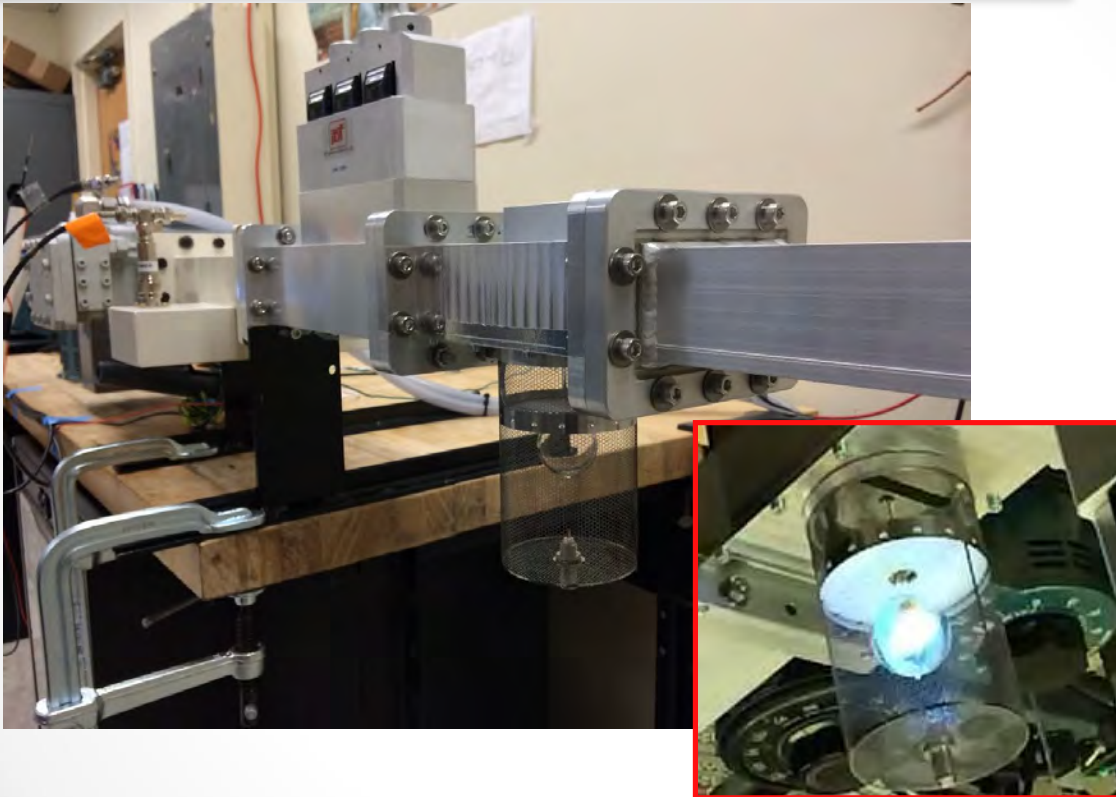
Prof. K. Weninger; Dr B. Kappus

Nature likes blackbodies, which means nature likes dense plasmas.

Goal –longtime confinement of a dense plasma with acoustics [Not B]

Additional payoff –plasma engines where acoustics keeps plasma off the walls.

UCLA



Direct acoustic probe of ion degrees of freedom of dense plasmas

Dense Plasma Seismology

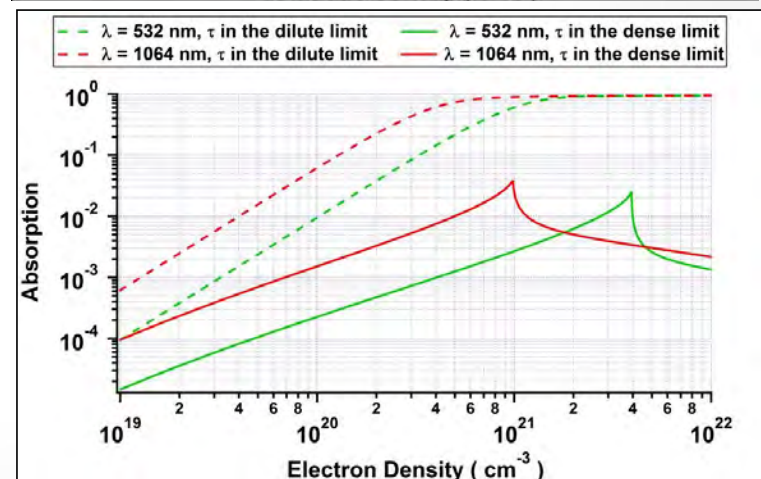
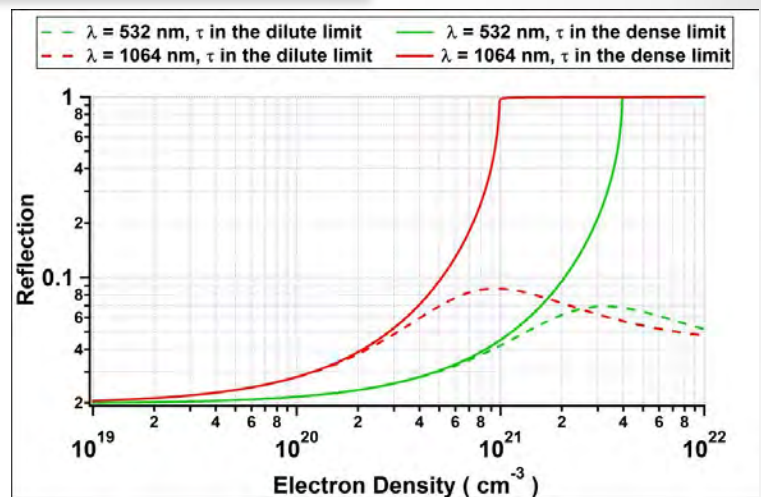
Theory of laser –dense plasma interaction:
although $\omega\tau_{\text{Dilute}} < 1$; $\omega\tau_{\text{Dense}} \gg 1$; $\Gamma \sim 3$

Closed from plasma dispersion law
incl Brem, inv. Brem, screening, ω_p , Γ , τ

UCLA

$$\frac{k^2 c^2}{\omega^2} = (1 - \gamma\beta) + \left(\gamma \frac{\beta}{\omega\tau} \right) i$$

$$\gamma = \frac{\omega_p^2}{\omega^2} \text{ and } \beta = \frac{\omega^2 \tau^2}{1 + \omega^2 \tau^2}$$



Plasma and Electroenergetics Annual Portfolio

Energy Flow in Dense Off-Equilibrium Plasmas



Submitted by Seth Putterman

December 19, 2014

UCLA

Equation of State and Transport Properties in a Dense Plasma

- We have demonstrated 3 different desktop labs for dense plasma science
- Kinetic theory of a dense plasma is easier than you think
- Ionization potential is dramatically lowered in a dense plasma
- Subnanosecond establishment of opacity in a dense plasma
- Transition to opacity occurs on micron length scale → **subns switch to block high power pulses!**
- Idea for a paradigm shifting 4th lab of warm dense plasma

Dense Plasma Lab "SL"

Concentrating a sound wave energy density by 12 orders: UCLA in a sperical geometry

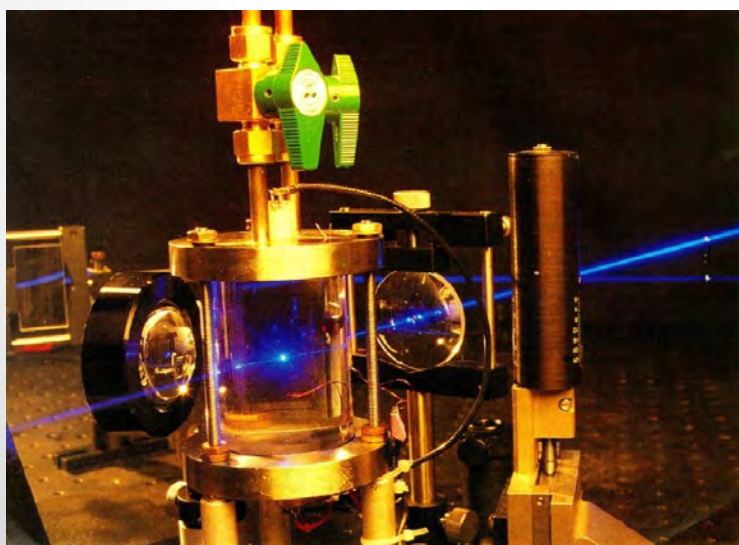
Background---

Sonoluminescence occurs from rapid collapse of oscillating gas bubble driven by an acoustic field.

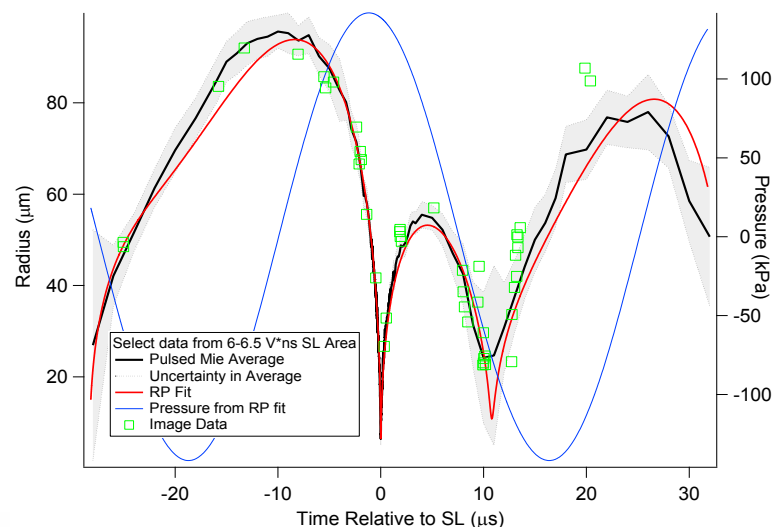
Adiabatic/shock--compression heats the gas during the collapse phase.

At maximum compression, energy density transforms gas into cold (\sim eV) dense ($>10^{21}$ cm $^{-3}$) plasma.

Light emission occurs due to thermal bremsstrahlung.

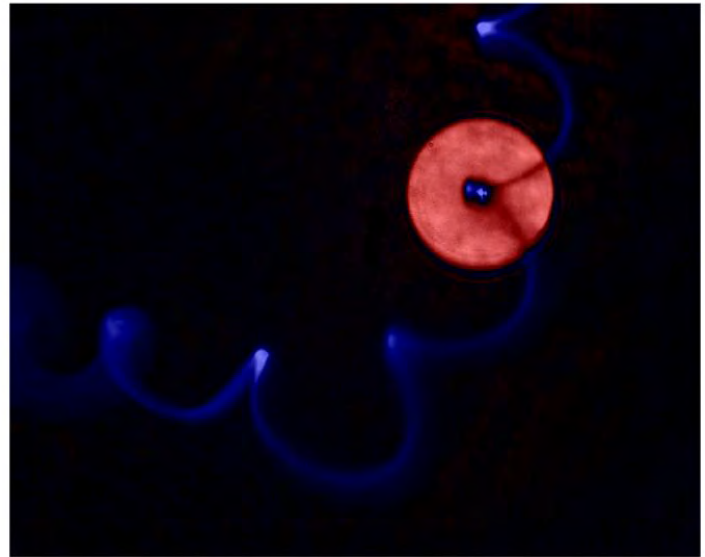
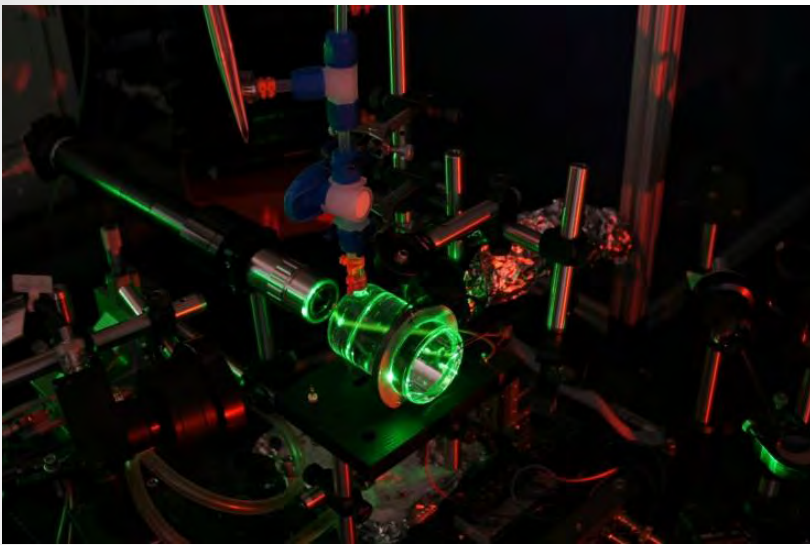


S. Putterman, Scientific American 272 (2) 46-51, 1995



B. Kappus et al., Phys. Rev. Lett., Accepted Nov. 6th 2013

Xenon Bubble in Sulfuric Acid Obeys Low UCLA Mach Number Hydrodynamics



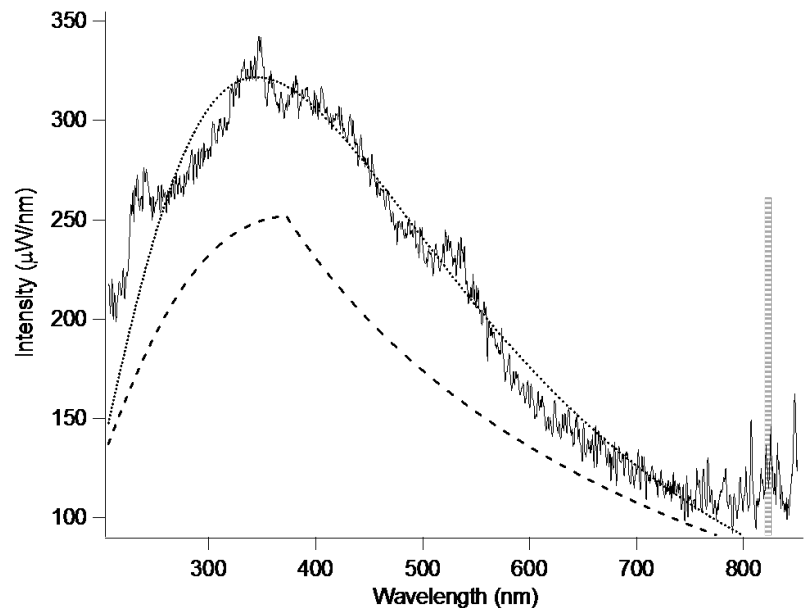
Xenon bubble in 85% sulfuric acid (low vapor pressure) was driven at 28.5 kHz.

Detailed Mie scattering provide complete characterization of hydrodynamics.

Blackbody spectrum emitted matches min UCLA radius, implying opacity is attained

Spectroscopy of 13 ns flash match ideal Planck blackbody (Mie radius matches blackbody emission radius)

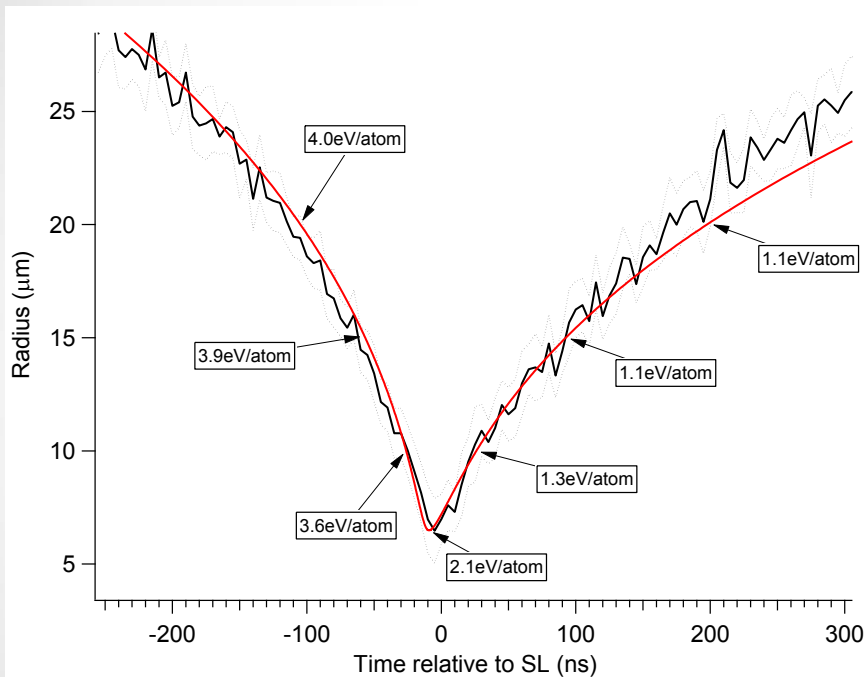
$\Rightarrow n_e > 4 \times 10^{20} \text{ cm}^{-3}$
required to satisfy opacity
($R_c = 6.5 \pm .9 \mu\text{m}$)



B. Kappus et al., Phys. Rev. Lett.,

Energy Balance Reveals That Ionization Potential is Lowered by > 80% in a Sonoluminescing Dense Plasma

UCLA



Analysis shows only 2.1 ± 0.6 eV/atom available at light emission: too low to explain >36% degree of ionization!

Collective processes reduce ionization potential by at least 80% (12.1 eV to 2.5 eV): highly-ionized plasma occurs during SL.

$$\frac{x^2}{1-x} = \frac{2g_1}{n_a \lambda^3} e^{-\chi_{\text{eff}}/kT}$$

$$\chi_{\text{eff}} = \chi_0 \left(1 - 2\gamma a_B n_a^{1/3} \right) - e^2 / 4\pi\epsilon_0 \delta_d$$

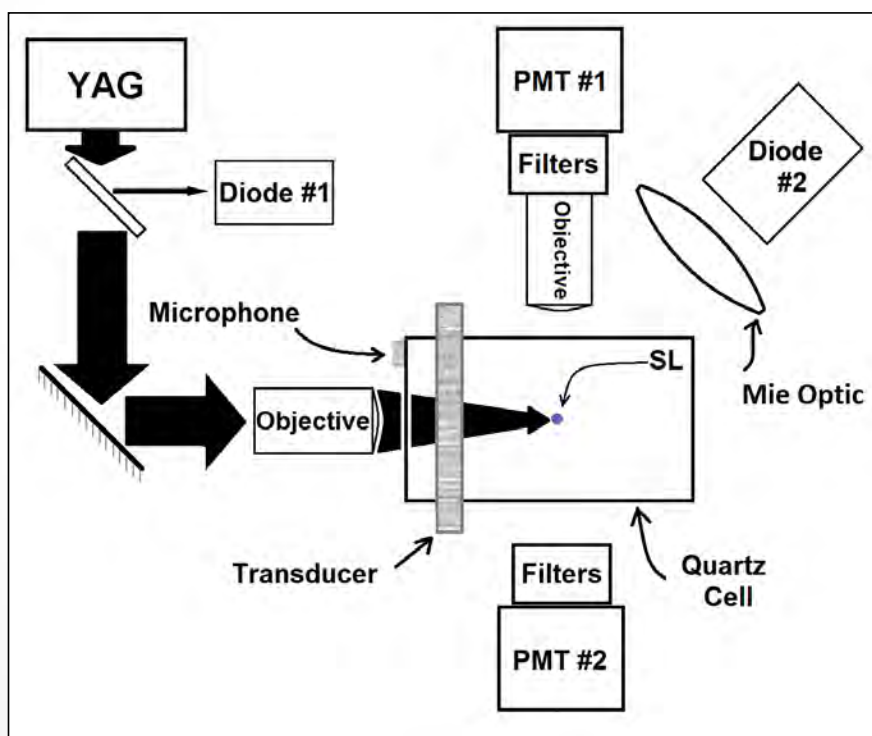
Model for Ionization potential lowering in a cold dense plasma

A complete equation of state also requires the pressure - - - - ->

Laser Probe of the Dense Plasma Inside a Sonoluminescing Bubble– 532nm and 1064nm

UCLA

The goal is to determine the collision time/kinetics of a dense plasma.

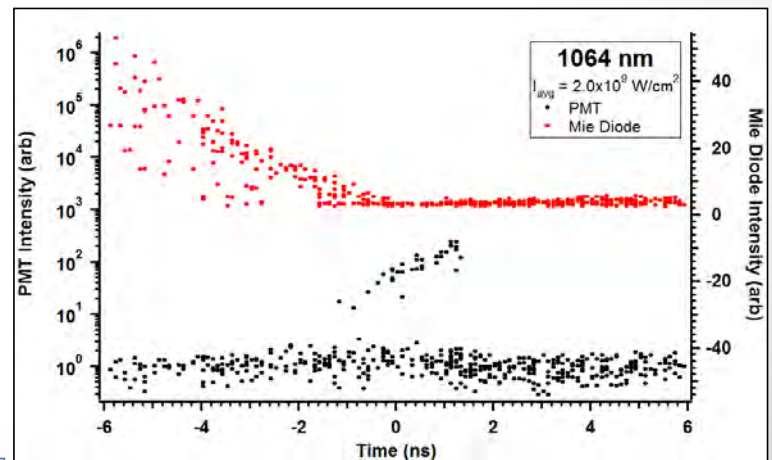
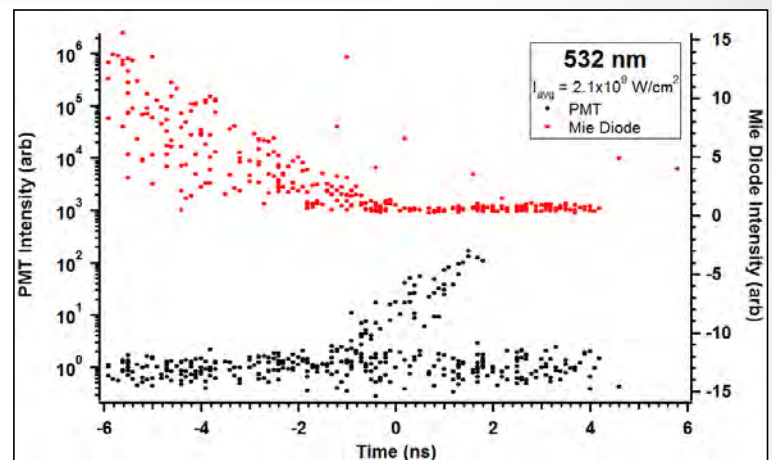


Interaction “gap” vs. wavelength

Measurement of both Mie scattering [red] and light emission [black] from a xenon gas bubble that implodes to about a one micron diameter where it forms a dense plasma, which corresponds to $t = 0$ in the bottom axis.

Our measurements find that 532nm always interacts with the plasma whereas for 1064nm there is a threshold for interaction.

This interaction “gap” can be ascribed to a large degree of reflection by 1064nm and a large absorption rate by 532 nm. This behavior occurs for plasma with low collisionality compared to the interacting light’s wavelength.



Bataller - Kappus

Collision Time in a Dense Microplasma

UCLA Strong Screening

$$\ln \Lambda = 2\sqrt{3} \ln \left(\sqrt{\frac{1}{6} \Gamma_{\omega}^{-3} + 1} \right)$$

Daligault-Weak Screening

$$\ln \Lambda = 2\sqrt{3} \ln \left(\frac{0.7}{\sqrt{6}} \Gamma_{\omega}^{-3/2} + 1 \right),$$

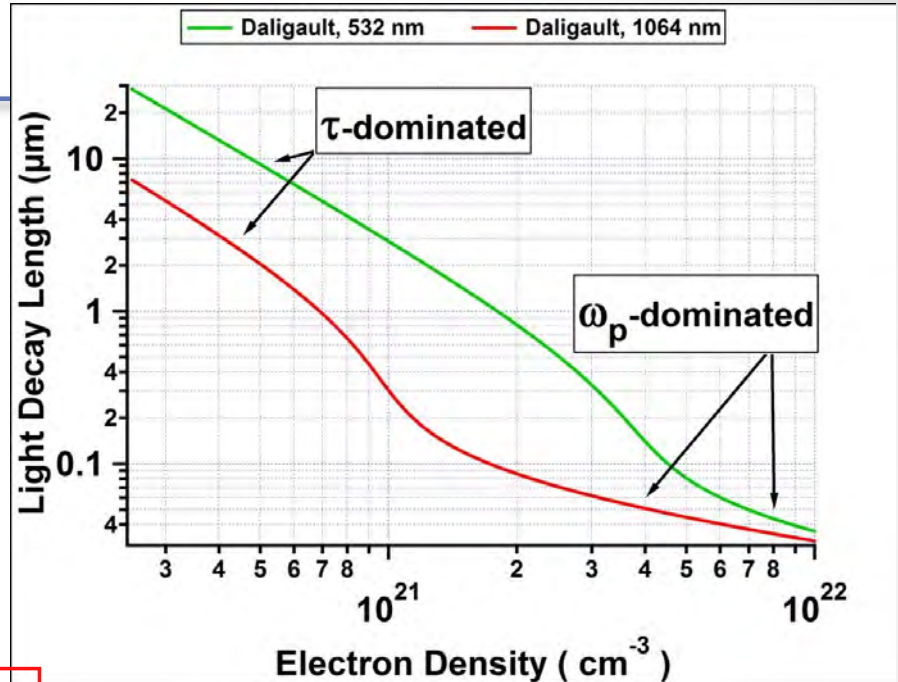
Dilute Plasma Theory

$$\ln \Lambda = 2\sqrt{3},$$

$$\tau = \frac{16\pi^2 \epsilon_0^2 \hbar \omega}{n_e e^4 [1 - e^{-\beta \hbar \omega}]} \frac{3}{2} \sqrt{\frac{3mkT}{2\pi}} \frac{1}{\ln \Lambda}$$

$$\Gamma_{\omega} = \frac{e^2}{\epsilon_0} \left(\frac{1 - e^{-\beta \hbar \omega}}{\hbar \omega} \right) \left(\frac{n_e}{3(4\pi)^2} \right)^{1/3}$$

Theory of dilute plasma is way off when applied to dense microplasmas



Plasma Coupling Parameter is $\Gamma \sim 5$

$$\frac{k^2 c^2}{\omega^2} = (1 - \gamma \beta) + \left(\gamma \frac{\beta}{\omega \tau} \right) i$$

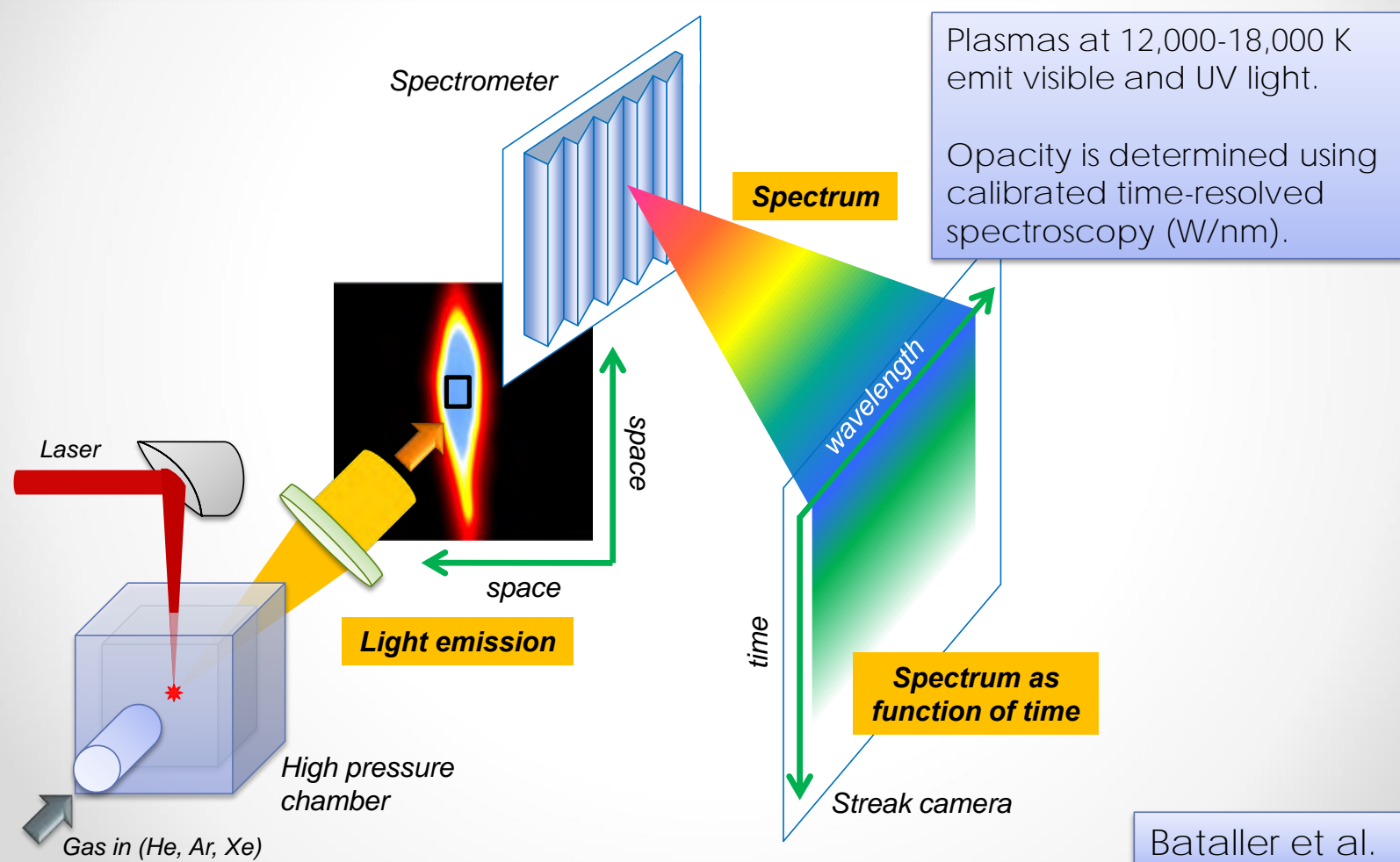
$$\gamma = \frac{\omega_p^2}{\omega^2} \text{ and } \beta = \frac{\omega^2 \tau^2}{1 + \omega^2 \tau^2}$$

Closed form Dense Plasma Dispersion Law

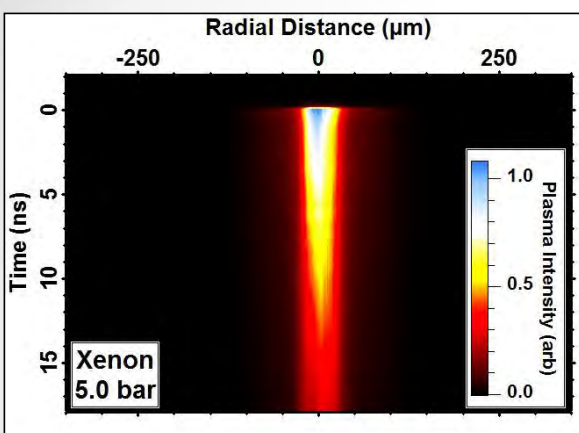
Dense Plasma Lab via Laser Breakdown Achieved Via Use of High Pressure Gases that Match Atomic Density in SL Bubble

UCLA

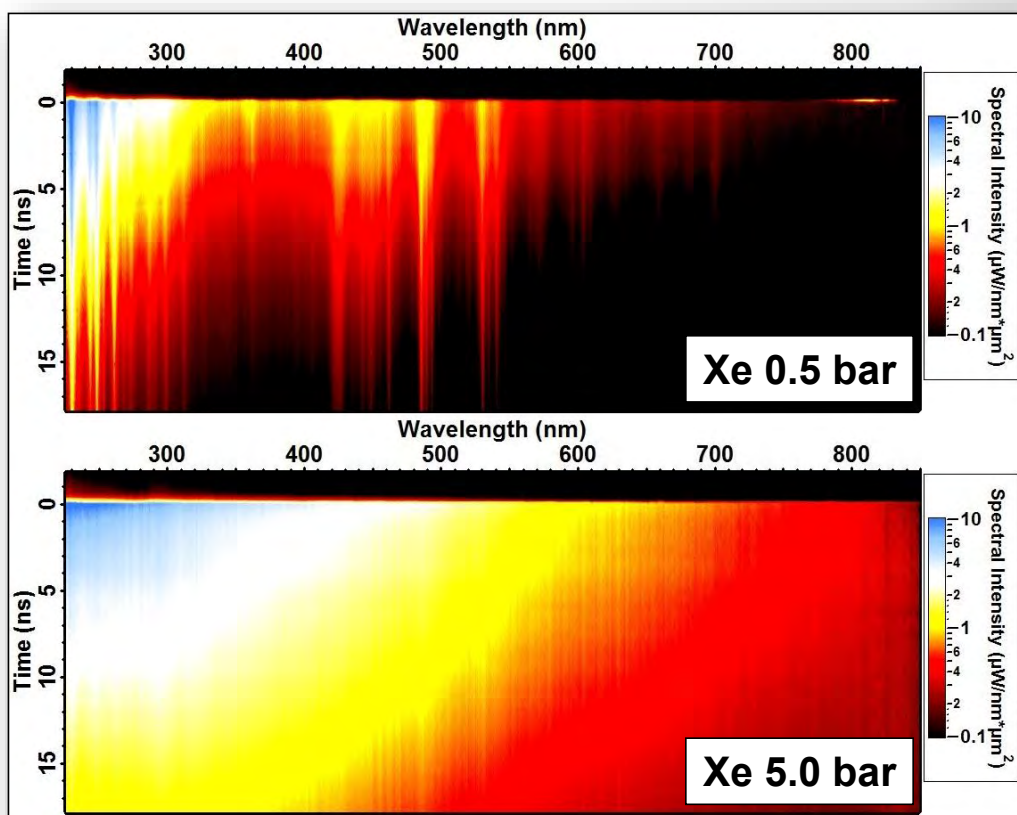
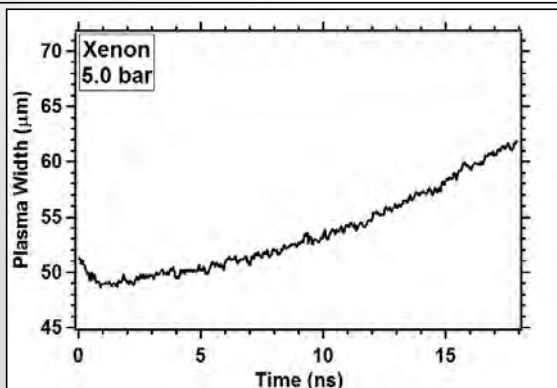
Bubble



UCLA Sonoluminescence blackbodies reproduced in Ar, Xe, and He !



Radial slice of breakdown as a function of time

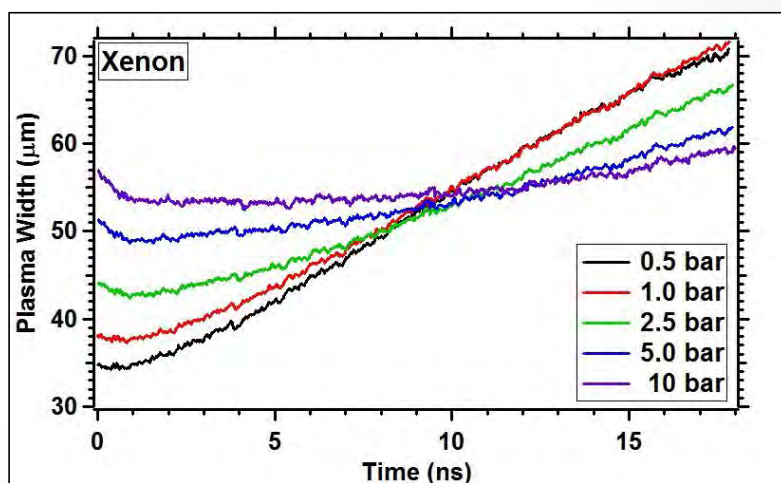
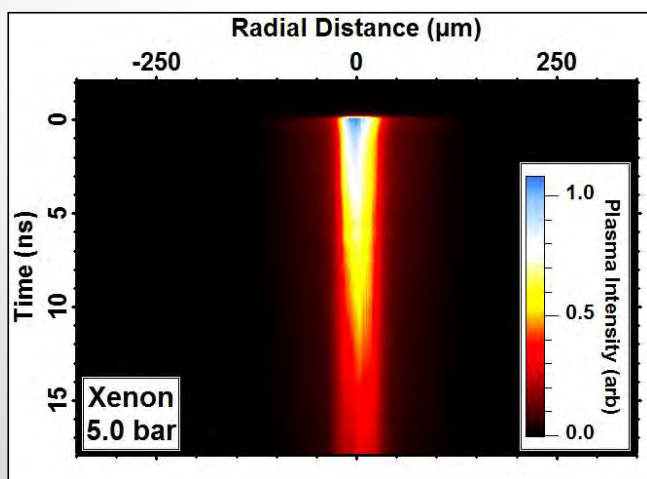
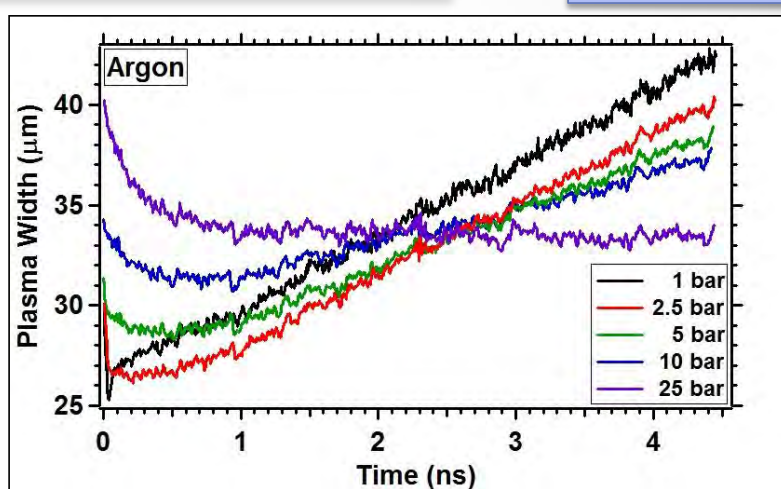
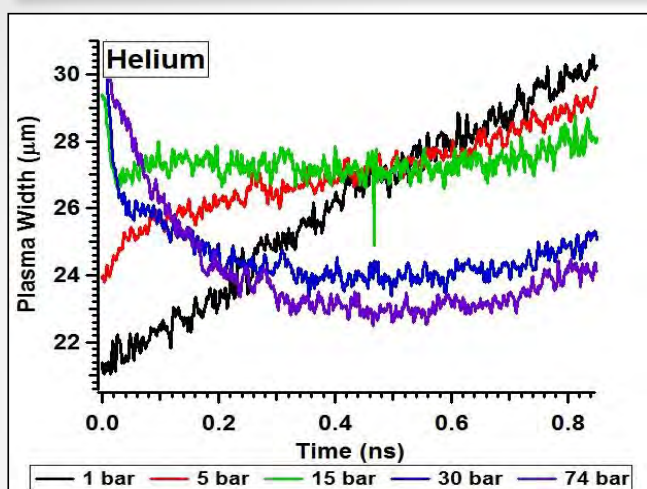


Spectrum transitions to blackbody emission at elevated pressures

Does Plasma Contraction at Short Times Imply that a Cold Dense Plasma acts like it has a Tensile Strength

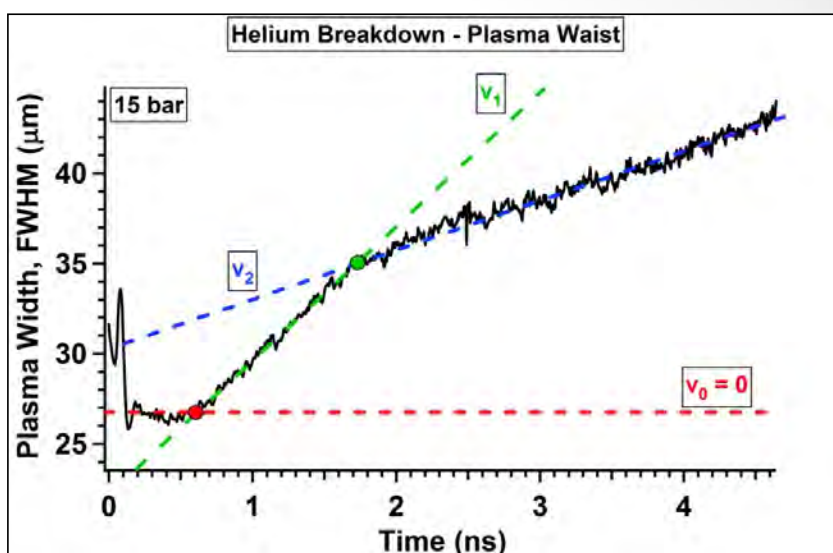
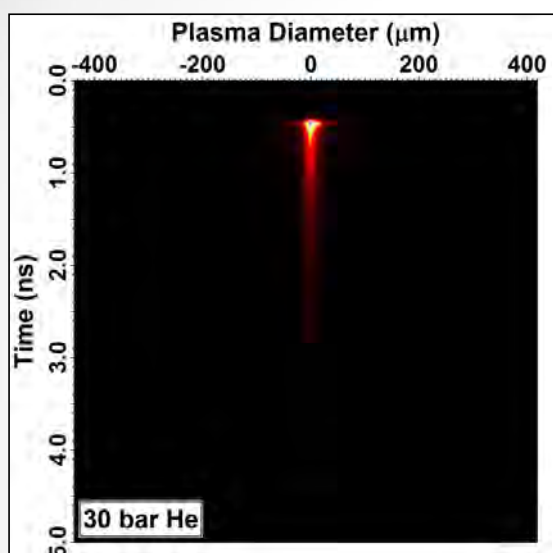
UCLA

Bataller et al.



Comparison of Plasma Sound Velocity to Plasma Expansion Velocity

UCLA



Helium			Linear Fit	Linear Fit
Pressure (bar)	t_{flat} (ns)	t_2 (ns)	v_1 (km/s)	v_2 (km/s)
1	< 0.05	~1.75	12.78 ± 0.07	3.07 ± 0.02
5	0.095	~1.75	7.58 ± 0.06	3.45 ± 0.05
15	0.85	~1.75	7.39 ± 0.06	2.57 ± 0.02
30	0.85	~1.75	5.75 ± 0.05	2.14 ± 0.02
40	0.85	~1.75	6.76 ± 0.05	2.19 ± 0.02

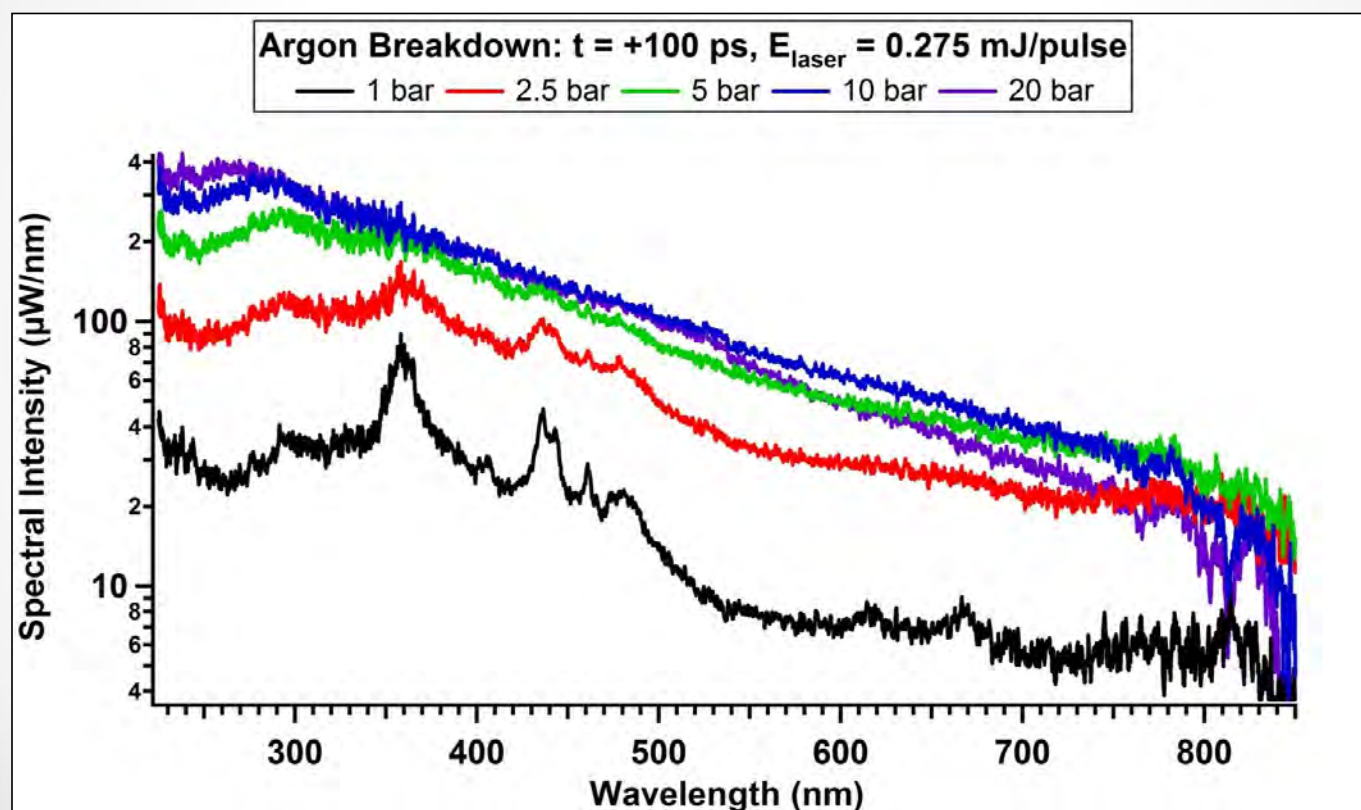
$$c_s = \sqrt{\frac{ZkT_e + 3kT_i}{m_i}}$$

For helium at $T = 11,000$ K, $Z = 1$, and $T_i \ll T_e$,

$$c_s = 4,780 \text{ m/s}$$

Dense Plasma Formation Under Pressure

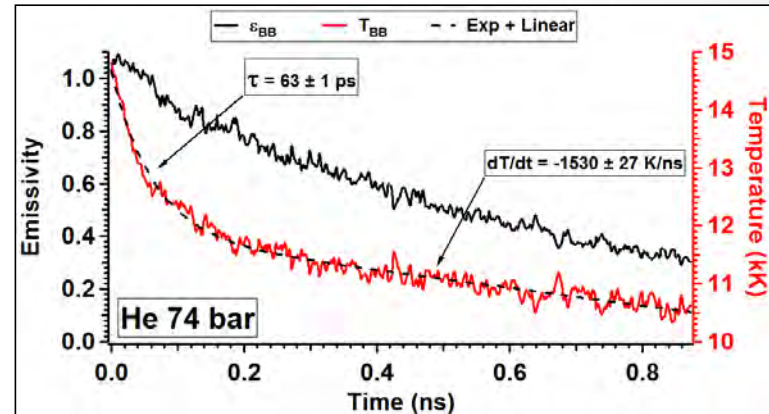
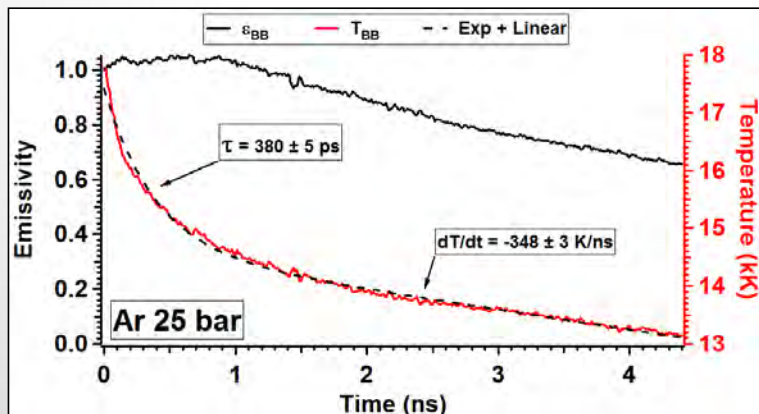
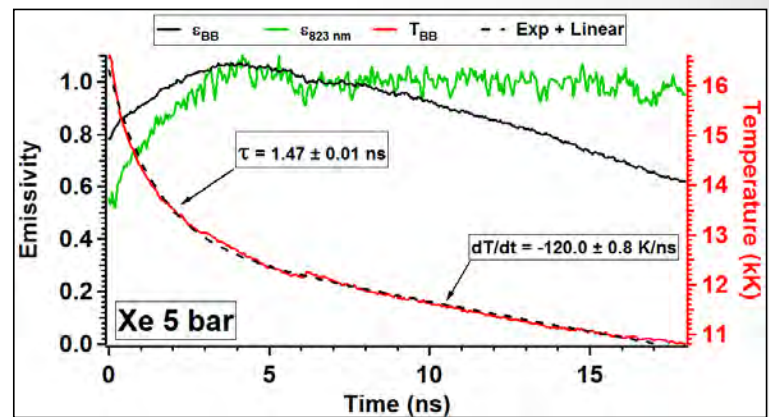
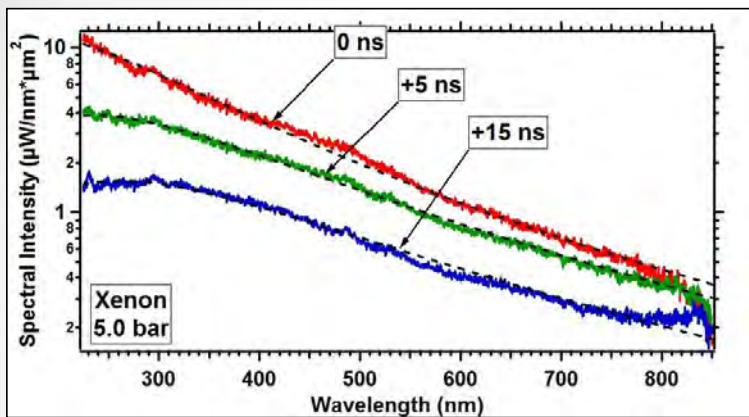
UCLA



Plasma Temperature Evolution

UCLA

12,000 – 18,000K
Blackbody fits



Ionization Required for Opacity

Opacity at 400 nm

- For measurements made, opacity condition governed by R_{BB}/ℓ_ν
- Bremsstrahlung is the dominant source of broadband emission/absorption in high density plasma.
- ℓ_ν is modified by high density effects (G. Dimonte and J. Daligault, Phys. Rev. Lett. **101**, 135001 (2008)).

	Helium	Argon	Xenon
t (ns)	+0.1	+1	+5
R (μm)	26	34	50
T (K)	12,550	14,550	12,350
n _a (cm ⁻³)	1.85x10 ²¹	6.3x10 ²⁰	1.25x10 ²⁰
Z	>0.38	>1.0	>3.2
n _e (cm ⁻³)	>7.0x10²⁰	>6.3x10²⁰	>4.0x10²⁰
Γ	>1.9	>1.6	>3.6

Thermalization Timescale Measured

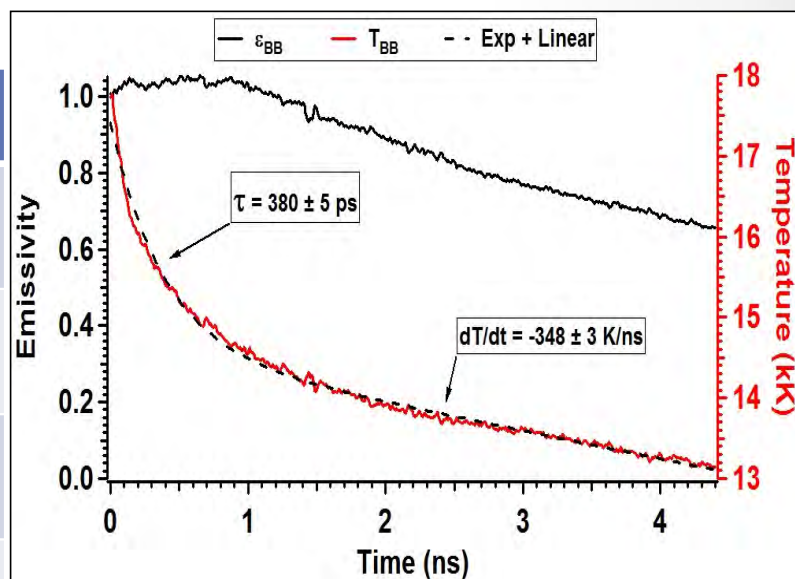
UCLA

- Thermalization time measured

$$\tau_{th} \approx \frac{M}{m} \tau_{e-i}$$
- τ_{e-i} is calculated using temperature and ionization with dense plasma theory (G. Dimonte and J. Daligault, Phys. Rev. Lett. **101**, 135001 (2008) *screened collisions*)

SELF-CONSISTENT VALIDATION OF TRANSPORT THEORY AND PROVIDES COLLISION TIME MEASUREMENT FOR A STRONGLY COUPLED PLASMA

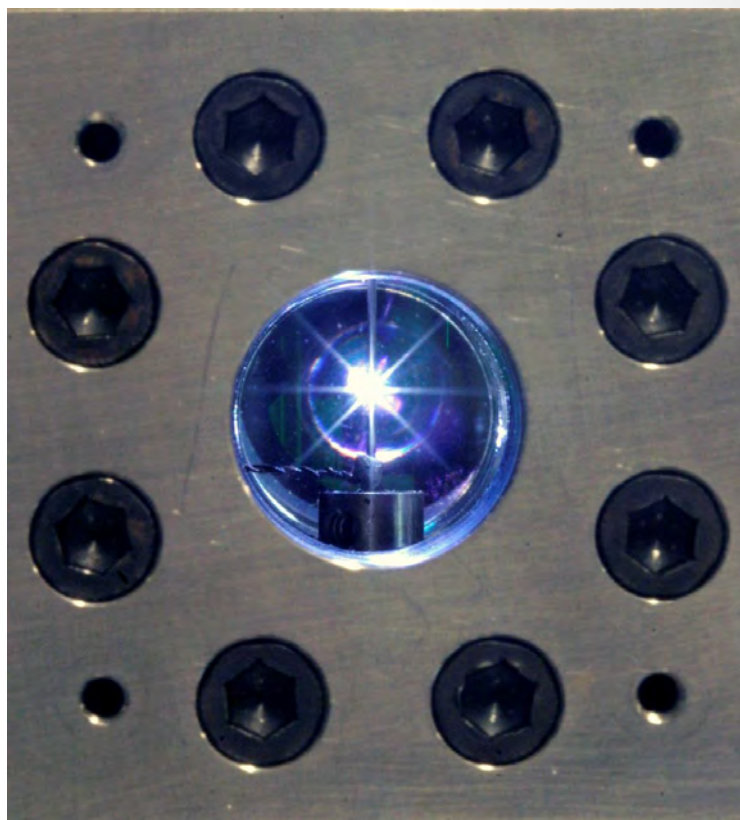
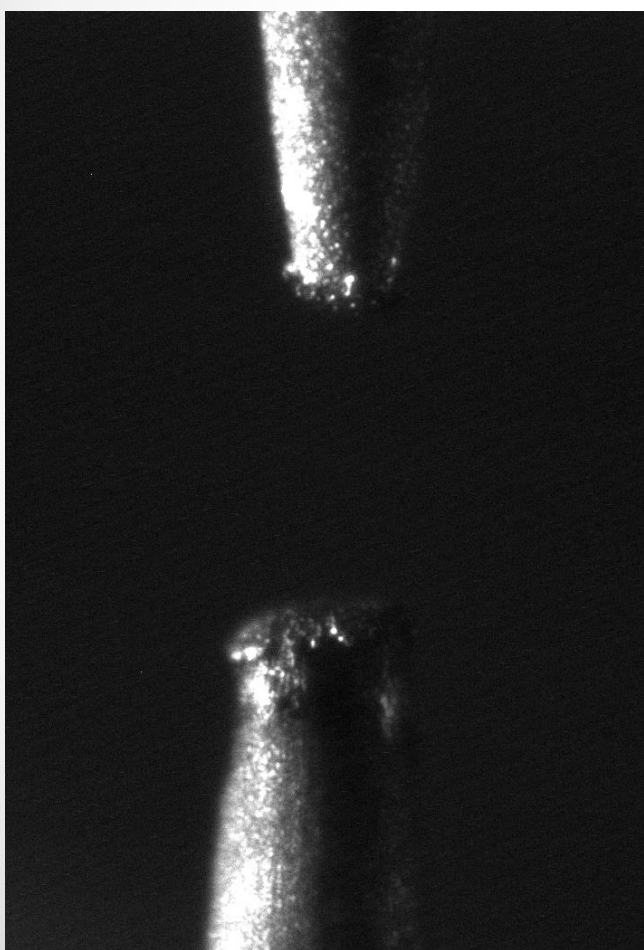
	Helium	Argon	Xenon
τ_{th} (meas.)	63 ps	380 ps	1.47 ns
τ_{th} (calc.)	37 ps	305 ps	1.17 ns
Mass Ratio	0.10	1.0	3.3
$\frac{\tau_{th}}{\tau_{e-i}}$	0.13	1.0	3.3



Ar 25 bar

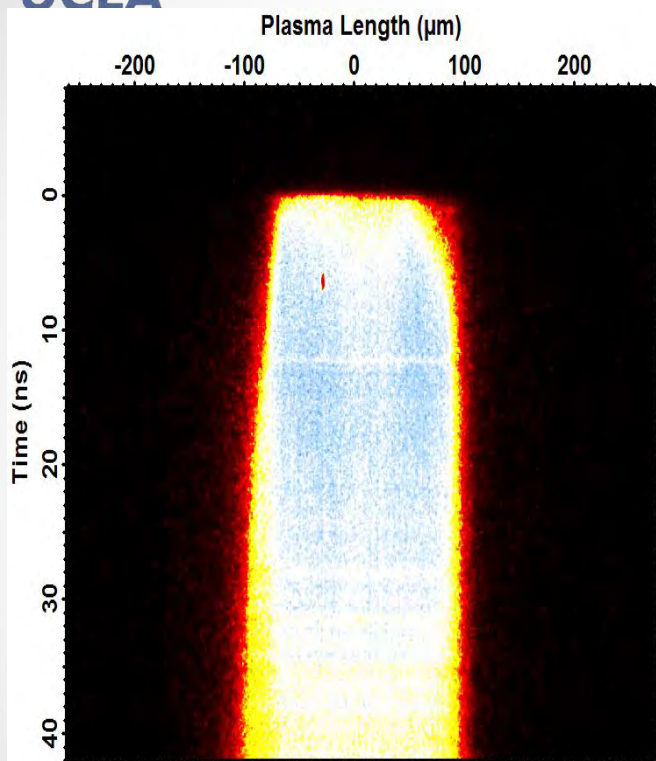
UCLA

Spark Discharges in a Dense Gas are also a – [New Ancient] Platform for Dense Plasmas

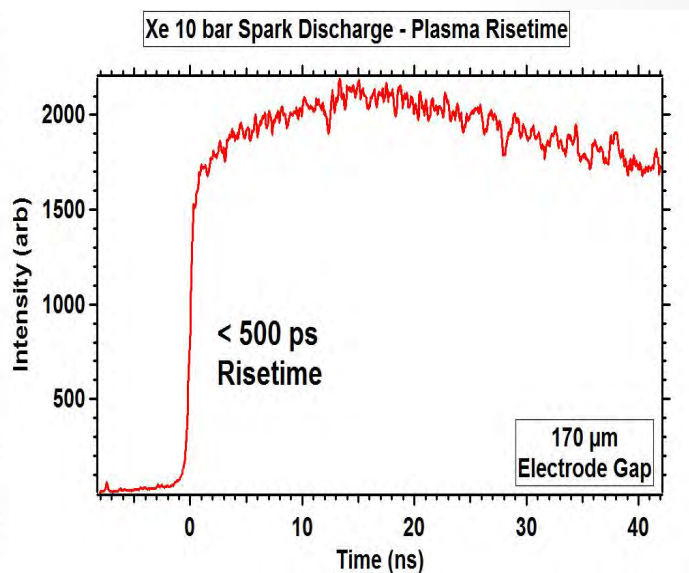


Sub-ns Homogeneous Arc Discharge Formation

UCLA



Xe 10 bar Spark Discharge - Across Electrodes

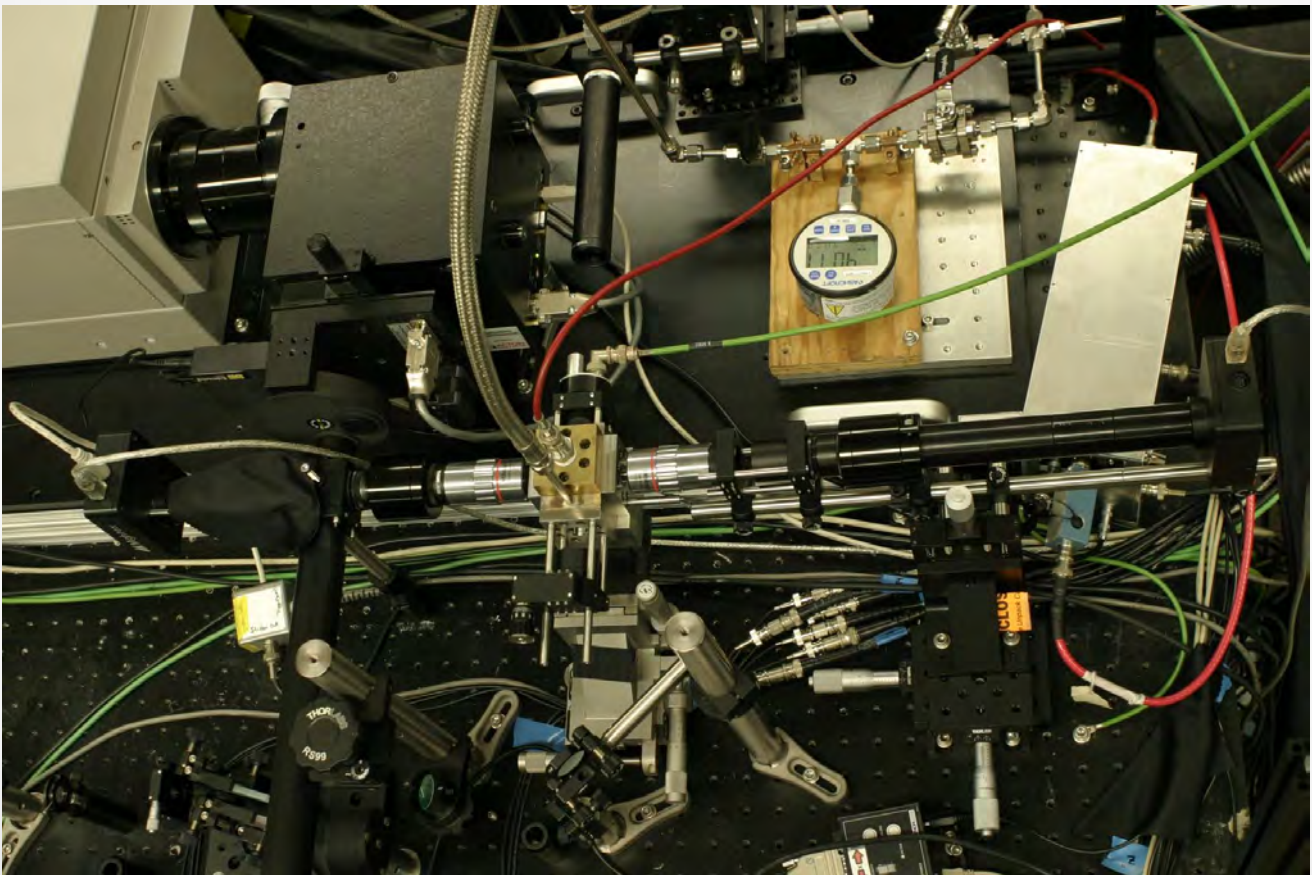


Ongoing measurements indicate that this is a very fast process as all measurements so far are instrument limited

Flat-top in intensity indicates that blackbody formation is 'immediate'

UCLA

Going Forward: Transport Measurements of Dense Spark Plasmas Using Fast Diagnostics



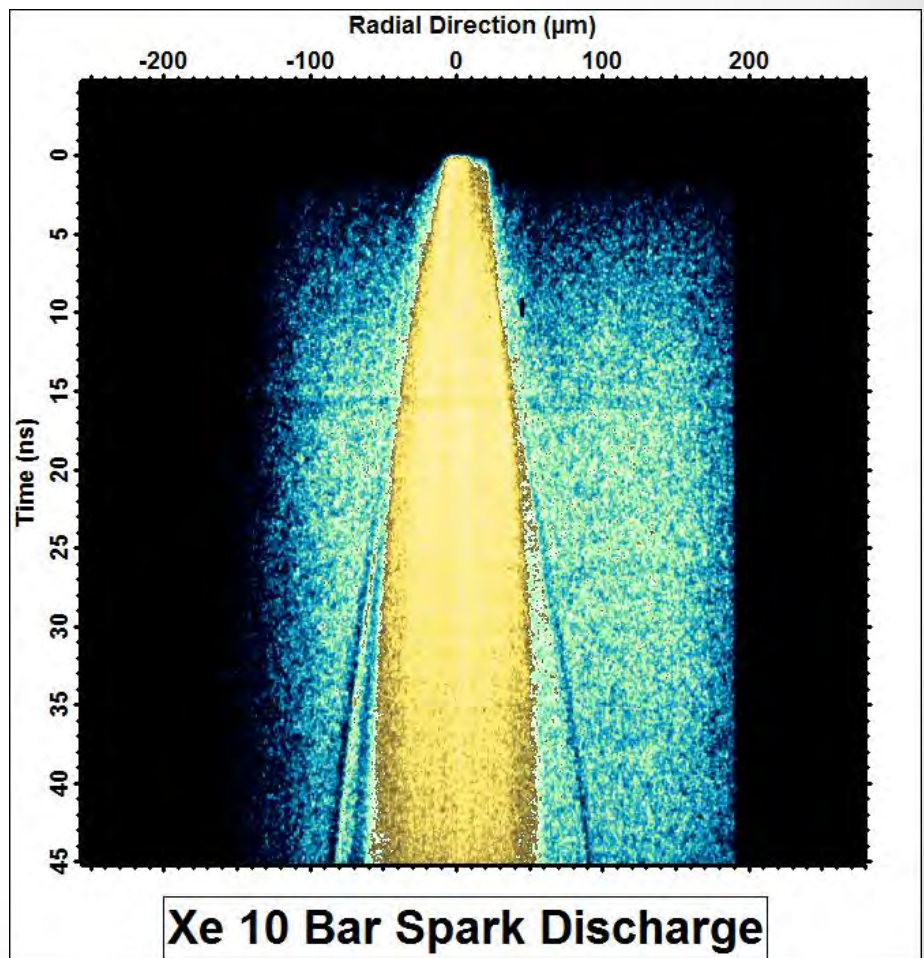
Battaller – Koulakis - Pree

Speed of Sound Measurements and Equation of State

UCLA

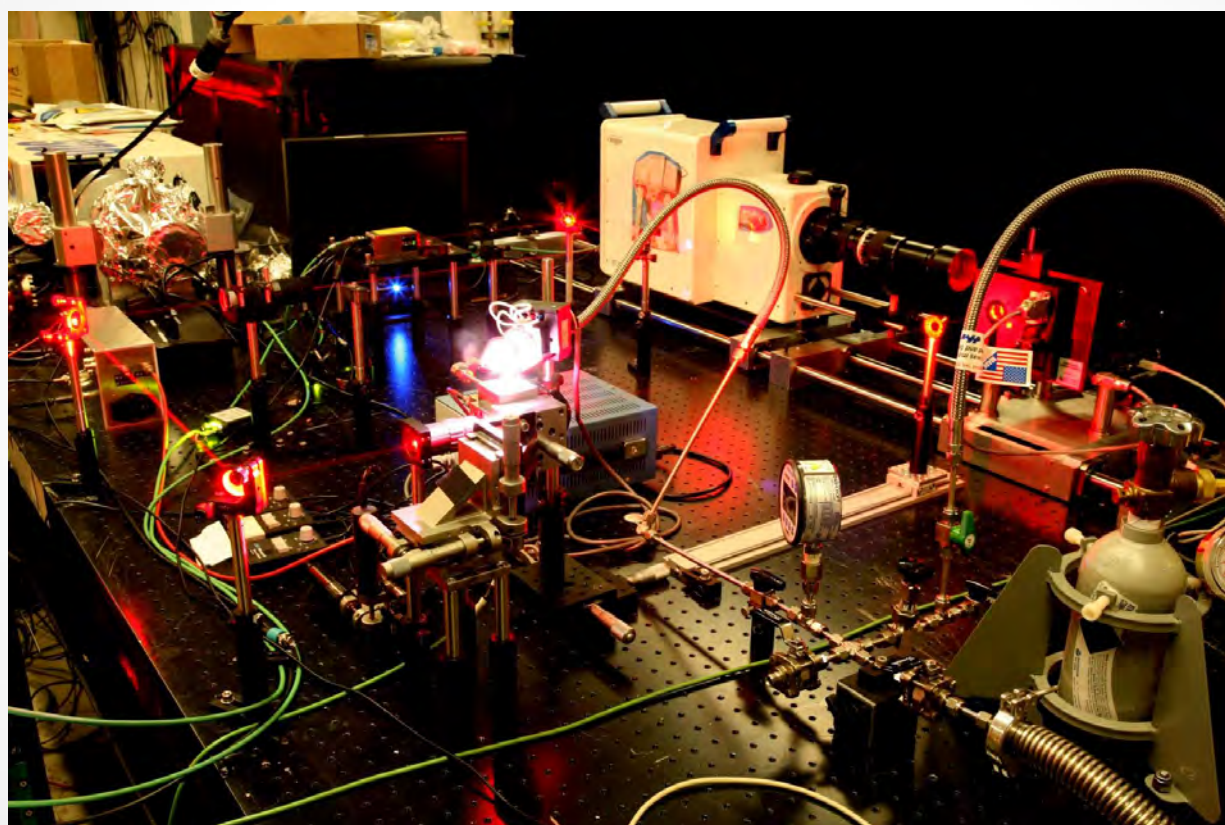
- Time-resolved shadowgraph of spark discharges test blast wave theory for dense plasmas.
- Femtosecond laser-plasma interactions can act as an acoustic probe –
“Spark Seismology”=missing part of dense plasma eq state

Battaller – Koulakis - Pree



UCLA

Nanosecond UV Framing Camera for Diagnosing Transport in Dense Plasmas



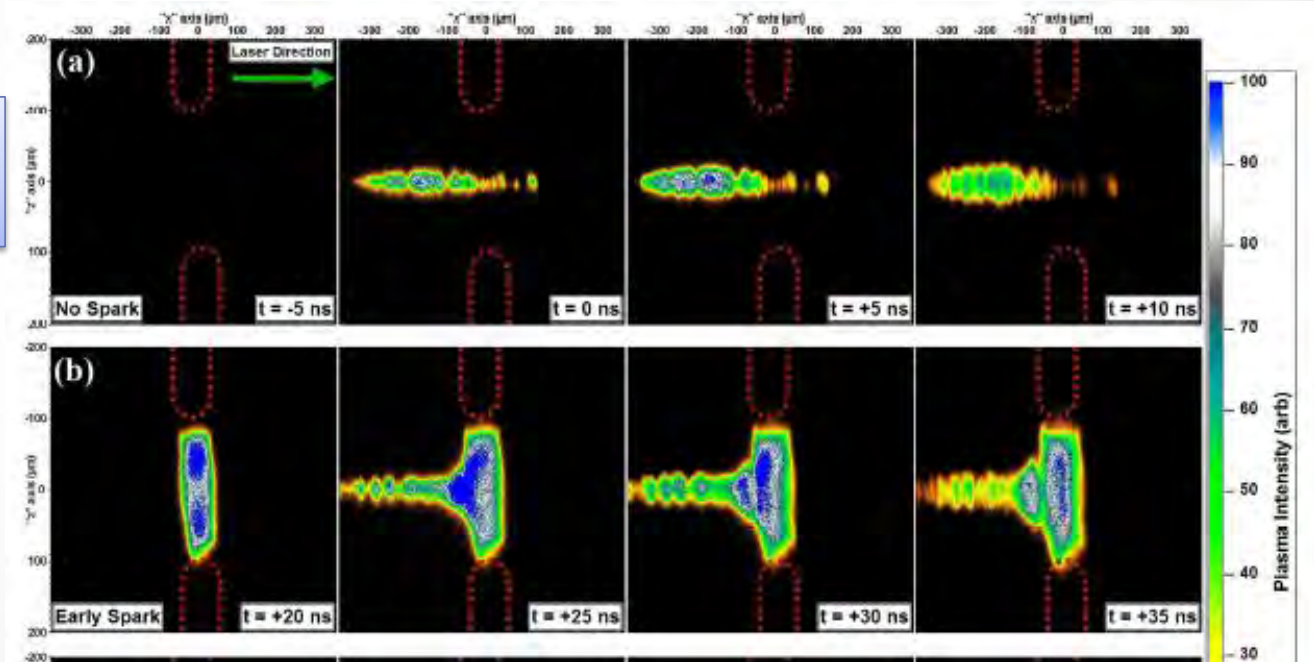
Bataller – Koulakis - Pree

Not Just a Pretty Plasma: Deterrence of High-Intensity Laser Pulses

UCLA

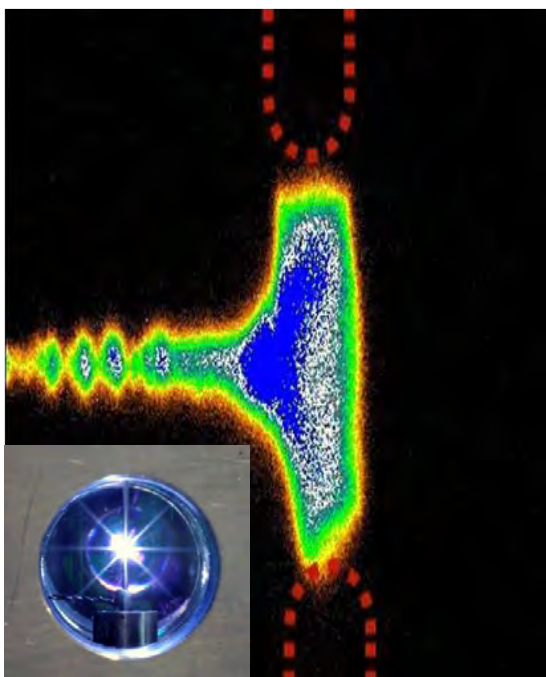
Practically limitless power handling capability. The switch cannot be broken as it is already the broken state of matter!

No spark protection



Spark activated

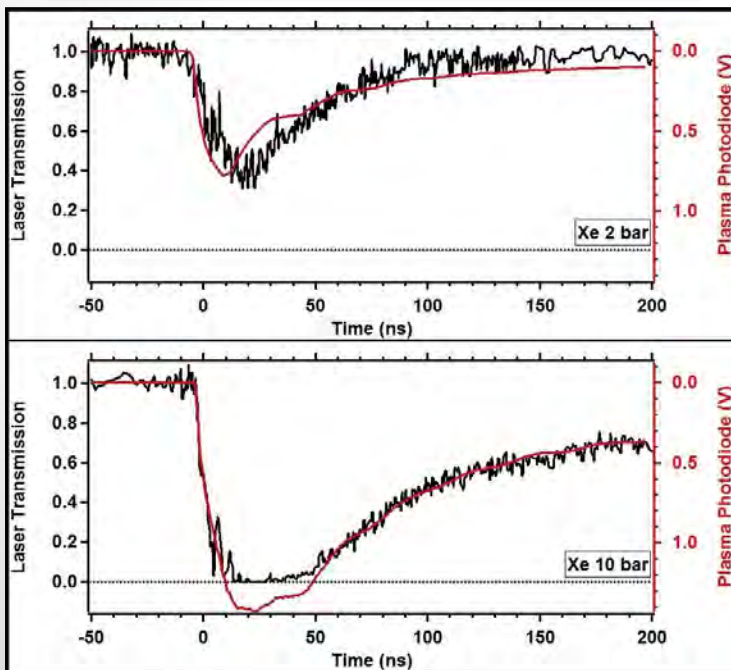
A. Bataller, J. Koulakis, S. Pree, S. Putterman, *Appl. Phys. Lett.* **105**, 223501 (2014)



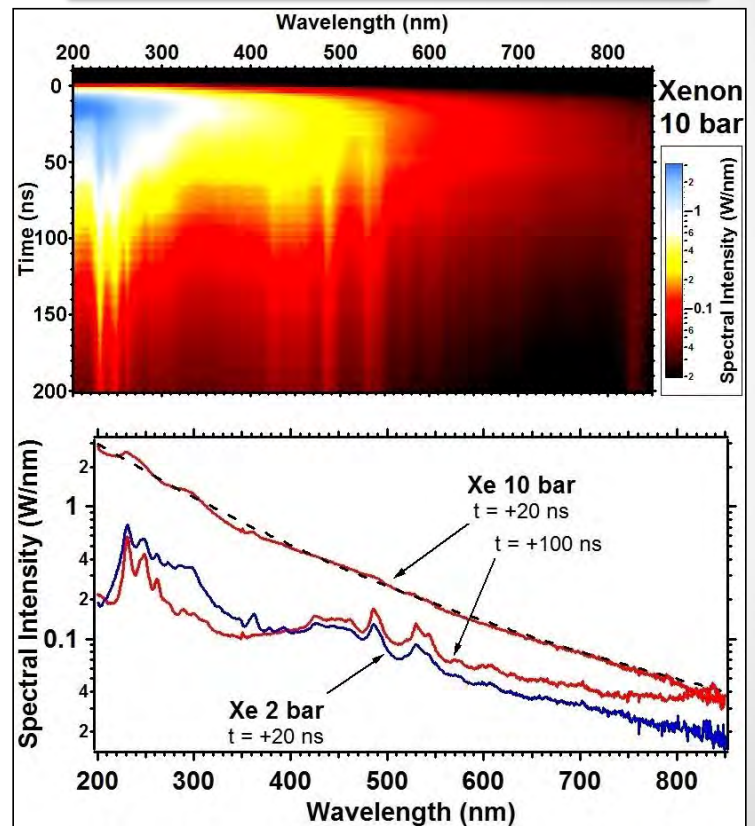
UCLA

Spark Opacity Determined Through BOTH Spectral Emission and Absorption

Laser Transmission



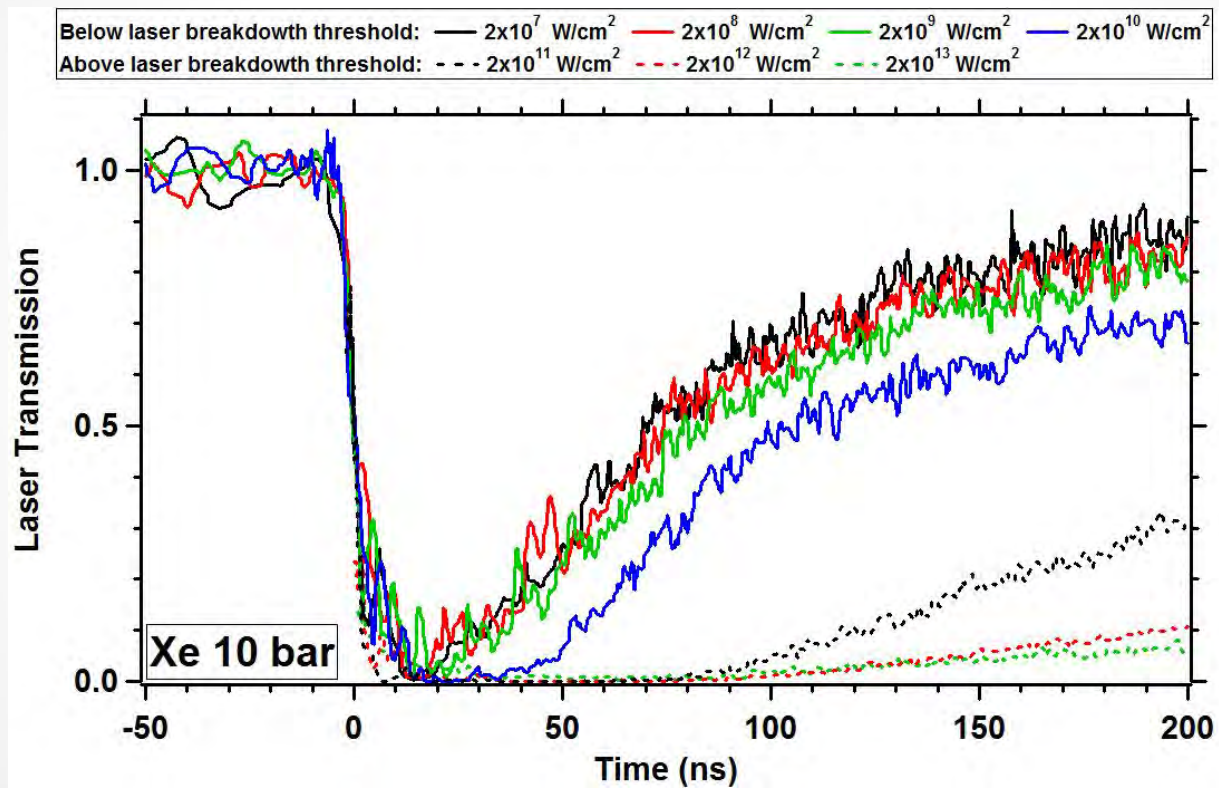
Blackbody Emission



A. Bataller, J. Koulakis, S. Pree, S. Putterman, *Appl. Phys. Lett.* **105**, 223501 (2014)

Sparking blocking laser over 6 orders of magnitude range

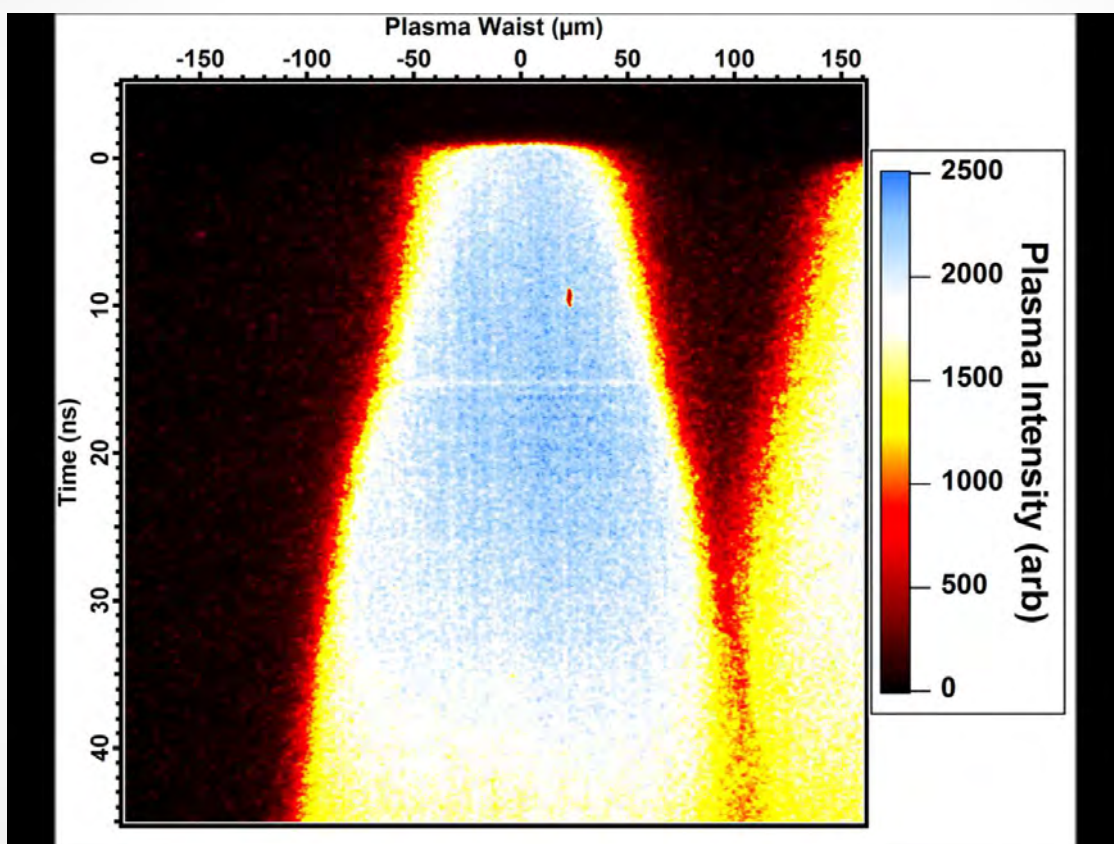
UCLA



With subns rise and micron edge

Demonstration of Spark Discharge Blocking Visible Light

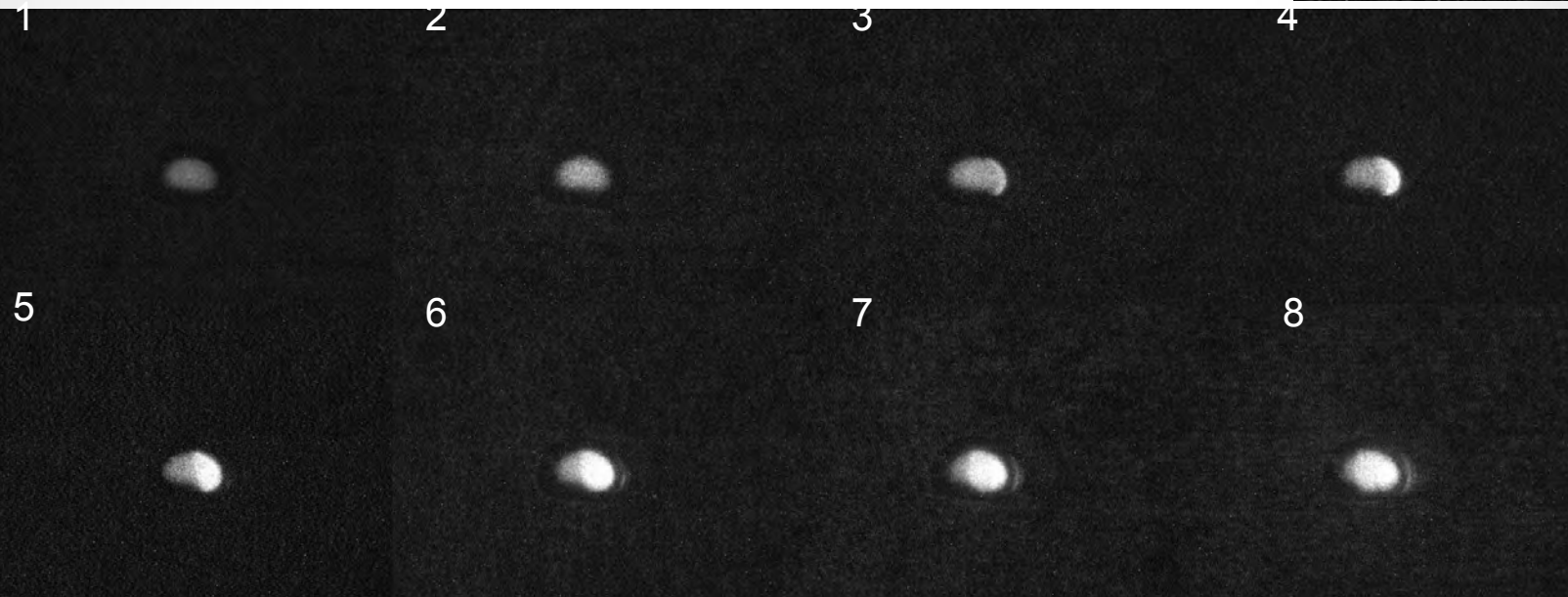
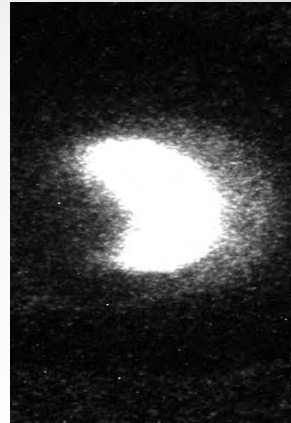
UCLA



Nanosecond Movies of Transport in a Dense Plasma

UCLA

Nanosecond framing camera reveals heat transport for a strong laser-Sonoluminescence interaction.



Frames from a movie of the propagation of an energy pulse across a dense plasma.
Free charge density = $10^{21}/\text{cc}$; diameter = $100.\mu\text{m}$; time between frames = 10ns.

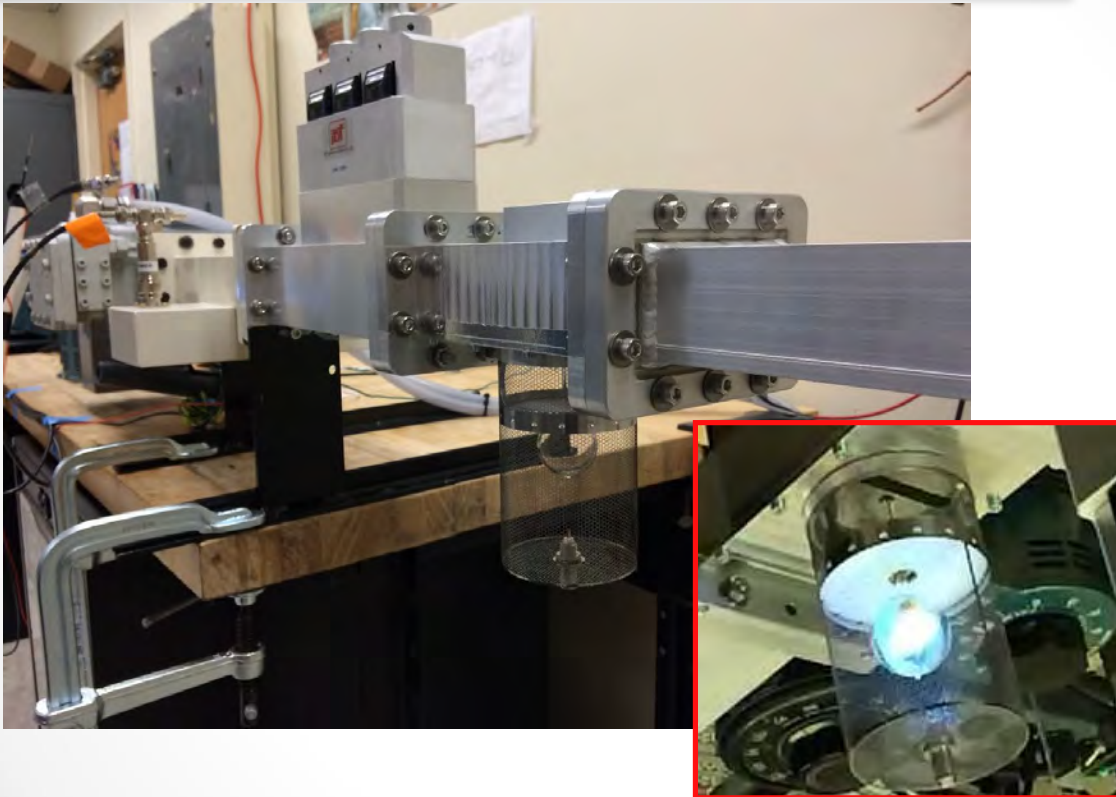
Prof. K. Weninger; Dr B. Kappus

Nature likes blackbodies, which means nature likes dense plasmas.

Goal –longtime confinement of a dense plasma with acoustics [Not B]

Additional payoff –plasma engines where acoustics keeps plasma off the walls.

UCLA



Direct acoustic probe of ion degrees of freedom of dense plasmas

Dense Plasma Seismology

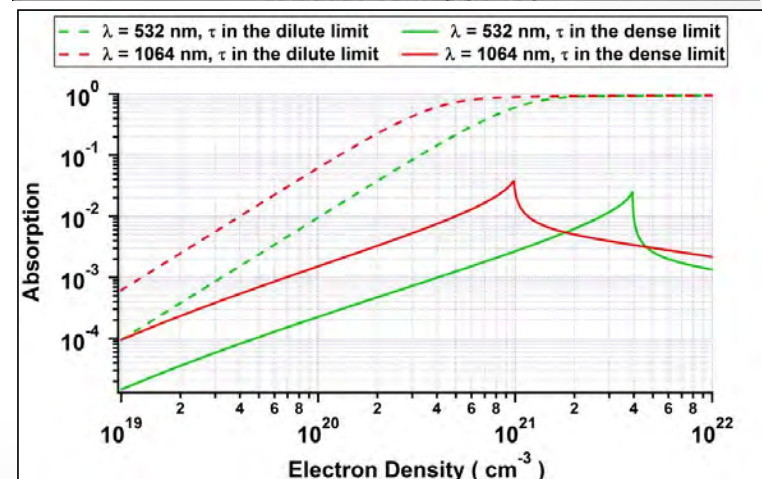
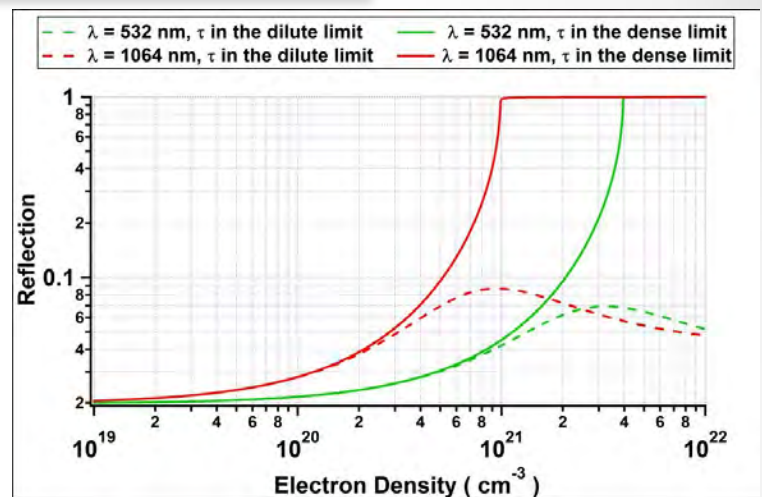
Theory of laser –dense plasma interaction:
although $\omega\tau_{\text{Dilute}} < 1$; $\omega\tau_{\text{Dense}} \gg 1$; $\Gamma \sim 3$

Closed from plasma dispersion law
incl Brem, inv. Brem, screening, ω_p , Γ , τ

UCLA

$$\frac{k^2 c^2}{\omega^2} = (1 - \gamma\beta) + \left(\gamma \frac{\beta}{\omega\tau} \right) i$$

$$\gamma = \frac{\omega_p^2}{\omega^2} \text{ and } \beta = \frac{\omega^2 \tau^2}{1 + \omega^2 \tau^2}$$



Plasma and Electroenergetics Annual Portfolio

Energy Flow in Dense Off-Equilibrium Plasmas



Submitted by Seth Putterman

December 19, 2015

UCLA

Equation of State and Transport Properties in a Dense Plasma

- We have demonstrated 3 different desktop labs for dense plasma science
- Kinetic theory of a dense plasma is easier than you think
- Ionization potential is dramatically lowered in a dense plasma
- Subnanosecond establishment of opacity in a dense plasma
- Transition to opacity occurs on micron length scale → **subns switch to block high power pulses!**
- Idea for a paradigm shifting 4th lab of warm dense plasma

Sonoluminescence creates a strongly coupled plasma

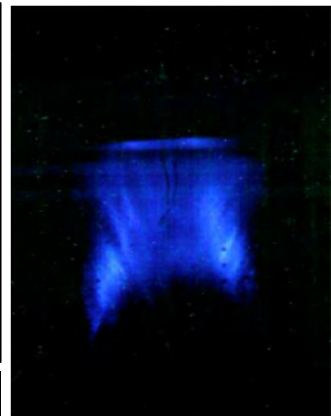


- Sonoluminescence can be generated in a variety of systems
- As a result, *extensive* properties of sonoluminescence span many orders of magnitude:

Hz to MHz, ps to μ s, $10^{-3} \mu\text{m}^3$ to $10^6 \mu\text{m}^3$

- However, *intrinsic* properties of sonoluminescence are similar:

$T \approx 0.5 - 2 \text{ eV}$, $n_a \approx 10^{21} - 10^{22} \text{ cm}^{-3}$, $1 < \square < 10$

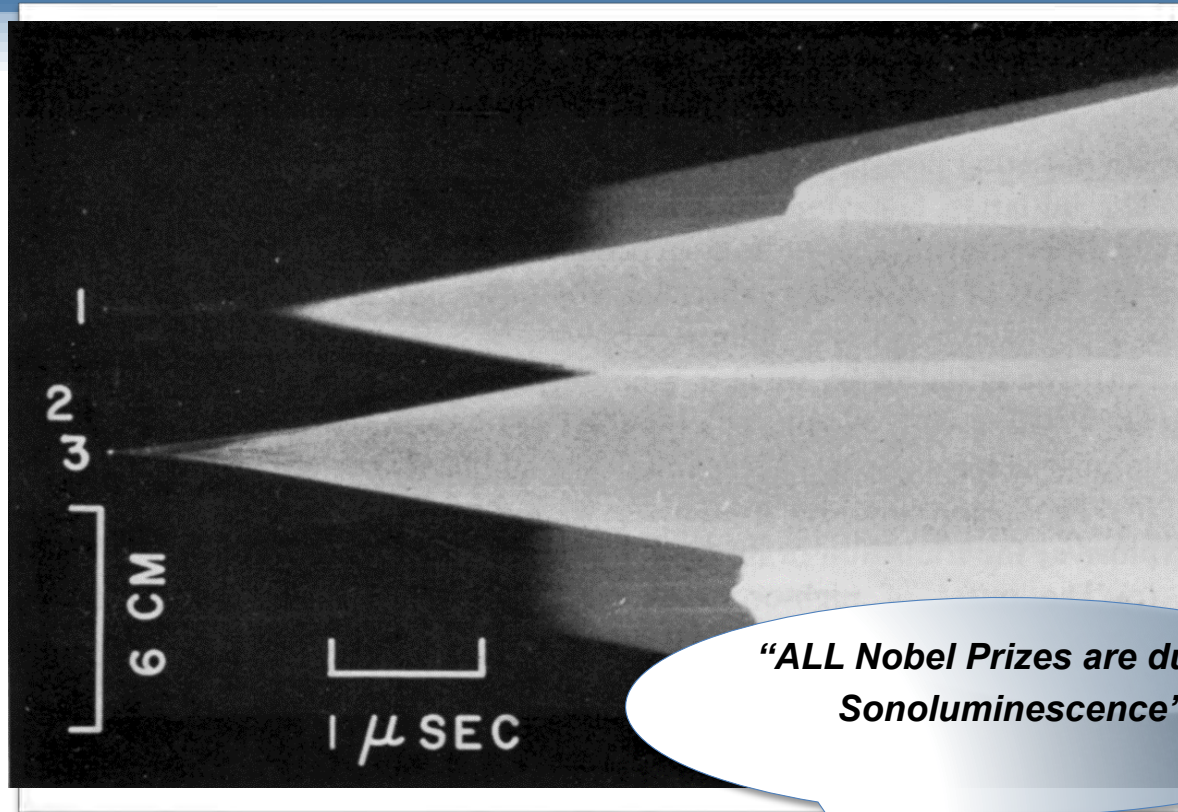


Kappus, B., Khalid, S., Chakravarty, A., Putterman, S., 2011, "Phase Transition to an Opaque Plasma in a Sonoluminescing Bubble". *Physical Review Letters*, **106**(234302),



\square is the
plasma
coupling
parameter

Explosions are initiated by the dense plasma formed inside of a crushed bubble



***“ALL Nobel Prizes are due to
Sonoluminescence”***

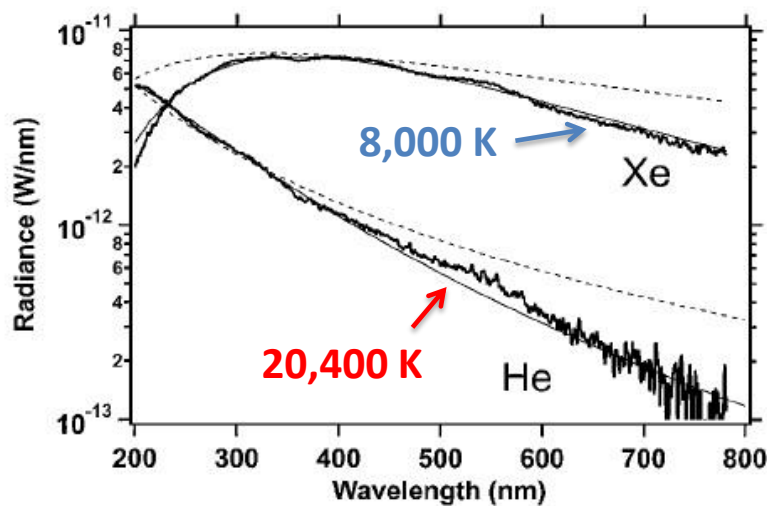
Kirk McDonald

P I M C O

Persson Book

<#>

Sonoluminescence: A micron-sized blackbody emitter dense plasma



Vazquez, G., Camara, C., Putterman, S., and Weninger, K., 2001, "Sonoluminescence: nature's smallest blackbody". *Optics Letters* **26**(9), p. 575–577

- Common feature to many sonoluminescence systems is its opacity (blackbody spectrum)
- Conditions for blackbody:
 1. Thermal equilibrium
 2. $R_{BB} \gg \ell_{\square}$,
where ℓ_{\square} is the photon mean free path
- **$n_e \gtrsim 10^{21}$ electrons/cm³ needed for micron scale opacity**

The sonoluminescing microplasma is a thermodynamic state

Question: Can this plasma be generated outside of a bubble?

Idea: Study the energy input to high-pressure gases. Static high-pressure gas matches the bubble's collapse density in sonoluminescence.

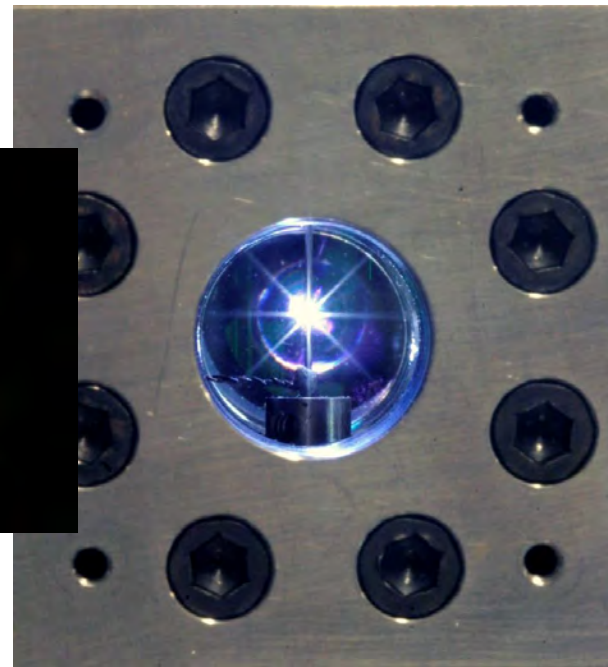
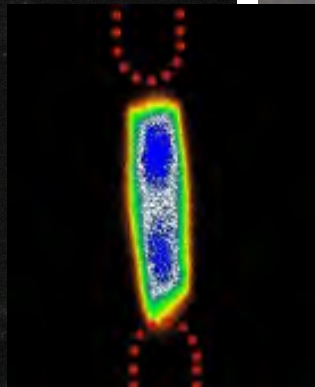
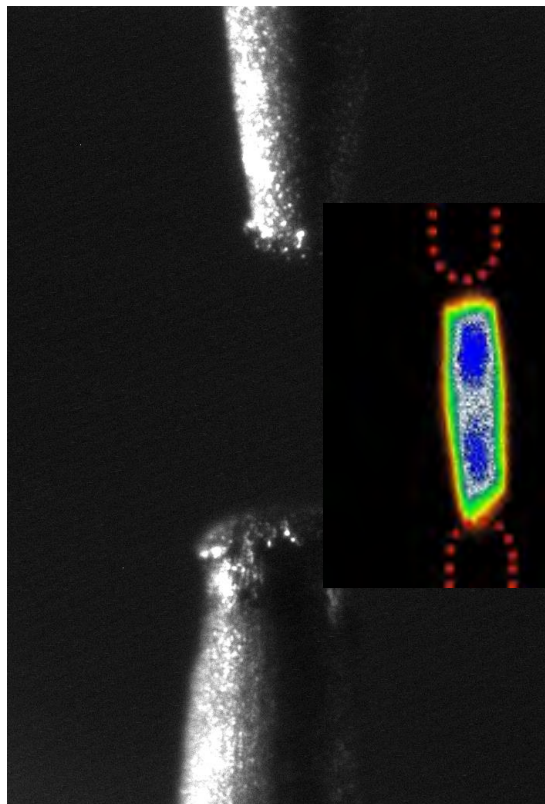
$$2500 \text{ psi} = 170 \text{ bar} = 4.25 \times 10^{21} \text{ atoms/cm}^3$$

Contents

- 1) Sonoluminescence: A micron blackbody
- 2) Sono(less)luminescence: Laser Breakdown
 - a) **Calibrated streaked spectroscopy**
 - b) Transport properties from new platform
- 3) Sono(less)luminescence: Spark Discharge

Spark Discharges in a Dense Gas are also a –[New Ancient] Platform for Dense Plasmas

- 5 kV potentials across 150 μm gap
- Tungsten needles in high-pressure gases can create bright nanosecond spark discharges
- Dense plasma triggered on-demand

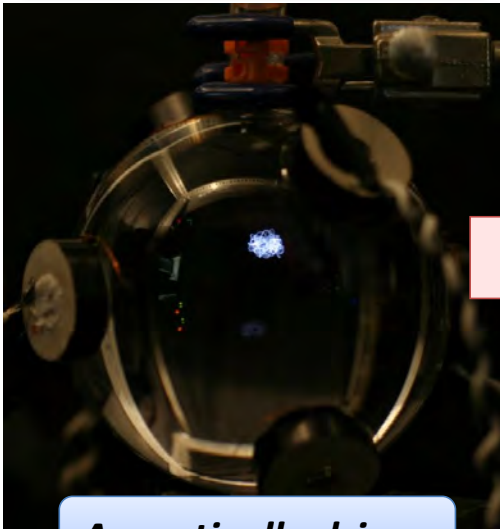


Laser Breakdown in high pressure gases

Taking the “sono” out of sonoluminescence...

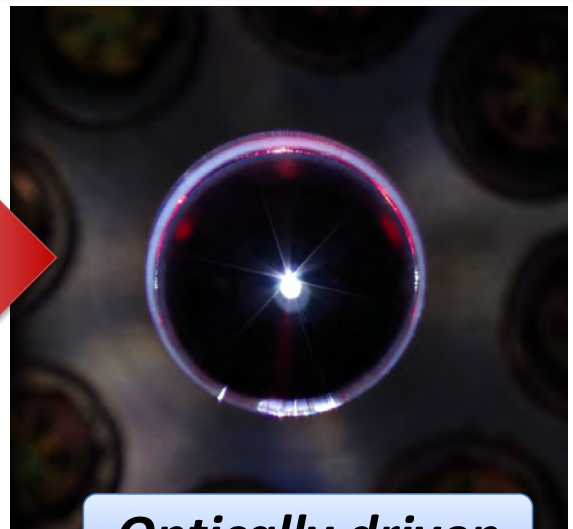
UCLA

Adiabatic heating in a collapsing gas bubble



Acoustically driven

Laser heating in a high static pressure gas by dielectric breakdown

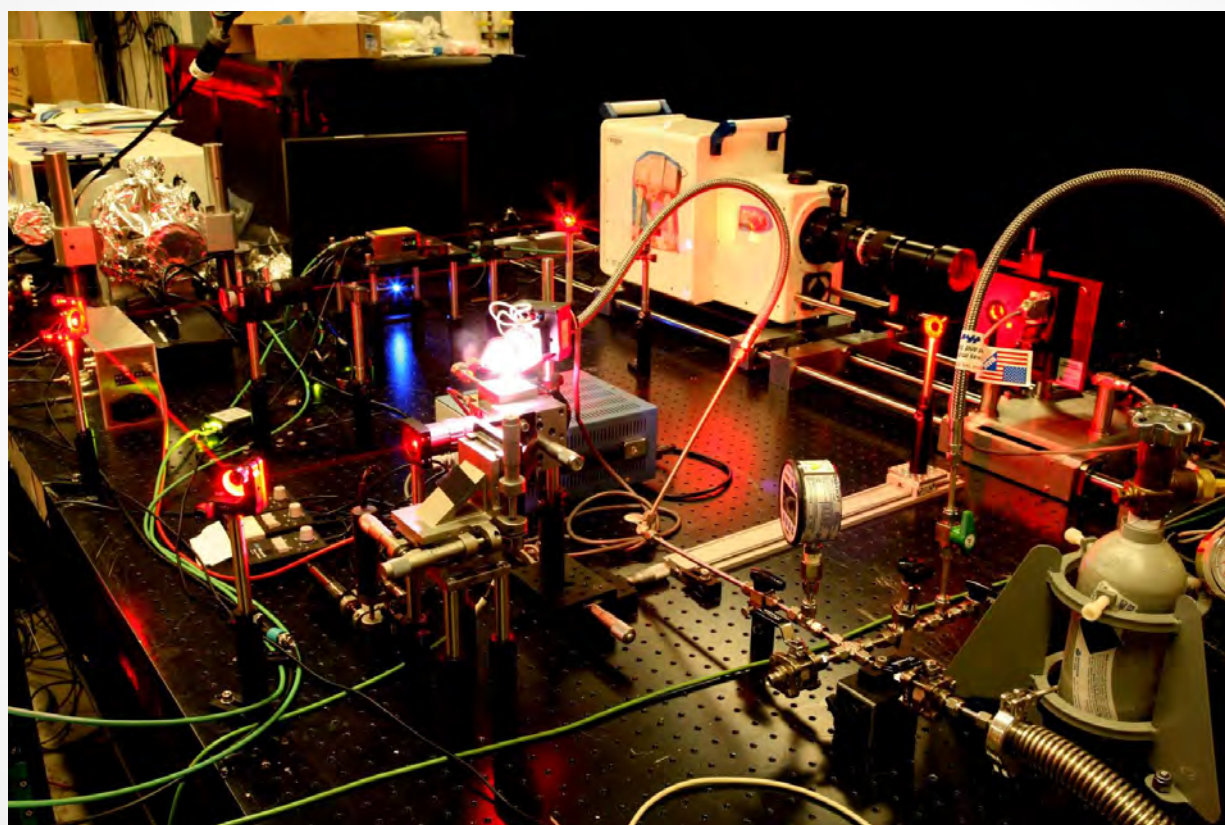


Optically driven

8

UCLA

Nanosecond UV Framing Camera for Diagnosing Transport in Dense Plasmas



Bataller – Koulakis - Pree

Density Corrections to Saha's Equation

$$\frac{x^2}{1-x} = \frac{2g_1}{n_0\lambda^3} \exp\{-\chi/kT\} \quad \text{Saha's Equation}$$

$$\chi \approx \chi_0(1 - \gamma a_0 n_0^{1/3}) - e^2 / \delta_D - \alpha e^2 / 2\delta_D^4$$

$$\Delta\chi = \text{hybridization} + \text{Debye screening} + \text{polarization}$$

$$\delta_D = \sqrt{kT / 8\pi n_e e^2} \quad \text{Debye Screening Length}$$

$$n_e = \gamma n_0$$

$\gamma = 2$ for hydrogen atom : theory

3.56 for cold Xe ; from diamond anvil experiments



<#>

Ebeling 1988

$$f_{\text{COUL}} = f_e + f_i + f_{\text{ei}},$$

$$f_e = -n_e \frac{\text{Ryd}[f_0 \tilde{n}^{1/2} + f_3 \tilde{n} - f_2 \tilde{n}^2 \varepsilon(r_s)]}{(1 + f_1 \tilde{n}^{1/2} + f_2 \tilde{n}^2)},$$

$$f_0 = \frac{2}{3} \left(\frac{\tau}{\pi} \right)^{1/4},$$

$$f_1 = 2^{1/2} \frac{1 + \ln 2}{8 f_0},$$

$$f_2 = 3,$$

$$f_3 = \frac{1}{4} \left(\frac{\tau}{\pi} \right)^{1/2},$$

$$\varepsilon(r_s) = -\frac{0.9163}{r_s} - 0.1244 \ln \left[\frac{1 + 0.3008 r_s^{1/2} + 2.117 r_s^{-1/2}}{1 + 0.3008 r_s^{1/2}} \right],$$

$$f_i = -n_e k_B T \frac{q_0^{(i)} \tilde{n}^{1/2} + q_3 \tilde{n} - q_2^{(i)} \tilde{n}^{3/2} (B_i^{(i)} \tilde{n}^{1/3})}{1 + q_1^{(i)} \tilde{n}^{1/2} + q_2^{(i)} \tilde{n}^{3/2}},$$

$$f_{\text{ei}} = -n_e k_B T \frac{q_0^{(n)} \tilde{n}^{1/2} - q_2^{(n)} \tilde{n}^{3/2} (B_i^{(n)} \tilde{n}^{1/3})}{1 + q_1^{(n)} \tilde{n}^{1/2} + q_2^{(n)} \tilde{n}^{3/2}},$$

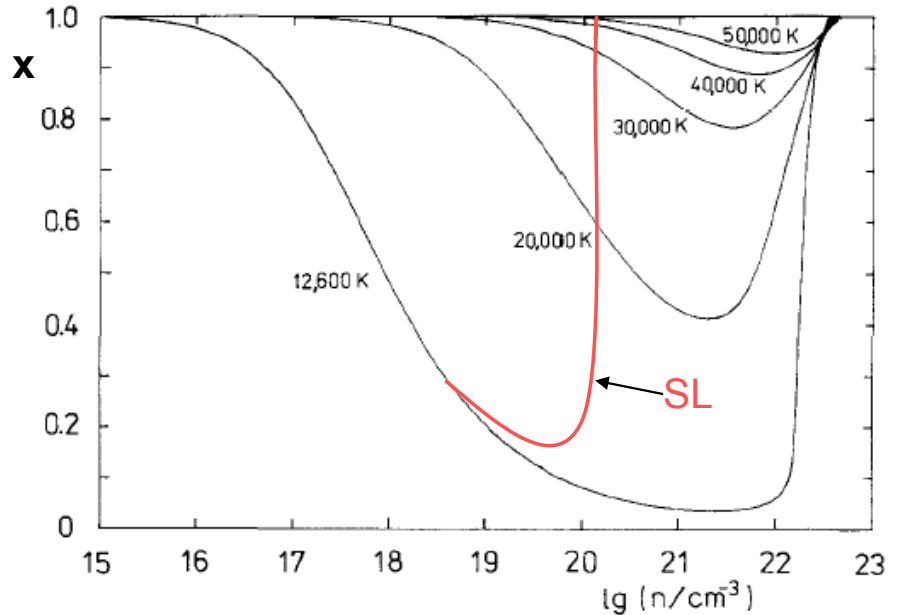
$$B_i^{(i)} = -1.4474 + 4.2944 \tilde{n}^{-1/4} - 0.6712 \tilde{n}^{-5/12} - (0.2726 \ln \tilde{n} + 2.983) \tilde{n}^{-1/3},$$

$$B_i^{(n)} = -r_s \left[\frac{0.8511 \tilde{n}^{-1/4}}{(1 + 0.3135 \tilde{n}^{-1/12})(1 + 2.5 \tilde{n}^{-1/3})} + \frac{0.0726 + 0.0161 r_s}{1 + 0.0887 r_s^2} \right],$$

$$q_0^{(i)} = \frac{2}{3} \pi^{1/2},$$

$$q_0^{(n)} = \frac{4}{3} \pi^{1/2} (2^{1/2} - 1),$$

$$q_1^{(i)} = \frac{3}{16} \pi (1 + \ln 2) (2 \gamma \tau)^{1/2},$$



$$q_1^{(n)} = \frac{3\pi\tau^{1/2}}{8(\sqrt{2}-1)} \left[K - \frac{1 + \ln 2}{2\sqrt{2}} (1 + \gamma^{1/2}) \right],$$

$$q_2^{(i)} = 10^3,$$

$$q_2^{(n)} = 1,$$

$$q_3 = \frac{1}{4} \tau \pi \gamma,$$

$$K = 1 + \frac{1}{2} \left(\frac{\tau}{\pi} \right)^{1/2} \exp \left\{ -\frac{[\tau \pi / 8]^{1/2}}{[1 - (\tau^{1/2} / 12) \ln(4/\tau)]} \right\}.$$

Phase transition to a dense plasma is achieved at 2 orders of magnitude lower density-----

Redmer 1997

$$V_{ed}^{eff}(12,1'2') = \begin{array}{c} \text{Diagram 1: } \text{wavy line } 1 \text{ to } 1', \text{ wavy line } 2 \text{ to } 2' \\ \text{Diagram 2: } \text{wavy line } 1 \text{ to } 1', \text{ box } T_2^L \text{ with } 2 \text{ to } 2' \\ \text{Diagram 3: } \text{wavy line } 1 \text{ to } 1', \text{ box } T_3^L \text{ with } 2 \text{ to } 2' \text{ and a loop on top} \\ \vdots \\ \text{Diagram 4: } \text{wavy line } 1 \text{ to } 1', \text{ box } T_2^L \text{ with } 2 \text{ to } 2' \text{ and a large wavy line on top} \\ \vdots \end{array} \quad (24)$$

The vertices in the last diagram describe the interaction between a two-particle cluster and free particles [ROE79]. For the polarization function $\Pi(q, \omega)$, a similar cluster decomposition is employed:

$$\Pi(q, \omega) = \Pi_1(q, \omega) + \Pi_2(q, \omega) + \Pi_3(q, \omega) + \dots, \quad (25)$$

$$\begin{array}{c} \text{Diagram 1: } \text{oval with } \Pi \\ \text{Diagram 2: } \text{empty oval} \\ \text{Diagram 3: } \text{oval with } T_2^L \text{ and } T_2^I \\ \vdots \\ \text{Diagram 4: } \text{oval with } T_3^L \text{ and } T_3^I \\ \vdots \end{array}$$

See also Fortov, Kraeft, Ebeling

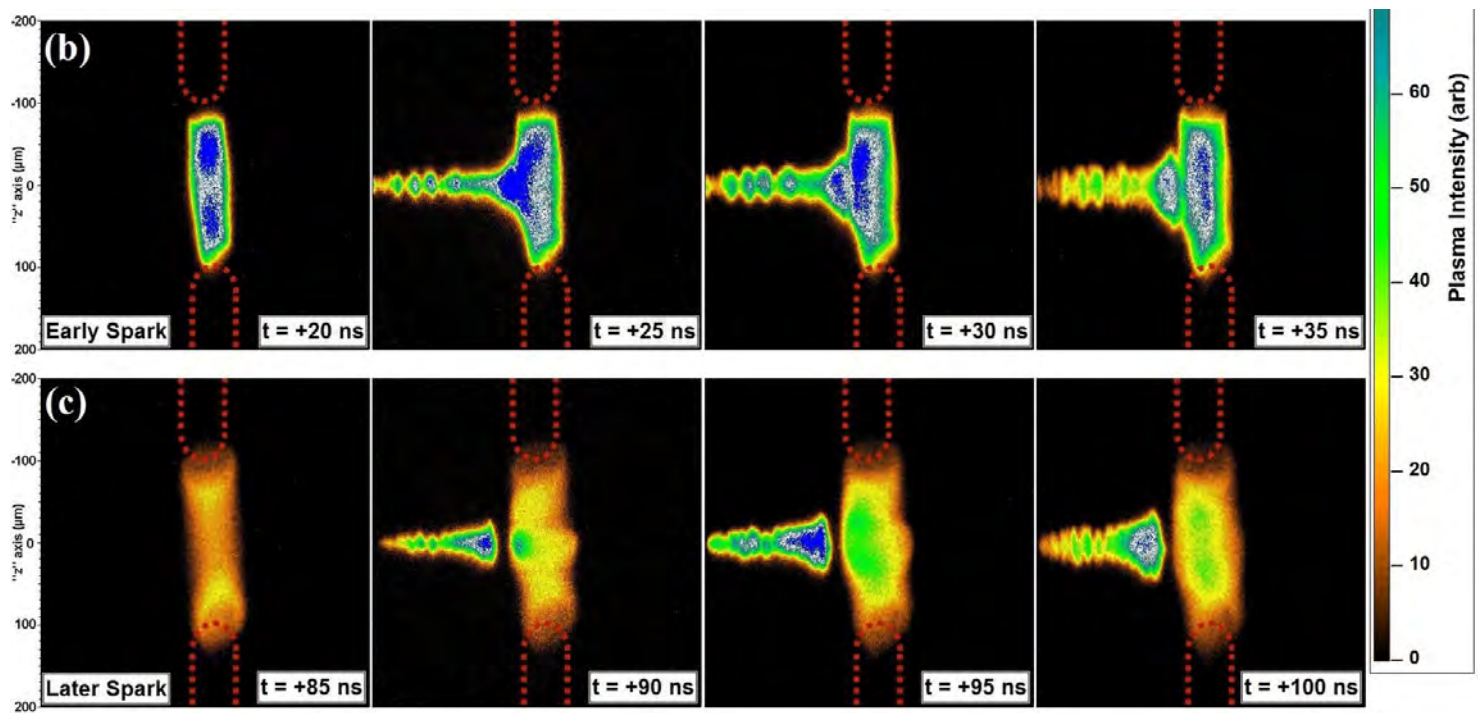
The first term in (25) describes the polarizability of a free electron gas within the RPA whereas

If we are correct about this being a thermodynamic effect then it is fundamental
And it applies to other situations where dense gases are energized
These include sparks in a dense gas
Laser breakdown in a dense gas
And initiation of explosions.

Demonstration of Opaque Plasma Discharge Blocking Intense Laser Pulse-due to formation of dense plasma condensate

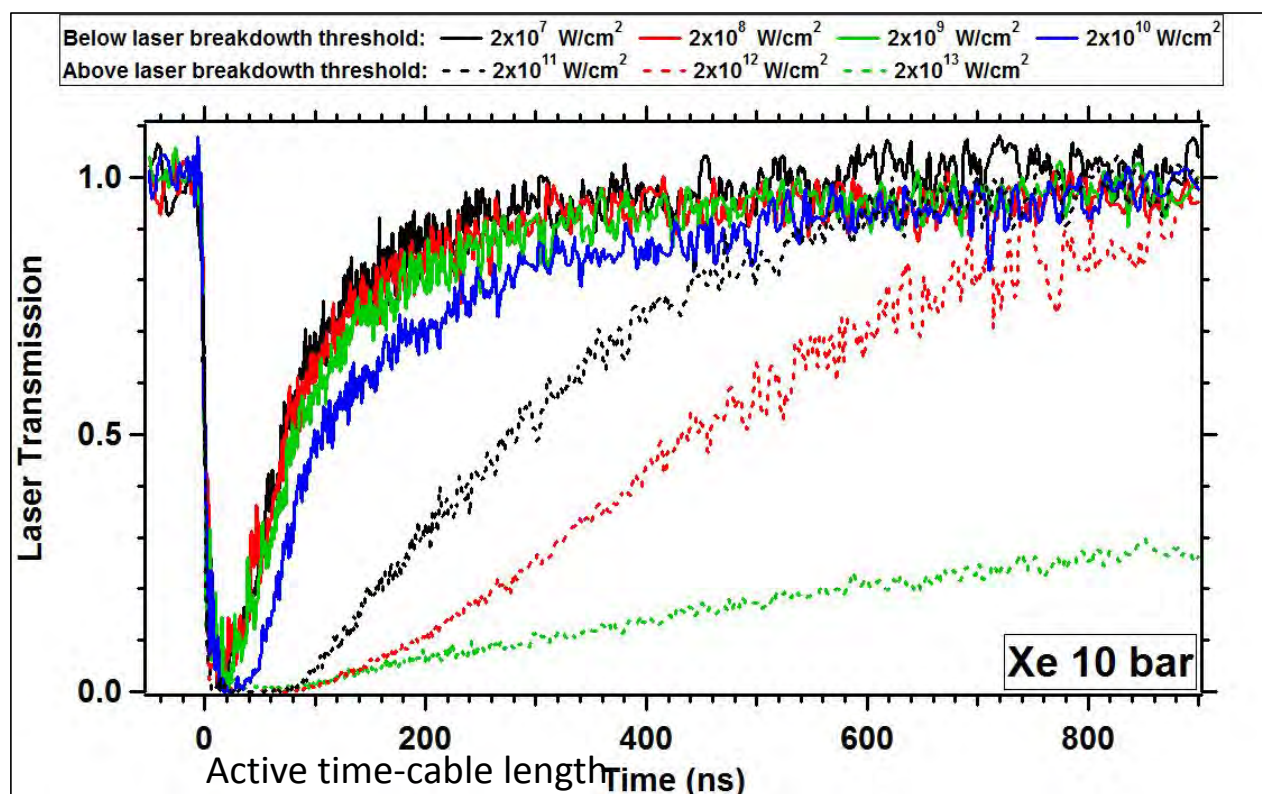
b) Intense laser pulse arrested at plasma surface

Practically limitless power handling capability. The switch cannot be broken as it is already the broken state of matter!

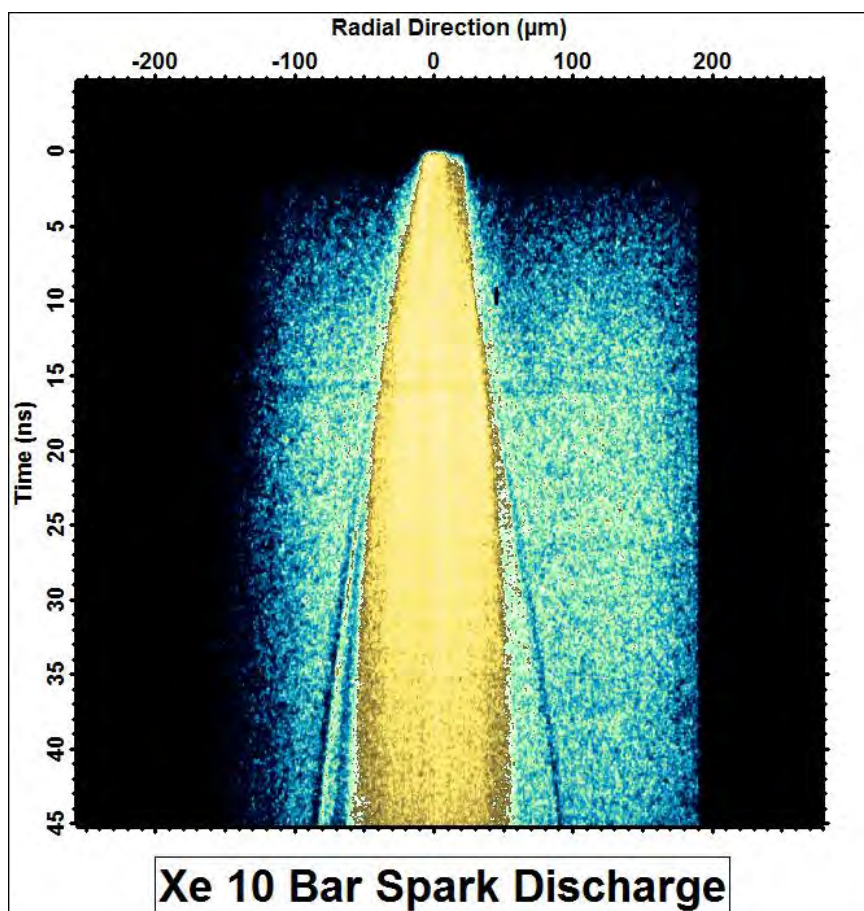


A. Bataller, J. Koulakis, S. Pree, S. Putterman, *Appl. Phys. Lett.* **105**, 223501 (2014)

Blocking light over six orders of magnitude of intensity; rise time not resolved-here



Shock Wave Emission from a Dense Plasma

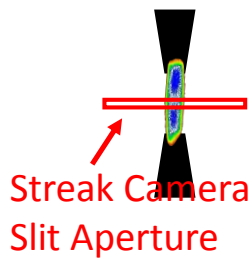


- Shock waves tell us hydrodynamic motion and that the plasma is expanding. This guides our efforts in both studying the dense plasma and designing an optimum switch.
- Shock waves also tell us the initial plasma energy and gives information towards an equation of state.

Although the field is as old as electricity, many spark discharge features remain unknown:

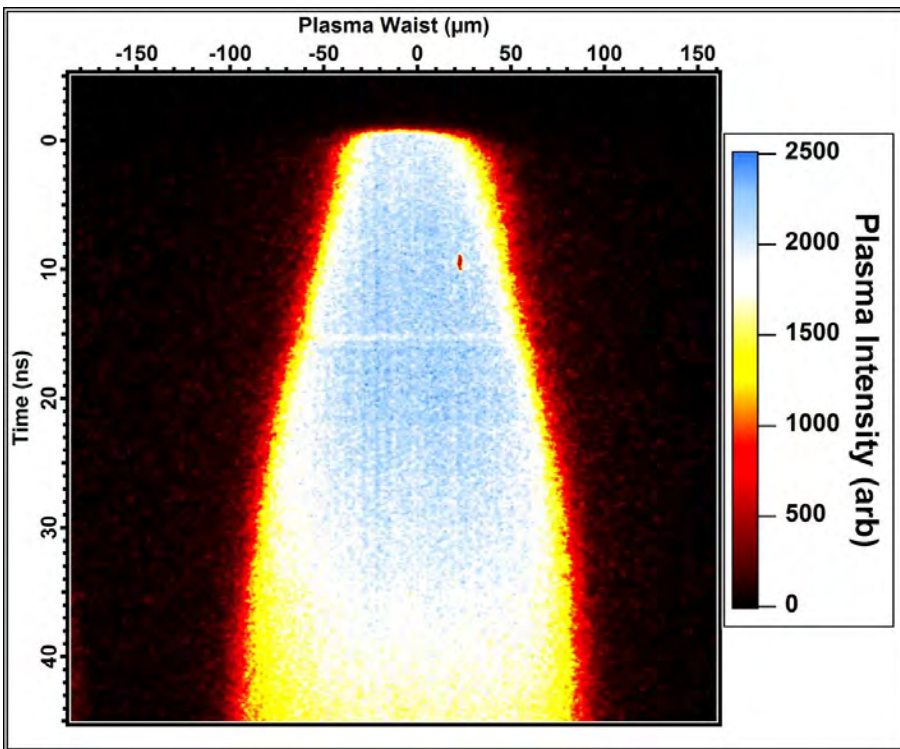
"We have pointed out that the problem of streamer head radius still remains to be solved. Today, there is no adequate theory, nor is there convincing experimental evidence to determine the head size reliably."

-Raizer, "*Spark Discharge*" 1998



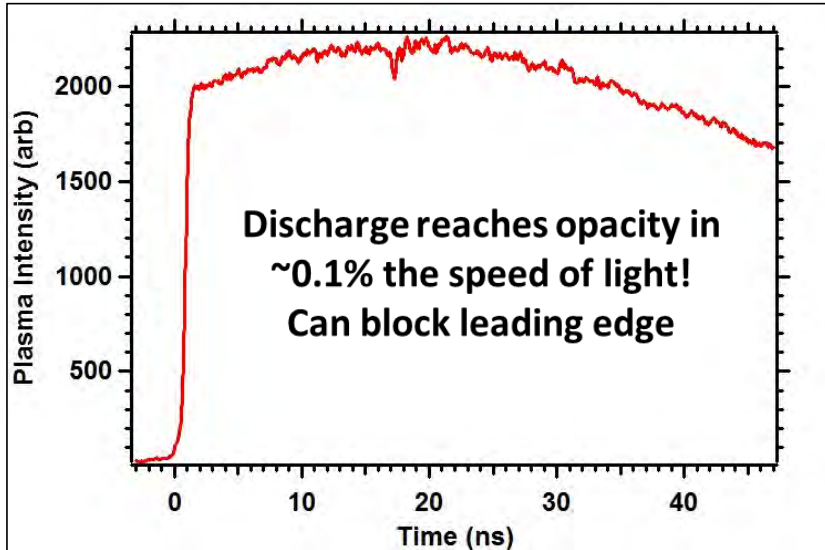
Switch Turns on Sub-ns Blackbody is Established Within a Few Microns

Sun is evenly bright and that is typical of a BB— contrast to a projection lamp

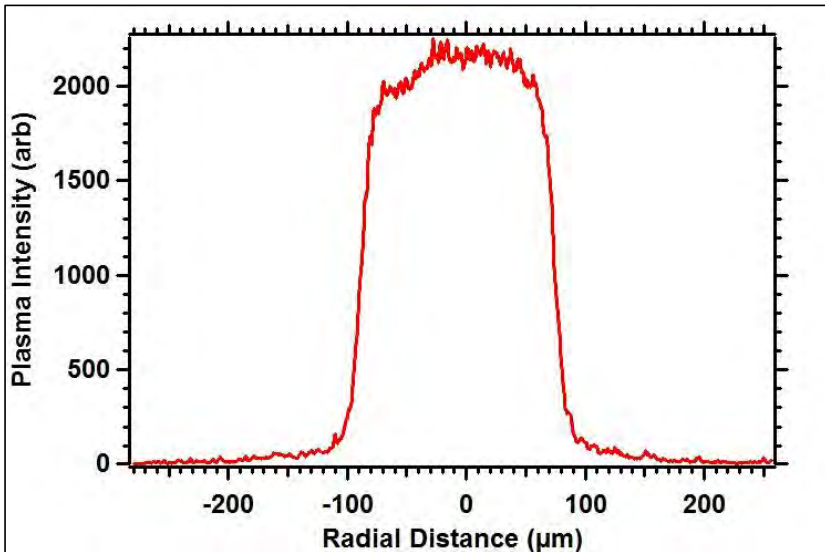


- Plasma is opaque within 500 ps making for an easier switch!
- Plasma opaque within 4 μm
- Plasma surface temperature (24,000K) is uniform in both time and space. The reason for this is unknown and points toward fundamental plasma processes.
- Plasma expansion is 2 km/s and points towards a hydrodynamic expansion...or perhaps an ionization wave?

Temporal and Spatial Line-Outs



Temporal line-out: Intensity flattop in time shows a uniform temperature in time and a blackbody which blocks incident light for over 20 ns.

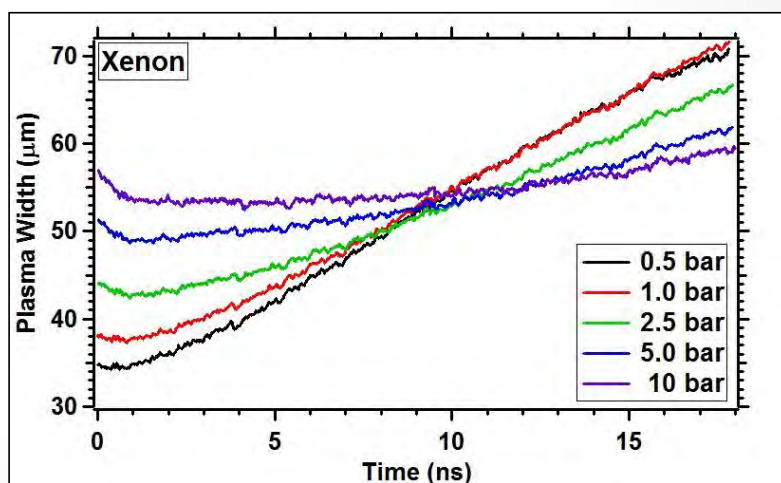
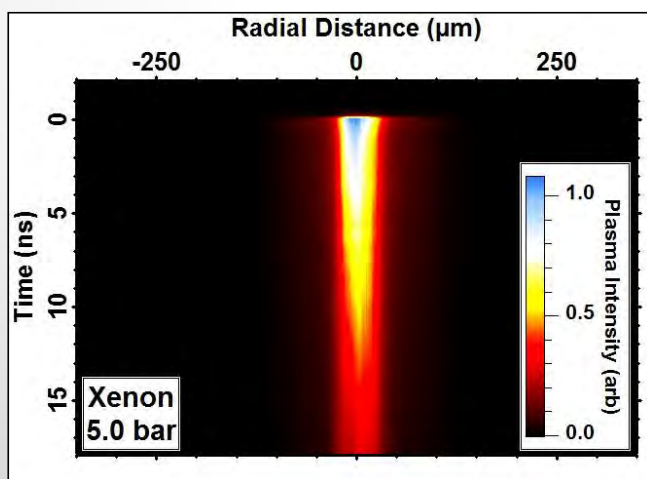
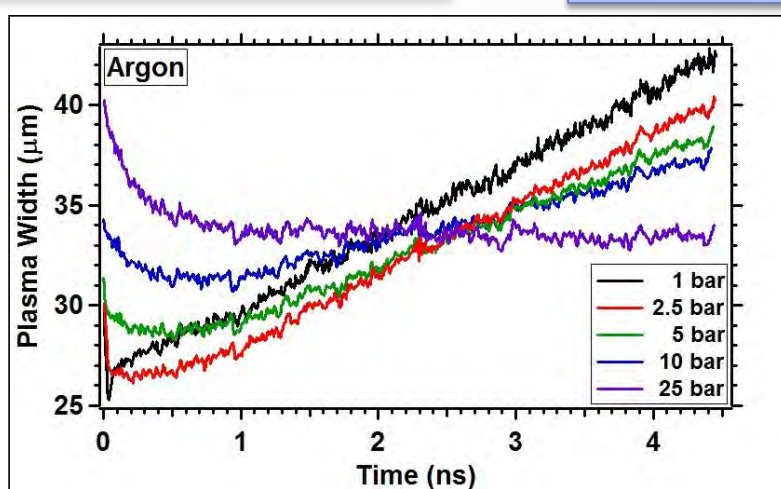
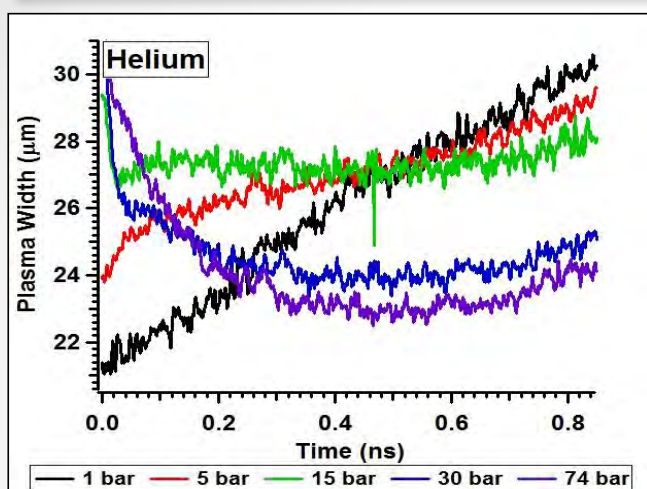


Spatial line-out: Intensity flattop in space infers a blackbody. Furthermore, the plasma has a uniform temperature across the plasma surface. This feature is robust and not fully understood.

Does Plasma Contraction at Short Times Imply that a Cold Dense Plasma acts like it has a Tensile Strength

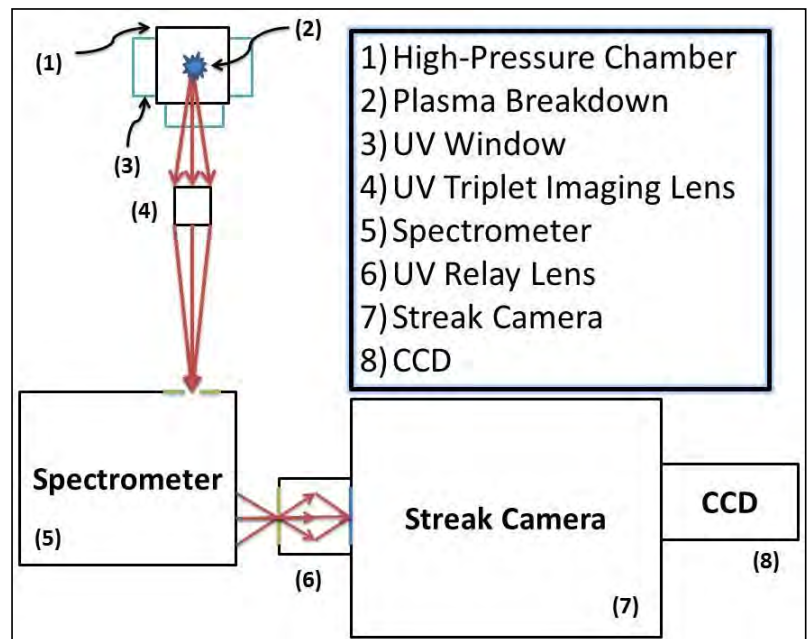
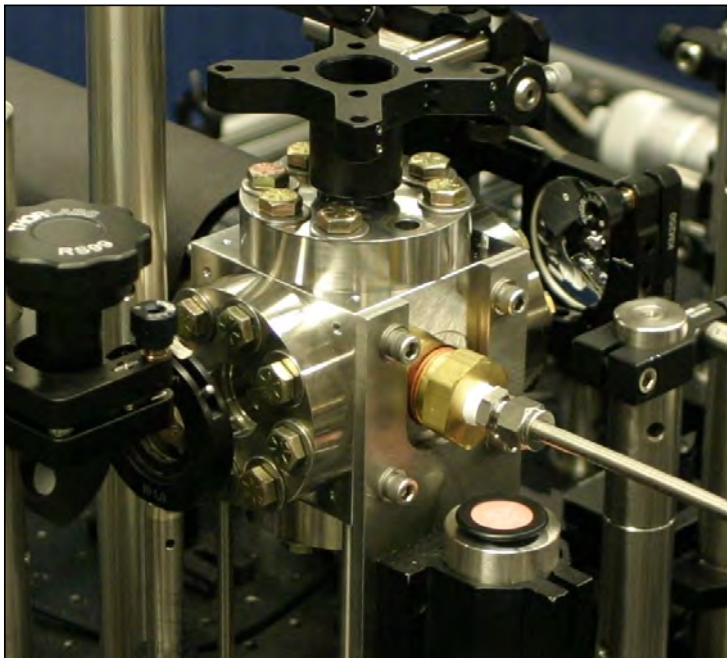
UCLA

Bataller et al.



Experimental setup: Chamber and optical diagram

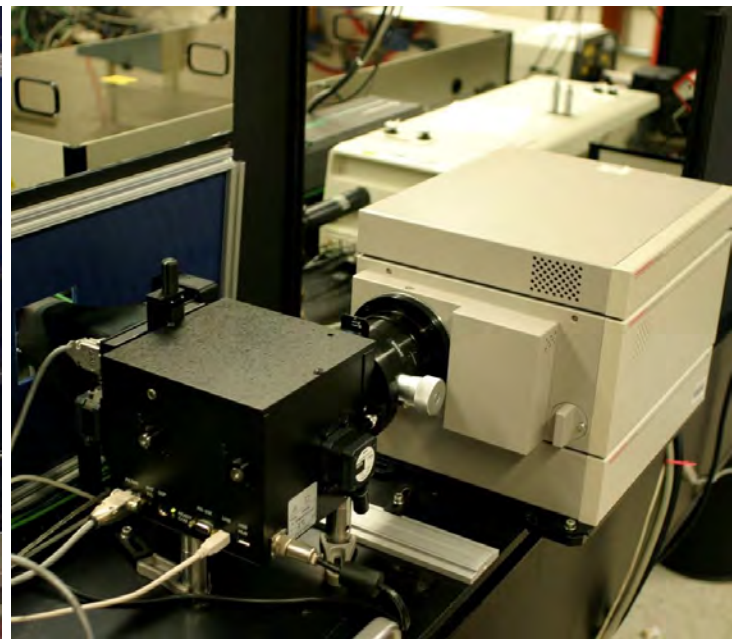
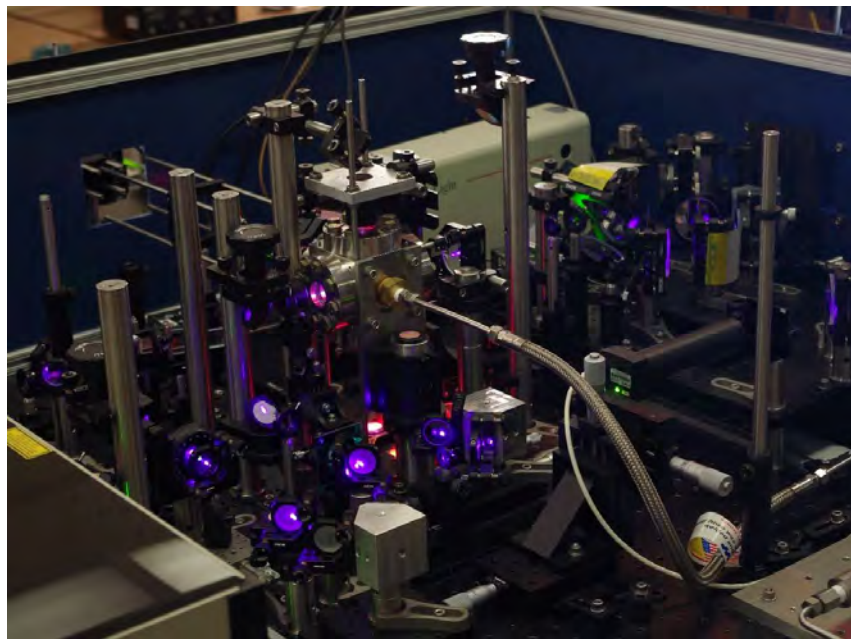
UCLA



20

Experimental setup: Optics and streak camera

UCLA

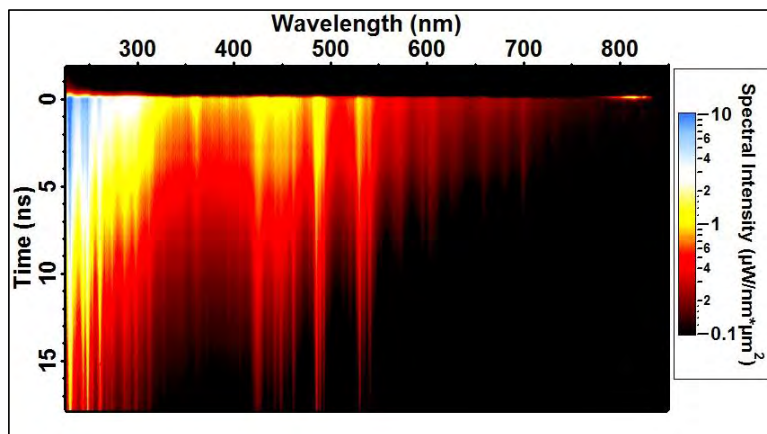


21

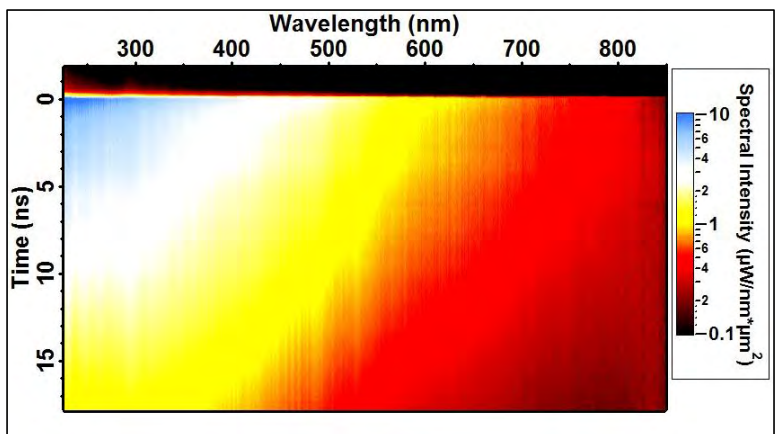
Xenon Spectrum

UCLA

Transition to continuum at high pressures



0.5 bar

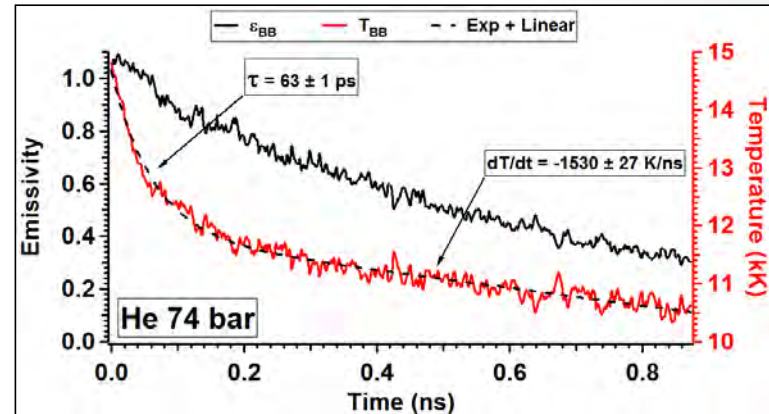
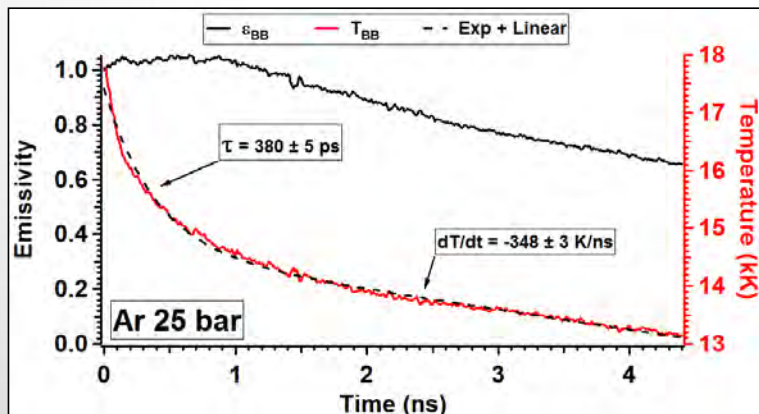
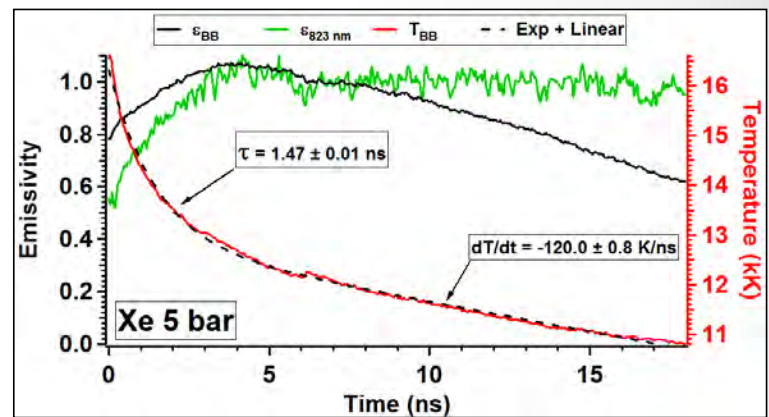
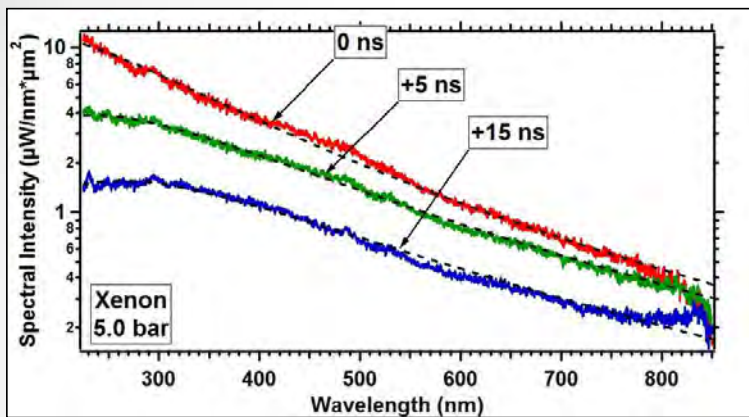


5 bar

Plasma Temperature Evolution

UCLA

12,000 – 18,000K
Blackbody fits



Ionization Required for Opacity

Opacity at 400 nm

- For measurements made, opacity condition governed by R_{BB}/ℓ_ν
- Bremsstrahlung is the dominant source of broadband emission/absorption in high density plasma.
- ℓ_ν is modified by high density effects (G. Dimonte and J. Daligault, Phys. Rev. Lett. **101**, 135001 (2008)).

	Helium	Argon	Xenon
t (ns)	+0.1	+1	+5
R (μm)	26	34	50
T (K)	12,550	14,550	12,350
n _a (cm ⁻³)	1.85x10 ²¹	6.3x10 ²⁰	1.25x10 ²⁰
Z	>0.38	>1.0	>3.2
n _e (cm ⁻³)	>7.0x10²⁰	>6.3x10²⁰	>4.0x10²⁰
Γ	>1.9	>1.6	>3.6

Thermalization Timescale Measured

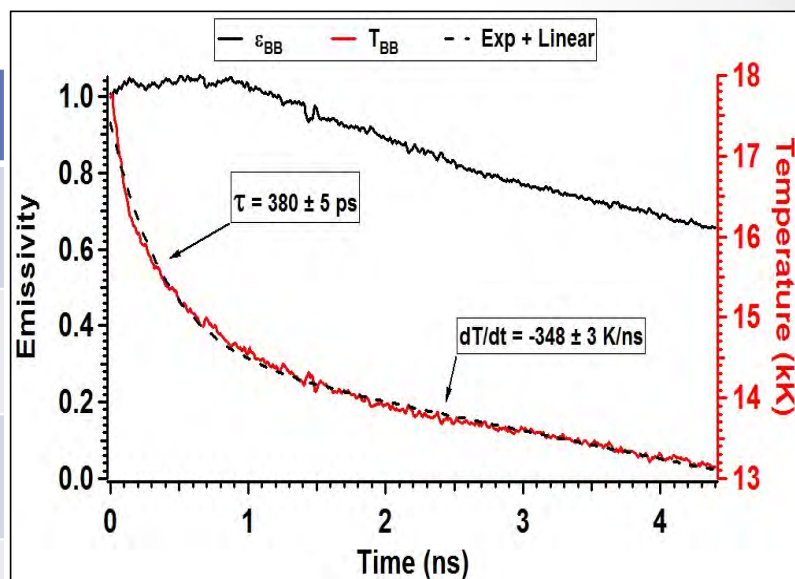
UCLA

- Thermalization time measured

$$\tau_{th} \approx \frac{M}{m} \tau_{e-i}$$
- τ_{e-i} is calculated using temperature and ionization with dense plasma theory (G. Dimonte and J. Daligault, Phys. Rev. Lett. **101**, 135001 (2008) *screened collisions*)

SELF-CONSISTENT VALIDATION OF TRANSPORT THEORY AND PROVIDES COLLISION TIME MEASUREMENT FOR A STRONGLY COUPLED PLASMA

	Helium	Argon	Xenon
τ_{th} (meas.)	63 ps	380 ps	1.47 ns
τ_{th} (calc.)	37 ps	305 ps	1.17 ns
Mass Ratio	0.10	1.0	3.3
$\frac{\tau_{th}}{\tau_{e-i}}$	0.13	1.0	3.3



Ar 25 bar

Dwell Time of Dense Micro-Plasma Condensate

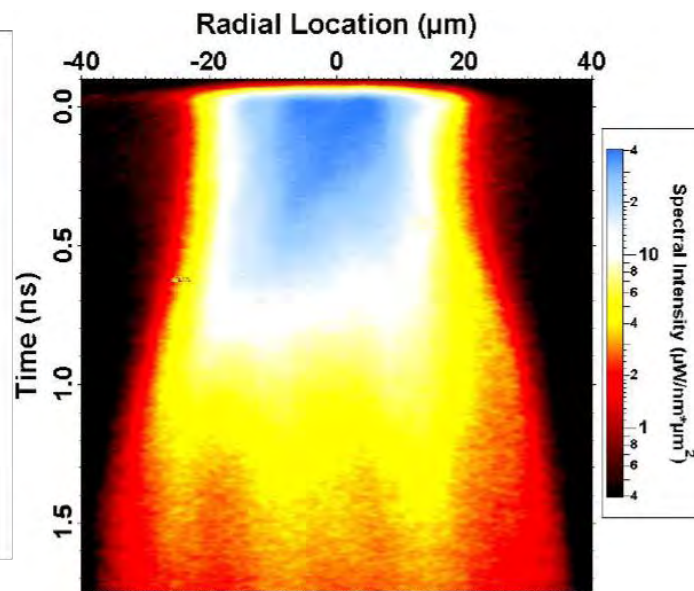
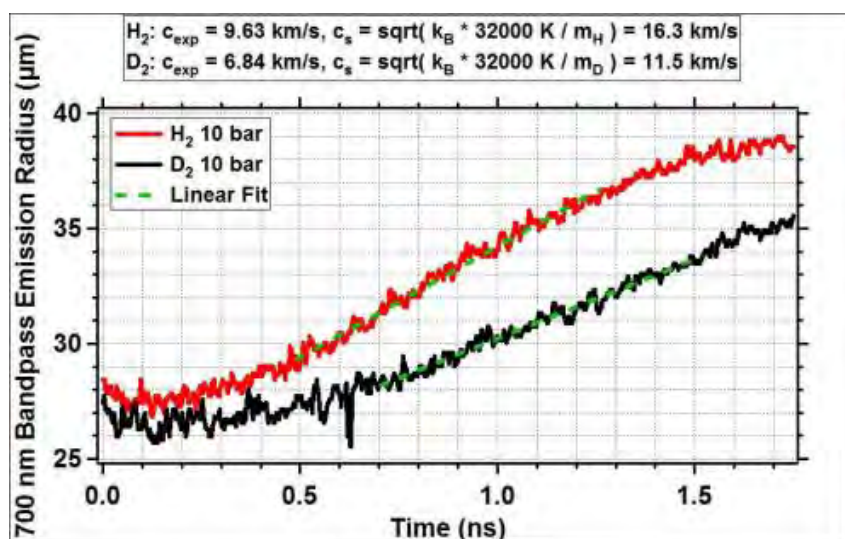
Ambient pressure before breakdown = 10.atm

Electron temperature after breakdown = 25,000K

Pressure. 3,000.atm

Plasma charge density $\sim 10^{21}/\text{cc}$

Yet H plasma dwells for 200ps; D plasma for 400.ps



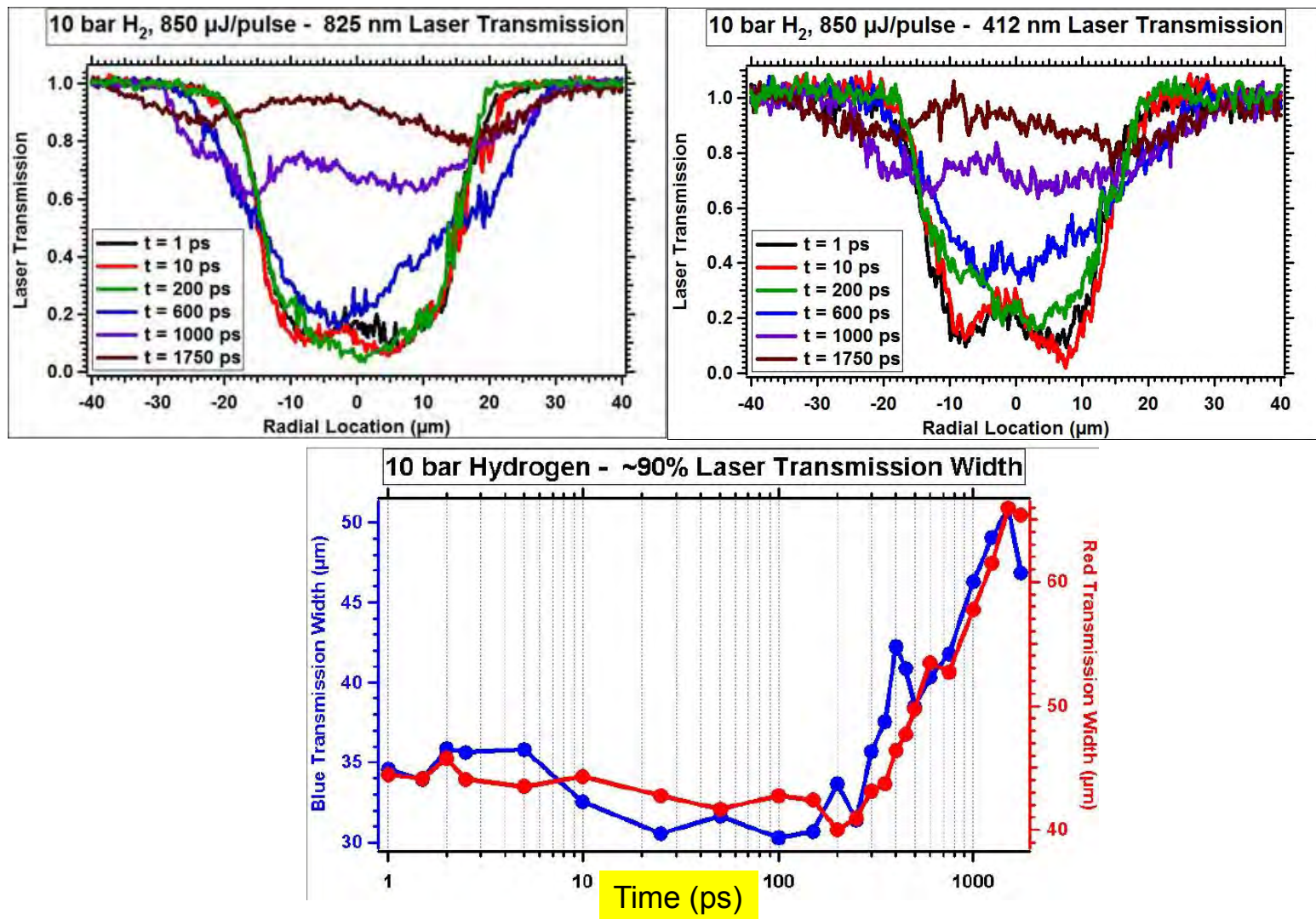
Plasma Parameter = Γ ; $a \sim 8\text{\AA}$

$$\Gamma = e^2 / akT ; a = (3 / 4\pi n_e)^{1/3}$$

If the ions are at ambient Temperature
then $\Gamma(\text{ions}) = 70$

Which is very strong coupling

Transmission measurements also match emission waist dwell times

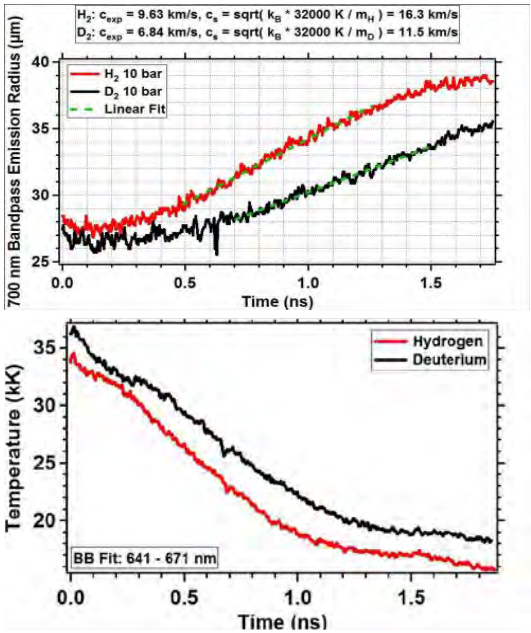


Competing Mechanisms for Dwell?

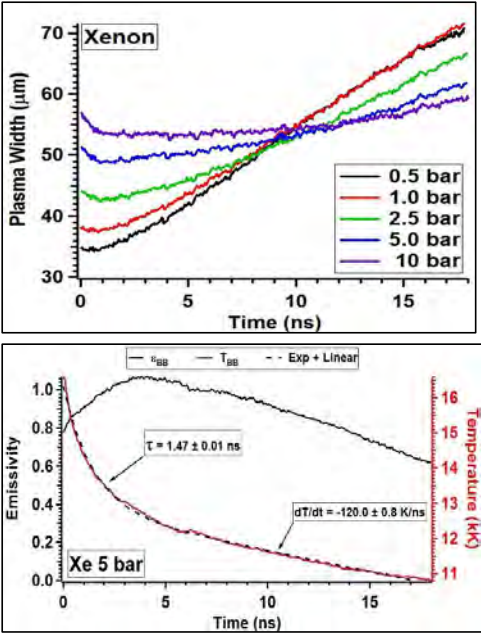
H_2 : $T_{\text{Dwell}} < T_{\text{Therm}}$
 He, Ar, Xe : $T_{\text{Dwell}} > T_{\text{Therm}}$

Gas	Calc T_{Therm}	Actual T_{Therm}	Dwell Time
H_2	10 ps	1 ns	200 ps
He	40 ps	100 ps	>800 ps
Ar	300 ps	1 ns	> 4 ns
Xe	1.2 ns	2 ns	15 ns

H_2 :



Xe :



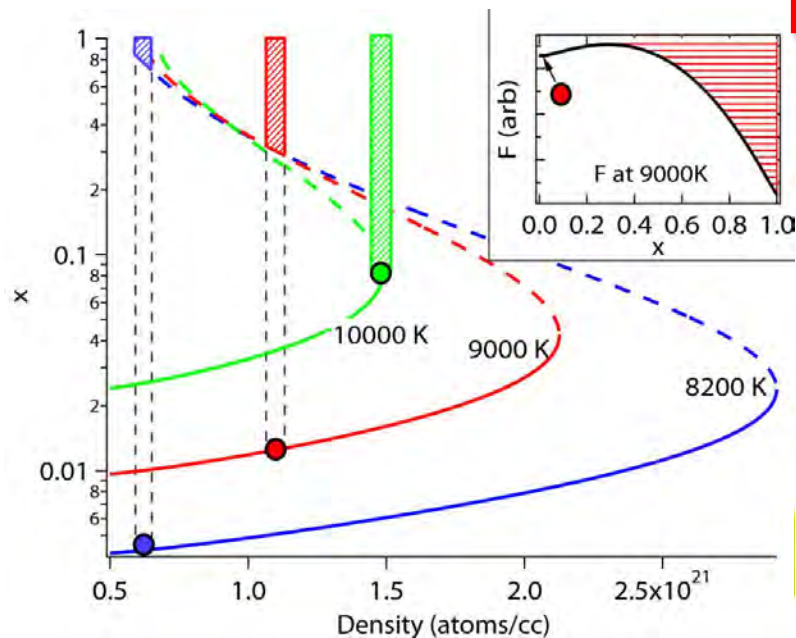
Dwell Time is Due to Electron-Electron Screening

Screening lowers ionization potential: $\chi \approx \chi_0 - \frac{e^2}{\delta_D}$ $\delta_D = \sqrt{\frac{kT}{8\pi n_e e^2}}$

Free Energy is modified: $F = N_0 k T_i \{\ln(n_0 \lambda_i^3)\} + N_0 k T_e \{\ln(n_0 \lambda_e^3)\} - N_0 \{2e^2 / 3\delta_D\}$

Leading to lowering of pressure: $p = -\partial F / \partial V = n_0 (k T_i + k T_e) - \frac{1}{3} n_0 \frac{e^2}{\delta_D}$

And phase transition:



Dwell Time is Due to Tensile Strength of Coulomb Plasma

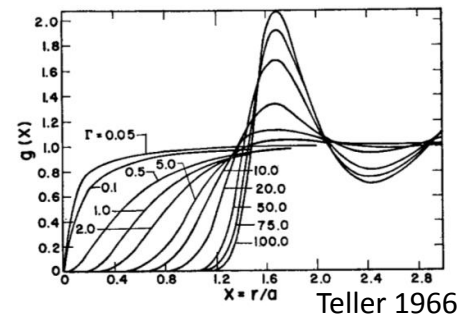
Ions are correlated in space (liquefying or crystalizing):

$$\frac{T_e}{T_i} \approx 100 \quad \Gamma_i = \frac{e^2}{akT_i} \approx 70 \quad \text{in our H}_2 \text{ system}$$

Free Energy is modified:

$$F = N_0 kT_i \{ \ln(n_0 \lambda_0^3) \} + N_0 kT_e \{ \ln(n_0 \lambda^3) \} - N_0 B kT_i \Gamma_i \tanh(\Gamma_i)$$

F = Ion Kinetic Energy + Electron Kinetic Energy – Coulomb Attraction



Leading to lowering of pressure:

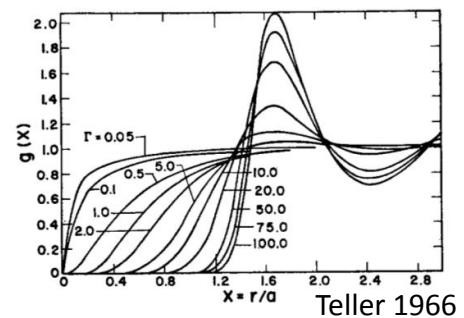
$$p = -\partial F / \partial V = n_0 (kT_i + kT_e) - n_0 kT_i B \Gamma_i \tanh \Gamma_i$$

- For $n_H = 5 \cdot 10^{20}/cc$ which is the number of H atoms at 10atm after dissociation, $e^2/a \sim 2eV$; and $ne^2/a \sim 1000atm$; so the coulomb energy is comparable to the pressures that we wish to balance.
- Laser breakdown ionizes and heats electrons leaving ions cold with $\Gamma \sim 70$. Transport is determined by electron-phonon interaction and NOT binary collisions. Therefore equilibration is slow and dwell is prolonged.

Dwell Time is Due to Tensile Strength of Coulomb Plasma

Ions are correlated in space (liquefying or crystalizing):

$$\frac{T_e}{T_i} \approx 100 \quad \Gamma_i = \frac{e^2}{akT_i} \approx 70 \quad \text{in our system}$$



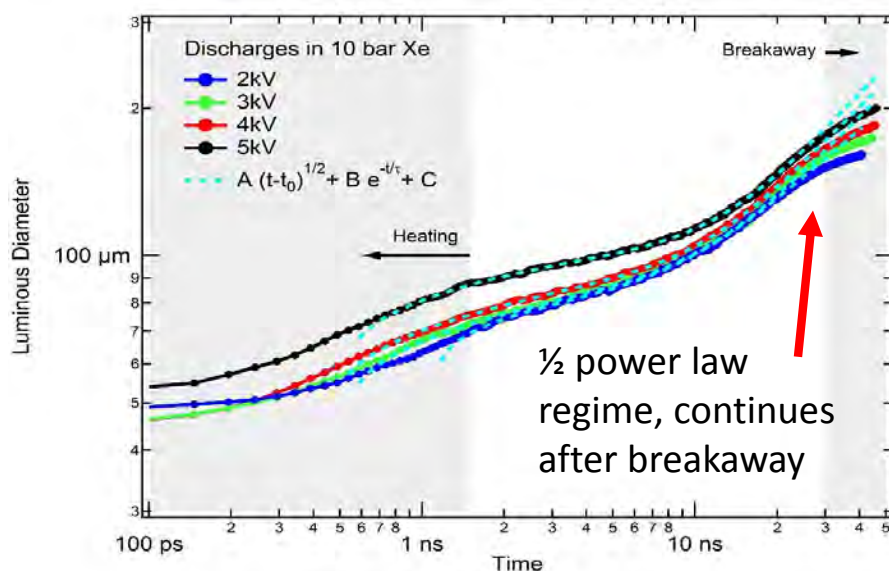
$$p = -\partial F / \partial V = n_0(kT_i + kT_e) - n_0 k T_i B \Gamma_i \tanh \Gamma_i$$

Smoking Gun Experiment: **Laser Breakdown in COLD gas**

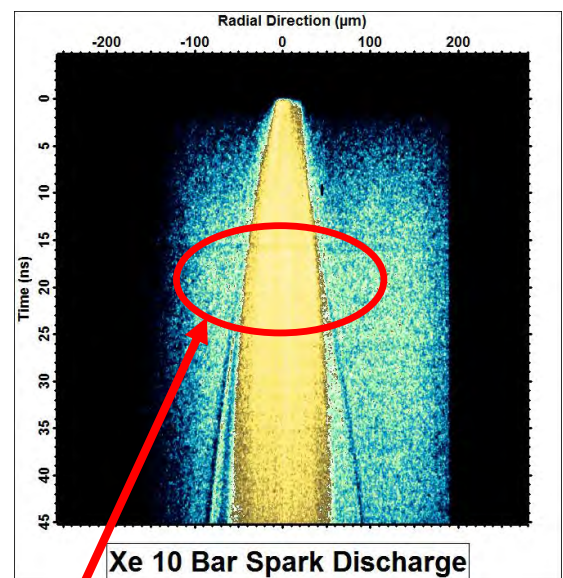
In going from room to liquid Nitrogen temperature – but the same density, Γ_i changes by 4x by the ELECTRONS ARE UNAFFECTED.

Depths of blackbody can be probed by looking at shock speed later in time

Sedov-Taylor for cylindrical shock: $R(t) \sim \left(\frac{E}{\rho L}\right)^{1/4} \sqrt{t} = \sqrt{Bt}$



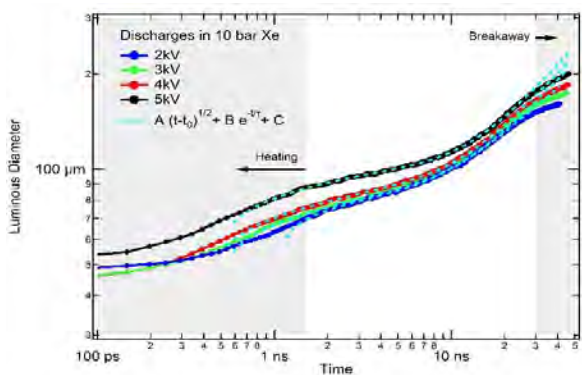
Experimental fits to shock speed at later times give the initial energy density.



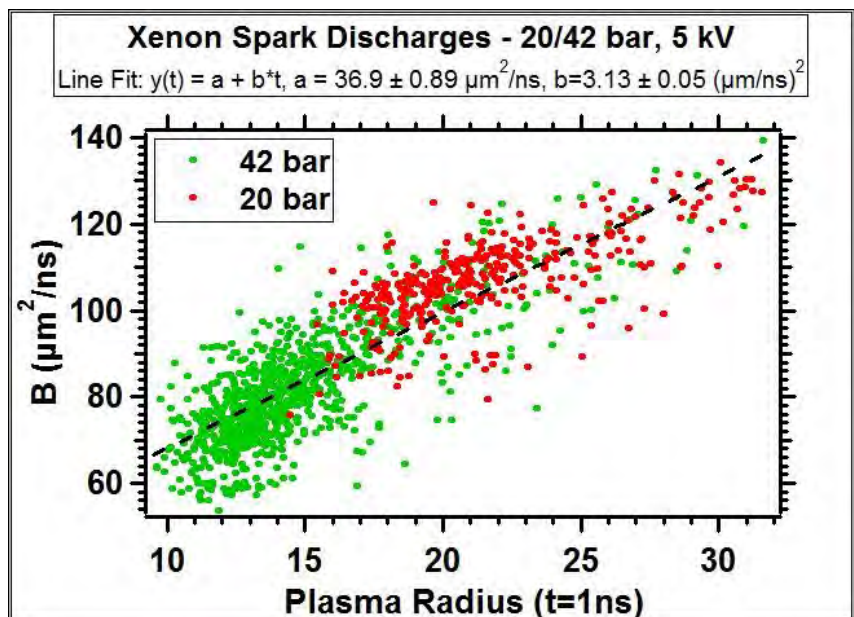
"Breakaway": The separation of a shock front from the luminous "fireball".
– Zel'dovich

Depths of blackbody can be probed by looking at shock speed later in time

Sedov-Taylor for cylindrical shock: $R(t) \sim \left(\frac{E}{\rho L}\right)^{1/4} \sqrt{t} = \sqrt{Bt}$



Experimental fits to shock speed at later times give the initial energy density.



Energy/particle is constant – independent of pressure and voltage (not shown)

By what phenomenon is the initial energy per particle limited?
And what phenomenon gives a constant luminous temperature up till breakaway?

1.

1. Report Type

Final Report

Primary Contact E-mail**Contact email if there is a problem with the report.**

puherman@ritva.ucla.edu

Primary Contact Phone Number**Contact phone number if there is a problem with the report**

3108252269

Organization / Institution name

UCLA

Grant/Contract Title**The full title of the funded effort.**

Energy Flow in Dense Off-Equilibrium Plasma

Grant/Contract Number**AFOSR assigned control number. It must begin with "FA9550" or "F49620" or "FA2386".**

FA9550-12-1-0062

Principal Investigator Name**The full name of the principal investigator on the grant or contract.**

Seth Putterman

Program Manager**The AFOSR Program Manager currently assigned to the award**

Jason Marshall

Reporting Period Start Date

04/01/2012

Reporting Period End Date

07/29/2016

Abstract

We created warm, dense plasmas with sonoluminescence, laser breakdown, and sparks – very different systems that all produce plasmas with a similar thermodynamic state. Probing sonoluminescence with visible-wavelength lasers yielded measurements of ionization potential lowering and collision times in dense plasmas, allowing us to distinguish between competing dense-plasma models. Hydrodynamic analysis of shockwaves generated by sparks yielded similar measurements in a different, more accessible system. Ultra-fast observations of laser breakdown have revealed a new phase of off-equilibrium plasma that has a tensile strength similar to a liquid, and reduced ion-electron collision cross-sections. By working at micron length scales, and nanosecond time scales, we are able to use table-top experiments to elucidate the properties of these exotic plasmas.

Distribution Statement**This is block 12 on the SF298 form.**

Distribution A - Approved for Public Release

Explanation for Distribution Statement**If this is not approved for public release, please provide a short explanation. E.g., contains proprietary information.****SF298 Form**

DISTRIBUTION A: Distribution approved for public release.

Please attach your [SF298](#) form. A blank SF298 can be found [here](#). Please do not password protect or secure the PDF. The maximum file size for an SF298 is 50MB.

[Form 298.pdf](#)

Upload the Report Document. File must be a PDF. Please do not password protect or secure the PDF. The maximum file size for the Report Document is 50MB.

[Energy Flow in Dense Off-Equilibrium Plasma - submitted.pdf](#)

Upload a Report Document, if any. The maximum file size for the Report Document is 50MB.

Archival Publications (published) during reporting period:

2. New discoveries, inventions, or patent disclosures:

Do you have any discoveries, inventions, or patent disclosures to report for this period?

No

Please describe and include any notable dates

Do you plan to pursue a claim for personal or organizational intellectual property?

Changes in research objectives (if any):

Change in AFOSR Program Manager, if any:

Extensions granted or milestones slipped, if any:

AFOSR LRIR Number

LRIR Title

Reporting Period

Laboratory Task Manager

Program Officer

Research Objectives

Technical Summary

Funding Summary by Cost Category (by FY, \$K)

	Starting FY	FY+1	FY+2
Salary			
Equipment/Facilities			
Supplies			
Total			

Report Document

Report Document - Text Analysis

Report Document - Text Analysis

Appendix Documents

2. Thank You

E-mail user

Jul 12, 2016 20:02:13 Success: Email Sent to: puherman@ritva.ucla.edu